

Biomimetic Formation of $CaCO_3$ Particles

Showing Single and Hierarchical Structures



Dissertation
zur Erlangung des Grades
Doktor der Naturwissenschaften (Dr. rer. nat.)
der Naturwissenschaftlichen Fakultät IV
Chemie und Pharmazie
der Universität Regensburg

vorgelegt von
Alina-Elena Voinescu

Regensburg 2008

Promotionsgesucht eingereicht am: 08. April 2008
Promotionskolloquium am: 13. Mai 2008

Die Arbeit wurde angeleitet von Prof. Dr. Werner Kunz

Prüfungsausschuss:

Vorsitzender:	Prof. em. Dr. Dr. h.c. Josef Barthel
1. Gutachter:	Prof. Dr. Werner Kunz
2. Gutachter:	Prof. Dr. Arno Pfitzner
3. Gutachter:	Prof. Dr. Georg Schmeer

For Adrian Marinescu

Acknowledgements

The present PhD project was undertaken at the Institute of Physical and Theoretical Chemistry, University of Regensburg (Germany) and it is my pleasure to thank numerous people, who became involved in many different ways.

First and foremost, I would like to thank my PhD supervisor, Prof. Werner Kunz, who offered me this fascinating topic and provided me the best scientific support. I am especially grateful to him for his constructive guidance during this time, which, combined with his stimulating participation, kept me motivated and always enthusiastic.

Sincere thanks go to Dr. Didier Touraud, who although initially not a fan of this project, he gave me all his guidance, support, encouragement and created an excellent base for a successful collaboration. He offered me always an advice when things got complicated.

Particular thanks are addressed to Prof. Stephen T. Hyde and Prof. Barry W. Ninham for having welcomed me warmly at the Research School of Physical Sciences and Engineering, Australian National University (ANU) and for giving me the opportunity to work at ANUEMU for three months. I would also like to thank them for their continuous interest in my studies and for the introduction in the biomorphs science.

I am indebted to Prof. Arno Pfitzner and part of his team (Irina Anusca, Alois Lecker, and Ulrike Schiessl) for their excellent collaboration and contribution in the field of crystallography.

I extend many thanks to Dr. Michael Faatz and Prof. Gerhard Wegner, Max Planck Institute (Mainz, Germany) for the helpful discussions concerning the formation of ACC. I acknowledge also Dr. Joel Gautron, INRA (Tours, France) for his comments and advices regarding the biological part of the Chapter 4. I thank Prof. Yves Bouligand, University of Angers (France) for his comments regarding the morphogenesis of ‘coralline’ silica-calcium carbonate.

I am grateful to Dr. Rainer Müller, University of Regensburg (Germany) and Dr. Ann-Kristin Larsson, ANU (Australia) for the competent initiation in infrared and scanning electron microscope analyses, respectively. I also thank Priv. -Doz. Dr. Lorenz Kienle (Max Planck Institute, Stuttgart, Germany), Dr. Thomas Burgemeister, Josef Kiermaier, W. Krutina and Björn Bartel, for performing HRTEM, ^{31}P NMR, ES-MS, elemental and EDX analyses, respectively.

Special thanks go to my lab mates, Barbara Widera and Sabine Raith, for their constant support and to my friends, Nina Vlachy, Jeremy Drapeau, Angelika Klaus, Viorica and Sigfried Binder, Mioara and Alexandru Campeanu, and Gerda and Ludwig Heitzer for the wonderful time I had with them and for helping me whenever I needed it.

Very warm thanks are reserved to all professors and colleagues from the institute, who created an ideal collaborative working atmosphere, important for me during the last years.

Finally, my deepest gratitude to my parents, Petrica and Elena, my brother, Marian, and my best friends, Anca Tig and Alin Maftei, for their never-ending support.

Table of Contents

Chapter 1 – Introduction	1
Chapter 2 – Theoretical Background.....	5
2.1. Biomineralization	5
2.2. Calcium Carbonate Mineralization	7
2.2.1. The Ions Involved.....	7
2.2.2. Classical Picture of Crystal Formation.....	10
2.2.2.1. Nucleation.....	11
2.2.2.2. Crystal Growth	12
2.2.3. Calcium Carbonate Polymorphs.....	14
2.2.3.1. Brief Depiction of Polymorphs	14
2.2.3.2. General Pathways of the Crystallization Process	16
2.2.3.3. Morphology and Polymorphs Selectivity Control in $CaCO_3$ Mineralization...	18
2.3. Properties of Egg White Lysozyme and Casein Proteins.....	26
2.3.1. Egg White Lysozyme	26
2.3.2. Casein Proteins	27
2.4. Biomorphs	29
2.5. References	34
Chapter 3 – Techniques.....	43
3.1. pH Measurements.....	43
3.2. Dynamic Light Scattering.....	43
3.3. Microscopic Techniques.....	45
3.3.1. Optical Microscopy	45
3.3.2. Electron Microscopy.....	46
3.3.2.1. Scanning Electron Microscope.....	47
3.3.2.2. Transmission Electron Microscope	48
3.4. Spectroscopic Techniques	49
3.4.1. Infrared Spectroscopy.....	50
3.4.2. Ultraviolet and Visible Spectroscopy.....	52
3.4.3. Nuclear Magnetic Resonance Spectroscopy	52
3.4.4. Mass Spectrometry	54
3.4.5. X-ray Diffraction	55
3.5. Chemical Composition	56
3.5.1. Energy Dispersive X-ray	56
3.5.2. CHNOS Elemental Analysis	57
3.6. References	57
Chapter 4 – The Formation of $CaCO_3$ Single-Crystal Particles Starting from Lysozyme Sols	59
4.1. Introduction	59

4.2. Experimental Section	61
4.2.1. Materials Preparation	61
4.2.2. Analytical Methods	62
4.2.2.1 Particle Characterisation	62
4.2.2.2 Techniques Used to Study the Lysozyme-Calcium Interaction	63
4.3. Results and Discussion	63
4.3.1. Influence of Lysozyme on the Metastable Form of $CaCO_3$	63
4.3.2. Ageing of the Ly-ACC Particles	67
4.3.2.1. Ly-ACC Nucleation, Lifetime and its Transformation to the Calcite Phase during the first Hour after Reactant Mixing	67
4.3.2.2. The Amorphous Precipitate left in Contact with Mother Liquor for 24 h	69
4.4. Conclusions	71
4.5. References	71

Chapter 5 – Initiation of Vaterite-Aragonite Particles with a Complex Morphology from Silicate-Casein Sols 75

5.1. Introduction	75
5.2. Experimental Section	77
5.2.1. Materials Preparation	77
5.2.2. Analytical Methods	78
5.3. Results	79
5.3.1. The Addition of Ca^{2+} Ions into the Alkaline Silica Solution and, subsequently, the Diffusion of Atmospherical CO_2	79
5.3.1.1. Early Stage of Precipitation Process	79
5.3.1.2. Later Stage of Precipitation Process	80
5.3.2. ^{31}P NMR Spectra of <i>Na</i> Caseinate Sols with and without Silicate Ions	80
5.3.3. The Addition of Ca^{2+} Ions into the <i>Na</i> Caseinate Solution and, subsequently, the Diffusion of Atmospherical CO_2	81
5.3.3.1. Early Stage of Precipitation Process	81
5.3.3.2. Later Stage of Precipitation Process	83
5.3.4. The Addition of Ca^{2+} Ions into the Silica- <i>Na</i> Caseinate Solution and, subsequently, the Diffusion of Atmospherical CO_2	83
5.3.4.1. Early Stage of Precipitation Process	83
5.3.4.2. Later Stage of Precipitation Process	83
5.3.4.3. Morphogenesis of Particles	86
5.3.4.4. Chemical Composition	88
5.3.4.5. Crystal Polymorphism	89
5.4. Discussion	91
5.4.1. The Addition of Ca^{2+} Ions into the Alkaline Silica Solution and, subsequently, the Diffusion of Atmospherical CO_2	91
5.4.2. The Addition of Ca^{2+} Ions into the <i>Na</i> Caseinate Solution and, subsequently, the Diffusion of Atmospherical CO_2	92
5.4.3. The Addition of Ca^{2+} Ions into the Silica- <i>Na</i> Caseinate Solution and, subsequently, the Diffusion of Atmospherical CO_2	93
5.5. Conclusions	94
5.6. References	95

Chapter 6 – Hierarchical Materials of $CaCO_3$ – Silica Composites..... 99**6.1. The Efficacy of TEOS as a new Silica Source for the Formation of Carbonate-Silica Composite Materials 99****6.1.1. Introduction 99****6.1.2. Experimental Section 101**

6.1.2.1. Materials Preparation..... 101

6.1.2.2. Analytical Methods..... 102

6.1.3. Results and Discussion 102

6.1.3.1. Influence of Ethanol on the Basic Hydrolysis of TEOS..... 102

6.1.3.2. Influence of Ethanol on Structure Formation of Biomorphs..... 104

6.1.3.3. Effect of pH on the Formation of Silica-Carbonate Biomorphs..... 107

6.1.4 Conclusions 111**6.1.5. References..... 111****6.2. Inorganic Self-Organised Silica Aragonite Biomorphic Composites 113****6.2.1. Introduction 113****6.2.2. Experimental Section 115**

6.2.2.1. Materials Preparation..... 115

6.2.2.2. Analytical Methods..... 115

6.2.3. Results..... 1176.2.3.1. Histogram of Calcium Carbonate Crystal Fractions as a Function of the Ca^{2+} Concentration..... 117

6.2.3.2. Optical and Electron Microscopy 118

6.2.3.3. Leaching Experiments 120

6.2.3.4. Influence of the Counterions 121

6.2.3.5. Crystal Polymorphism 121

6.2.3.6. Morphogenesis of ‘Coralline’ Particles 125

6.2.4. Discussion 126**6.2.5. Conclusions..... 128****6.2.6. References..... 128****6.3. Why Calcium Ions Behave so Different from its Homologue, Barium, in Alkaline Silica Sol? 131****6.3.1. Introduction 131****6.3.2. Experimental Section 132**

6.3.2.1. Materials Preparation..... 132

6.3.2.2. Analytical Methods..... 139

6.3.3. Results..... 139

6.3.3.1 Attempts to Prepare Filamentous Particles of Self-Organised Silica-Calcium Carbonate without using any type of Additives 141

6.3.3.2 Attempts to Prepare Filamentous Particles of Self-Organised Silica-Calcium Carbonate using Additives..... 145

6.3.4. Discussion	150
6.3.5. Conclusions	157
6.3.6. References	158
Chapter 7 – Conclusions and Summary	161
Chapter 8 – Appendices	165
8.1. Reactions Occurring during the Precipitation Process of $CaCO_3$	165
8.2. Lysozyme-Calcium Interactions	166
8.3. Self-Assembled ‘Floral Dumbbell’ Silica-Calcium Carbonate	169
8.4. List of Abbreviations.....	171
8.5. List of Symbols	173
8.6. List of Figures	175
8.7. List of Tables.....	183
8.8. List of Publications and Presentations	184
8.9. Curriculum Vitae	186

Chapter 1

Introduction

Biomaterials are remarkably examples of nature's ability to produce *bioorganic-inorganic* composites on several length scales ranging from the nanometre to the macroscopic scale. They exhibit distinct geometric shapes that can be classified as either amorphous, polycrystalline or single crystal in structure. These amazing materials contain multiple functions in nature; for example many living organisms (humans, birds as well as corals and molluscs) incorporate minerals into their body structures for support, protection and cellular processes. For this reason, today's biologists, chemists, physical chemists, and engineers are reunited under the same umbrella to synthesise materials identical in properties with those naturally produced. They consider nature as a model and an educator trying to understand and imitate it. Thus, a new area in science appeared, called *biomimetics*. The term itself is derived from *bios*, meaning life, and *mimesis*, meaning to imitate. This new science represents the study and imitation of nature's methods, designs, and processes.

During my thesis, three biomimetic systems were in my attention. All three systems involve the mineralization of calcium carbonate, $CaCO_3$, which is an important biogenic mineral used by nature as an inorganic component in exoskeletons and tissues of many mineralising organisms. For example, chickens and other birds have eggshells made of calcium carbonate. Other animals, such as corals and molluscs, use calcium carbonate to produce protective coverings. In medicine, it is used as a calcium supplement or as an antacid. It is also important in industry, where it is used in coatings and fillers.

The aim of this thesis is to seek answers to the following questions: Has the lysozyme-mineral interaction an implication in the building of amorphous materials and their ageing? Can silicate-casein interaction alter the calcium carbonate mineralization in aqueous sols? Is tetraethylorthosilicate (TEOS) a better alternative silica source for the growth of biomorphs? Can biomorphs-like aggregates of calcium carbonate be prepared? Why calcium ions behave so different from its homologue barium, in alkaline silica sols?

The thesis is organized as follows. **Chapter 2** presents a short overview about the principles and the concepts of calcium carbonate mineralization as well as the properties of the proteins involved in this work and a short introduction on biomorphs.

Chapter 3 describes briefly the physicochemical techniques used in the present work. Thereafter, the thesis continues with three chapters that represent the *results section* of the thesis.

Chapter 4 describes a possible influence of egg white lysozyme, an important protein which is present in the shell of eggs, on the precipitation of amorphous calcium carbonate (ACC) *in vivo* and its transition to calcite during eggshell calcification. The mineralization of the calcitic eggshell is simulated by starting from lysozyme- CaCl_2 - $\text{CO}(\text{OCH}_3)_2$ - NaOH solution. A transformation to the final crystalline biomineral, calcite, is observed. This report may be also of general interest to understand protein-mineral interaction in the building of amorphous materials and their ageing.

Chapter 5 discusses the formation of novel crystalline CaCO_3 particles starting from silicate-casein sols. The formed particles have a complex morphology and a hierarchical structure. This is an interesting system with a significant complexity, which is also often found in biominerals.

Chapter 6 contains three subheadings regarding the formation of hierarchical materials of carbonate-silica composites. Thus, *subheading 6.1* reports results of the formation of carbonate-silica composite materials known as ‘biomorphs’ using TEOS as an alternative silicate source. We observed that the basic hydrolysis of TEOS furnishes silica in a controllable fashion, allowing a significantly higher reproducibility of the obtained silica-barium and silica-strontium carbonate co-precipitates compared to commercial water glass silica used so far. We further discuss the influence of ethanol, used as a co-solvent, on the

morphologies of biomorphs. *Subheading 6.2* deals with the formation and the growth of novel curvilinear morphologies in inorganic composites containing crystalline aragonite and amorphous silica. These biomimetic morphologies show remarkable hierarchical structures with structural similarity to natural corals. The significance of this work is that the realm of biomorphs is shown to extend beyond the previously studied barium and strontium carbonates, to now include calcium carbonate. The extension of the biomorphs work to calcium carbonate is an important step as $CaCO_3$ is an important biomineral. In addition, we show here that the formation and the growth of calcium-based biomorphs require specific conditions to favour the orthorhombic polymorphic (aragonite – the common $CaCO_3$ phase in biominerals) rather than the stable trigonal polymorph (calcite). Such system can serve as a model for the complex and often hardly accessible natural archetypes with the possibility to reveal principles of the complex hierarchical structure formation. Previously reported work on this topic has not been successful. *Subheading 6.3* describes attempts to transfer the helicoidal morphology of biomorphs – the most outstanding features of barium or strontium carbonate silica biomorphs – onto calcium carbonate. In addition, we will try to give a reasonable explanation to the last question written above.

Finally, **Chapter 7** concludes the thesis by summarising its results and **Chapter 8** contains nine appendices including supporting information of the previous chapters, lists of abbreviations, symbols, figures and tables as well as a list of the scientific activity of the author comprising publications, oral presentations, and posters performed during the doctoral program.

Chapter 2

Theoretical Background

2.1. Biomineralization

Biomineralization is the process by which living organisms form inorganic structures (i.e., biominerals)¹. Biologically, two distinct ways are known to generate biominerals, namely *biologically induced mineralization* and *biologically controlled mineralization*². In the first case, the organism modifies its local environment creating conditions suitable for chemical precipitation³. So, the process is unintended, uncontrolled and irreproducible. The best known examples are the pathological mineralization, such as kidney and biliary stones, and the deposition of minerals by bacteria. In contrast, *biologically controlled mineralization* is a highly regulated process² that occurs within two biological sites (i.e., intracellular and extracellular) and involves two steps: the selective absorption of the elements from the environment and their incorporation into biominerals under biological and chemical control. The key mediator of the *biologically controlled mineralization* process is a preformed insoluble macromolecular framework present in the environment and called organic matrix². The matrix subdivides the mineralization spaces⁴, offers structural support and mechanical strength to an organism, and it is interfacially active in nucleation^{5, 6}. The framework macromolecules found in bones, shells and plants are collagen, chitin and cellulose, respectively. Finding a solution to mimic and to understand both ways of biomineralization process is essential for the fields of palaeontology, marine chemistry, sedimentology and medicine.

The inorganic chemical composition of biominerals is dominated by calcium carbonate, calcium phosphate and silica. Of these, calcium carbonate is the most familiar biomineral, found in biological systems in a number of different forms including amorphous calcium

carbonate (ACC), vaterite, aragonite and calcite. The first two polymorphs are less abundant in nature than the last two. For example, many organisms, such as molluscs⁷, echinoderms⁸, calcisponges⁹, corals¹⁰, certain algae¹¹, chicken eggs, human ear² and other¹², form their hard parts out of calcite and aragonite. However, recently studies suggest that, in most of the cases, ACC phase is in fact the precursor phase of the other polymorphs. Beniash et al.^{13, 14} is the first who reported that the larva of the sea urchin, an echinoderm, forms its calcitic spicules from an amorphous calcium carbonate precursor phase. Mollusc larvae have also been found by Weiss et al.¹⁵ to form their aragonitic shells from such a precursor phase¹⁶. Likewise, adult sea urchins⁷ and quails¹⁷ apparently follow the same way for generating their carbonate skeleton. Moreover, corals and crustaceans use this approach to produce their skeletons as well^{18, 19}. Because molluscs, echinoderms, crustaceans as well as corals and eggs are on different classes of animals, it seems likely that many other organisms could follow the same strategy. According to Meldrum²⁰, this phase is easy to overlook when present in combinations with crystalline phases, and so it may be more common than is currently believed. Figure 2.1 shows examples of biominerals with hierarchical structures consisting of calcium carbonate polymorphs.

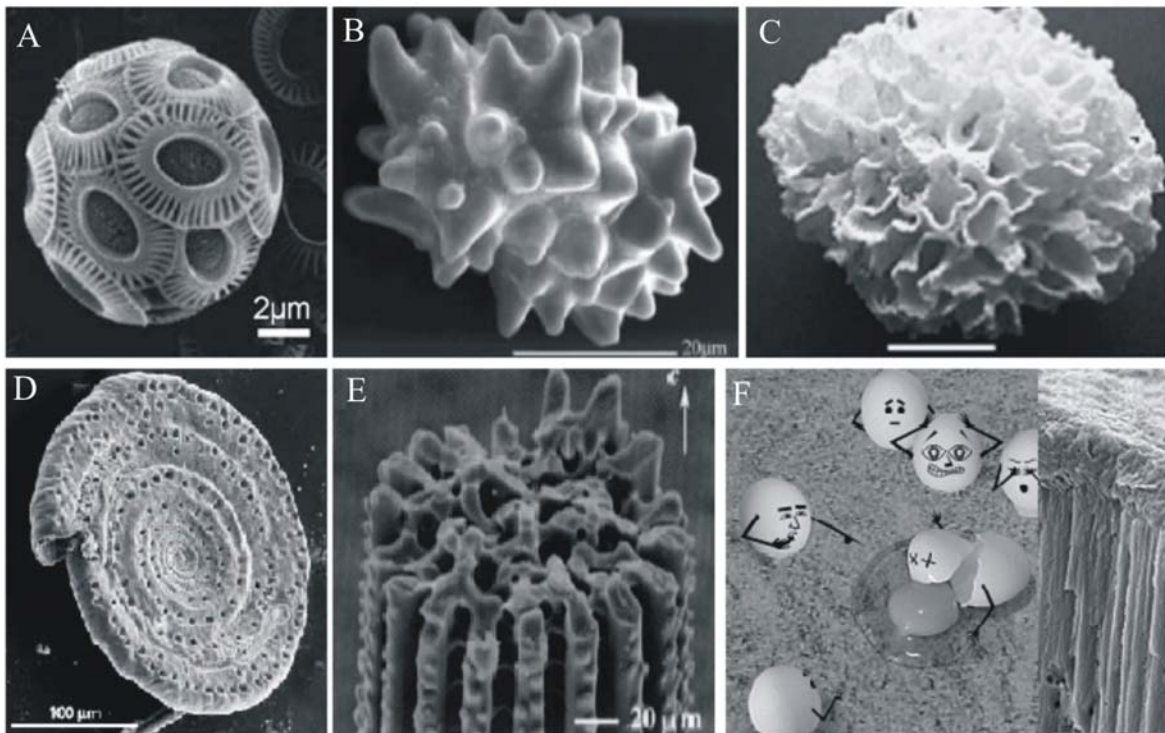


Figure 2.1 Examples of biominerals. (A) Coccosphere of *E. huxleyi* composed of calcite plates called coccoliths. (Reproduced from [3]) (B) Cystolith from the leaves of *Ficus microcarpa* composed of stable ACC. (Reproduced from [21]) (C) Natural coral from the south-eastern Australian seaside composed of aragonite. (D) Whole shell of the foraminifera *Spirillina* supposed to arise from a transient of amorphous calcium carbonate phase. (Reproduced from [7]) (E) Fracture surface of a young spine, showing the sponge structure of the stereom. (Reproduced from [22]) (F) Eggs. Inset: a cross-section through a formed eggshell which reveals the vertical calcite crystal layers. (Reproduced from [23])

2.2. Calcium Carbonate Mineralization

2.2.1. The Ions Involved

Calcium Ion, Ca^{2+}

When life originated on earth, calcium (the name derived from the Latin word *calx* meaning *limestone*) was abundant in the igneous rocks²⁴, present in the earth's hot crust, and was unavailable for use by living matter²⁵. As the earth cooled, various chemical and biological reactions appeared and, thus, calcium became the chemical basis of many compounds essential for life. The biogeochemistry of calcium²⁶ is shown in Figure 2.2.

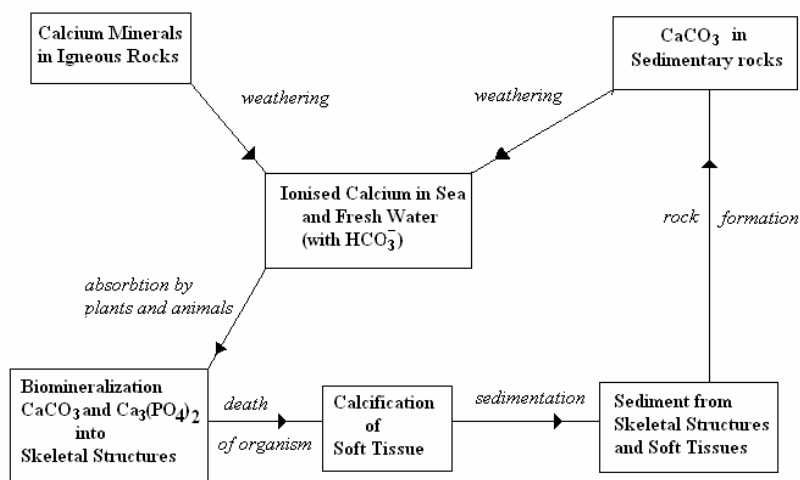


Figure 2.2 The biogeochemistry of calcium. The precipitation of calcium carbonate and phosphate are the major inorganic constituents of skeletal structures. (Redrawn after [26])

Calcium is an earth-alkaline element with the atomic number 20 and a radius of 0.99 Å. The story of calcium began in 1808, when Humphry Davy isolated this element from alkaline earth²⁷. Later on, Sydney Ringer first demonstrated the biological significance of calcium; for example: its role in egg fertilization²⁸ and development of tissues²⁹ (bones, teeth and shells). Further, calcium has been found to be involved in the conduction of nerve impulse to muscle³⁰, in the plant growth³¹ and to maintain the cytoskeletal architecture of all cells³². Calcium forms part also of biogeochemical compounds that include carbonates (calcite, aragonite and vaterite), sulphates (gypsum), phosphates (apatite) and silicates.

The wide-range of the calcium's role lies in the chemistry of this element³³ (molecular structure, irregular geometry, valence state, binding strength, ionization potential and kinetic parameters in biological reactions). Its chemical proprieties are similar with barium and strontium which have been found to be able to substitute the requirement of Ca^{2+} ions, for example in regulating enzyme activity^{34, 35}. However, in Chapter 6, we will observe the contrary.

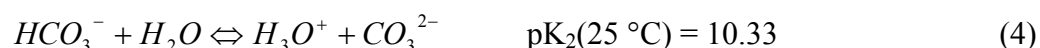
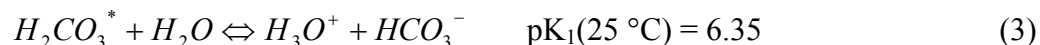
Carbonate Ion, CO_3^{2-}

The carbonate ion is a polyatomic anion consisting of one central carbon atom surrounded by three identical oxygen atoms in a trigonal planar arrangement with a $\text{O}-\text{C}-\text{O}$ bond angle of 120° . It is formed by dissolving carbon dioxide in water.

According to Henry's law, carbon dioxide ($CO_{2(g)}$) dissolves in water and further reacts with water forming carbonic acid³⁶, H_2CO_3 . Carbonic acid is an unstable intermediary of the reaction first isolated by Loerting et al.³⁷. We note that only a certain amount of the dissolved $CO_{2(aq)}$ exists as H_2CO_3 .



In aqueous solutions, carbonic acid is in equilibrium with hydrated carbon dioxide³⁸, $H_2CO_3^*$ (conventionally, both are treated together as they were one substance), and dissociates in two steps:



The relative concentrations of $H_2CO_3^*$ and the deprotonated forms, HCO_3^- (bicarbonate) and CO_3^{2-} (carbonate), depend on the pH (Figure 2.3)³⁹.

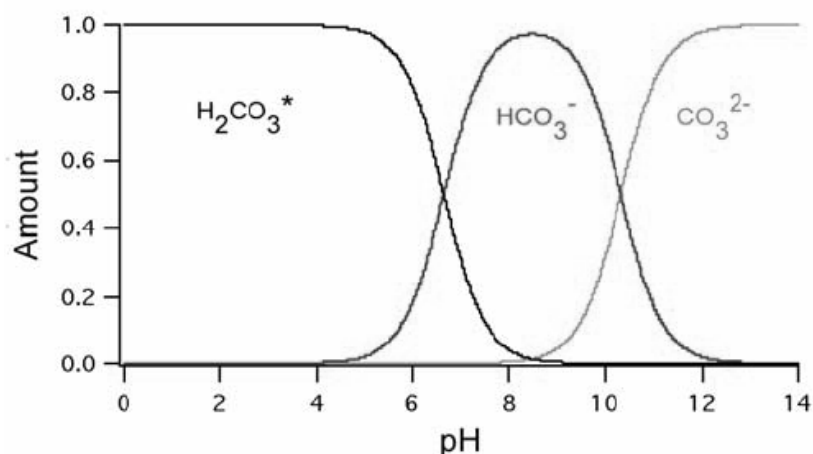


Figure 2.3 Distributions of the carbonate species in relation to the pH of the solution. $H_2CO_3^*$, represents the sum of dissolved CO_2 and H_2CO_3 , and predominates at low pH range. HCO_3^- is the most abundant species at intermediate pH values; CO_3^{2-} dominates at high pH values. (Reproduced from [39])

2.2.2. Classical Picture of Crystal Formation

The calcium carbonate salt forms when the positively charged calcium ion attaches to the negatively charged oxygen atoms of the carbonate ion. The onset of the $CaCO_3$ crystals in solution is determined by a critical factor called the solubility product (K_{sp}), which indicates the level of supersaturation of a solution. When the solubility product is less than the activity product (K_{ap}) of a solution then the precipitation occurs until $K_{sp} = K_{ap}$.

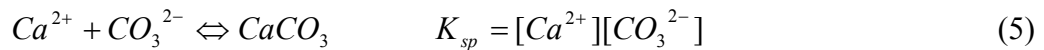


Figure 2.4 schematically shows a general precipitation mechanism proposed by Nielsen⁴⁰. We observe that the formation of crystals proceeds in two either consecutive or simultaneous steps, i.e., formation of nuclei (nucleation) and crystal growth⁴¹. This two steps draw up the classical picture of crystallization.

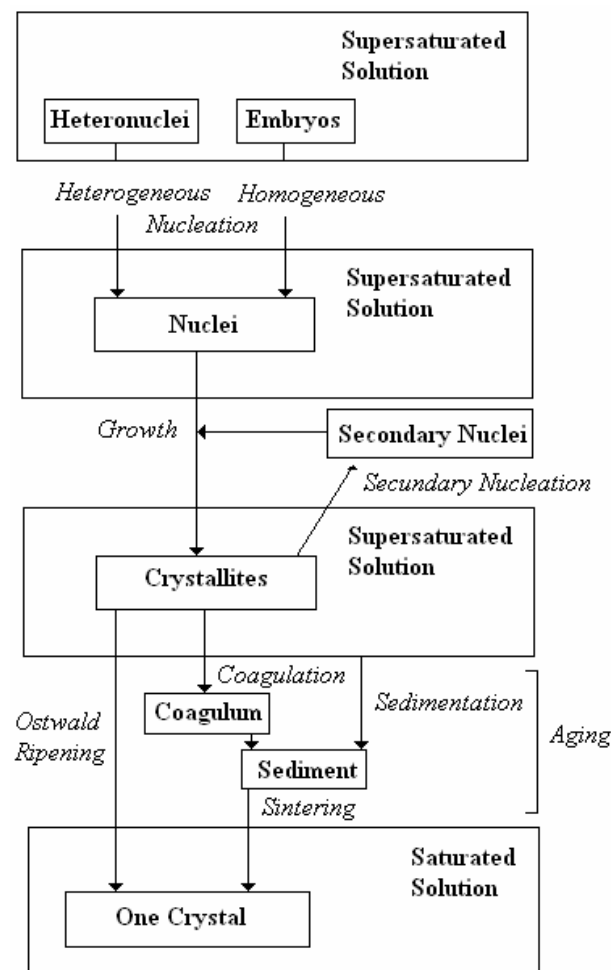


Figure 2.4 A concept of the crystallization process. (Redrawn after [40])

2.2.2.1. Nucleation

There are two types of nucleation: *homogeneous nucleation* and *heterogeneous nucleation*. The first occurs spontaneously and randomly in a supersaturated solution free of foreign objects. The nuclei form through associations of solutes. The second involves the formation of nuclei by adsorbing the solutes on the surface of the heterogeneous solid particles (e.g. impurities) present in the solution, which can act as a template for crystallization. Without the presence of the nucleator substrate, the heterogeneous nucleation is thought to occur on the tube walls.

When a nucleus forms, a surface is created that separates two volumes, namely the cluster and the solution. The free energy of formation of a cluster, ΔG_N , is the sum between the interfacial surface, ΔG_I , and bulk energies, ΔG_B . Assuming that the cluster has a spherical form, ΔG_B has a negative value and is proportional to the cube of the radius of the cluster, whereas ΔG_I has a positive value and is directly proportional to the r^2 (Figure 2.5).

$$\Delta G_N = \Delta G_B + \Delta G_I = -\frac{4\pi r^3}{3V} \Delta G_V + 4\pi r^2 \sigma \quad (6)$$

In which, ΔG_V represents the free energy per mole associated with the solid-liquid phase change, V is the molar volume and σ is the interfacial free energy per unit surface area.

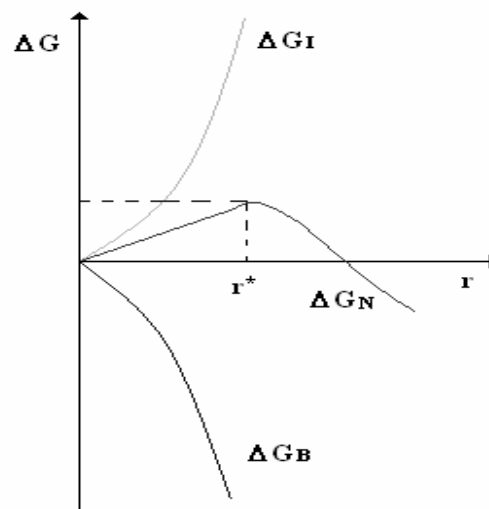


Figure 2.5 Free energy of nucleation as a function of cluster size.

As seen in the Figure 2.5, ΔG_N curve shows a maximum, which corresponds to the critical cluster size, r^* . This is the minimum size that must be formed by atoms clustering together in the bulk, before the solid particle is stable and begins to grow. The energy required for the formation of the critical radius, $r^* = \frac{2\sigma V}{\Delta G_v}$, is called the activation energy for homogeneous nucleation and is given by:

$$\Delta G_N^* = \frac{16\pi\sigma^3 v^2}{3(kT \ln S_R)^2} \quad (7)$$

The activation energy depends on the interfacial energy of the critical nucleus and the level of supersaturation (S_R). Thus, when the cluster has reached a certain critical size, the volume term takes over, and the free energy decreases.

2.2.2.2. Crystal Growth

When the supersaturation level falls to the equilibrium, then the growth of the crystal nuclei occurs. The growth rate², J_G , is given by:

$$J_G = k(S_A)^x \quad (8)$$

where k is the rate constant and S_A is the absolute supersaturation raised to the power x . In principal, there are three models involved in the crystal growth and these depend on the supersaturation level.

Under moderate supersaturation ($x = 1$), the crystals grow by the classical layer-by-layer mode furnished by Stranskii⁴² and Kossel⁴³. Figure 2.6 A shows a graphical representation of this mechanism that involves a surface of the crystal having active sites, called step (s) and kink (k). The kink sites have higher binding energy than the steps and are the most favourable positions for the incorporation of the ions into the solid phase. This model includes the following consecutive steps²: (i) bulk diffusion of ions A from solution to the crystal surface; (ii) absorption of ions on the surface of crystal and dehydration of ions on the crystal terraces B ; (iii) diffusion on the surface in a two-dimensional way to reach the step C ; (iv) one-dimensional diffusion along the step to the kink site D ; (v) integration of ions into the kink site E .

At higher supersaturation ($x > 2$), the growth process is governed generally by the two-dimensional growth mechanism (Figure 2.6 B). This model consists in multiple two-dimensional surface nuclei formed on the crystal surfaces that spread by further incorporation of ions into the kink site.

At lower supersaturation ($x = 2$), the predominant growth mechanism can be described by the screw-dislocation model proposed by Frank⁴⁴. The growth is induced by crystals with lattice defects, which are sites for further crystal growth (Figure 2.6 C).

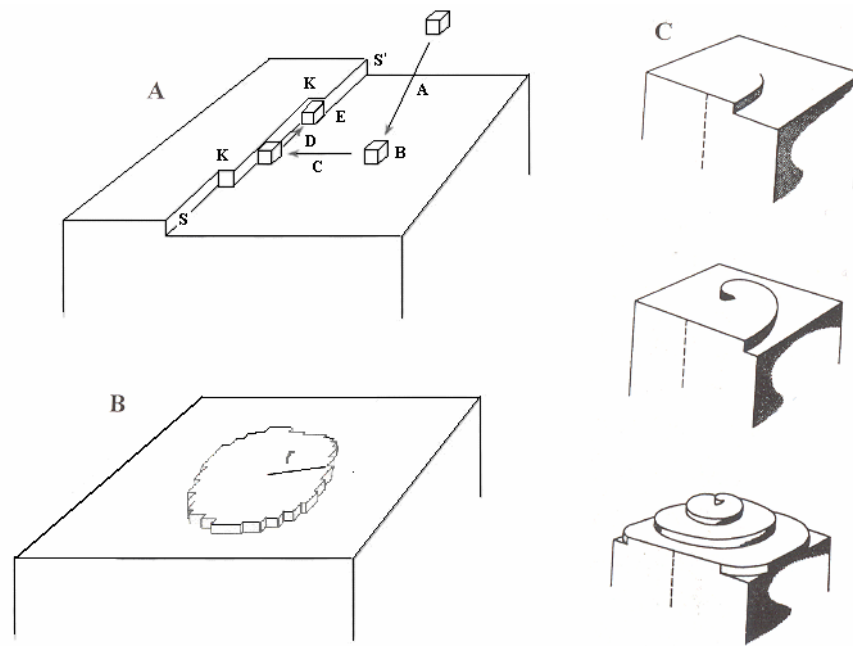


Figure 2.6 (A) Layer-by-layer mechanism of crystal growth. (The scheme is partly based on that in [41]) (B) Two-dimensional mechanism. (Reproduced from [41]) (C) Screw-dislocation mechanism. (Reproduced from [2])

In reality, the crystal growth mechanism from aqueous solution is more complex than described above. During the ageing time of particles in the mother liquor, other process, such as coagulation, sedimentation and/or Ostwald ripening, can also occur (Figure 2.4). Furthermore, the reactions 1 to 5 are not the only reactions occurring during the precipitation process of $CaCO_3$; 12 more reactions may proceed⁴⁵ (Appendix 1), which show the complexity of the system.

2.2.3. Calcium Carbonate Polymorphs

2.2.3.1. Brief Depiction of Polymorphs

Polymorphs are minerals with the same chemical composition but a different arrangement of the ions in the crystal lattice. Calcium carbonate exists in six forms that are divided into three classes: well-known anhydrous crystalline polymorphic forms (calcite, aragonite and vaterite), hydrated crystalline forms (calcium carbonate monohydrate (MCC), calcium carbonate hexahydrate (ikaite)) and amorphous calcium carbonate (ACC). Table 2.1 summarizes the crystallographic and physical data of the all calcium carbonate forms.

Calcite, first observed by Bridgman⁴⁶, is deposited extensively as a biomineral due to its high thermodynamically stability at ambient temperature⁴⁷. It has a rhombohedral crystal structure, consisting of Ca^{2+} ions and planar CO_3^{2-} groups, located in alternate layers and orientated perpendicular to the c axis (Figure 2.7). Each Ca^{2+} ion has six immediate CO_3^{2-} neighbours, orientated in such a way that one oxygen from each forms the immediate neighbours of calcium²⁰.

Aragonite is thermodynamically less stable than calcite but occurs also often in biological and geological samples. It has an orthorhombic crystal structure with the same alternating structure⁴⁸ of Ca^{2+} and CO_3^{2-} ions as calcite (Figure 2.7). In aragonite, however, the CO_3^{2-} layers are split into layers parallel to the a axis and each Ca atom is surrounded by nine closest oxygens.

Vaterite is metastable with respect to calcite and aragonite and is rare in nature. It has a hexagonal crystal structure (Figure 2.7) and a similar alternating structure with calcite and aragonite. In contrast to aragonite and calcite, the plane of CO_3 is parallel to the c axis⁴⁷.

Table 2.1 Crystallographic and physical data of the different calcium carbonate phases. (The table is partly based on the corresponding one in [49])

Property	Calcite	Aragonite	Vaterite	MCC	Ikaite	ACC
Formula	$CaCO_3$	$CaCO_3$	$CaCO_3$	$CaCO_3 \cdot H_2O$	$CaCO_3 \cdot 6H_2O$	$CaCO_3 \cdot nH_2O$ $0 < n > 1$
Solubility Product ^{50,51} (25 °C) K_{sp} (mol/L)	$10^{-8.48}$	$10^{-8.34}$	$10^{-7.91}$	$10^{-7.39}$	$10^{-6.62}$	$10^{-6.40}$
Space Group	$R\bar{3}c$	Pmcn	$P6_3/mmc$	$P3_112$	C2/c	---
Point Group	$\bar{3}2/m$	2/m 2/m 2/m	6/m 2/m 2/m	32	2/m	---
Crystal System	trigonal ⁵²	orthorhombic ⁵³	hexagonal ⁵⁴	trigonal ⁵⁵	monoclinic ⁵⁶	---
Lattice Constants ⁵⁷ (Å)	$a = b = 4.99$ $c = 17.062$ $\gamma = 120^\circ$	$a = 4.959$ $b = 7.964$ $c = 5.738$ $\alpha = \beta = \gamma = 90^\circ$	$a = b = 4.13$ $c = 8.490$ $\gamma = 120^\circ$	$a = b = 10.55$ $c = 7.544$ $\gamma = 120^\circ$	$a = 8.792$ $b = 8.312$ $c = 11.012$ $\beta = 110.53^\circ$	---
Density (g/cm ³)	2.71	2.93	2.65	2.43	1.83	1.6
Abundance	very common	common	rare	very rare	very rare	common

$CaCO_3 \cdot H_2O$ and $CaCO_3 \cdot 6H_2O$ are unstable with respect to the anhydrite forms^{58, 59}. There are only a few examples of calcium carbonate monohydrate in biology (marine sediments⁶⁰) and none of the ikaite.

ACC, first synthesized in vitro by Johnson et al.⁶¹, is thermodynamic unstable and has a higher solubility than all the other polymorphs. However, it has been widely found in biological organisms⁵ (see Section 2.1). There are two forms of ACC in nature: a stable form and a transient form. The stable form is hydrated, containing circa 1 mol of water per mole of $CaCO_3$, with water present in the coordination spheres around calcium. The transient form, however, contains little if any water and shows short range order very similar to that of calcite⁶².

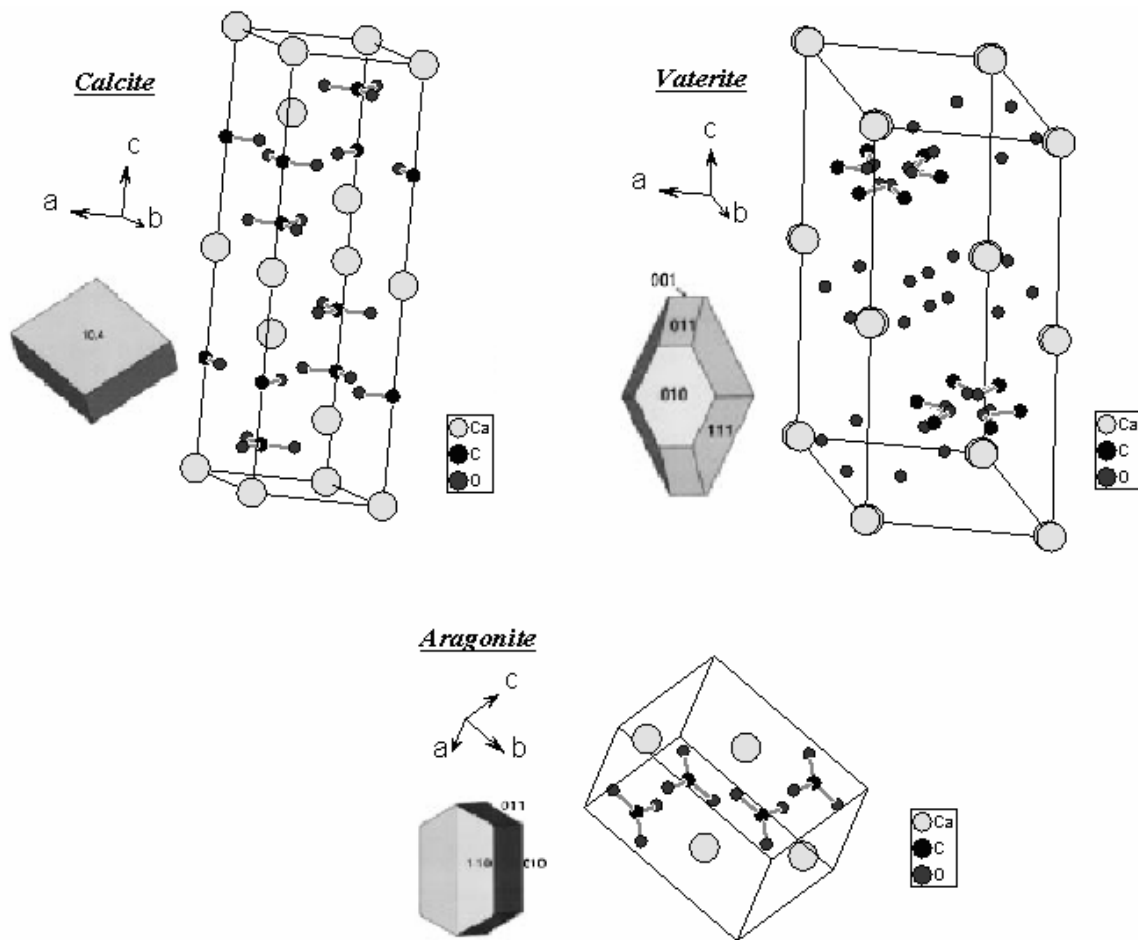


Figure 2.7 Schematic representation of the crystal morphologies (Reproduced from [57]) and the crystal structure of anhydrous CaCO_3 polymorphs. The crystal structures were drawn with *Endeavour* software.

2.2.3.2. General Pathways of the Crystallization Process

As shown in Figure 2.8, whether a system follows a one step route to the final mineral phase (pathway A) or proceeds via sequential precipitation (pathway B), depends on the activation energy barriers² of nucleation (N), growth (g) and transformation (i).

The most important factor in controlling the crystallization pathway is the structure of the critical nucleus. When the nucleus involves strong interaction between the ions, then the pathway A should be considered. This is in agreement with macroscopic thermodynamics⁶³, stating that the phase that is formed first is the one having the lowest free energy. When the nucleus involves weak interactions between the ions, the amorphous

phase is precipitated first, followed by a polymorphic series, consistent with Ostwald* step rule⁶⁴ and pathway *B* in Figure 2.8.

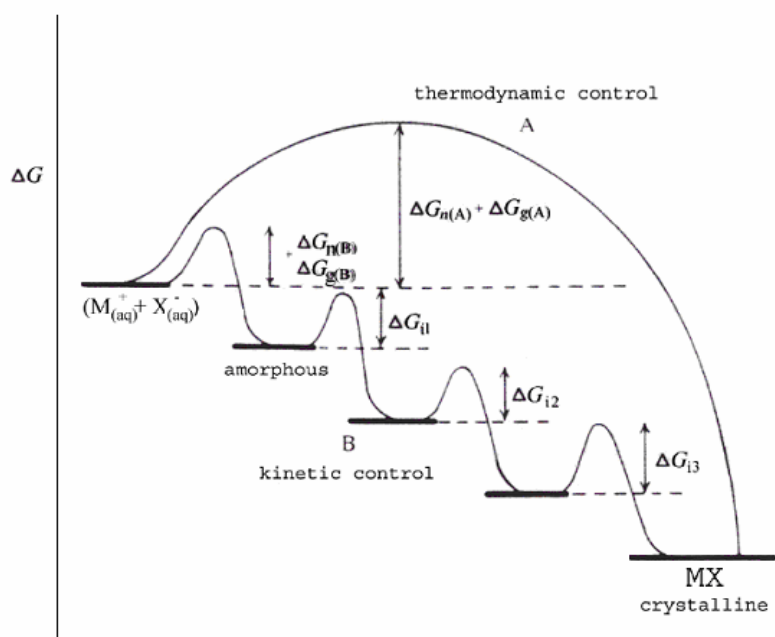


Figure 2.8 Pathways to crystallization and polymorph selectivity: (A) direct and (B) sequential. (Reproduced from [49])

Nowadays, one can predict the sequence of polymorphs produced in crystal growth due to an empirical observation called the Ostwald-Lussac law of stages⁶⁵, stating that under conditions of sequential precipitation, the initial phase formed is the one with the highest solubility followed by hydrated polymorphs and then a succession of crystalline phases in order of decreasing solubility. Thus, for calcium carbonate crystallization, we just have to read off the solubility product from the Table 2.1 and the order shown in Figure 2.9 will follow.

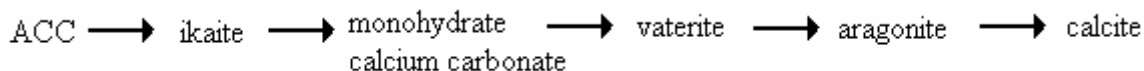


Figure 2.9 Sequence of calcium carbonate polymorphs based on Ostwald-Lussac law of stages.

* In 1867, Ostwald formulated his step rule, stating that the crystal phase that is nucleated from the melt need not be the one that is thermodynamically most stable, but the one that is closest in free energy to the fluid phases.

However, Rieger et al.⁶⁶ found that this sequence may be only true for the case of low supersaturation. In contrast, at high supersaturation, the appearance of ACC is preceded by even another precursor stage where a spinodal-like phase separation between a denser and a less dense phase occurs. Only by restructuring of this short-lived structure does the ACC form. This route was also supposed by Faatz et al.⁶⁷, who postulate a liquid-liquid phase segregation with a lower critical solution temperature point at about 10 °C in a saturated calcium carbonate solution without additives (Figure 2.10).

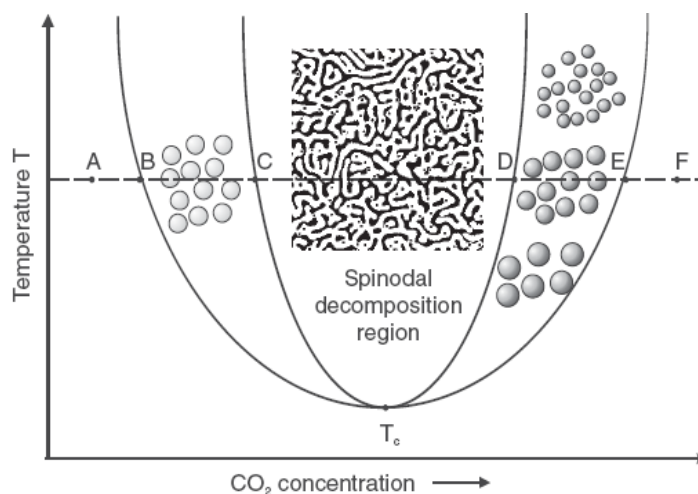


Figure 2.10 Schematic virtual phase diagram that explains the formation of spherical particles by liquid-liquid phase segregation. (Reproduced from [67])

2.2.3.3. Morphology and Polymorphs Selectivity Control in CaCO_3 Mineralization

Biologically, it is important to know how to stop the process at a particular structure in order to be able to understand how the nature produces its own calcium carbonate biominerals. According to the research done so far, the formation of a certain polymorph is kinetically controlled by changing the external parameters, such as temperature, pressure, etc. and/or by adding inorganic and/or organic additives. Moreover, these factors lead also to dramatic modifications in the crystal morphology.

a). Amorphous Calcium Carbonate

As mentioned above, ACC is highly unstable and rapidly transforms into a crystalline phase. Under these conditions, a detailed physical-chemical characterisation of this phase is difficult to obtain due to its short life. This is confirmed by several methods including

bubbling CO_2 through a calcium salt solution^{68, 69} or mixing of saturated solutions of calcium and carbonate salts^{70, 71}. However, Faatz et al.⁶⁸ propose a method, in which the release of carbon dioxide by the hydrolysis of a dialkyl carbonate takes place homogeneously in aqueous solution and on a timescale ideally suited for physical-chemical experiments. Likewise, certain organic and inorganic additives have been used to inhibit the transformation of ACC. Loste et al.⁷² demonstrate that *Mg* incorporation within amorphous calcium carbonate retards the transformation into crystalline phase, and that this effect increases with the quantity of magnesium occluded within the ACC structure. Xu et al.⁷³ and DiMasi et al.⁷⁴ report how polyacrylic acid prolongs the lifetime of ACC by sequestering locally Ca^{2+} ions. Additionally, the presence of *EDTMP* (ethylenediamine-N,N,N',N'-tetrakis(methylenephosphonic acid))^{75, 76}, phosphorus-containing compounds⁷⁷ or poly(propylenimin)-dendrimers⁷⁸ retards also the ACC transition. Donners et al.⁷⁹ report on a synthetic system in which aggregates, consisting of assemblies of poly(propylene imine) dendrimers modified with long hydrocarbon chains and single chain surfactants, stabilised spheroids of ACC for 14 days. Recently, this time is prolonged up to three months by using small phytic acid molecules with a tremendous phosphate group density and resulting in ACC with hollow spherical superstructure⁸⁰.

b). Vaterite, Aragonite and Calcite

b₁. Influence of Temperature and Pressure

Earlier studies show that the temperature^{81, 82} and the pressure⁸³ have a controlling effect on the polymorphs selectivity (Figure 2.11 and Figure 2.12). Thus, calcite is the dominant polymorph at low temperature (<20 °C). With increasing the temperature, the calcite abundance decreases. At intermediate temperatures (40–50 °C), the formation of all three polymorphs is observed. At higher temperature (>60 °C), the transformed polymorph is aragonite in agreement with Zhou et al.⁸⁴. On the other hand, calcite is dominant at low pressure and aragonite is dominant at high pressure.

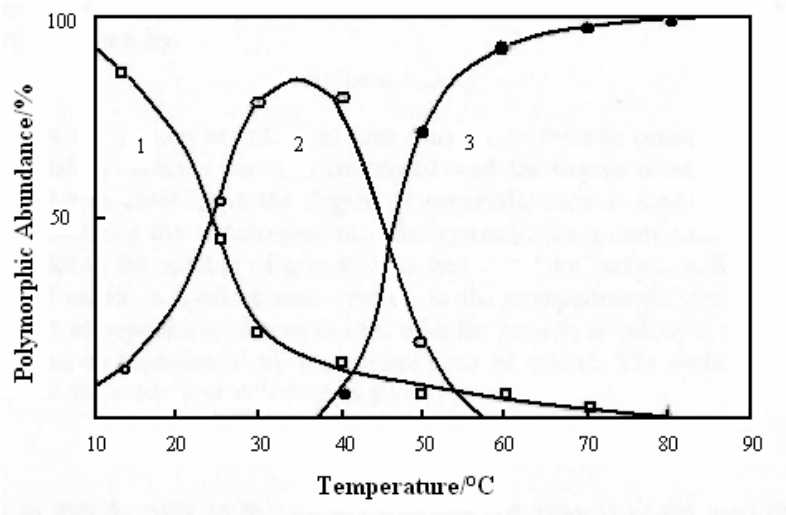


Figure 2.11 Abundance of crystalline calcium carbonates as a function of temperature. (Reproduced from [82])

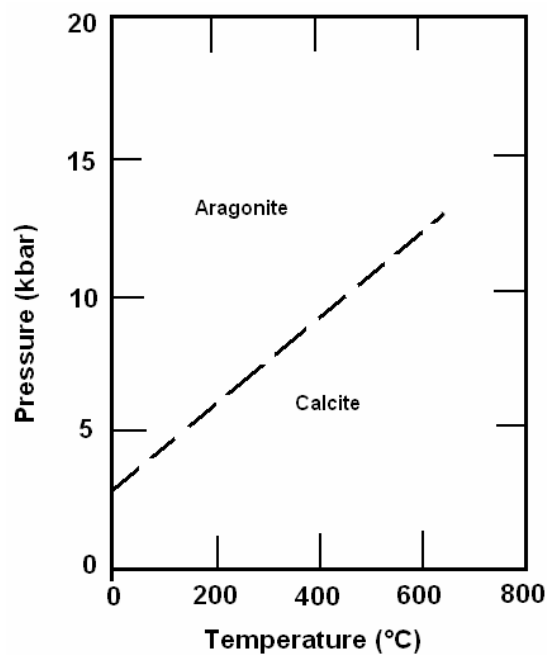


Figure 2.12 The pressure-temperature phase diagram of $CaCO_3$. (Reproduced from [83])

b₂. The Effect of Inorganic and Organic Additives

Nowadays, a huge number of papers on the formation of calcium carbonate are published, starting with the description of single crystals and ending with the presentation of self-assembled hierarchical materials. This is possible by using additives that incorporate into

the crystal lattices or adsorb on certain positions of the crystal surfaces and, thus, have a significant effect on the crystal growth, morphology and polymorphic transformation.

Effect of Inorganic Additives. The presence of alkali metal ions (Li^+ , Na^+ , K^+ , Rb^+) during the mineralization process results in a mixture of aragonite and calcite. Moreover, the transition from aragonite to calcite is significantly retarded^{85, 86}. When coprecipitate with aragonite, the alkali metal ions substitute the calcium ions from the aragonite structure. When they coprecipitate with calcite, these ions occupy the interstitial sites from the calcite structure⁸⁷. The effect of alkali metal ions on the crystal morphology is less important⁸⁸ except in the case of the lithium ions⁸⁹. A large amount of the lithium ions, which has a small ionic size, can be incorporated into calcite causing the lattice distortion on the surface⁹⁰. Likewise, Sims et al.⁹¹ report that the addition of lithium to supersaturated calcium hydrogen carbonate sols results in the preferential expression of the (001) faces of aragonite, Figure 2.13. The resulting cluster is a reminiscent of the tabular aragonite morphology observed in the nacreous shells of many molluscs.

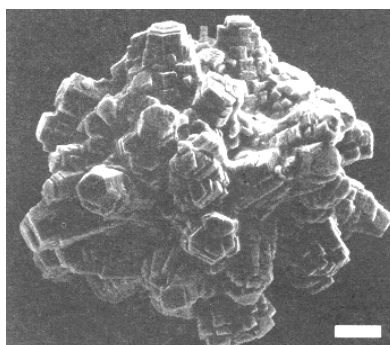


Figure 2.13 SEM image showing the expression of (001) tabular faces in aragonite crystals grown in the presence of Li^+ . Scale bar: 10 μm . (Adopted from [91])

The alkaline earth metal ions exert a significant effect on the $CaCO_3$ precipitation. When present in sufficient concentration, they generally cause the precipitation of aragonite⁹²⁻⁹⁶ rather than the thermodynamical favoured phase, calcite. In time, however, the aragonite phase transform to calcite phase. The formation of aragonite phase is suppressed⁹⁷ only when the temperature is higher than 50 °C. A sample of pure aragonite forms only in the presence of $SrCO_3$ and $BaCO_3$ seed crystals⁸⁴.

Polyvalent ions, such as Fe^{3+} , Cr^{3+} , Al^{3+} , or WO_4^{2-} , MoO_4^{2-} , PO_4^{2-} , influence the size and the form of the crystals as well as its polymorphs⁹⁸⁻¹⁰⁰. Likewise, the precipitation of

calcium carbonate from an alkaline silica-rich environments results in a wide variety of morphologies including shapes with both crystallographic and non-crystallographic symmetry elements^{102, 103} (see Section 2.4).

Effect of Organic Additives. As a result of many papers reported so far, it is assumed that the organic additives have two functions¹⁰³. First, they can inhibit crystal growth by binding to the growth sites of the crystals through a combination of electrostatic and stereochemical interactions. Thus, they can control the growth direction, the orientation, the texture, the crystal size and the polymorphism. For example, Table 2.2 summarises the influence of some organic additives on the yield of vaterite (*V*), calcite (*C*) and aragonite (*A*) crystals. However, the chemistry of organic additives/inorganic crystal interface as well as the mechanism of interactions between them are not clearly understood yet¹⁰⁴.

Second, they can act as a heterogeneous nucleator and, thus, provide important insight into the relationships between the structure of the substrate (such as well-ordered two dimensional structure of a self-assembled film on a solid substrate¹⁰⁵, Langmuir films^{106, 107} at the air/water interface, monolayers of 5-hexadecyloxyisophthalic acid¹⁰⁸, monolayers of eicosanoic acid and n-eicosyl sulphate¹⁰⁹ and chitin-silk fibroin substrates¹¹⁰) and the overgrowing crystals¹¹¹.

Table 2.2 Influence of additives on the yield of vaterite (*V*), calcite (*C*) and aragonite (*A*)

<i>Additives</i>	<i>T</i> •C	<i>V</i> %	<i>A</i> %	<i>C</i> %	<i>Additives</i>	<i>T</i> •C	<i>V</i> %	<i>A</i> %	<i>C</i> %
β-Alanine ¹¹²	20	0	0	100	Canavalia urease ¹¹⁹	25	0	0	100
L-Glutamine ¹¹³	20	0	0	100	EtOH ¹²⁰	25	~100	0	0
Glutaric acid ¹¹³	20	0	0	100	Isopropanol ¹¹³	25	~100	0	0
L-aspartic acid ¹¹⁴	20	100	0	0	Poly α,β-aspartate ¹²¹	25	~100	0	0
Sodium Glycolate ¹¹³	20	0	0	100	Lysozyme ¹²²	25	0	0	100
Ammonium Acetate ¹¹³	20	12.1	0	87.9	Chloroform ¹²³	25	0	100	0
Glycine ¹¹³	20	16.1	0	83.9	Mg²⁺/Malic Acid ⁹⁸	25	0	100	0
L-Glutamic Acid ¹¹³	20	55.4	0	44.6	Mg²⁺/Citric Acid ⁹⁸	25	0	80	20
Sodium L-Glutamate ¹¹³	20	60.8	0	39.2	EDTA ¹²⁴	25	0	0	100
Sodium L-Aspartate ¹¹³	20	81.9	0	18.1	Citrate ¹⁰⁴	25	0	0	100
Ethylenediamine ¹¹³	20	81.9	0	18.1	EtOH ¹²⁵	20	0	100	0
D-(+)-Glucose ¹¹⁵	25	~3	0	~97	SDS ¹²⁶	20	0	0	100
D-(+)-Mannose ¹¹⁵	25	~44	0	~56	SDBS ¹²⁷	26	100	0	0
D-Fructose ¹¹⁵	25	~55	0	~45	CTAB ¹²⁸	25/80	0/0	0/100	100/0
D-(+)-Galactose ¹¹⁵	25	~39	0	~61	PVA ¹²⁹	25/80	0/0	0/93.1	100/6.9
D-(+)-Sucrose ¹¹⁵	25	~85	0	~15	PEG ¹²⁹	25/80	0/0	0/0	100/100
D-(+)-Maltose ¹¹⁵	25	~58	0	~42	PAA ¹²⁹	25/80	0/0	0/0	100/100
D-(+)-Lactose ¹¹⁵	25	~8	0	~92	PMAA ¹²⁹	22	0	0	100
D-Cellobiose ¹¹⁵	25	~55	0	~45	PEG-b-PMAA ¹²⁹	22	0	0	100
α-Amilose ¹¹⁵	25	0	0	100	PSMA ¹³⁰	22	69	0	31
Chondroitin sulphate ¹¹⁶	25	100	0	0	PSMA-CTAB ¹³⁰	22	24	0	76
Pepsin ¹¹⁷	25	92.4	0	7.6	PDEAEMA-b-PNIPAM-b-PMAA ¹³¹	22	0	100	0
Bacillus urease ¹¹⁸	25	~95	0	~5	PEG-PMMA-SDS ¹³²	25	0	0	100

Abbreviations: Polyvinyl alcohol (PVA); Polyethylene glycol (PEG); Polyacrylic acid (PAA); Poly(ethylene glycol)-block-poly(methacrylic acid) (PEG-b-PMAA); Poly(styrene-alt-maleic acid) (PSMA); Cetyltrimethylammonium bromide (CTAB); Sodium dodecyl sulphate (SDS); Sodium dodecylsulfonate (SDBS); poly(diethylaminoethyl methacrylate)-b-poly(N-isopropylacrylamide)-b-Poly(methacrylic acid) (PDEAEMA-b-PNIPAM-b-PMAA).

Furthermore, the organic additives promote also a wide variety of biomimetic calcium carbonate materials. Thus, complex cakelike vaterite superstructures¹¹⁸ composed of stacked porous multilayers are easily realised in an ethanol/water mixed solutions. Hexagonal vaterite mesocrystals are synthesized in the presence of a N-trimethylammonium derivate of hydroxyethyl cellulose via aggregation-mediated mineralization¹³³. Double hydrophilic block copolymers¹³⁴ with monophosphate ester moieties are used as an environment for the precipitation of complex superstructures (Figure 2.14 A) of calcium carbonate too. Another example of biomimetic structure¹³⁵ is based on controlled aggregation of surfactant-coated ACC primary particles, which results in micrometer-sized doughnut-shaped aragonite structures (Figure 2.14 B). Vaterite-type calcium carbonates with flower-like structure (Figure 2.14 C) are synthesized through a sonochemical process under higher acoustic amplitude¹³⁶. Addition of charged poly(aspartate) to a supersaturated solution of calcium carbonate induces vaterite nucleation and the formation of helicoids morphologies (Figure 2.14 D-F)^{91,114}. These crystals exhibit features reminiscent of the morphologies observed in biogenic minerals. Thin cellular frameworks of porous calcium carbonate in form of aragonite are prepared from oil-water-surfactant microemulsions supersaturated with calcium bicarbonate and magnesium chloride. The latter is added to promote the growth of the aragonite polymorph (Figure 2.14 G). Further, using micrometer-sized polystyrene beads as substrate for the microemulsion, hollow spherical aggregates with cellular substructure, referred to as 'biomimetic cocoliths', are formed¹³⁷, Figure 2.14 H. Single crystals of calcite with sponge-like shape (Figure 2.14 I, J) are produced either using a polymer membrane, which has an identical morphology to a sea urchin skeletal plate^{138, 139}, (Figure 2.14 I) or by simple crystallization on colloidal monolayers of polystyrene and silica spheres¹⁴⁰. The organic component acts as a morphological modifier to the growing calcium carbonate.

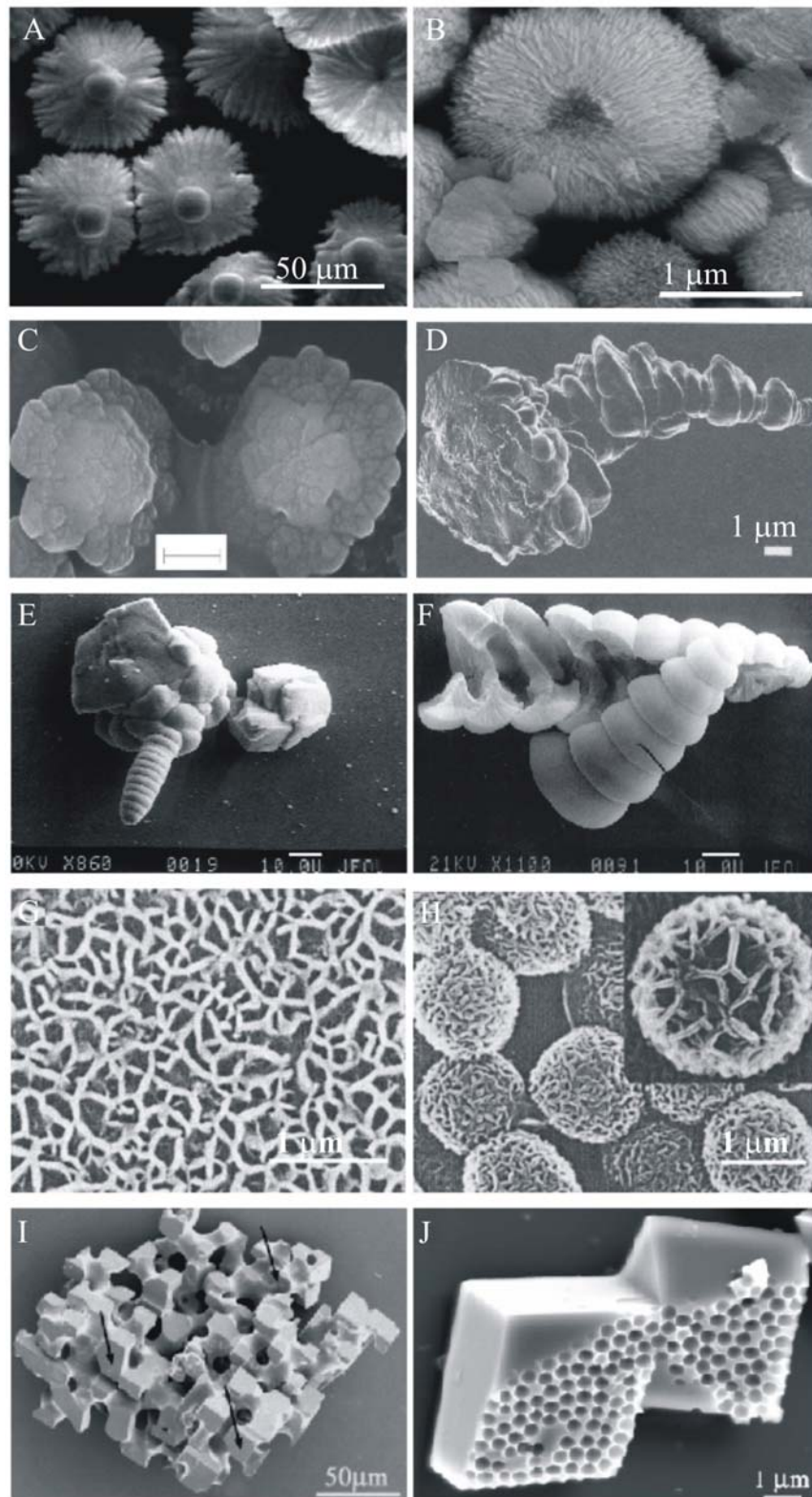


Figure 2.14 Complex shapes of CaCO_3 . (A). Complex CaCO_3 superstructure with block copolymers. (Reproduced from [134]) (B) Doughnut-like crystals produced in microemulsion. (Reproduced from [135]) (C) SEM image of vaterite flower-like shape. (Reproduced from [136]) (D) SEM image showing helicoids outgrowth of stacked vaterite

disks grown in the presence of linear poly α,β -aspartate. (Reproduced from [91]) (E) A crystalline aggregate containing a helical protrusion resulting from the addition of poly α,L -aspartate. (Reproduced from [114]) (F) Hollow helix fractured by micro-manipulation. (Reproduced from [114]) (G) Cellular film of aragonite synthesized by using a biliquid foam as template. (Reproduced from [137]) (H) Hollow spheres of aragonite with cellular substrate synthesized by using both a biliquid foam and microbeads as templates. (Reproduced from [137]) (I) Templated single crystal of calcite precipitated in the polymeric replica of a sea urchin skeletal plate. (Reproduced from [138]) (J) Calcite crystals grown on colloidal polystyrene monolayer after dissolution of polystyrene spheres, showing the crystal phase growing in contact with the monolayer. (Reproduced from [140])

2.3. Properties of Egg White Lysozyme and Casein Proteins

2.3.1. Egg White Lysozyme

Lysozyme, a protein discovered by Fleming¹⁴¹, is a monomeric globular protein with α helix, β sheet and a radius of gyration of 22 Å. It contains 129 amino acids ($M_w = 14300$ Da) and its isoelectric point is 11.35 due to the high proportion of lysine and arginine.

Lysozyme is the first enzyme, whose structure was determined by X-ray crystallography¹⁴², known to damage bacterial cell walls^{143, 144}. Therefore, it is used in the pharmaceutical and food industry. Moreover, lysozyme shows an affinity for metal ions. For instance, in the presence of Ca^{2+} , lysozyme conserves only 26% of the free enzyme activity because calcium binds the catalytic site of lysozyme activity¹⁴⁵.

This protein is widely found in the natural environment, such as physiological liquids (milk, blood, saliva, tears, urine and in different plants). Large amounts of lysozyme are also found in the non-calcified shell membranes and in the mammillary cone layer²³, along with calcium carbonate.

At the interface between the non-calcified and the calcified cone layer, the mammillary core zone is situated²³ (Figure 2.15). The mammillary core represents the place where the calcium carbonate biomineralization process is initiated. Because the lysozyme is presented at very high concentration in the mammalian cartilage, we suppose that it should

interfere in the onset of eggshell calcification process and modify the growth morphology of the particles. Therefore, the $CaCO_3$ precipitation in *in vitro* experiments was performed in the presence of egg white lysozyme (see Chapter 4).

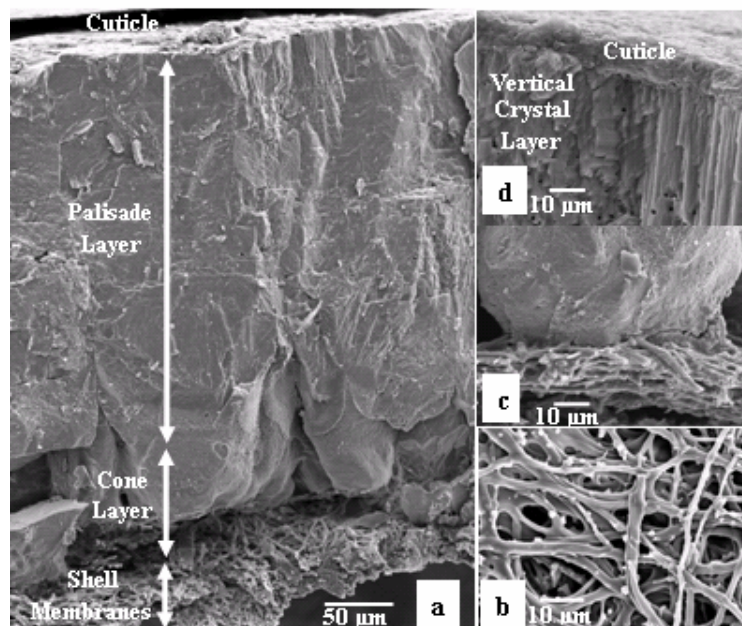


Figure 2.15 Scanning electron micrographs illustrating the highly ordered calcareous structure of the chicken eggshell. (a) cross-section through a fully formed eggshell which reveals the eggshell membranes, the cone mammillary layer, the palisade layer and the cuticle; (b) the inner shell membranes showing the network of interlacing fibbers: (c) cross-section through the cone layer showing the insertion of fibbers into the tips of the cone; (d) the vertical crystal layer at the upper part of the palisade layer and the cuticle overlying on the mineralized eggshell. (Reproduced from [23])

2.3.2. Casein Proteins

Caseins, the major proteins of milk, consist of several types of phosphoproteins (α_{s1} -, α_{s2} -, β - and κ - casein) and each has its own amino acid composition, genetic variations, and functional properties. Furthermore, α_{s1} -, α_{s2} - and β - casein, richer of phosphate groups, are distinguishing from κ -casein for their more or less marked tendency to ‘precipitate’ in presence of calcium ions¹⁴⁶.

In milk, casein proteins form complexes called casein micelles¹⁴⁷ (Figure 2.16) which show some resemblance with surfactant-type micelle in a sense that the hydrophilic parts

reside at the surface. The casein micelles are spherical dynamic structures with diameters ranging from 0.05 to 0.25 μm in diameter. Moreover, the micelles are porous structures that allow the water phase to move freely in and out of the micelle. Earlier studies show that the hydrophobic interior of casein micelles consists of spherical subunits called submicelles (15–20 nm in diameter)¹⁴⁸, which are kept together by hydrophobic interaction between proteins and by calcium phosphate linkages¹⁴⁹.

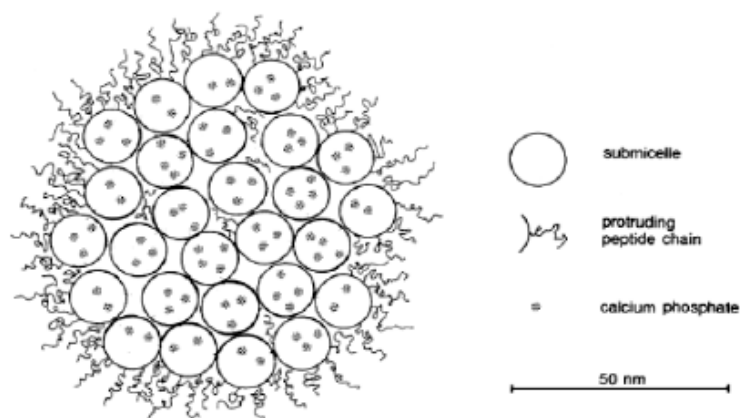


Figure 2.16 The structure of casein micelle in the sub-micelles model showing the protruding C-terminal parts of κ -casein as proposed by Walstra. κ -casein plays a role of colloidal protector towards the other caseins. (Reproduced from [149])

The casein fraction is relatively hydrophobic, making it poorly soluble in water in the pH range from 3 to 5.5 (IP = 4.7), where the surface net charge is near zero and most of the carboxylic and amine functions in casein are ionized¹⁵⁰. Thus, the electrostatic interactions between carboxylate and ammonium groups, in and between casein biopolymers, are strong. This effect leads to the precipitation of the casein. In more basic or acidic aqueous media, the casein becomes very soluble. The solubility curve¹⁵¹ of the casein we used was determined as a function of pH at 20 °C, see Figure 2.17.

The natural function of casein proteins is to supply young mammals with the essential aminoacids, required for the development of muscles¹⁵². Moreover, caseins are a high source of calcium and glutamine. In addition, casein is used in the manufacture of adhesives, binders, protective coatings, plastics (such as for knife handles and knitting needles), paints, cosmetics, food additives¹⁵³, etc..

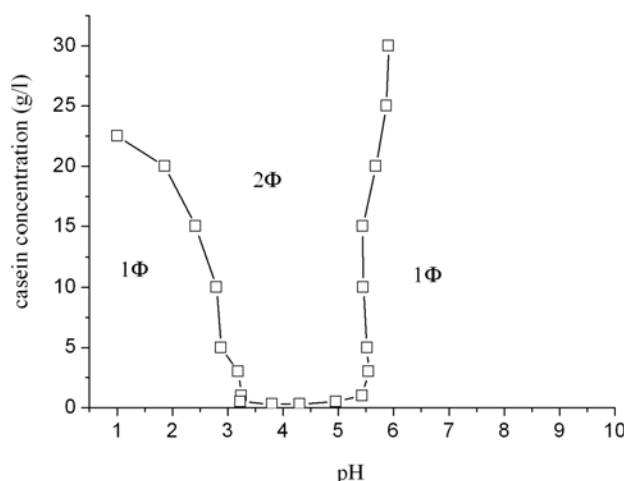


Figure 2.17 Solubility of casein as a function of pH at 20 °C. 1Φ and 2Φ denote the monophasic regions, where casein is highly soluble, and the two-phase precipitation region, respectively. The pH was adjusted by addition of concentrated *HCl* or *NaOH* without using a buffer. (Reproduced from [151])

2.4. Biomorphs

Biomorphs are inorganic, self-assembled silica-carbonate composites showing a wide range of non-crystallographic, biomimetic morphologies and sizes¹⁵⁴. Their forms include curvilinear sheets, helical filaments, braids and floral spherulites (Figure 2.18), accompanied by the packing of carbonate crystalline rods within the self-assembled aggregates.

The carbonate crystals implicated are calcium, strontium and barium carbonate. Of these, CaCO_3 is the most familiar biomineral found in biological systems in a number of different forms (see Section 2.1 and 2.2). In contrast, SrCO_3 , and BaCO_3 are less abundant in nature and occur only in the aragonite phase, namely strontianite and witherite. Earlier studies reported also a high-temperature, cubic and rhombohedral polymorphs of Sr ^{155, 156} and Ba ¹⁵⁷ carbonates that are reminiscent of calcite. However, little is known about the high-temperature polymorphs of *Sr* and *Ba* carbonates because they are not quenchable.

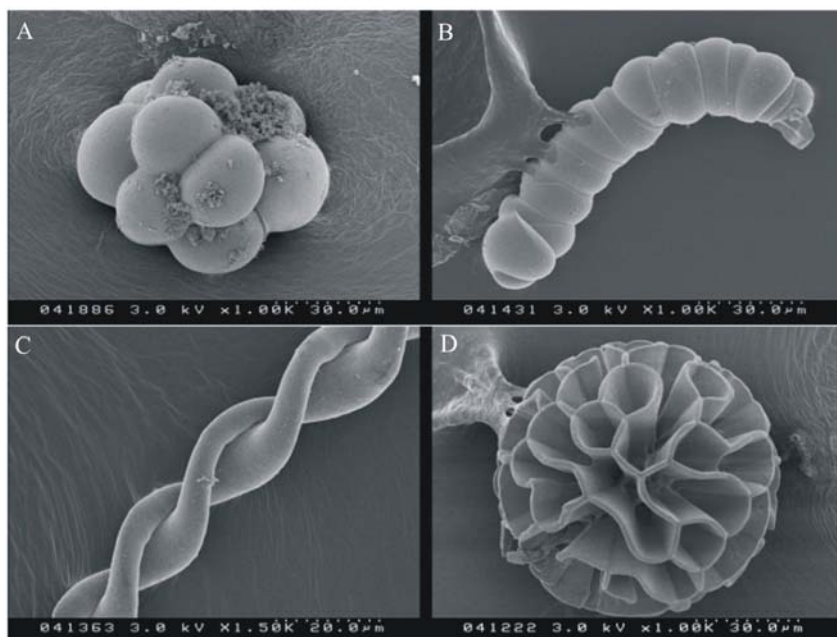


Figure 2.18 FESEM images of a selection of various barium-carbonate biomorphs. [Reproduced from García-Ruiz's lecture, Regensburg]

Biomorphs can be obtained either in silica gels¹⁵⁸ or sols¹⁵⁹. In solution (the method used also in this work), the biomorphs are produced using a simple laboratory process, involving the mixing of water glass and alkaline earth metal ions at room temperature and the diffusion of atmospheric CO_2 into the solution. A systematic study¹⁶⁰ of the precipitation behaviour reveals that the morphological modification is strongly sensitive to pH changes (Figure 2.19). This correlation is due to the different types of interactions that take place in the neutral and moderately alkaline solutions. Thus, at pH below 8.5, no interaction occurs, because carbonate concentration is not sufficient for the nucleation to start; furthermore, silicic acid is mainly undissociated. At higher pH (>9), monomeric ($H_3SiO_4^-$) and dimeric ($Si_2O_2(OH)_5^-$ and $Si_2O_3(OH)_4^{2-}$) species of silicic acid are present in the solution. The interaction with the carbonate crystals takes place likely via $Si-OH$ groups bonded to carbonate crystals surfaces. Increasing the pH to 11, the percentage of the dimeric species of silica in solutions is high in comparison with the monomeric acid and in the presence of metal ions, a wide range of non-crystallographic and biomimetic morphological outputs form, depending of the metal's nature. Thus, in the presence of Ba^{2+} or Sr^{2+} ions, curvilinear forms arise, such as those presented in Figure 2.18, whereas the presence of Ca^{2+} ions produces non-crystallographic shapes such as sheaf-of-wheat¹⁶¹ with

self-organised banding (Figure 2.20 A–C) and spheres with an open cellular architecture¹⁶² (Figure 2.20 D–E) but *never* complex curvilinear forms characteristic to biominerals.

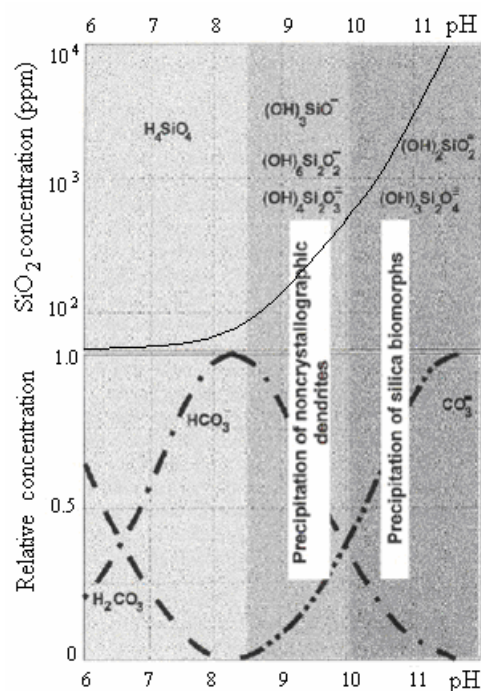


Figure 2.19 A plot of the relative concentrations of species derived from SiO_2 and CO_2 dissociation as a function of pH. (Reproduced from [160])

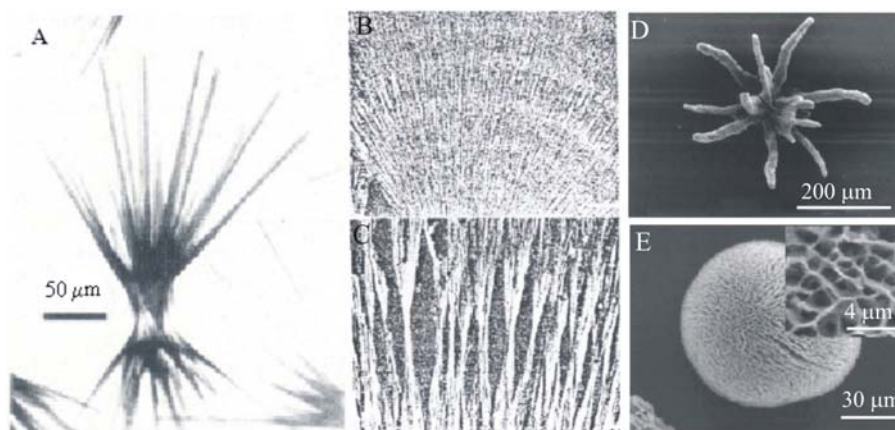


Figure 2.20 (A–C) SEM images of sheaf of wheat aggregates with banding calcite structure. (Reproduced from [161]) (D and E). Coral-like (D) and spherical (E) morphologies of aragonite produced with silica gel at pH 10.5. (Reproduced from [162])

The shapes obtained in the presence of barium and strontium ions provide a coherent, plausible scenario for the formation of the Warrawoona microfossils without involving any

living materials¹⁶³ (Figure 2.21 A and B). According to Brasier et al.¹⁶⁴, the Warrawoona microfossils possess a kerogenous[†] carbonaceous stoichiometry. Immersion of witherite-silica filaments in formaldehyde-phenol mixtures and subsequent heating at 125 °C for at least 15 hours forms kerogen also. Besides, the kerogen obtained on the biomorphs has the same Raman spectrum that the one obtained from Warrawoona microfossils (Figure 2.21 C) reported by Schopf et al.¹⁶⁵. Clearly, these observations suggest an abiotic pathway to the formation of microfossils.

These morphologies are a dual composite of the carbonate crystals surrounded by a silicate membrane. The chemical nature of biomorphs is ascertained by selective dissolution in acidic or alkali solutions¹⁶⁶, Figure 2.23. Thus, immersion of the aggregates in dilute *HCl* solution (dissolving all carbonate material) leaves only the silica skin, whereas immersion of the biomorphs in mild base retains the carbonate material, consisting of packed arrays of rods. X-ray and electron diffraction pattern reveal that the crystallites are witherite barium carbonate.

Two mechanisms were postulated for the physical origins of these extraordinary forms¹⁶⁷. One is the ‘bottom-up’ model, based on the analogy of the microstructure of the aggregates with chiral liquid crystals. This model holds the twisted self-assembly of carbonate nanorods responsible for the overall shape of the biomorphs aggregate. The second is a ‘top-down’ model, with the global form set first and the smaller-scale structural features following. In this case, the biomorphs are probably templated by a preformed silica skin that is grown in the presence of metal ions. Between both postulated models, the top-down one seems to be more in agreement with the experimental results. However, Terada et al.¹⁶⁸ reinvestigated the formation of strontium carbonate and proposed a crystallographic mechanism based on the second model. So, it is also possible that both models occur simultaneously.

Biomorph geometries show striking resemblances to standard surface forms found in texts¹⁶⁹ on differential geometry (Figure 2.21 D). The sheets are typically hyperbolic and mimic surfaces of constant negative Gaussian curvatures. Such geometry is expected assuming a constant silica coordination number (Figure 2.22), exceeding six, in the silica skin. In turn, the twisted filaments resemble surfaces of constant positive Gaussian

[†] Kerogen is organic matter in sedimentary rocks that remains insoluble in both acids and organic solvents.

curvature called ‘twisted spheres’. For this curvature, a fixed silica coordination number less than six is required.

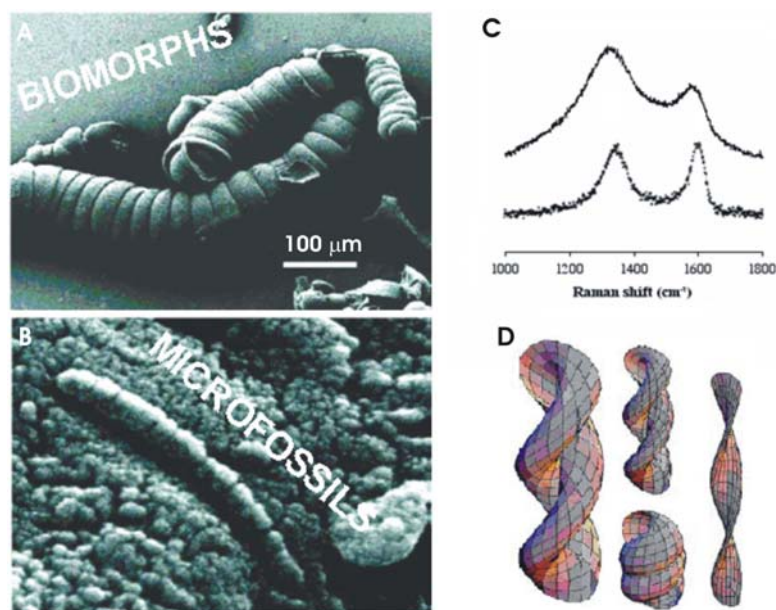


Figure 2.21 Comparison of synthetic filaments with the ancient microfossils. (A) Worm-like biomorphs synthesized at pH 11. (Reproduced from [163]) (B) Carbonate aggregate in the Martian meteorite ALH84001. (Reproduced from [163]) (C) Raman spectrum of heat-cured biomorphs compared with the spectrum of kerogen-like Warrawoona microfossils. (Reproduced from [154]) (D) Computer-generated twisted spheres. (Reproduced from [167])

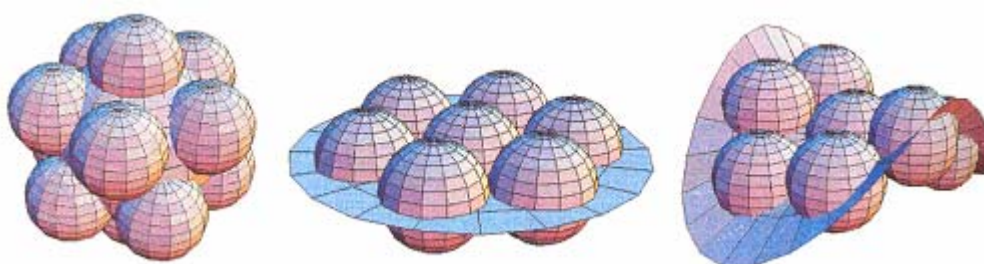


Figure 2.22 The coordination number of spherical colloids (N) and their effect on the membrane curvature: N = 5 (left), N = 6 (center) and N=7 (right). (Reproduced from [170])

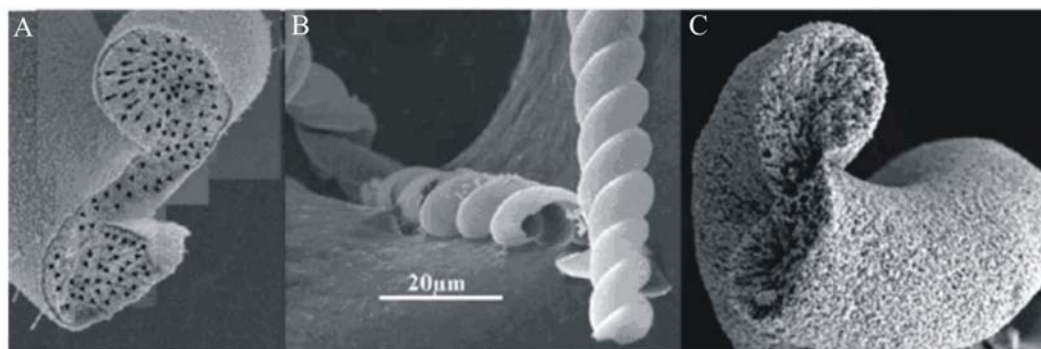


Figure 2.23 (A) FESEM images of hollow silica skin left after immersion of the biomorphs in dilute acid. (B) Removal of silica by immersion in weak base, leaving the aggregated carbonate nanorods. (C) As-prepared biomorphs, with the orientated ordering of silica-coated carbonate nanorods indicated by the arrows. (Reproduced from [166])

Although, comparing the three isostructural carbonates of aragonite ($CaCO_3$, $SrCO_3$ and $BaCO_3$), it is found that they are very similar in most respects¹⁷¹, however, hitherto the precipitation of the $CaCO_3$ in silica solution failed to give ‘ruled surfaces’ like barium or strontium^{163, 170}. Given the presence of calcium carbonate polymorphs in many biominerals as well as the geochemical abundance of calcium relative to barium and strontium, the possibility of forming curvilinear sheets of silica-calcium carbonate biomorphs deserves further exploration.

2.5. References

- (1) Lowenstam, H. A. *Science* **1981**, *211*, 1126.
- (2) Mann, S. *Biomineralization: Principles and Concepts in Bioinorganic Materials Chemistry*, Oxford Univ. Press: New York, 2001.
- (3) Treccani, L. *Protein-Mineral Interaction of Purified Nacre Proteins with Calcium Carbonate Crystals*, Doctor Thesis: Bremen University, 2006.
- (4) Wilbur, K. M. *American Zoologist* **1984**, *24*(4), 839.
- (5) Lowenstam, H. A.; Weiner, S. *On biomineralization*, Oxford Univ. Press: Oxford, 1989.
- (6) Mann, S.; Webb, J.; Williams, R. J. P. *Biomineralization: Chemical and Biochemical Perspectives*, VCH: New York, 1989.
- (7) Weiner, S.; Sagi, I.; Addadi, L. *Science* **2005**, *309*, 1027.
- (8) Politi, Y.; Arad, T.; Klein, E.; Weiner, S.; Addadi, L. *Science* **2004**, *306*, 1161.

- (9) Addadi, L.; Geva, M. *Cryst. Eng. Comm.* **2003**, *5*, 140.
- (10) Barnes, D. G. *Science* **1970**, *170*, 1305.
- (11) Aizenberg, J.; Lambert, G.; Weiner, S.; Addadi, L. *J. Am. Chem. Soc.* **2002**, *124*, 32.
- (12) Simkiss, K.; Wilbur, K. *Biom mineralization. Cell Biology and Mineral depositions*, Academic Press: San Diego, 1989.
- (13) Beniash, E.; Aizenberg, J.; Addadi, L.; Weiner, S. *Proc. R. Soc. Lond. Ser. B* **1997**, *264*, 461.
- (14) Beniash, E.; Addadi, L.; Weiner, S. *J. Struct. Biol.* **1999**, *125*, 50.
- (15) Weiss, I. M.; Tuross, N.; Addadi, L.; Weiner, S. *J. Exp. Zool.* **2002**, *293*, 478.
- (16) Marxen, J. C.; Becker, W.; Finke, D.; Hasse, B.; Epple, M. *J. Molluscan Stud.* **2003**, *69*, 113.
- (17) Lakshminarayanan, R.; Loh, X. J.; Gayathri, S.; Sindhu, S.; Banerjee, Y.; Kini, R. M.; Valiyaveetil, S. *Biomacromolecules* **2006**, *7* (11), 3202.
- (18) Meibom, A.; Cuif, J.P.; Hillion, F.; Constantz, B.; Juillet-Leclerc, A.; Dauphin, Y.; Watanabe, T.; Dunbar R.B. *Geophys. Res. Lett.* **2004**, *31*, L23306.
- (19) Dillaman, R.; Hequembourg, S; Gay, M. *J. Morphol.* **2005**, *263*, 356.
- (20) Meldrum, F. C. *Int. Mater. Rev.* **2003**, *48*(3), 187.
- (21) Addadi, L.; Raz, S; Weiner, S. *Adv. Mater.* **2003**, *15*(12), 959
- (22) Aizenberg, J.; Hanson, J.; Koetzle, T. F.; Weiner, S.; Addadi, L. *J. Am. Chem. Soc.* **1997**, *119*, 881.
- (23) Nys, Y.; Gautron, J.; McKee, M. D.; García-Ruiz, J. M.; Hincke, M. T. *World's Poult. Sci. J.* **2001**, *57*, 401.
- (24) Wiercinski, F. *J. Biol. Bull.* **1989**, *176*, 195.
- (25) Jaiswal, J. K. *J. Biosci.* **2001**, *26*(3), 357.
- (26) Campbell, A. K. *Intracellular Calcium: Its Universal Role as Regulator*, John Wiley & Sons: Chichester, England, 1983.
- (27) Trifonov, D. N.; Trifonov, V. D. *Chemical elements: How they were discovered*, MIR Publishers: Moscow, 1982, 116.
- (28) Ringer, S. *J. Physiol* **1883**, *4*, 29.
- (29) Ringer, S.; Sainsbury, H. *J. Physiol* **1894**, *16*, 1.
- (30) Mooren, C. C.; Kinne, R. K. H. *Biochim. Biophys. Acta* **1998**, *1406*, 127.
- (31) Campbell, A. K. *Survey Biochem. Anal.* **1988**, *19*, 485.
- (32) Chakaborty, P. *Biochemistry* **1990**, *29*, 651.

- (33) Swain, A. L.; Amma, E. L. *Inorg. Chim. Acta* **1989**, *163*, 5.
- (34) Price, P. A. *J. Biol. Chem.* **1975**, *250*, 1981.
- (35) Goodwin, M. G.; Anthony, C. *Biochem. J.* **1996**, *318*, 673.
- (36) Mortimer, C. E. *Chemie*, Georg Thime Verlag: Stuttgart, 1996.
- (37) Loering, T.; Moore, M. H.; Khama, R. K. *Spectrochim. Acta A* **1991**, *47*, 255.
- (38) Holleman, A. F.; Wiberg, E. *Lehrbuch der Anorganischen Chemie*, Walter de Gruyter: Berlin, 1995.
- (39) Heinemann, F. *Nukleation und Wachstum von Modulierten Kalziumkarbonate Kristallen durch Biopolymere*, Diploma Thesis: University of Bremen, 2005.
- (40) Nielsen, A. E. *Croat. Chem. Acta* **1970**, *42*, 319.
- (41) Ohtaki, H. *Crystallization Process*, John Wiley & Sons: New York, 1998.
- (42) Stranskii, Z. *Phys. Chem.* **1928**, *A136*, 259.
- (43) Kossel, W. *Ann. Phys.* **1938**, *33*, 651.
- (44) Frank, F. C. *Faraday Soc. Discussions* **1949**, *5*, 48.
- (45) Somasundaran, P.; Agar, G. E. *J. Colloid Interface Sci.* **1967**, *24*, 433.
- (46) Bridgman, P. W. *American Journal of Science* **1939**, *237*, 7.
- (47) Carson, W. D. *Carbonates: Mineralogy and Chemistry*, Mineralogy Society of America: Washington DC, 1983.
- (48) Lippmann, F. *Sedimentary carbonate minerals*, Springer-Verlag: Berlin, 1973.
- (49) Becker, A. *Structural Characterisation of Biominerals and Biomimetic Crystallization of Calcium Carbonate*, Dissertation: University of Duisburg-Essen, 2005.
- (50) Plummer, L. N.; Busenberg, E. *Geochim. Cosmochim. Acta* **1982**, *46*, 1011.
- (51) Brecevic, L. *J. Cryst. Growth* **1989**, *98*, 504.
- (52) Deer, W. A.; Howie, R. A.; Zussman, J. *Introduction to the Rock Forming Minerals*, Longman: Harlow, UK, 1992.
- (53) Dickens, B.; Bowen, J. S. *J. Res. Natl. Bur. Stand., Sect. A: Phys. Chem.* **1971**, *75*, 27.
- (54) Kamhi, S. R. *Acta Crystallogr.* **1963**, *16*, 770.
- (55) Effenberger, H. *Monatsh. Chem.* **1981**, *112*, 899.
- (56) Clarkson, J. R.; Price, T. J.; Adams, C. J. *J. Chem. Soc. Faraday Trans.* **1992**, *88*, 243.
- (57) De Leeuw, N. H.; Parker, S. C. *J. Phys. Chem. B* **1998**, *102*, 2914.
- (58) Giannimaras, E. K.; Koutsoukos, P. G. *Langmuir* **1988**, *4*, 855.

- (59) Krauss F, Schriever W. *Z. Anorg Chem* **1930**, 188, 259.
- (60) Sapozhnikov, D. G.; Zvetkov, A. I. *Dokl. Akad. Nauk SSSR* **1959**, 124, 402.
- (61) Johnson, J.; Merwin, H. E.; Williamson, E. D. *Amer. J. Sci.* **1916**, 41, 473.
- (62) Wilt, F. H. *Dev. Biol.* **2005**, 280, 15.
- (63) Rein ten Wolde, P.; Frenkel, D. *Phys. Chem. Chem. Phys.* **1999**, 1, 2191.
- (64) Ostwald, W. *Z. Phys. Chem.* **1897**, 22, 289.
- (65) B. Leadbeater *Biomineralization in lower Plants and animals*, Clarendon Press: New York, 1986.
- (66) Rieger, J.; Frechen, T.; Cox, G.; Heckmann, W.; Schmidt, C.; Thieme, J. *Faraday Discuss.* **2007**, 1, 1.
- (67) Faatz, M.; Gröhn, F.; Wegner, G. *Adv. Mater.* **2004**, 16, 996.
- (68) Dorfmueller, G. *Deutsch. Zuckerind.* **1938**, 51, 1217.
- (69) Matsuchita, I.; Hamada, Y.; Moriga, T.; Ashida, T.; Nakabayashi, I. *J. Ceram. Soc. Jpn.* **1996**, 104, 1081.
- (70) Koga, N.; Nakagoe, Y.; Tanaka, H. *Thermochim. Acta* **1998**, 318, 239.
- (71) Ma, Z.; Huang, J.; Sun, J.; Wang, G.; Li, C.; Xie, L.; Zhang, R. *J. Biol. Chem.* **2007**, 282, 23253.
- (72) Loste, E.; Wilson, R. M.; Seshadri, R.; Meldrum, F. C. *J. Crys. Growth* **2003**, 254, 206.
- (73) Xu, X.; Han, J. T.; Cho, K. *Chem. Mater.* **2004**, 16, 1740.
- (74) DiMasi, E.; Kwak, S. Y.; Amos, F. F.; Olszta, M. J.; Lush, D.; Gower, L. B. *Phys. Rev. Lett.* **2006**, 97(4), 045503.
- (75) Nancollas, G. H.; Sawada, K. *J. Petrol. Technol.* **1982**, 34, 645.
- (76) Koutsoukos, P. G.; Kontoyannis, C. G. *J. Chem. Soc.* **1984**, 80, 1181.
- (77) Kjellin, P.; Holmberg, K.; Nyden, M. *Colloids Surf. A* **2001**, 194, 49.
- (78) Donners, J.; Heywood, B.; Meijer, E. W.; Nolte, R.; Sommerdijk, N. *Chem. Eur. J.* **2002**, 8(11), 2561.
- (79) Donners, J. J. J. M.; Heywood, B. R.; Meijer, E. W.; Nolte, R. J. M.; Roman, C.; Schenning, A. P. H. J.; Sommerdijk, N. A. J. M. *Chem. Commun.* **2000**, 19, 1937.
- (80) Xu, A.; Yu, Q.; Dong, W.; Antonietti, M.; Cölfen, H. *Adv. Mater.* **2005**, 17, 2217.
- (81) Wray, J. L.; Daniels, F. *J. Am. Chem. Soc.* **1956**, 79(9), 2031.
- (82) Ogino, T.; Suzuki, T.; Sawada, K. *Geochim. et Cosmochim. Acta* **1987**, 51, 2757.
- (83) Klein, C.; Hurlbut, C.S. *Manual of Mineralogy*, Wiley: New York, 1993.
- (84) Zhou, G. T.; Zheng, Y. F. *J. Mater. Sci. Lett.* **1998**, 17, 905.

- (85) Okumura, M.; Kitano, Y. *Geochim. Cosmochim. Acta* **1985**, *50*, 49.
- (86) Taft, W. H. *Developments in sedimentology*, vol 9B, eds. Chilingar, G. V.; Bissell, H. J.; Fairbridge, R. W. Elsevier: Netherlands, 1967.
- (87) Busenberg, E.; Plummer, L. N. *Geochim. Cosmochim. Acta* **1985**, *49*, 713.
- (88) Ishikawa, M.; Ichikuni, M. *Chem. Geol.* **1984**, *42*, 137.
- (89) Ogino, T.; Susuki, T.; Sawada, K. *J. Cryst. Growth* **1990**, *100*, 159.
- (90) Okumura, M.; Kitano, Y. *Geochim. Cosmochim. Acta* **1986**, *50*, 49.
- (91) Sims, S. D.; Didymus, J. M.; Mann, S. *J. Chem. Soc., Chem. Commun.* **1995**, 1031.
- (92) Wary, J. L.; Daniels, F. *J. Am. Chem. Soc.* **1957**, *79*, 2031.
- (93) Kitano, Y.; Kanamori, N.; Oomori, T. *Geochim. J.* **1971**, *4*, 183.
- (94) Kinsman, D. J. J.; Holland, H. D. *Geochim. Cosmochim. Acta* **1969**, *33(1)*, 1.
- (95) Kitano, Y. *Bull. Chem. Soc. Jpn.* **1962**, *35*, 1973.
- (96) Holland, H. D.; Holland, H. J.; Munoz, J. L. *Geochim. Cosmochim. Acta* **1964**, *28*, 1287.
- (97) Meldrum, F. C.; Hyde, S. T. *J. Cryst. Growth* **2001**, *231*, 544.
- (98) Zawacki, S. J.; Koutsoukos, P.; Salimi, M. H.; Nancollas, G. H. *ACS Symposium* **1986**, 322.
- (99) Mucci, A. *Geochim. Cosmochim. Acta* **1986**, *50*, 2255.
- (100) Reddy, M. M. *J. Cryst. Growth* **1977**, *41*, 287.
- (101) García-Ruiz, J. M.; Amoros, J. L. *J. Cryst. Growth* **1981**, *55*, 379.
- (102) García-Ruiz, J. M. *Orig. Life Evol. Biosph.* **1994**, *24*, 451.
- (103) Wada, N.; Kanamura, K.; Umegaki, T. *J. Colloid Int. Sci.* **2001**, *233*, 65.
- (104) Yu, G.; Yao, N.; Aksay, I. A.; Groves, J. T. *J. Am. Chem. Soc.* **1998**, *120*, 11977.
- (105) Li, Q.; Ding, Y.; Li, F.; Xie, B.; Qian, Y. *Thin Solid Films* **2002**, *414*, 180.
- (106) Loste, E.; Diaz-Marti, E.; Zorbakhsh, A.; Meldrum, F. C. *Langmuir* **2003**, *19*, 2830.
- (107) Mann, S.; Heywood, B. R.; Rajam, S.; Walker, J. B. A. *J. Phys. D: Appl. Phys.* **1991**, *24*, 154.
- (108) Litvin, A. L.; Valiyaveetil, S.; Kaplan, D. L.; Mann, S. *Adv. Mater.* **1997**, *9*, 124.
- (109) Heywood, B. R.; Mann, S. *Chem. Mater.* **1994**, *6*, 311.
- (110) Fallini, G.; Albeck, S.; Weiner, S.; Addadi, L. *Science* **1996**, *271*, 67.
- (111) Lochhead, M. J.; Letellier, S. R.; Vogel, V. *J. Phys. Chem. B* **1997**, *101*, 10821.
- (112) Manolia, F.; Kanakisa, J.; Malkajb, P.; Dalas, E. *J. Cryst. Growth* **2002**, *336*, 363.
- (113) Matsushita, I.; Hamada, Y.; Moriga, T.; Ashida, T.; Nakabayashi, I. *J. Ceramic Soc. Japan* **1996**, *104*, 1081.

- (114) Tong, H.; Ma, W.; Wang, L.; Wan, P.; Hu, J.; Cao, L. *Biomaterials* **2004**, *25*, 3923.
- (115) Dickinson, R. S.; McGrath, K. M. *Cryst. Growth & Design* **2004**, *4*(6), 1411.
- (116) Monoli, F.; Dalas, E. *J. Cryst. Growth* **2000**, *217*, 416.
- (117) Yang, L.; Guo, Y.; Ma, X.; Hu, Z.; Zhu, S.; Zhang, X.; Jiang, K. *J. Inorg. Biochem.* **2003**, *93*, 197.
- (118) Sondi, I.; Matijevic, E. *J. Colloid Interface Sci.* **2001**, *238*, 208.
- (119) Sondi, I.; Salopek-Sondi, B. *Langmuir* **2005**, *21*, 8876.
- (120) Manoli, F.; Dalas, E. *J. Cryst. Growth* **2000**, *218*(2–4), 359.
- (121) Gower, L. A. Tirell, D. A. *J. Cryst. Growth* **1998**, *191*, 153.
- (122) Jimenez-Lopez, C.; Rodriguez-Navarro, A.; Dominques-Vera, J.; García-Ruiz, J. M. *Geochim. et Cosmochim. Acta* **2003**, *67*(9), 1667.
- (123) Rautaray, D.; Banpurkar, A. *Adv. Mater.* **2003**, *15*, 1273.
- (124) Westin, K.; Rasmuson, A. C. *Desalination* **2003**, *159*, 107.
- (125) Chen, S.; Yu, S.; Jiang, J.; Li, F.; Liu, Y. *Chem. Mater.* **2006**, *18*, 115.
- (126) Chibowski, E.; Szczes, A.; Holysz, L. *Langmuir* **2005**, *21*, 8114.
- (127) Wie, H.; Shen, Q.; Zhao, Y.; Zhou, Y.; Wang, D.; Xu, D. *J. Cryst. Growth* **2004**, *260*, 545.
- (128) Yu, J.; Lei, M.; Cheng, B.; Zhao, X. *J. Cryst. Growth* **2004**, *261*, 566.
- (129) Cölfen, H.; Qi, L. *Chem Eur. J.* **2001**, *7*(1), 106.
- (130) Yu, J.; Zhao, X.; Cheng, B.; Zhang, Q. *J. Solid State Chemistry* **2005**, *178*, 861.
- (131) Nassif, N.; Gehrke, N.; Pinna, N.; Shirshova, N.; Tauer, K.; Antonietti, M.; Cölfen, H. *Angew. Chem. Int. Ed.* **2005**, *44*, 6004.
- (132) Deng, S. G.; Cao, J. M.; Feng, J.; Guo, J.; Fang, B. Q.; Zheng, M. B.; Tao, J. *J. Phys. Chem. B* **2005**, *109*, 11473.
- (133) Xu, A.; Antonietti, M.; Cölfen, H.; Fang, Y. *Adv. Funct. Mater.* **2006**, *16*, 903.
- (134) Rudloff, J. Antonietti, M. Cölfen, H.; Petrula, J.; Kaluzynsky, K; Penczek, S. *Macromol. Chem. Phys.* **2002**, *203*, 627.
- (135) Thachepan, S.; Li, M.; Davis, S. A.; Mann, S. *Chem Mater.* **2006**, *18*, 3557.
- (136) Zhou, G.; Yu, J. C.; Wang, X.; Zhang, L. *New. J. Chem.* **2004**, *28*, 1027.
- (137) Walsh, D.; Mann, S. *Nature* **1995**, *377*, 320.
- (138) Park, R. J.; Meldrum, F. C. *Adv. Mater.* **2002**, *14*(16), 1167.
- (139) Park, R. J.; Meldrum, F. C. *J. Mater. Chem.* **2004**, *14*, 2291.
- (140) Hetherington, N. B. J.; Kulak, A. N. Sheard, K.; Meldrum, F. C. *Langmuir* **2006**, *22*, 1955.

- (141) Fleming, A. *Proc. Roy. Soc. Ser. B* **1922**, 93, 306.
- (142) Blake, C. C. F.; Koenig, D. F.; Mair, G. A.; North, A. C. T.; Phillips, D. C.; Sarma, V. R. *Nature* **1965**, 206, 757.
- (143) Ibrahim, H. R.; Higashiguchi, S.; Koketsu, S.; Juneja, L. R.; Kim, M.; Yamamoto, T.; Sugimoto, Y; Aoki, T. *J. Agr. Food Chem.* **1996**, 44, 3799.
- (144) Wang, S.; Murao, S.; Arai, M. *Agric. Biol. Chem.* **1990**, 111, 141.
- (145) Imoto, T.; Ono, T.; Yamada, T. *Biochem. (Tokyo)*, **1981**, 90, 335.
- (146) Jenness, R. *Milk Proteins, Chemistry and Molecular Biology I*, Academic Press: New York, 1970.
- (147) Farrell, H. M. Jr.; Kumosinsky, T. F.; Malin, E. L.; Brown, E. M. *Methods in Molecular Biology* **2002**, 172(1), 97.
- (148) McMahon, D. J.; McManus, W. R. *J. Dairy Sci.* **1998**, 81, 2985.
- (149) Walstra, P. *Int. Dairy J.* **1999**, 9, 189.
- (150) Horne, D.S. *Curr. Opin. Colloid Interface Sci.* **2002**, 7, 456.
- (151) Voinescu, A.E.; Bauduin, P.; Pinna, C.; Touraud, D.; Kunz, W.; Ninham, B. W. *J. Phys. Chem. B* **2006**, 110, 8870.
- (152) Fox, P. F.; McSweeney, P. L. H. *Dairy Chemistry and Biochemistry*, Blackie Academic & Professional: London, 1998.
- (153) LeBlank, J. G.; Matar, C.; Valdéz, J. C.; LeBlank, J.; Perdigon, G. *J. Dairy Sci.* **2002**, 85, 2733.
- (154) García-Ruiz, J. M.; Hyde, S. T.; Carnerup, A. M.; Christy, A. G.; Van Kranendonk, M. J.; Welham, N. J. *Science* **2003**, 302, 1194.
- (155) Boeke, H.E. *Carbonatschmelzen unter Kohlensauredruck*, Mitt. Natur Gesellsch., vol. 3, 1913.
- (156) Lander, J. J. *J. Chem. Physics* **1949**, 17, 892.
- (157) Baker, E. H. *A high-temperature form of strontium carbonate*, Chem. Soc.: London, 1962.
- (158) García-Ruiz, J. M. *J. Cryst. Growth* **1985**, 73, 251.
- (159) García-Ruiz, J. M. *Geology* **1998**, 26(9), 843.
- (160) García-Ruiz, J. M. *SEPM* **2000**, 67, 75.
- (161) Domingues Bella, S.; García-Ruiz, J. M. *J. Cryst. Growth* **1986**, 79, 236.
- (162) Imai, H.; Terada, T.; Miura, T., Yamabi, S. *J. Cryst. Growth* **2002**, 244, 200.
- (163) García-Ruiz, J. M.; Carnerup, A. M.; Christy, A. G.; Welham, N. J.; Hyde, S. T. *Astrobiology* **2002**, 2 (3), 353.

- (164) Brasier, M. D.; Green, O. R.; Jephcoat, A. P.; Kleppe, A. K.; Van Kranendonk, M. J.; Lindsay, J. F.; Steele, A.; Grassineau, N. V. *Nature* **2002**, 416, 76.
- (165) Schopf, J. W.; Kudryavtsev, A. B.; Agresti, D. G.; Wdowiak, T. J.; Czaja, A. D. *Nature* **2002**, 420, 476.
- (166) Hyde, S. T.; García-Ruiz, J. M. *Actualite Chimique* **2004**, 275, 406.
- (167) Hyde, S. T.; Carnerup, A. M.; Larson, A. K.; Christy, A. G.; García-Ruiz, J. M. *Physica A* **2004**, 339, 24.
- (168) Terada, T.; Yamabi, S.; Imai, H. *J. Cryst. Growth* **2003**, 339, 24.
- (169) Hyde, S.; Larsson, K.; Blum, Z.; Landh, T.; Lidin, S.; Ninham, B.W.; Andersson, S. *The Language of Shape*, Elsevier Science B. V.: Amsterdam, 1997.
- (170) Kellermeier, M. *Isocapillary gels and biomorphs as examples for equilibrium and non-equilibrium self-assembly*, Diplomthesis: University of Regensburg, 2005.
- (171) De Villiers, J. P. R. *The American Mineralogist* **1971**, 56, 758.

Chapter 3

Techniques

3.1. pH Measurements

The pH of the solutions were measured with an electrode (standard glass electrode 84907 from Bioblock Scientific) and a pH meter (Consort C835). The filling solution of the reference *Ag/AgCl* electrode was 4 M *KCl*, and a ceramic diaphragm was used for the liquid junction, as delivered by Bioblock Scientific. The calibration was done before each measurement with three standard solutions at pH 4, 7 and 9 (CertiPUR from Merck).

3.2. Dynamic Light Scattering

Dynamic light scattering (DLS), also referred to as quasi-elastic light scattering¹, was used for sizing of sub-micrometer particles in solution and for monitoring the kinetics of time-dependent processes, such as particle growth. This method is based upon a mechanism of absorption and re-emission of electromagnetic radiation^{2,3}.

Samples Preparation. Usually, the samples were filtered through a 0.2 μm syringe filter and deposited into a clean and dust free plastic cuvettes. However, in the case of the casein micelle solutions, the filtering was avoided because the dust particles and the micelles are of similar size. Afterwards, the cuvettes were placed into the DLS devise.

Instrumentation and Principle of Operation. DLS measurements were done using a Zetasizer spectrometer (Malvern Instruments Ltd., Model Z3000) equipped with a 5 mW *He-Ne* laser. The basic components of the DLS instrument are presented in Figure 3.1. In a typical experiment, the sample is illuminated with an incident light beam (monochromatic

red light at 633 nm) with an intensity I_0 and a wave vector \vec{k}_i . The wave vector has a magnitude $k_i = 2\pi n_1/\lambda$, in which λ is the wavelength of the light in vacuum and n is the refractive index of the medium. The radiation is scattered with an intensity I and a wave vector \vec{k}_s and it is monitored at a known scattering angle θ by a detector (i.e., the photomultiplier). In this work, the measurements were carried out exclusively at a scattering angle of 90° .

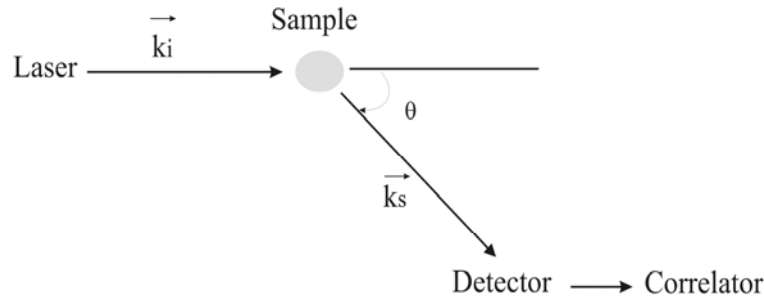


Figure 3.1 Schematic of light scattering experiment.

Since the wavelengths of the incident and scattered light are almost identical⁴ ($k_i \sim k_s$, elastic scattering), the resultant scattering vector magnitude q is determined by the scattering angle θ , the refractive index of the solution n , and the wavelength λ :

$$q = \frac{4\pi n \sin(\theta/2)}{\lambda} \quad (1)$$

Particle Size Determination. The information about the particle size was obtained from the autocorrelation function of the scattered light intensity that was approximated by the digital correlator:

$$g_2(\tau) = \frac{\langle I(t)I(t+\tau) \rangle}{\langle I^2 \rangle} = 1 + g_1(\tau)^2 \quad (2)$$

where $I(t)$ and $I(t + \tau)$ are the scattered intensities registered at an arbitrary time t and at a time delay τ later, respectively; $g_1(\tau)$ is the normalised autocorrelation function of the electric field. Thus, from $g_1(\tau)$ was extracted the characteristic decay rate⁵, Γ , that depends on the magnitude of the scattering vector and on the diffusion coefficient.

$$\Gamma = q^2 D \quad (3)$$

The diffusion coefficient of the particles is closely linked to the particle size by the Stokes-Einstein relationship:

$$D = \frac{k_B T}{6\pi\eta R_h} \quad (4)$$

where k_B is the Boltzmann constant, T the absolute temperature, η the viscosity of the solvent, and R_h the hydrodynamic radius of the particles.

While a monodisperse sample is characterized by a single exponential decay $g_1(\tau) = \exp(-\Gamma \tau)$, a polydisperse sample gives rise to a series of exponentials and several complex methods have been invented for the fitting process⁵. The methods used in this work were Contin and Non-Negatively Constrained Least Squares (NNLS).

3.3. Microscopic Techniques

3.3.1. Optical Microscopy

The optical microscope uses a series of glass lenses to bend light waves and to create a magnified image⁶⁻⁸. The wavelength of light imposes a limit in light microscopy that makes it suitable for the particles examination in the size range 0.8 to 150 μm ⁹.

Sample Preparation. During the crystallization process, the particles were mainly accumulated on the bottom of the used cell wells. After the supernatant was removed, the particles could be direct investigated. In some cases, the particles were collected with the help of a needle and deposited on the ground-in and polished cavities of a microscope slide. Then, the slide cavities were covered with a cover slip and examined.

Instrumentation and Principles of Operation. The devise, used in the present work, was a polarizing light microscope (Model Eclipse E400), equipped with two polarizing filters (Figure 3.2), namely *polarizer* and *analyzer*. Both are orientated perpendicular to one another and consist of long-chain organic molecules (i.e., polarization directions) aligned in one direction and placed in a plastic sheet.

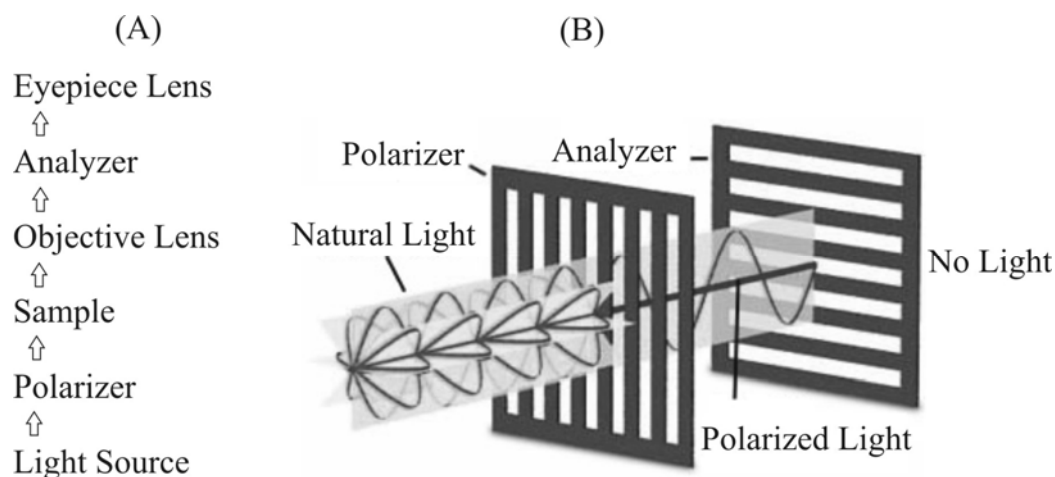


Figure 3.2 (A) Basic components of a polarizing microscope. (Reproduced from [8]) (B) Light passing through crossed polarizers.

The polarizer is used to change the natural light (i.e., nonpolarised light) to linearly polarized light. The analyzer may be placed *in* or *out* of the path of light. If the analyzer is *in*, then no light will pass through the analyzer. If the analyzer is *out*, so that it is not in the light path, then the polarized light will be transmitted towards the ocular lens (i.e., eyepiece lens)⁸ and the microscope behaves as a simple magnifying microscope.

Our samples were investigated with the analyzer alternatively *out* and *in*. When the analyzer was *out*, we noted the size and the shape of the crystal. When the analyzer was *in*, the sample was viewed between crossed polars, and was possible to see whether the sample is isotropic (dark) or anisotropic (bright or coloured). Images were taken with the help of a JVC CCD colour video camera (Model TKC1380).

3.3.2. Electron Microscopy

The electron microscope operates on the same basic principles as the light microscope but the magnified image is created by using electrons instead of light waves. This technique can yield information about morphology, topography and crystallography of the sample. The electron microscope is used for the particles examination in the size range 0.1 to 150 μm .

There are two main electron microscopy techniques: scanning electron microscope (SEM), which looks *at* the crystal surface, and transmission electron microscope (TEM), which looks *through* the specimen.

3.3.2.1. Scanning Electron Microscope

SEM Sample Preparation. The dried sample was placed on double-sided conducting carbon tape, supported on a plate, and sputter-coated with a very thin layer of gold (at circa 30 mA for one minute). Sputtering was performed in an argon atmosphere using either an Emitech or a Polaron Equipment LTD sputter coater.

Instrumentation and Principle of Operation. SEM was performed either using a microscope FEI Quanta 400 or Jeol JSM 840, both operating at 0.2–30 kV. *Field-emission scanning electron microscopy (FESEM)* was performed using a microscope (Hitachi, Model S4500) operating at 0.5–30 kV. It has ‘upper and lower’ secondary electron detectors (Robinson, Model Mk 6). The upper detector collects the secondary electrons SE₁ (secondary electrons generated by the primary electrons; they are known to be the high-resolution signal) and SE₂ (secondary electrons generated by the backscatter electrons), whereas the lower detector collects only the SE₃ (secondary electrons generated by the collision with of the backscatter electrons with the chamber) and is, in practice a backscatter electron detector¹⁰. The upper detector gives a better resolution than the lower detector.

The basic components of the instrument are: the column, the detector, the amplifier and the display. Inside the microscope’s column there are: the electron gun (i.e., a cathode of tungsten[‡] (SEM) or field emission (FESEM)), several coils (condensing lenses, scan coils and objective lens) and the sample target (Figure 3.3 A). After the air is pumped out of the column, the electron gun emits a beam of high energy electrons (3–30 kV). The condensing lenses focus the electron beam on the specimen, where the scanning coils move the focused beam back and forth over the specimen in a series of lines and frames called a raster. The objective lenses help to focus the image.

[‡] Tungsten is used because it has the highest melting point of all metals, thereby allowing it to be heated for electron emission.

As the beam ‘plays’ over the specimen, both X-rays and secondary electrons are emitted from the specimen. The former are used for chemical analysis (see EDX technique) and the latter are collected by the detector for creating the 3D image.

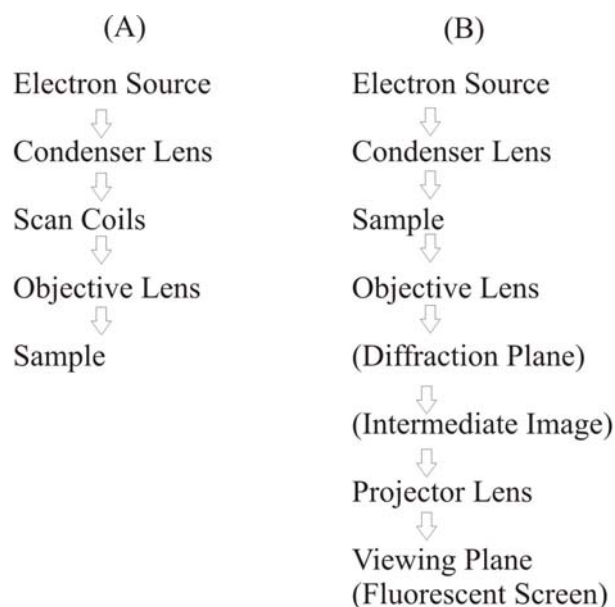


Figure 3.3 Basic components inside the (A) SEM’s column and (B) TEM’s column. (Redrawn after [9])

3.3.2.2. Transmission Electron Microscope

TEM Sample Preparation. The powder was suspended in ethanol. A drop of the suspension was placed on a copper grid by means of a pipette. Then, the grid was allowed to dry before use. The specimen must be very thin, transparent to electrons accelerated to 50–300 kV and able to withstand the high vacuum present inside the instrument.

Instrumentation and Principle of Operation. The used TEM (300 kV) was from Philips (Model EM 430). It is equipped with a TVIPS CCD camera (1024 x 1024 pixels) and an ultra-thin window Oxford ISIS EDXA with element mapping. The basic components of the TEM’s column are listed in Figure 3.3 B. Electrons, emitted from the electron gun (tungsten filament), are accelerated through a high voltage. The higher is the acceleration voltage, the shorter are the electron waves and the higher is the power of resolution. The accelerated ray of electrons is first focused by the condenser lens onto the specimen and, then, passes through sample, where is partially deflected. The degree of deflection depends

on the electron density of the specimen. The greater is the mass of the atoms, the greater is the degree of deflection.

After passing through sample, the transmitted electrons are collected by the objective lens. Thus an image is formed, that is subsequently enlarged by the projector lens. Finally, the image of the specimen appears on the fluorescent screen. If the specimen is crystalline, a diffraction pattern will appear. By changing the strength of the projector lens, it is possible to enlarge the diffraction pattern and project it onto the fluorescent screen. Furthermore, the used TEM was equipped with a specimen holder that allows the user to tilt the sample to a range of angles to obtain specific diffraction conditions.

3.4. Spectroscopic Techniques

The basic principle of the spectroscopic techniques (Figure 3.4) is that under certain conditions the materials absorb or emit energy. The spectra are usually a plot of the intensity of absorption or emission as a function of energy. The energy is usually expressed as frequency f , or wavelength λ of the radiations and related by the following formulas:

$$E = hf = hC\lambda^{-1} \quad (5)$$

where h is the Plank's constant ($6.62608 \cdot 10^{-34}$ J·sec) and C is the speed of light ($2.99 \cdot 10^{10}$ cm·sec⁻¹). The spectroscopic techniques used in our work are as follows.

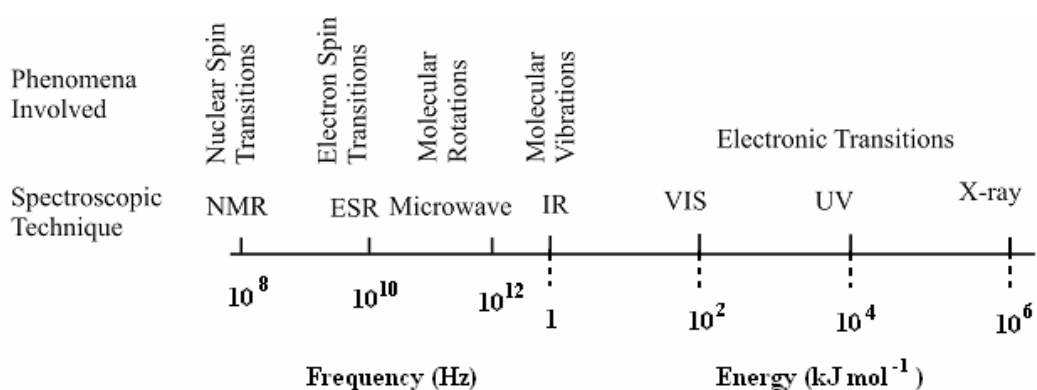


Figure 3.4 Principle regions of the electromagnetic spectrum and the association spectroscopic techniques. (Redrawn after [5])

3.4.1. Infrared Spectroscopy

General Concepts. Infrared spectroscopy deals with the interaction of infrared light with matter. The infrared radiation is absorbed by molecules and is converted into energy of molecular vibration. There are two types of the molecular vibrations: stretching (change in inter-atomic distance along bond axis, which can be symmetric and asymmetric) and bending (change in angle between two bonds that can occur in the plane of molecule or out of plane).

The infrared region is divided into three regions: near (below 400 cm^{-1}), middle ($400\text{--}4000\text{ cm}^{-1}$) and far (above 4000 cm^{-1}) infrared. Usually, the middle region is the most used.

The IR spectrum is the plot of intensity of the transmittance (or absorbance) as a function of wavenumber. Absorbance is the logarithm of the reciprocal of the transmittance:

$$A = \log \frac{1}{T_{IR}} \quad (6)$$

The wavenumber is the inverse of the wavelength, λ :

$$\bar{\nu} = \frac{1}{\lambda} \quad (7)$$

FTIR Sample Preparation. The solid samples were mixed with *KBr* powder. Afterwards, the resultant mixture was grinded for 3–5 minutes in an agate mortar and deposited on the sample holder. For the analysis of liquids, an ATR accessory was used. The ATR crystal was of a trapezoid shape and is 80 mm long, 10 mm wide and 4 mm thick. The samples were deposited on the ATR holder with the help of a pipette.

Instrumentation and Principle of Operation. The used instrument was a Fourier transform spectrometer (Jasco FTIR–610) that was capable of simultaneous analysis of the full spectral range using interferometry. This single beam instrument is based on the use of a Michelson interferometer type placed between the source and the sample (Figure 3.5). Irradiation from the source impacts the *beam splitter* (e.g. a component of the interferometer) that allows the generation of two beams, one of which falls on a fixed

mirror and the other on a mobile mirror. The two beams, later recombine along the optical path, travel through the sample before hitting the detector. The detector measures the global light intensity received. The transmitted signal is recorded as an interferogram, $I=f(\delta)$, where δ is the optical path difference between both beams. Afterwards, using the Fourier transform algorithm, a classical representation of the spectrum can be obtained, $T=f(\bar{\varrho})$. To obtain the sample spectrum, two spectra of transmitted intensities were recorded: the first without sample (absorption background) and the second with sample.

Light Source \Rightarrow Interferometer \Rightarrow Sample \Rightarrow Detector

Figure 3.5 Schematic diagram of a Fourier transform instrument.

Characteristic Bands for CaCO₃. In the present work, IR–technique was used to gather information about the crystal structure of the carbonate minerals. According to literature^{11,12}, there are four fundamental absorption bands in the spectra of the carbonates: a symmetric stretching (ν_1), an out-of-plane bending (ν_2), a double degenerate asymmetric stretching (ν_3), and a double degenerate planar bending (ν_4). The wavenumber of these absorption bands correspond to particular deformations modes of the CO_3^{2-} ion. According to Andersen et al.¹³, there are differences in the infrared spectra of the $CaCO_3$ polymorphs (Table 3.1), which result in part from a modification of the lattice structure.

Table 3.1 Characteristic bands for $CaCO_3$. (Reproduced from [13])

<i>Mode</i>	<i>ACC</i>	<i>Vaterite</i>	<i>Aragonite</i>	<i>Calcite</i>
$\nu_1(\text{cm}^{-1})$	1067	1089	1083	–
$\nu_2(\text{cm}^{-1})$	864	877	854	877
$\nu_3(\text{cm}^{-1})$	1490	1487	1488	1420
	1425	1445	1440	
$\nu_4(\text{cm}^{-1})$	725	746	713	713
	690	738	700	

3.4.2. Ultraviolet and Visible Spectroscopy

General Concepts. The ultraviolet and visible regions (Figure 3.4) cover ranges between 190–380 nm and 380–800 nm, respectively. These radiations interact with matter and cause electronic transitions from the ground state to the high energy state ($\pi-\pi^*$, $n-\pi^*$ and $n-\sigma^*$).

UV-VIS Sample Preparation. The samples were placed in the transparent cells, known as cuvettes. The cuvettes, made up of transparent material such as quartz or polymethyl methacrylate, are rectangular in shape with an internal width of 1 cm. This width is the path length in the Lambert-Beer law:

$$A = \epsilon cl \quad (8)$$

where c is the concentration of absorbing molecules and ϵ is the extinction coefficient.

Instrumentation and Principle of Operation. UV-VIS absorption spectra were measured on a Perkin Elmer Lambda 18 dual-beam spectrophotometer. The UV-VIS spectrophotometer measures the intensity of light passing through a sample, I , and compares it to the intensity of light before it passes through the sample, I_0 . The basic components of a UV-VIS spectrophotometer are listed in Figure 3.6. The light source is usually a hydrogen or deuterium lamp for UV measurements and a tungsten lamp for VIS measurements. The wavelengths of these sources are selected with a monochromator, which filters the light so that only light of a single wavelength reaches the detector. The resulting spectrum is presented as a graph of absorbance, A , versus wavelength, λ .

Light Source \Rightarrow Monochromator \Rightarrow Sample \Rightarrow Detector

Figure 3.6 Basic components of the UV-VIS spectrometer.

3.4.3. Nuclear Magnetic Resonance Spectroscopy

Nuclear magnetic resonance spectroscopy (NMR) is based on resonant absorption by certain atoms of frequencies radiated by the electromagnetic radiation¹⁵ ranging from 4 to 900 MHz (Figure 3.4). Contrary to the spectroscopic techniques described above, nuclei of

atoms are involved in the absorption process. This method was employed to determine the influence of the silicate ions in the casein structure.

General Concepts of NMR¹⁴. The nucleus has a positive charge and is spinning around its axis generating a small magnetic field. So, the nucleus possesses a magnetic moment, μ , proportional to the spin quantum number, I_s .

$$\mu = \frac{\gamma I_s h}{2\pi} \quad (9)$$

The constant, γ , is called the *magnetogyric ratio* and it has a different value for every nucleus, h is Planck's constant. The phosphorus nucleus, ^{31}P , which was of interest in this work, has the spin quantum number $\frac{1}{2}$. When such a nucleus, with a spin quantum number of one half, is brought into an external field B , its magnetic moment can have $2I_s+1$ possible orientation: aligned ($m_I^\S = +\frac{1}{2}$) and opposed ($m_I = -\frac{1}{2}$) to the direction of the external field. The energy of the spin state $-\frac{1}{2}$ is higher than the energy of the spin state $+\frac{1}{2}$. The difference in energy ΔE between the two states is:

$$\Delta E = \frac{\gamma h B}{2\pi} \quad (10)$$

For NMR purposes, this small energy differences ΔE is usually expressed as a frequency in units of MHz (10^6 Hz).

Irradiation of a sample with radiofrequency energy $f = \Delta E/h = \gamma B/2\pi$ (Larmor's equation) causes excitation of the nuclei from the lower $+\frac{1}{2}$ spin state to the higher $-\frac{1}{2}$ spin state until the population of the higher and lower energy levels become equal. When this occurs, the system slowly returns to its original state. As the system returns to equilibrium, which can take several seconds, the instrument records a complex signal due to the combination of the different frequencies present, and the intensity of the signal decays exponentially with time. Using Fourier transform, this signal can be transformed from the *time domain* into *frequency domain*.

[§] m_I - the magnetic quantum number.

NMR Sample Preparation. After the solute was dissolved in D_2O solution (10%, w/w), about 1 mL of sample was transferred to a 203 mm length high-resolution NMR tube (Norell, Inc).

Instrumentation. Phosphorus-31 nuclear magnetic resonance spectra (^{31}P NMR) measurements were carried out with a Bruker Avance 400 spectrometer working at 161.98 MHz under proton-decoupling conditions. The number of scans was 1000 in all measurements and the applied exponential line broadening 2 Hz. Chemical shifts are given relative to external 85% aqueous H_3PO_4 .

3.4.4. Mass Spectrometry

Mass spectrometry (ES-MS) was employed to determine the lysozyme molecular mass and to study its interaction with inorganic ions (e.g. Ca^{2+} and CO_3^{2-}) under positive ionization mode where the acetic acid solvent is added to aid protonation (pH 4).

General Concepts. The beam of ions is accelerated into the magnetic and/or electric field (depending on the type of the instrument) and is deflected along circular paths according to the masses of the ions. The dynamic of the charged particles in electric and magnetic field is described by the classical equation of motion of charged particles:

$$(m/q_i)a = E_f + v \times B \quad (11)$$

where m is the mass of the ion, q_i is the ionic charge, a is the acceleration, E_f is the electric field, and the $v \times B$ is the vector cross product of the ion velocity and the magnetic field. During the measurements, the sample undergoes the following successive processes: ionization, acceleration, separation and detection.

Instrumentation and Principle of Operation. ES-MS was carried out using a Thermoquest Finnigan TSQ 7000 (San Jose, CA, USA) with a triple stage quadrupole mass spectrometer. Data were collected using the Xcalibur software. The instrument is calibrated using myoglobin and has an error of 0.2 Th. The basic components of the mass spectrometer¹⁶ are: inlet system, ionization source, mass analyser, detector and signal processor. The sample is inserted through a stainless steel capillary held at 4 kV into the inlet system, where its components are volatilized and then allowed to leak into ionization

region. Once the sample is inside the ionization source, the components of the sample are converted into ions. The ionization method used in this work is *electrospray ionization*¹⁷ (*ES-MS*), in which the sample is ionized by the addition (positive ionization mode) or removal (negative ionization mode) of protons. Immediately after their formation, these ions are extracted into the mass analyzer region where they are separated according to their mass-to-charge ratios (m/z). After separation, the ions terminate their path and strike the detector, which convert the beam of ions into an electrical signal. The signal is then transmitted to the data system (i.e., signal processor) where it is recorded in the form of mass spectra.

3.4.5. X-ray Diffraction

X-ray diffraction (XRD) was used here for identification and quantitative¹⁸ (in the case of mixtures of crystalline materials) determination of the various crystalline phases, present in the calcium carbonate powders. X-rays are electromagnetic radiations with wavelengths of the order of 10^{-10} m = 1 Å, produced by the deceleration of high-energy electrons or by electronic transitions involving electrons in the innermost orbitals of the atoms⁴. The X-ray region of the electromagnetic spectrum (Figure 3.4) occurs between gamma-rays and the ultraviolet region.

XRD Sample Preparation. The sample holder was a plate with a through hole in the center. A polyethylene plastic film (Mylar) was greased on one side with silicon (Baysilone-Paste, Bayern) and placed over the hole with the sticky side up. After the sample was grinded for 3–5 minutes in an agate mortar, it was spread on the plastic film, smoothed flat and covered with another plastic film. The film was amorphous and so did not interfere with the pattern being collected.

Instrumentation and Principle of Operation. The diffraction patterns were recorded in transmission geometry on a STOE STADI P diffractometer (STOE & CIE). The main components of the diffractometer are: X-ray source, sample holder and position sensitive detector (PSD). It is equipped with a primary Ge-monocromator to obtain monochromatic $Cu K_{\alpha 1}$ radiation, whose characteristic wavelength is 1.54051 Å. When a monochromatic X-ray beam strikes the powder sample; diffraction occurs in every possible orientation of 2θ . The diffracted beam is collected by the detector, which records a powder diffraction

pattern consisting of peaks using the software WinX^{POW}. The occurrence of peaks depends on constructive interferences of the diffracted X-rays and is described by the Bragg equation:

$$n\lambda = 2d_{hkl} \sin(\Theta) \quad (12)$$

where n is an integer value, λ is the wavelength of X-rays, d is the spacing between the planes in the atomic lattice, and Θ is the angle between the incident ray and the scattering planes. The diffraction patterns were recorded in the range of $8^\circ < 2\Theta < 90^\circ$ at a scanning speed of $0.8^\circ/\text{min}$.

Interpretation of X-ray Powder Diffractograms. Identification of the calcium carbonate phases was achieved by comparing the X-ray diffraction pattern obtained from our sample with reference pattern found in the Internationally Center for Diffraction Data (ICDD). If no peaks were observed, the sample examined was X-ray amorphous.

3.5. Chemical composition

3.5.1. Energy Dispersive X-ray

Energy Dispersive X-ray (EDX) analysis was performed in conjunction with SEM, and gives qualitative and quantitative information on the elemental composition of the specimen under examination.

Sample Preparation. The preparation procedure was similar with SEM measurements, only that the sample was not covered with gold because would induce errors in the chemical composition.

Instrumentation and Principle of Operation. EDX analysis was performed using an EDAX microanalyser mounted on a FEI Quanta 400T scanning electron microscope at 15 kV. This technique utilizes X-rays that are emitted from the SEM sample during bombardment by the electron beam. The emitted X-rays are collected by the EDX detector. The detector measures the number of emitted X-rays versus their energy. The energy of the X-ray is characteristic of the element from which the X-ray is emitted.

3.5.2. CHNOS Elemental Analysis

Sample Preparation. Samples were weighed into various sized tin vessels and dropped into the combustion tube.

Instrumentation and Principle of Operation. Elemental analysis was carried out using a *vario EL III* elemental analyzer (Elemental Analysensysteme GmbH), which yielded the amounts of CHNOS in the sample. The basic principle of quantitative CHNOS analysis is high temperature combustion of the sample. Complete combustion is ensured with special oxygen jet injection. The gaseous combustion products are purified, separated into various components and analyzed with a thermoconductivity detector (TCD).

3.6. References

- (1) Borkovec, M. *Handbook of Applied Surface and Colloid Chemistry*, John Wiley & Sons, Ltd: New York, 2001.
- (2) Kerker, M. *The scattering of Light and Other Electromagnetic Radiation*, Academic Press: New York, 1969.
- (3) Bohren, C. F.; Huffmann, D. R. *Absorption and Scattering Light by Small Particles*, John Wiley: New York, 1998.
- (4) Finsy, R. *Adv. Colloid Int. Sci.* **1994**, 52, 79.
- (5) Bantchev, G. B.; Russo, P. S.; McCarley, R. L.; Hammer, R. P. *Rev. Sci. Instrum.* **2006**, 77, 043902.
- (6) Allen, T. *Particle size distribution*, 4th Edn., Chapman and Hall: London, 1990.
- (7) Schdel, M.; Behrens, H.; Holthoff, H; Kretzschmar, R.; Borkovec, M. *J. Colloid Int. Sci.* **1997**, 196, 241.
- (8) West, A. R. *Basic solid state chemistry*, John Wiley & Sons, Ltd: England, 2001.
- (9) Rowe, S. H. *Microscope* **1966**, 15, 216.
- (10) Gauvin, R.; Robertson, K.; Elwazri, A. M.; Yue, S. *JOM* **2006**, 28(3), 20.
- (11) Adlar, H. H.; Kerr, P. F. *Am. Mineralogist* **1962**, 47, 700.
- (12) Herzberg, G. *Molecular Spectra and Molecular structure. Infrared and Ramon Spectra of Polyatomic Molecules*, Van Nostrand: New York, 178, 1945.
- (13) Anderson, F. A.; Brecevic, L. *Acta Chem. Scand.* **1991**, 45, 1018.

-
- (14) Rouessac, F.; Rouessac, A. *Chemical Analysis. Modern Instrumentation Methods and Techniques*, John Wiley & SONS, Ltd: New York, 2000.
- (15) Atkins, P.; De Paula, J. *Atkins' Physical Chemistry*, 7th Ed, Oxford University Press Inc.: New York, 2002.
- (16) Skoog, D. A.; Leary, J. J. *Principals of instrumental analysis*, 4th Ed, Saunders College Publishing: New York, 1992.
- (17) Fenn, J. J. *Phys. Chem.* **1984**, 88, 4451.
- (18) Jenkins, R.; Gould, R. W.; Gedcke, D. *Quantitative X-ray Spectroscopy*, Marcel Dekker: New York, 1981.

Chapter 4

The Formation of $CaCO_3$ Single-Crystal Particles Starting from Lysozyme Sols

Abstract

The influence of egg white lysozyme on the size, shape, crystallography and chemical composition of amorphous calcium carbonate (ACC) particles obtained from $CaCl_2$ –dimethyl carbonate (DMC)– $NaOH$ solutions was studied. At the onset of precipitation, the presence of lysozyme led to much smaller particles (50–400 nm spherical amorphous lysozyme-calcium carbonate particles (Ly–ACC)) than those obtained from lysozyme-free solution. The nanospheres were in some cases aggregated and in addition embedded in a faint network. Their size and interconnection depended on the concentration of the egg white lysozyme. When the Ly–ACC particles were left in contact with the mother liquor ($CaCl_2$ /DMC/ $NaOH$ /lysozyme solution) for 24 h, they transformed directly and exclusively into crystalline calcite. The observed results may be of relevance for a better understanding of the role of lysozyme in the process of eggshell mineralization.

4.1. Introduction

Lysozyme is a monomeric globular protein known to be present in the eggshell matrix¹, along with calcium carbonate. Calcium carbonate is an important biogenic mineral in organisms^{2, 3} and it exists in a variety of polymorphic forms: hydrates (i.e., amorphous calcium carbonate (ACC), calcium carbonate monohydrate, and calcium carbonate hexahydrate) and anhydrous (calcite, aragonite, and vaterite) calcium carbonate.

Synthetic ACC contains 0.5 mole water per formula unit ($\text{CaCO}_3 \cdot 0.5\text{H}_2\text{O}$)^{4, 5}. It is thermodynamically and kinetically highly unstable under ambient conditions, and it transforms quickly into one of the anhydrous crystalline phases^{6, 7}. Nevertheless, this transformation can be significantly retarded by a substantial level of inorganic and synthetic organic additives within the mineral phase (such as magnesium^{8, 9} and triphosphate¹⁰ ions and hydrophilic blockcopolymers¹¹, poly(propylenimin)-dendrimers^{12,13}, diphosphate-substituted poly(ethylene glycol)¹⁴, poly(acrylic acid)¹⁵, polysaccharides^{16, 17}, poly(vinyl alcohol)¹⁸ and polyaspartate¹⁹, respectively).

In contrast, a biogenic amorphous precipitate can be stable for a long period of time²⁰ because of biological matrices²¹, which prevent crystallization. Stable ACCs have been reproduced in vitro by adding specific proteins rich in glutamic acid and glutamine, extracted from spicules²², sponges²³, and gastroliths of crustaceans²⁴. ACC also serves as a precursor phase during the formation of other minerals (calcite, aragonite and vaterite) in the biomineralization process.

Thus, Raz et al.²² reported that ACC is the precursor of calcite for the growth of spicules in sea urchin larvae of different species. Recently, Lakshminarayanan et al.²⁵ demonstrated the possible formation of the ACC phase in the first stages of precipitation and its subsequent transformation to calcite in quail eggshell biomineralization.

Avian eggshell contains 95% inorganic calcite crystals along with an organic matrix consisting of three groups: *ubiquitous matrix* protein including clusterin and osteopontin, the *novel eggshell matrix* (ovocleidins and ovocalyxins), which is unique of the eggshell calcification process, and *egg white* proteins²⁶. The later identified in chicken eggshells are composed of ovotransferrin²⁷, ovalbumin²⁸, and lysozyme¹.

The calcification process occurs in the uterine fluid of the oviduct, an acellular milieu that is supersaturated with Ca^{2+} and HCO_3^- as well as the organic precursor of the eggshell matrix^{27, 29}. Mineral deposition takes place in three stages: initial nucleation, growth, and inhibition of growth²⁹. The uterine fluid collected in each stage of shell formation shows that lysozyme is particularly abundant during the initial stage of shell formation²⁷. One indication that shell calcification may be controlled by lysozyme is that the concentration of the protein in the uterine fluid changes at different stages of shell formation. The key

question therefore concerns the role of lysozyme in the calcification process. To date, the implication of lysozyme is unclear¹ and there are only a few qualitative ideas³¹ about it.

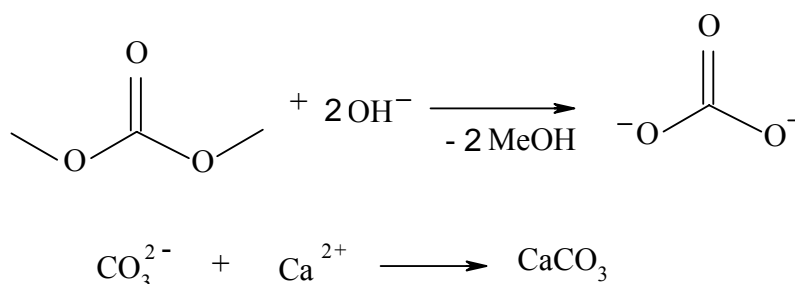
Lakshminarayanan et al.²⁵ reports that amorphous calcium carbonate could be the initial phase formed in eggshell calcification but without the implication of lysozyme. Firstly, this result is based on images of the calcified quail eggshell that indicate that the mammillary layer (the first layer formed during eggshell formation) consists of closely assembled nanoparticles. Second, the ACC precursor phase is obtained *in vitro* experiments in the presence of soluble organic matrices extracted from quail eggshell but not in the presence of lysozyme. Nevertheless, lysozyme being present in the eggshell matrix during the first stage of shell formation may influence the precipitation of ACC particles *in vivo*. This is the motivation for the present study of the influence of lysozyme on ACC during *in vitro* experiments. Moreover, the Ly-ACC transition to calcite is studied to understand the lysozyme functional properties during eggshell biomineralization.

4.2. Experimental Section

4.2.1. Materials Preparation

Dimethyl carbonate (DMC, purity >98%), calcium chloride dihydrate (purity >99%) and sodium hydroxide (purity 99%) were purchased from Sigma-Aldrich and used without further purification. Lysozyme was purchased from Aldrich (purity 95%, IP = 11.35, M=14 kDa. Purified water with an electrical conductivity less than 10^{-6} S·m⁻¹ was taken from a Millipore Milli-Q system.

The preparation of amorphous calcium carbonate was performed according to the method reported by Faatz et al.³⁰, and the reactions implicated are the following:



Method 1. The aqueous solution was prepared in a 100 mL flask containing 147 mg of $\text{CaCl}_2 \cdot 2\text{H}_2\text{O}$ (0.001 mol), 450 mg dimethyl carbonate (0.005 mol), 0–5 g/L protein and diluted to 100 mL with water. The reaction was started by adding 20 mL 0.5 M NaOH to a stirred reaction mixture. The initial pH of the solutions was 12.6 ± 0.1 .

Method 2. 147 mg $\text{CaCl}_2 \cdot 2\text{H}_2\text{O}$ (0.001 mol), 90 mg dimethyl carbonate (0.001 mol), and 1 g/L lysozyme were dissolved in ~98 mL of water. The reaction was started by adding 2 mL of 1 M NaOH to a stirred reaction mixture. The initial pH of the solutions is 12.3 ± 0.1 .

The pH of the aqueous solutions was measured using an Ag/AgCl plastic-body electrode (TPS, Model smart CHEM-Lab) and a Consort C835 pH meter. The solutions were stirred for 1 min and then left under static conditions. Afterwards, the precipitate was either collected when first signs of turbidity were observed or left in its mother liquor for 24 h. The precipitate was removed from the solutions by filtration using 0.65 μm membrane filters (MCE Mf-Millipore filters purchased by Fisher Scientific). The powders were collected and washed several times with water and acetone. Experiments were prepared at ambient temperature (20 °C).

4.2.2. Analytical Methods

4.2.2.1. Particle Characterisation

Field-emission Scanning Electron Microscopy (FESEM) was performed using a microscope (Hitachi, Model S4500) operating at 0.5–30 kV. The samples were coated with Au/Pd in an Emitech sputter coater using a rotational stage.

Transmission Electron Microscopy (TEM) was carried out on a 300 kV TEM from Philips (Model EM 430). It is equipped with a TVIPS CCD camera (1024 pixels x 1024 pixels) and an ultrathin window Oxford ISIS EDXA with element mapping.

X-ray Diffraction (XRD) measurements were made using a STOE STADI P diffractometer (STOE & CIE) providing $\text{Cu K}\alpha_1$ radiation monochromated with a germanium single crystal ($\lambda = 1.540598 \text{ \AA}$). Typical diffraction patterns were recorded in the range of $8^\circ < 2\theta < 90^\circ$ at a scanning speed of 0.8 °/min.

4.2.2.2. Techniques Used to Study the Lysozyme-Calcium Interaction

Elemental Analysis was carried out using a *vario EL III* elemental analyzer (Elemental Analysensysteme GmbH), which yielded the amounts of CHNOS in the samples.

Dynamic Light Scattering (DLS) measurements were made using a Zetasizer spectrometer (Malvern Instruments Ltd., model Z3000) equipped with a 5 mW *He-Ne* laser. Measurements were carried out at a scattering angle of 90°, and the intensity autocorrelation functions were analysed using the Contin software. Before DLS measurements were performed, the solutions were filtered through a 2.2 µm membrane filter.

Electrospray Mass Spectrometry (ES-MS) was carried out using a Thermoquest Finnigan TSQ 7000 (San Jose, CA) with a triple-stage quadrupole mass spectrometer. The solutions were sprayed through a stainless steel capillary held at 4 kV, generating multiply charged ions. Data were collected using the Xcalibur software. The instrument is calibrated using myoglobin and has an error of 0.2 Th. ES-MS was employed to study the affinity of calcium to lysozyme molecules at pH 4.

Fourier transform infrared spectroscopy (FTIR) was recorded on a Jasco FTIR-610 spectrometer. The samples were mixed with *KBr* powder. Subsequently, the resultant mixture was grinded for 3–5 minutes in an agate mortar and deposited on the sample holder. The spectra were recorded in reflection mode from 4000 to 400 cm⁻¹ at a resolution of 2 cm⁻¹. For the reaction kinetic experiment, an ATR accessory was used. This accessory is available for the analysis of liquids and it was used for monitoring the transition of Ly-ACC to calcite crystals.

4.3. Results and Discussion

4.3.1. Influence of Lysozyme on the Metastable Form of $CaCO_3$

In previous studies, it was shown that lysozyme is detected in the non-calcified shell membranes and in the mammillary cone layer¹. The mammillary core zone is situated at the interference between the non-calcified and the calcified cone layer³¹ (Figure 2.15). The mammillary core consists of organic material, and it represents the place where the

biomineralization process is initiated. Because the lysozyme is presented at very high concentration in the mammalian cartilage, we assume that it should interfere at the onset of eggshell calcification process and modifies the growth morphology of the particles. Therefore, the $CaCO_3$ precipitation during *in vitro* experiments was performed in the presence of egg white lysozyme.

Figure 4.1 shows FESEM images of calcium carbonate synthesized in aqueous solution in the presence of different lysozyme concentrations (*Method 1*). In a control experiment, without lysozyme, amorphous calcium carbonate particles 400–600 nm in diameter (as reported by Faatz et al.³⁰) were formed when the precipitate was isolated from the solution after 2 min (Figure 4.1 A). It is interesting to note that the obtained ACC particles are highly spherical, not interconnected (Figure 2 A), and reveal uniform holes (not reported by Faatz et al.³⁰) with diameters ranging from 50 to 90 nm (Figure 4.1 A inset). Xu et al.³² also detected holes in spherical $CaCO_3$ particles in the presence of phytic acid.

The presence of lysozyme during the calcium carbonate precipitation process also led to the formation of spherical particles, but with considerable changes. The particle size depended on the lysozyme concentration (e.g., the size of the particles in solution containing 1 g/ L protein was roughly one quarter of that found in the control experiment without organic additives). In some cases, these nanoparticles were aggregated and were also embedded in a faint network (Figure 4.1 B). The degree of interconnectivity increases with lysozyme concentration (Figure 4.1 C, D). In a previous study, it was reported that lysozyme also directs the formation of interconnected nanoparticles of silica or titania³³.

The FESEM images were interpreted in terms of histograms of the $CaCO_3$ particle size distribution depending on lysozyme concentration (Figure 4.1 E). The size distribution of the control experiment, without lysozyme, was broad, with a maximum at a diameter of ca. 500 nm. At lower lysozyme concentration, the size distribution was roughly bimodal. At higher protein concentration, the size distribution became monomodal and narrow. Mean diameters obtained for the samples containing 0.4 and 1 g/ L lysozyme are 230 and 125 nm, respectively. As the lysozyme concentration was further increased (>2 g/ L), the Ly–ACC particle sizes were reduced even more. However, contrary to the case described above, where the particles were more dissociated, the Ly–ACC nanoparticles were more

strongly interconnected (Figure 4.2 B) and had a more sintered appearance at higher lysozyme concentration.

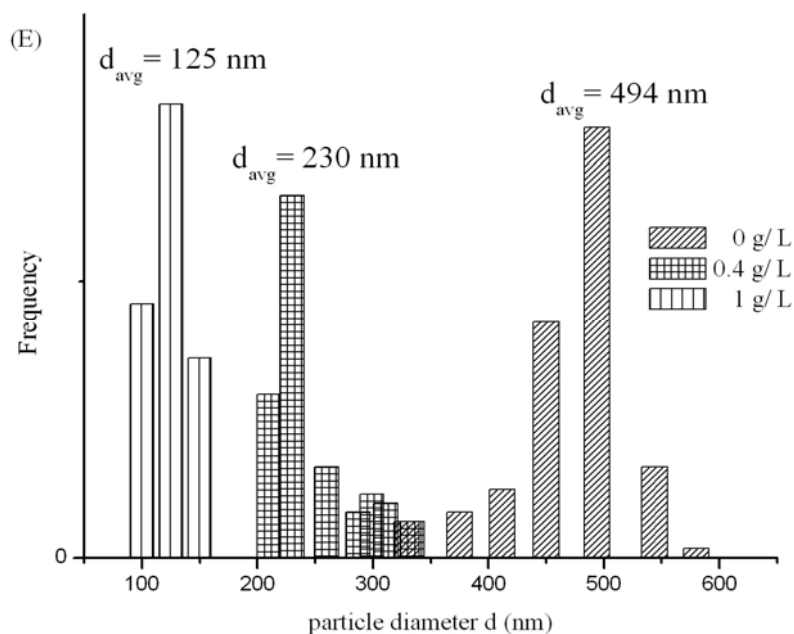
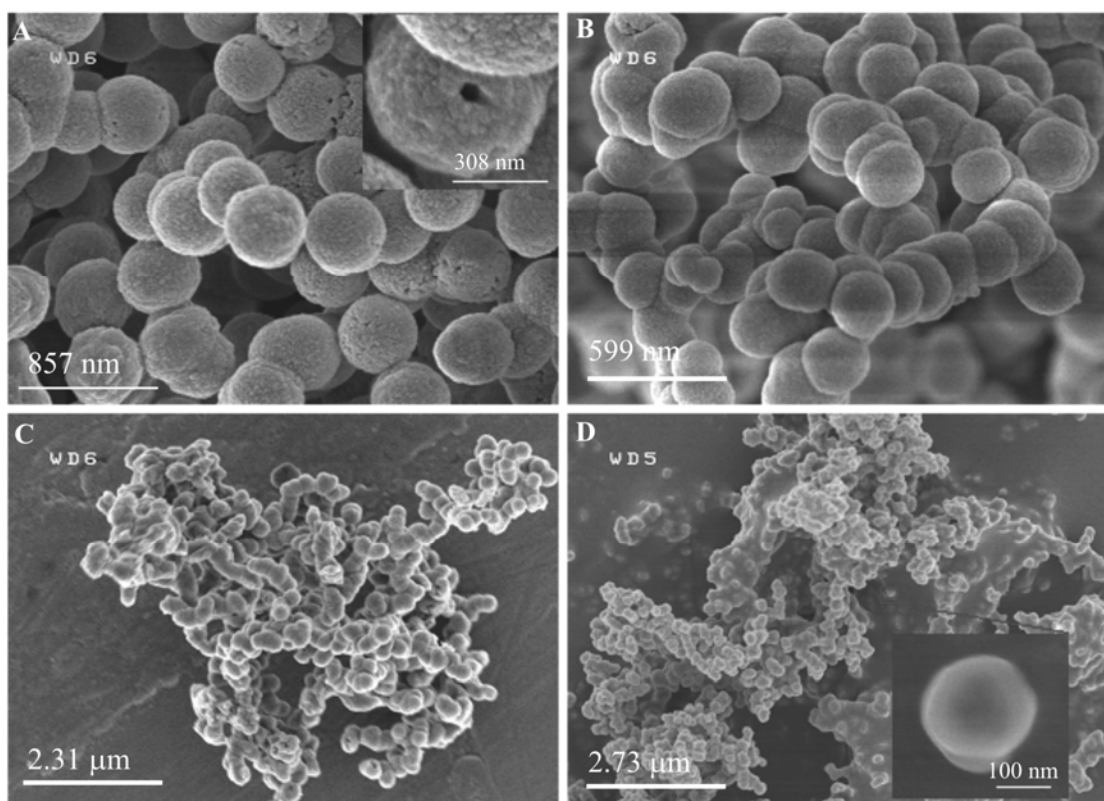


Figure 4.1 FESEM images of calcium carbonate obtained in aqueous solutions in the presence of different lysozyme concentrations: (A) 0, (B) 0.4, (C) 0.7, and (D) 1 g/L. (E) Histograms of CaCO_3 particle size distributions as a function of lysozyme concentration based on FESEM images.

Figure 4.3 presents an XRD diffraction pattern recorded for the Ly-ACC particle synthesized in 1 g/ L lysozyme solutions. The lack of distinct diffraction peaks shows that the material is amorphous.

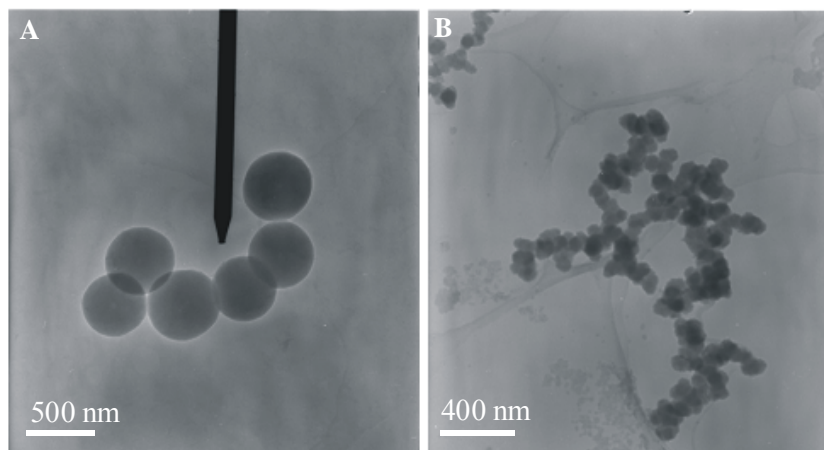


Figure 4.2 TEM images of (A) ACC grown in the control experiment, i.e., in a lysozyme-free solution and (B) Ly-ACC particles synthesized in 2 g/ L lysozyme solution.

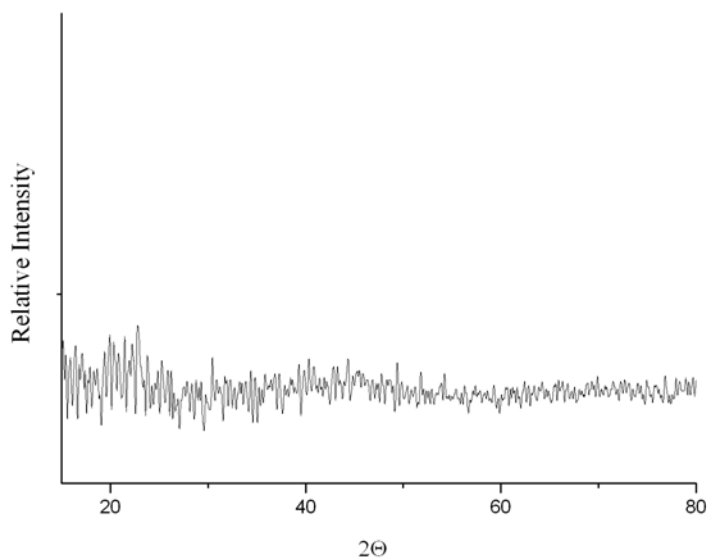


Figure 4.3 XRD pattern of Ly-ACC particles obtained in the presence of 1 g/ L lysozyme and collected after 2 min.

The effect of lysozyme on the particle size is in agreement with previous observations¹, where calcite crystals were grown in the presence of purified hen lysozyme. The lysozyme

molecules, in the calcite growth solution, reduced the size of the crystals. This effect was also proportional to the lysozyme concentration.

At the onset of precipitation, we observe that lysozyme influences the size and the association phenomenon of the particles, whereas the amorphous nature of calcium carbonate is preserved (Figure 4.3). Nevertheless, lysozyme changes the chemical composition of the particles. Elemental analysis shows the presence of nitrogen in the powder. Because of this finding, the interaction between calcium carbonate and lysozyme was investigated in more detail (Appendix 8.2).

As a result, we assume that lysozyme creates a local distribution of calcium ions, which can play the role of calcium carbonate nucleation sites. At high Ca^{2+}/Ly molar ratios (360/1), calcium carbonate nucleates on the few lysozyme particles and produces large objects. At lower calcium to lysozyme molar ratios (72/1) many nucleation centers exist, leading to many small particles of $CaCO_3$ that form a network. This is a confirmation of the ionotropic effect (electrostatic accumulation)³⁴. This effect influences the interaction and recognition process between organic and inorganic phases.

4.3.2. Ageing of the Ly–ACC Particles

4.3.2.1. Ly–ACC Nucleation, Lifetime and its Transformation to the Calcite Phase during the first Hour after Reactant Mixing

Generally, amorphous calcium carbonate transforms into a crystalline phase by a dissolution-recrystallization³⁵ process in solution. ACC transforms into the corresponding crystalline form when it is in contact with the master solutions. It has been shown³⁶ that during the precipitation of the ACC phase, the calcium ion concentration in solution decreased, followed by an increase in calcium ion concentration due to the redissolution of ACC. In the end, the Ca^{2+} concentration decreased again during calcite crystallization.

Then, the Ly–ACC nucleation, lifetime, and phase transformation to calcite polymorph in solution were monitored over time using FTIR measurements. We prepared the solution according to *method 2*, in which the induction time (the time elapsed to observe the first crystal) is significantly higher (~7 min) than for *method 1* (~2 min). Thus, the reactions

take place on a time scale ideally suited for infrared experiments. We note that the change in *NaOH* and *DMC* concentrations had no effect on particle size and morphology.

FTIR spectra of the CaCO_3 sol were interpreted in the range $700 \text{ cm}^{-1} \leq \nu \leq 1700 \text{ cm}^{-1}$ in which the most important absorption bands of calcium carbonate appear (Figure 4.4). Although the spectrum after 5 min had no absorption bands, after 7 min, the spectrum exhibited bands characteristic of ACC: the symmetric stretch (ν_1) at 1077 cm^{-1} , the carbonate out-of-plane bending absorption at around 864 cm^{-1} (ν_2), and a split peak at 1418 and 1480 cm^{-1} (ν_3). Between 7 and 56 min, many changes in the characteristic absorption bands took place: the ν_1 absorption band disappeared; the ν_2 band intensity increased, its peak shifted from 864 to 874 cm^{-1} , and it became narrower; the double peaks (ν_3) changed to a broad band at 1412 cm^{-1} . All these changes indicate the transition of Ly-ACC to the calcite phase exclusively.

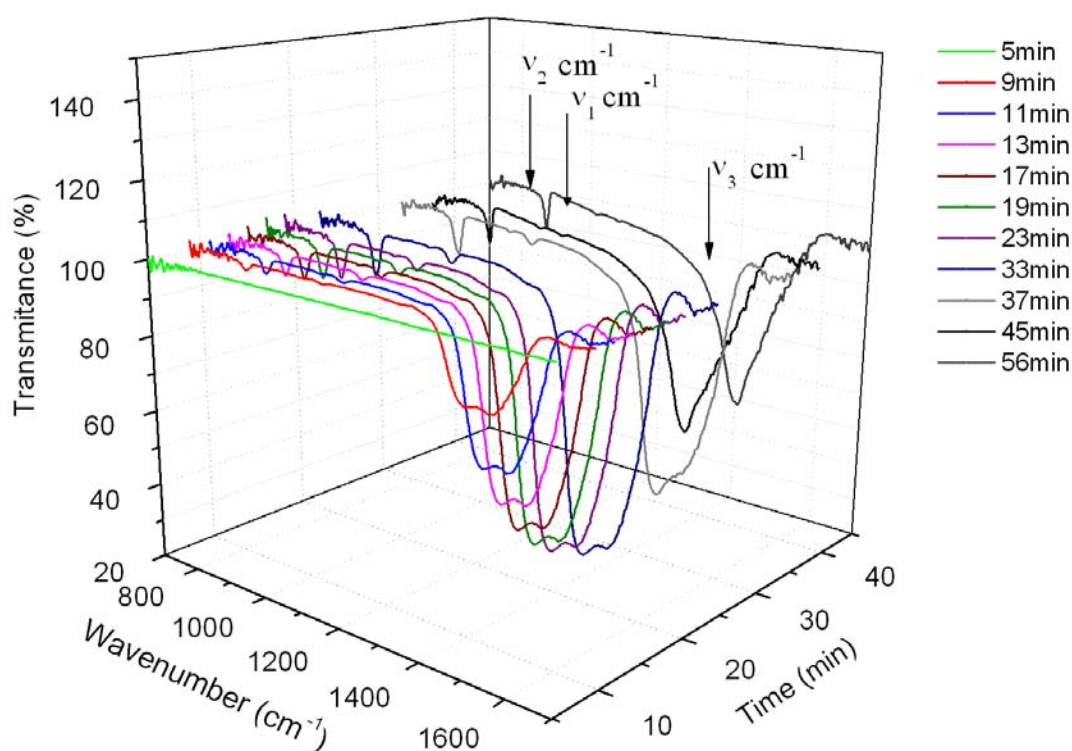


Figure 4.4 FTIR spectra of the CaCO_3 solution at various intervals after the rapid mixing of the reactants.

4.3.2.2. The Amorphous Precipitate left in Contact with the Mother Liquor for 24 h

In the control experiment without lysozyme, the ACC precipitate left in contact with the aqueous solution for 24 hours favours the formation of various CaCO_3 crystal polymorphs and morphologies (Figure 4.5 A and Figure 4.6 A). Thus, different types of morphologies, such as cauliflower-like (vaterite) calcium carbonate (see inset image in Figure 4.5 A), spherical microparticles (vaterite), rhombohedral-like particles (calcite) and dendrite (aragonite), were obtained. The cauliflower-like morphology is composed of lateral projections (extensions) that grow from the center with a size dispersion of around 3 μm in diameter, and 5 μm in length. Counting the particles in the SEM micrograph (Figure 4.5 A) shows that the sample is composed of 73% calcite, 25.1% vaterite and 1.9% aragonite. The corresponding XRD spectrum (Figure 4.6 A) exhibits characteristic reflections of vaterite (V_{110} , V_{112} , and V_{114}) and calcite (C_{104}), but no peaks characteristic of aragonite. The lack of aragonite peaks is certainly owing to its low mass percentage, which is below the detection limit of the X-ray diffractometer. By contrast, the overgrowth of Ly-ACC particles furnished 100% calcite crystals with no other contamination (Figure 4.5 B and Figure 4.6 B), and the particle size is roughly one-half ($\sim 9 \mu\text{m}$) of those in the control experiment without organic additives ($\sim 20 \mu\text{m}$). These results indicate that the organic additive considerably inhibited the crystal growth and favoured the formation of the calcite crystalline form. The calcite crystals were aggregated and partially adopted a predominant random coil conformation.

Earlier studies confirm that lysozyme also modifies the morphology of calcite crystals^{1,36}, which preferentially interacted with faces parallel to the c -axis³⁶. Besides, another protein from the goose eggshell matrix (ansocalcin) used as reaction medium for CaCO_3 nucleates also aggregates from modified calcite crystals *in vitro* mineralization experiments³⁷. However, in those studies the rhombohedral calcite crystals were observed in the absence of protein. Therefore, the influence of lysozyme on a possible *favouring* of calcite phase could not be detected. By contrast, in our systems without lysozyme all kinds of morphologies are found and *only* in the presence of lysozyme pure calcite is formed.

It is interesting that during the eggshell biomineralization, the calcite phase is also privileged³⁸. Calcite crystals found in the chicken eggshell exhibit a preferential orientation with their c -axes perpendicular to the surface of the shell³⁹.

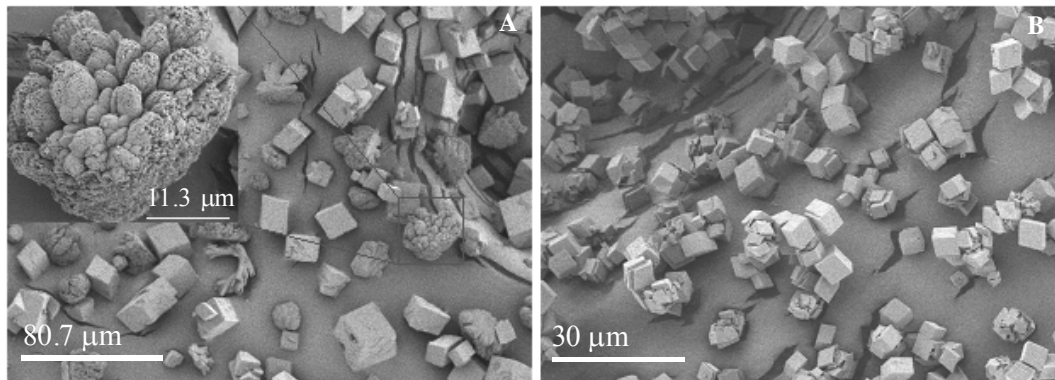


Figure 4.5 FESEM images of $CaCO_3$ crystals synthesized in the absence (A) and in the presence (B) of 1 g/ L lysozyme. The precipitates were in contact with the mother liquor for 24 h.

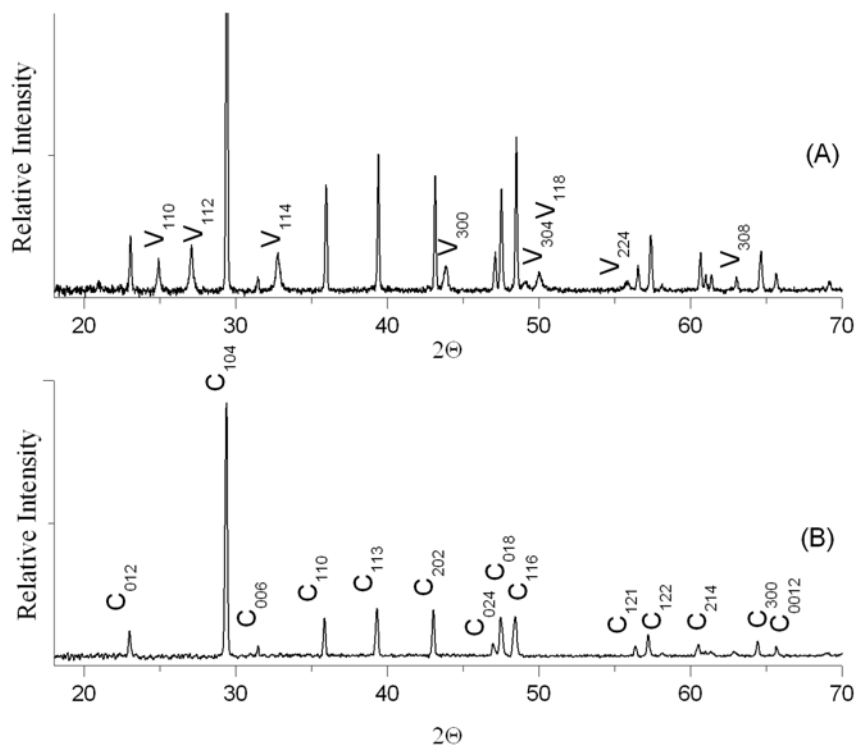


Figure 4.6 XRD pattern of $CaCO_3$ particles obtained in the absence (A) and in the presence (B) of 1 g/ L lysozyme and collected after 24 h. *V* and *C* denote peaks from vaterite and calcite, respectively.

Our observations on the calcite polymorph are in concordance with observations made by Gautron et al.⁴⁰, who studied the influence of uterine fluid on calcium carbonate crystal growth. The uterine fluid is the liquid surrounding the egg during its formation. It contains

the organic precursor of eggshell matrix proteins (i.e., lysozyme) and minerals. In the absence of uterine fluid, the crystal polymorphs were distributed as following: 55% calcite, 22.5% aragonite, and 22.5% vaterite. The presence of uterine fluid during CaCO_3 precipitation drastically modified the kinetics and the total number of crystals and induced the formation of *only* the calcite polymorph, so, in some aspects, the uterine fluid behaves similarly to a lysozyme solution used as a precipitation medium.

4.4. Conclusions

This chapter reports the influence of lysozyme on the calcium carbonate mineralization process. From our experimental results, the following conclusions can be drawn:

(1) Lysozyme considerably decreases the average diameter of the metastable amorphous calcium carbonate particles and promotes a network of associated particles. Moreover, this protein is incorporated *in* (or *on*) the precipitate.

(2) We assume that lysozyme attracts calcium ions and creates a local distribution of calcium ions which can play the role of calcium carbonate nucleation sites. At high Ca^{2+}/Ly molar ratios, large individual objects (however, still smaller than in the absence of lysozyme) are formed, whereas at lower Ca^{2+}/Ly molar ratios many small interconnected particles are formed.

(3) When the precipitate is left in the solution for 24 h, the Ly-ACC particles reorganize exclusively into crystalline calcite. No other morphologies are found. Further, the presence of lysozyme molecules has also a strong effect on the kinetics of CaCO_3 precipitation.

(4) Taking into account that lysozyme is present during the eggshell biomineralization process, it is probable that lysozyme also interferes *in vivo*.

4.5. References

- (1) Hincke, M. T.; Gautron, J.; Panhéleux, M.; García-Ruiz, J. M.; McKee, M. D.; Nys, Y. *Matrix Biol* **2000**, *19*, 443.
- (2) Mann, S. *Biomineralization: Principles and Concepts in Bioinorganic Materials Chemistry*, Oxford University Press: Oxford, U.K., 2001.

- (3) Weiner, S.; Addadi, L. *J. Mater. Chem.* **1997**, 7(5), 689.
- (4) Brecevic, L. *J. Cryst. Growth* **1989**, 98, 504.
- (5) Levi-Kalisman, Y.; Raz, S.; Weiner, S.; Addadi, L. *Adv. Funct. Mat.* **2002**, 12, 43.
- (6) Johnson, J.; Merwin, H. E.; Williamson, E. D. *Am. J. Sci.* **1916**, 41, 473.
- (7) Pantoni, D.; Bolze, J.; Dingenouts, N.; Narayanan, T.; Ballauff, M. *J. Phys. Chem. B* **2003**, 107(22), 5123.
- (8) Loste, E.; Wilson, R. M.; Seshadri, R.; Meldrum, F. C. *J. Cryst. Growth* **2003**, 254, 206.
- (9) Raz, S.; Weiner, S.; Addadi, L. *Adv. Mater.* **2000**, 12, 38.
- (10) Clarkson, J. R.; Price, T. J.; Adams, C. J. *J. Chem. Soc., Faraday Trans* **1992**, 88, 243.
- (11) Cölfen, H.; Qi, L. *Chem. Eur. J.* **2001**, 7(1), 106.
- (12) Donners, J. J. M.; Heywood, B. R.; Meijer, E. W.; Nolte, R. J. M.; Roman, C.; Schenning, A.; Sommerdijk, N. *Chem. Commun.* **2000**, 19, 1937.
- (13) Donners, J. M.; Meijer, E. W.; Nolte, R. J.M.; Sommerdijk, N. *Polym. Mat. Sci. Eng.* **2001**, 84, 1039.
- (14) Kjillin, P.; Holmberg, K.; Nyden, M. *Colloids Surf. A* **2001**, 194 (1–3), 49.
- (15) Xu, G.; Yao, N.; Aksay, I.A.; Grove, J.T. *J. Am. Chem. Soc.* **1998**, 120, 11977.
- (16) Sugawara, A.; Kato, T. *Chem. Commun.* **2000**, 6, 487.
- (17) Hosoda, N.; Kato, T. *Chem. Mater.* **2001**, 13, 688.
- (18) Hosoda, N.; Sugawara, A.; Kato, T. *Macromolecules* **2003**, 36, 6449.
- (19) Gower, L.A.; Tirrell, D.A. *J. Cryst. Growth* **1998**, 191, 153.
- (20) Meldrum, F.C. *Int. Mater. Rev.* **2003**, 48 (3), 187.
- (21) Lowenstam, H.A.; Weiner, S. *On Biomineralization*, Oxford University Press: New York, 1989.
- (22) Raz, S.; Hamilton, P. C.; Wilt, F. H.; Weiner, S.; Addadi, L. *Adv. Funct. Mater.* **2003**, 13(6), 480.
- (23) Aizenberg, J.; Lambert, G.; Addadi, L.; Weiner, S. *Adv. Mater.* **1996**, 8, 222.
- (24) Tsutsui, N.; Ishii, K.; Takagi, Y.; Watanabe, T.; Nagasawa, H. *Zool. Sci.* **1999**, 16, 616.
- (25) Lakshminarayanan, R.; Loh, X. J.; Gayathri, S.; Sindhu, S.; Banerjee, Y.; Kini, R. M.; Valiyaveetil, S. *Biomacromolecules* **2006**, 7 (11), 3202.
- (26) Nys, Y.; Gautron, J.; García-Ruiz, J. M.; Hincke, M. T. *C. R. Palevol* **2004**, 3, 549.

- (27) Nys, Y.; Hincke, M.T.; Arias, J. L.; García-Ruiz, J. M.; Solomon, S. E. *Poult. Avian Biol. Rev.* in press
- (28) Hincke, M.T. *Connect. Tissue Res.* **1995**, *31*, 227.
- (29) Gautron, J.; Hincke, M. T.; Nys, Y. *Connect. Tissue Res.* **1997**, *36*, 195.
- (30) Faatz, M.; Gröhn, F.; Wegner, G. *Adv. Mater.* **2004**, *16*, 996.
- (31) Nys, Y.; Gautron, J.; García-Ruiz, J.M.; Hincke, M. T. *World's Poult.Sci. J.* **2001**, *57*, 401.
- (32) Xu, A.; Yu. Q.; Dong, W.; Antonietti, M.; Cölfen, H. *Adv. Mater.* **2005**, *17*, 2217.
- (33) Luckarift, H. R.; Dickerson, M. B.; Sandhage, K. H.; Spain, J. C. *Small* **2006**, *2*, 640.
- (34) Mann, S. *Nature* **1988**, *332*, 119.
- (35) Sawada, K. *Pure Appl. Chem.* **1997**, *69*, 921.
- (36) Jimenez-Lopez, C.; Rodriguez-Navarro, A.; Domingues-Vera, J.; García-Ruiz, J.M. *Geochim. Cosmochim. Acta* **2003**, *67*, 1667.
- (37) Lakshminarayanan, R.; Kini, R.M.; Valiyaveetil, S. *Proc Natl. Acad. Sci. U.S.A.* **2002**, *99*, 5155.
- (38) Nys, Y.; Gautron, J.; McKee, M. D.; García-Ruiz, J. M.; Hincke, M. T. *World's Poult. Sci. J.* **2001**, *57*, 401.
- (39) Hamilton, R. M. G. *Food Microstruct.* **1986**, *5*, 99.
- (40) Gautron, J.; Rodriguez-Navarro, A. B.; Gomez-Morales, J.; Hernandez-Hernandez, M. A.; Dunn, I.C.; Bain, M.; García-Ruiz, J.M.; Nys, Y. *Evidence for the implication of chicken eggshell matrix proteins in the process of shell mineralization*, in: Proceeding of the 9th international symposium on biomineralization (Biom 09) Pucon, Chile, 2005.
- (41) Croguennec, T.; Nau, F.; Molle, D.; Le Graet, Y. *Food Chem.* **2000**, *68*, 29.
- (42) Lysozyme (from chicken egg white), Datasheet Sigma Aldrich, Product Number L 6876.
- (43) Galvani, M. *Electrophoresis* **2001**, *22*, 2058.
- (44) Imoto, T.; Ono, T.; Yamada, H. *J. Biochem.* **1981**, *90*, 335.
- (45) Addadi, L.; Raz, S.; Weiner, S. *Adv. Mater.* **2003**, *15*, 959.
- (46) Surewicz, W. K.; Mantsch, H. H. *Biochim. Biophys. Acta* **1988**, *952* (2),115.
- (47) Yang, L.; Guo, Y.; Ma, X.; Hu, Z.; Zhu, S.; Zhang, X.; Jiang, K. *J. Inorg. Biochem.* **2003**, *93*,197.

Chapter 5

Initiation of Vaterite-Aragonite Particles with a Complex Morphology from Silicate-Casein Sols

Abstract

^{31}P NMR difference spectra of sodium caseinate sols with and without silicate ions provide direct evidence of interactions between silicate ions and casein serine phosphate groups. The addition of Ca^{2+} to sodium caseinate solution without silicate ions and, subsequently, the diffusion of atmospheric CO_2 to the resulting mixture do not lead to CaCO_3 mineralization, whereas comparable experiments in the presence of silicate ions induce the precipitation of hemispherical three-component microstructures composed of silica, casein, and calcium carbonate. Apparently, the silicate-protein interaction plays a role as promoter for calcium carbonate mineralization in aqueous sols. XRD and FTIR analysis reveal that vaterite is the crystalline phase of the composites. The observed materials are flat on one side and curved outward on the other side. In time, the flat surface cracks to display a star-like shape. Occasionally, in the center of the crack, layer-by-layer spheres-like particles grow, probably due to a secondary nucleation. These spheres are composed of a large number of two-dimensional aragonitic sheets, which are densely packed and form a multilayered structure.

5.1. Introduction

Biominerals are usually a complex assemblage consisting of inorganic ions intimately associated with organic macromolecules. Among all essential elements required by living organisms, calcium and silicon are of particular interest. They are the common constituents of the crust of the earth¹, tissues (bones, teeth and shells)² and leaves³ along with acidic

proteins. Above all, these two ions are presented also in a number of body fluids⁴ (i.e., saliva), where the phosphopeptides tend either to bind calcium or to form serine-silicate complexes. These complexes likely involve *H*-bonds or direct *C–O–Si* covalent bonds, where *Si* is in tetra- and penta-coordination^{5–11}, respectively.

Important sources of phosphoproteins are the casein proteins (used in the present work) that are released by enzymatic hydrolysis, gastrointestinal digestion, or food processing¹². The caseins (α_{s1} -, α_{s2} -, β - and κ -) represent circa 80% of the proteins in milk¹³ and in colloidal state exhibit a strong tendency to assemble into casein micelles¹⁴, which are roughly spherical colloidal complexes of proteins and salts with diameters ranging from 50 to 250 nm¹⁵. The casein micelle has a hydrophobic interior, surrounded with a hydrophilic charged layer. According to Holt et al.¹⁶, the hydrophilic layer is composed of κ -caseins, which ensure the stability of the casein micelle through a steric stabilization mechanism against further aggregation. Earlier studies show that the hydrophobic interior of casein micelles consists of spherical subunits called submicelles (15–20 nm in diameter)^{17–19}, which are kept together by hydrophobic interaction between proteins and by calcium phosphate linkages²⁰. The calcium ions are essential for casein micelle formation and represent 2.81 w% of the casein micelle content. One of the biological roles of casein is to inhibit crystal growth in the secretory cell.

As mentioned, the phosphoproteins build complexes with silicate ions. Previously, it has been suggested that such complexes play a key role in biomineralization reactions^{2–5, 21}. For example, silica-associated phosphoproteins have been identified and implicated in diatomic biosilica formation²². Today, the silicic-macromolecules interaction is explored in relation with calcium carbonate precipitation too. Recently, Jiang et al.^{23, 24} prepared PMMA (poly(methacrylic acid))/SiO₂/CaCO₃ composite particles via emulsion polymerisation and observed that the surfaces of the modified inorganic particles are grafted with PMMA molecules. The present paper reports on a further, particular example, in which the synthetic polymer is replaced by the casein phosphoprotein. This protein, known as a calcium sponge molecule with integrated nucleation sites, will remove the calcium ions from the bulk and, thus, it will have a big influence in the mineralization process. Moreover, we will see that the silicate ions have an influence on the protein structure, which in turn promotes the calcium carbonate formation.

As a source of silicate ions, we used tetraethylorthosilicate (TEOS), which, when hydrolysed under basic conditions, results in the formation of negatively charged silica species^{25,26}.

5.2. Experimental Section

5.2.1. Materials Preparation

Casein technical grade was supplied by Lancaster and used without further purification. Tetraethylorthosilicate (TEOS, purity >98%), calcium chloride dihydrate ($CaCl_2 \cdot 2H_2O$, purity >99%) and sodium hydroxide ($NaOH$, purity 99%) were purchased from Sigma-Aldrich and used as received. Deuterium oxide (D_2O , 99.8 atom% D), urea (CH_4N_2O) and ethanol (EtOH, purity 99.9%) were supplied by Deutero GmbH, Merck and J. T. Baker, respectively. Purified water with an electrical conductivity of less than $10^{-6} \text{ S} \cdot \text{m}^{-1}$ was taken from a Milli-Q system.

(1) Preparation of the Alkaline Silica Solution. Alkaline silica solution was prepared by mixing 0.17 mL TEOS, 0.17 mL ethanol, 7.5 mL $NaOH$ (0.1 M), ~92 mL water and stirring for 60 min at room temperature. Afterwards, the pH was adjusted to 11 ± 0.1 with aqueous sodium hydroxide (1 M).

(2) Preparation of the Na Caseinate Solution. According to HPLC-UV analyses performed at the institute Agrobio (France), 100 g of product contains 27.34 g α_{s1} -, 3.86 g α_{s2} -, 23.61 g β - and 28.56 g κ - casein. Other series of proteins, namely α lactalbumin, β lactoglobulin, bovine serum albumin, lactoperoxydase and immunoglobulin G, were present below the limit of detection of 10 ppm. The casein granules (0.1–5 g/ L) were dissolved by addition of aqueous $NaOH$ to yield a solution of pH 11 and stirred for one hour until an isotropic solution was obtained. According to DLS measurements, a 1 g/ L solution contained casein submicelles (dominant species, ~90% submicelles) and casein micelles with hydrodynamic radii of ~18 and ~200 nm, respectively.

(3) Preparation of the Alkaline Silica-Casein Solution. Alkaline silica-casein solution was prepared in a 100 mL plastic beaker by mixing 0.17 mL TEOS, 0.17 mL ethanol, 7.5 mL $NaOH$ (0.1 M), 0–5 g/ L casein, water and stirring for 90 min until the solution became isotropic. The pH was adjusted to 11 ± 0.1 with aqueous sodium hydroxide (1 M).

Mineralization of CaCO_3 . The reaction was started by adding 1.4 mL of a calcium chloride solution (0.5 M) to the afore-mentioned solutions (1 to 3). The total amount of the mixture was 100 mL. After the addition of calcium salt, the solutions were then transferred to open cells (plastic circular wells (Linbro Tissue Culture), 1.7 cm deep and 1.6 cm in diameter) and let at 20 °C for about 24 h. During this time, precipitation and growth of crystals occurred, due to the slow diffusion of atmospheric CO_2 into the mixture. The products were then washed several times in water and ethanol and examined by the following analytical techniques.

5.2.2. Analytical Methods

The **pH** of the solutions was measured before and after the addition of calcium chloride using an *Ag/AgCl* plastic-body electrode (TPS, Model smartCHEM-Laboratory).

Protein Structure. *Phosphorus-31 nuclear magnetic resonance* (^{31}P NMR) spectra measurements were carried out with a Bruker Avance 400 spectrometer working at 161.98 MHz under proton-decoupling conditions. The number of scans was 1000 in all measurements and the applied exponential line broadening 2 Hz. Chemical shifts were referenced to external 85% aqueous H_3PO_4 . The samples consisted of 50 mg casein dissolved in 10 mL of D_2O solution (10%, w/v) that either contains or not 17 μL TEOS. Additionally, we performed an experiment in the presence of urea (6 M), hydrogen bond disrupter, to probe the hydrogen bonds formation between silicate ions and the protein. The pH of the solution was adjusted to 11. About 1 mL of sample in 203 mm length high-resolution NMR tubes (Norell, Inc) were used for NMR measurements.

Particle Size. *Dynamic Light Scattering (DLS)* measurements were made using a Zetasizer spectrometer (Malvern Instruments Ltd., Model Z3000) equipped with a 5 mW *He-Ne* laser. Measurements were carried out at a scattering angle of 90° and the intensity autocorrelation functions were analyzed using the NNLS software.

Turbidity. *UV-VIS* absorption spectra were recorded on a Perkin Elmer Lambda 18 spectrophotometer and used for detecting the sample turbidity by measuring the absorbance at 280 nm.

Microscopy was used to determine the crystal habit. *Light microscopy* was performed using a Nikon transmission microscope (Model Eclipse E400). Images were taken between cross polarizers and produced with the help of a JVC CCD colour video camera (Model TKC1380). *Scanning electron microscopy (SEM)* was performed using a microscope Jeol JSM 840 operating at 0.2–30 kV. The sample was coated with *Au* in a Polaron Equipment LTD sputter coater.

Crystal Polymorphism. *Fourier transform infrared spectroscopy (FTIR)* was recorded on a Jasco FTIR–610 spectrometer. The spectrum was recorded in reflection mode from 4000 to 400 cm^{-1} at a resolution of 2 cm^{-1} . *X-ray diffraction (XRD)* measurements were done using a STOE STADI P diffractometer (STOE & CIE) providing *Cu K α 1* radiation monochromated with a germanium single crystal ($\lambda = 1.540598 \text{ \AA}$). Typical diffraction patterns were recorded in the range of $8^\circ < 2\theta < 90^\circ$ at a scanning speed of 0.8 $^\circ/\text{min}$. *Transmission electron microscopy (TEM)* was performed with a Philips CM30 ST electron microscope (300 kV, *LaB $_6$* cathode, Gatan multiscan CCD camera).

Chemical Composition. *Energy dispersive X-ray (EDX)* analysis was performed using an EDAX microanalyser mounted on a FEI Quanta 400T scanning electron microscope at 15 kV. This technique was used to quantify the approximate composition of the self-assembled silica-casein-calcium carbonate crystals.

5.3. Results

5.3.1. The Addition of Ca^{2+} Ions into the Alkaline Silica Solution and, subsequently, the Diffusion of Atmospheric CO_2

5.3.1.1. Early Stage of Precipitation Process

The addition of calcium chloride to a hydrolyzed TEOS solution induced cloudiness in the mixture immediately. The growth of particles was monitored by dynamic light scattering (DLS) and is shown in Figure 5.1. The onset of nucleation ($R_h = 200 \text{ nm}$) was followed by a fast and linear growth of the aggregates with time. After a few minutes macroscopic flocs, which settled down very quickly, were formed. Previously, it was reported that in the presence of calcium cations silica species nucleate and grow^{27, 28}. To study these flocs in detail, they were collected and analysed by means of SEM, XRD, FTIR and EDX analysis

(see Figures 6.34, 6.36 and 6.37, Chapter 6). From these analyses, it results that the cloudiness in the mixture is due to the formation of amorphous SiO_2 particles.

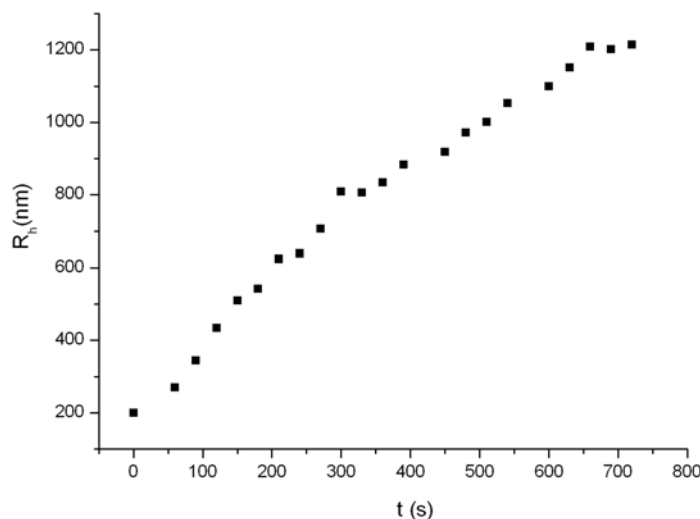


Figure 5.1 The light scattering curve obtained after the addition of calcium chloride to alkaline silica solution. $[TEOS] = 7.5$ mM, $[Ca^{2+}] = 7$ mM, pH = 11.

5.3.1.2. Later Stage of Precipitation Process

After 24 hours in contact with atmospheric CO_2 , distinct $SiO_2/CaCO_3$ composite crystal morphologies precipitated. The SEM image (Figure 6.21 D, Chapter 6) shows modified calcite (in agreement with Imai et al.²⁹) and aragonite crystals with diameters around 70–90 μm . The corresponding XRD pattern (Figure 6.22, Chapter 6) exhibits characteristic reflections of calcite (C_{104} , the dominant phase) and aragonite (A_{221}), but no peaks characteristic for vaterite.

5.3.2. ^{31}P NMR Spectra of Na Caseinate Sols with and without Silicate Ions

Figure 5.2 shows the ^{31}P NMR spectra of Na caseinate sols in the absence (left) and in the presence of silicate ions (right). In the absence of silicate ions, the spectrum shows an NMR signal between 3.9 and 4.1 ppm consisting of a broadly quartet peak. The chemical shift range of the peak fits with the chemical shift range of 3 to 4.6 ppm, which has been published previously for serine monophosphate peaks ($Ser-O-PO_3^{2-}$) in casein

solutions³⁰⁻³³. In the presence of silicate ions, the NMR spectrum shows also a broadly based quartet peak. Comparing the both spectra, it follows that in the presence of silicate ions the NMR signal of $Ser-O-PO_3^{2-}$ was shifted ca. 0.7 ppm *upfield*. Further, the quartet peak profile looks different from the signal obtained in the absence of silicate ions. All four peaks that compose the broad NMR signal became narrower. From all this changes, it follows that the silicate ions interact with the protein and lead up to a change in the protein structure conformation.

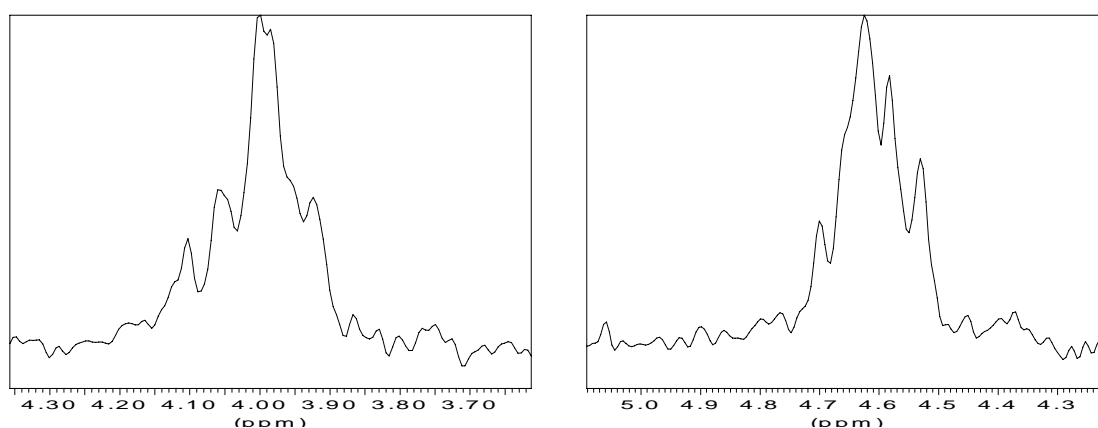


Figure 5.2 The liquid state ^{31}P -NMR spectra of *Na* caseinate sols in the absence (left) and in the presence (right) of silicate ions at pH 11 and 25 °C. Protein and silica concentrations were 5 g/L and 7.5 mM, respectively.

5.3.3. The Addition of Ca^{2+} Ions into the *Na* Caseinate Solution and, subsequently, the Diffusion of Atmospheric CO_2

5.3.3.1. Early Stage of Precipitation Process

The addition of calcium ions to the *Na* caseinate solution induces no change in the hydrodynamic radius (Figure 5.3) and in the absorbance A_{280} within one hour (Figure 5.4 A, inset). After one hour, the initial colourless solution becomes slightly bluish (Figure 5.4 B) and this behaviour is confirmed also by the increase of its absorbance with time (Figure 5.4 A).

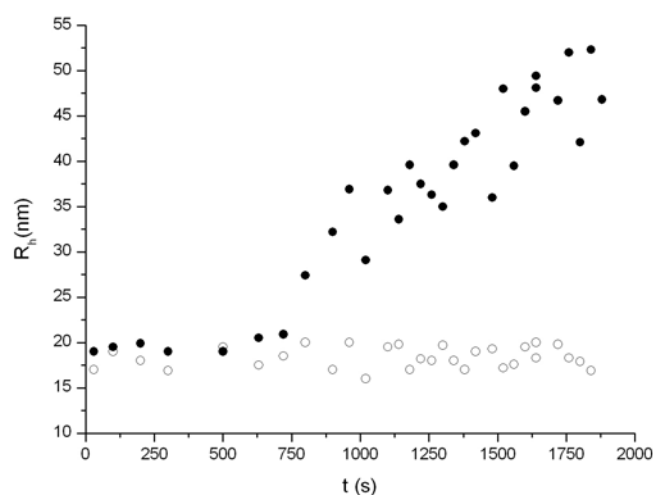


Figure 5.3 Dynamic light scattering curves obtained after rapidly mixing solutions of CaCl_2 with either Na caseinate (\circ) or silica-casein (\bullet) solution.

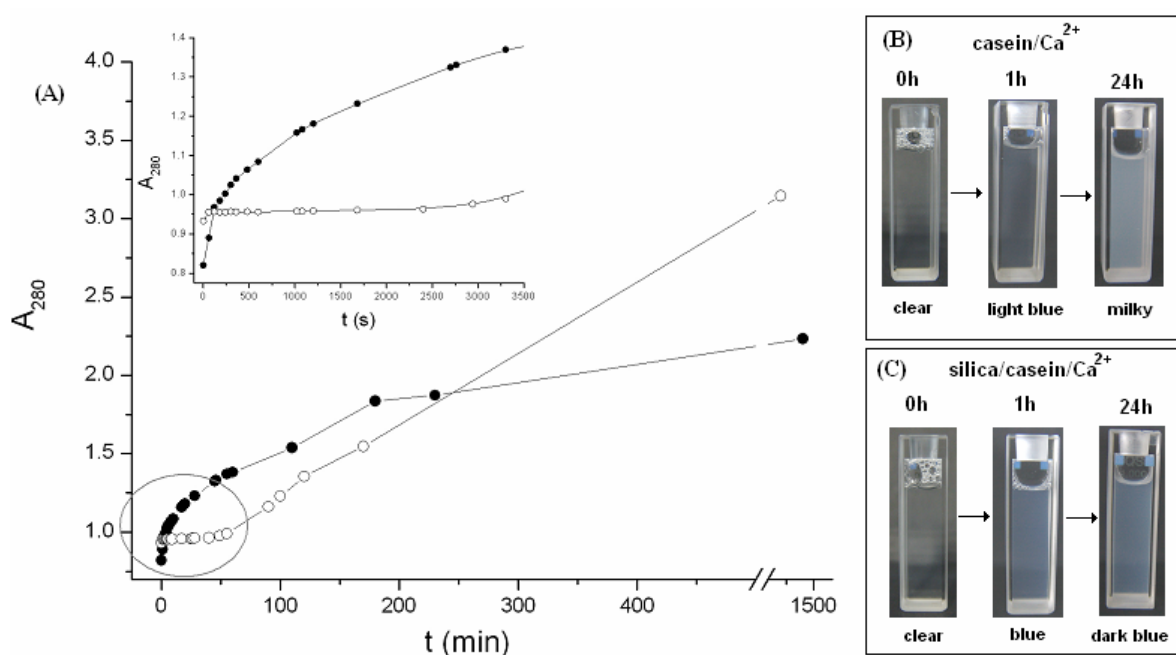


Figure 5.4 (A) Changes of the absorbance at 280 nm during ageing of casein/ Ca^{2+} solution (\circ) and silica/casein/ Ca^{2+} solution (\bullet). Inset is the enlarged image of the surrounded area. (B and C) Visual observations made during the absorbance measurements showing the transition from colourless sols to either a milky casein/ Ca^{2+} solution (B) or a blue silica/casein/ Ca^{2+} solution (C) within 24 hours. The cuvette labelled with '0 h' corresponds to the solution before the addition of calcium, i.e., Na caseinate solution (B) and alkaline silica-casein solution (C), respectively.

5.3.3.2. Later Stage of Precipitation Process

After 24 hours, the solution becomes milky (Figure 5.4 B), gelled and the absorbance dramatically increases (Figure 5.4 A). It is likely that the turbidity change is due to the casein micelle formations, which become the dominant species. Furthermore, in contact with atmospherical CO_2 , no visible $CaCO_3$ crystals are precipitated. Even after four days, when half of the water is evaporated and the sample is contaminated by bacteria, the calcium carbonate precipitation does not take place. However, we did not exclude the presence of colloidal amorphous calcium carbonate. For this reason, we performed an additional experiment, in which the ageing solution is analysed by means of FTIR. We observed no absorption bands characteristic to amorphous calcium carbonate.

5.3.4. The Addition of Ca^{2+} Ions into the Silica-*Na* Caseinate Solution and, subsequently, the Diffusion of Atmospherical CO_2

5.3.4.1. Early Stage of Precipitation Process

The addition of calcium ions to the colourless alkaline silica-casein solution induces a bluish colour in the mixture immediately. This observation is in agreement with the dramatic increase of the absorbance at 280 nm with time (Figure 5.4 A, inset). Moreover, the hydrodynamic radius (Figure 5.3) of the resulting aggregates increases slowly with time too. The increase in the radius is likely due to the formation of SiO_2 particles. Of particular interest is that the protein presence controls the silica particle size, while in the absence of casein, macroscopic flocs (see Section 5.3.1.1.) that settle down very quickly, are formed.

5.3.4.2. Later Stage of Precipitation Process

Between one and 24 hours, the bluish solution (Figure 5.4 C) is more intense and the absorbance at 280 nm increases slowly (Figure 5.4 A). Besides, after 24 hours in contact with atmospherical CO_2 , hemispherical $CaCO_3$ crystals are precipitated (Figure 5.5).

Figure 5.5 shows the experimental data referring to the dependence of the average particle size on the concentration of the casein. It is found that the particle diameter decreased sharply, from 100 μm to 30 μm , when the concentration of casein is increased to 0.5 g/L, but further increase has almost no effect on this index. When the concentration of the

solution is lower than 0.5 g/ L, the precipitation process leads to a low number of big particles (Figure 5.5 A and B), whereas at high casein concentration a very high number of small particles (Figure 5.5 C to E) is observed (c.f. the ionotropic effect^{34, 35}).

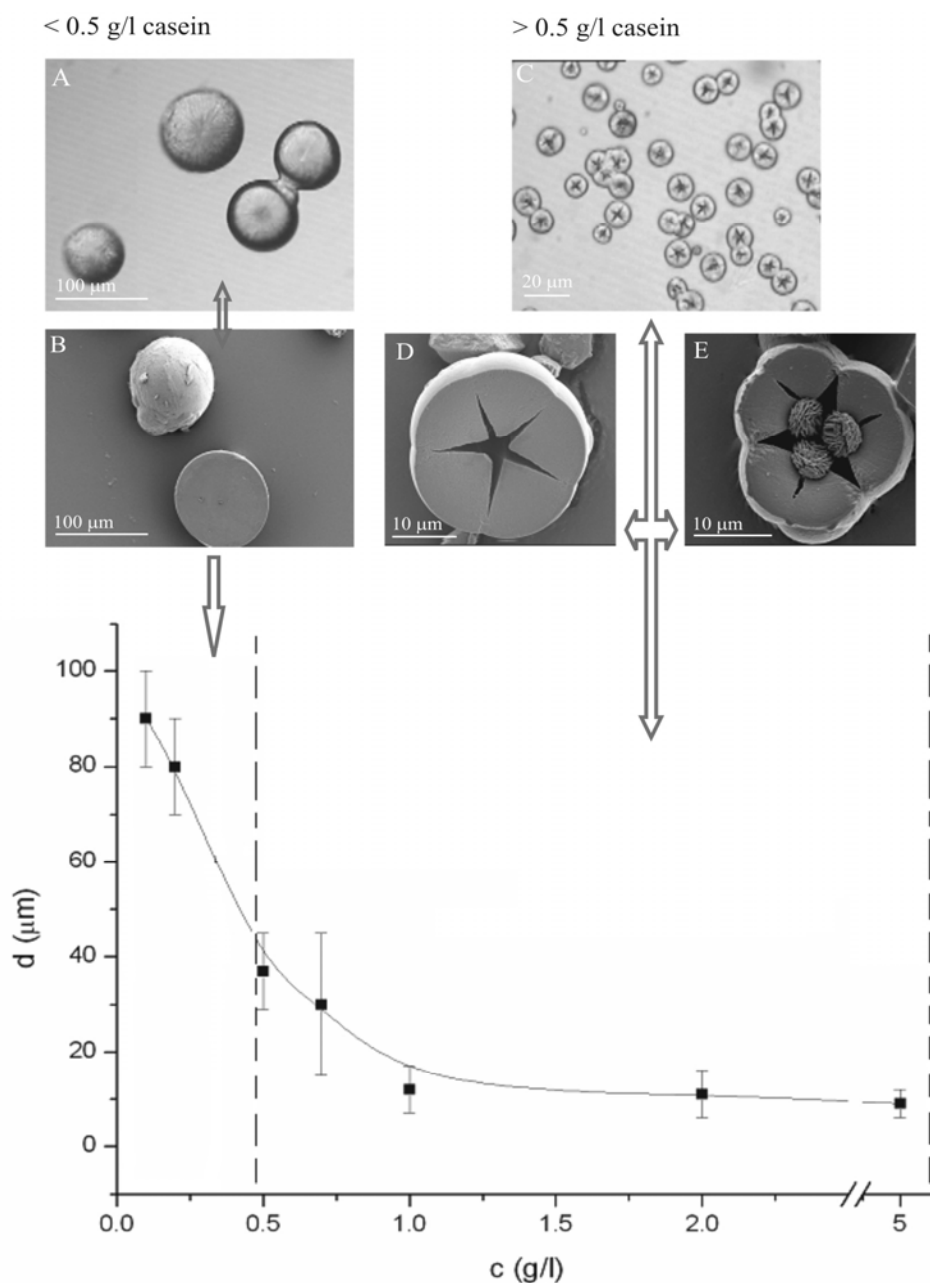


Figure 5.5 The dependence of the average size of $\text{SiO}_2/\text{casein}/\text{CaCO}_3$ three-composite particles as a function of increasing casein concentration. (A to E) Optical micrographs and SEM images of the hemispherical crystals. $[\text{TEOS}] = 7.5 \text{ mM}$, $[\text{Ca}^{2+}] = 7 \text{ mM}$, $\text{pH} = 11$, $t = 24 \text{ h}$.

The particle morphology changes from a hemispherical shape to a cracked hemispherical shape by increasing the concentration of the protein above its critical micelle concentration, CMC ~ 0.5 g/L^{36,37}, in aqueous solutions. These hemispherical particles are flat on one side and curved outward on the other side. The flat surface cracks to display a star-like shape (Figure 5.5 D). Occasionally, in the origin of the cracks, ‘layer-by-layer’ spheres-like particles (Figure 5.5 E) grow, probably due to a secondary nucleation. Nevertheless, the casein concentration plays a role on the morphology of hemispherical crystals. As stated before, in the absence of silicate ions the precipitation of calcium carbonate does not occur. Thus, the silicate ions play a role as nucleator for the calcium carbonate mineralization process.

Figure 5.6 shows the particle diameter, calculated from optical images of the particles versus the reaction time in a 1 g/L casein solution. It is observed from the plot that during the first nine hours no visible precipitates are detected in the reaction cell. After ten hours, a small amount of crystals with an average size of 3 to 5 μm is observed. The crystal size sharply increases with the ageing time. After an ageing period of 24 hours, the particle reached an average size of about 15 μm .

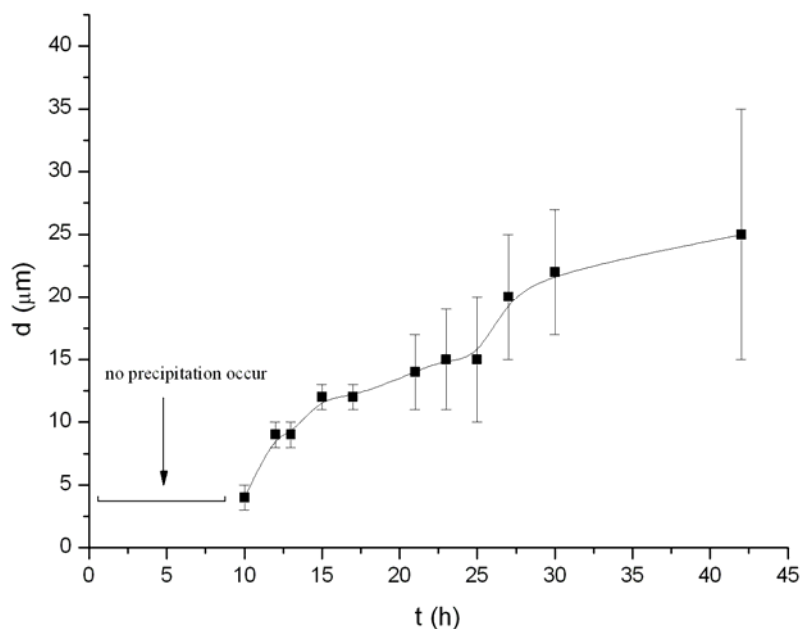


Figure 5.6 Dependence of the particle size on the reaction time of $\text{SiO}_2/\text{casein}/\text{CaCO}_3$. [TEOS] = 7.5 mM, [casein] = 1 g/L, $[\text{Ca}^{2+}] = 7$ mM, pH = 11, T = 20 $^\circ\text{C}$.

5.3.4.3 Morphogenesis of Particles

To get more information about the self-organised process of the observed particles, we tried to monitor the morphological evolution of the big polycrystalline particles (Figure 5.7). After 10 hours, the particles around 5 μm have a hemispherical shape being convex on one side and concave on the other surface (Figure 5.7 A). The convex outer surface is fully continuous, while in the center of the concave inner surface the particle starts to crack. Due to the breakage, we can see that the particles are not hollow (Figure 5.7 A, inset). With time, the concave inner surface develops into a flat surface, where the cracks display always a star like shape (Figure 5.7 B). We note that the plano-convex shape is not an issue of the cell walls because the particles lay down, on the cell bottom, with the crack side up (Figure 5.5 C).

The formation of cracks on the concave side of the particles indicates a different composition from the convex side (Figure 5.7 B, inset). One explanation of the crack formation could be the initial formation of amorphous calcium carbonate (ACC), which later on crystallizes under significant volume decrease (density ACC is about 1.6 g/mL; crystalline CaCO_3 around 2.7 g/mL). This can very well create stresses large enough to crack the overall particle.

Occasionally, on the flat surface silica particles (i.e., the coproduct of the reaction formed in the solution at the early stage) of around 20 nm glue and accumulate (Figure 5.8). Subsequently, the silica spheres are assembled in an edge-to-edge growth³⁸ (Figure 5.7 C and E) with the gradual enlargement of 2D nanosheets surface areas that are very thin, with a thickness less than 300 nm. In time, the nanosheets develop into a layer-by-layer³⁹ spheres-like particles (Figure 5.7 D) consisting of numerous interconnected nanosheets (Figure 5.7 F). Probably, the casein plays an important role in the formation of integrated nanosheets and multilayered structures. Simultaneously, the particle grows and the cracks enlarge more and more until it cleaves into small crystal fragments (Figure 5.9).

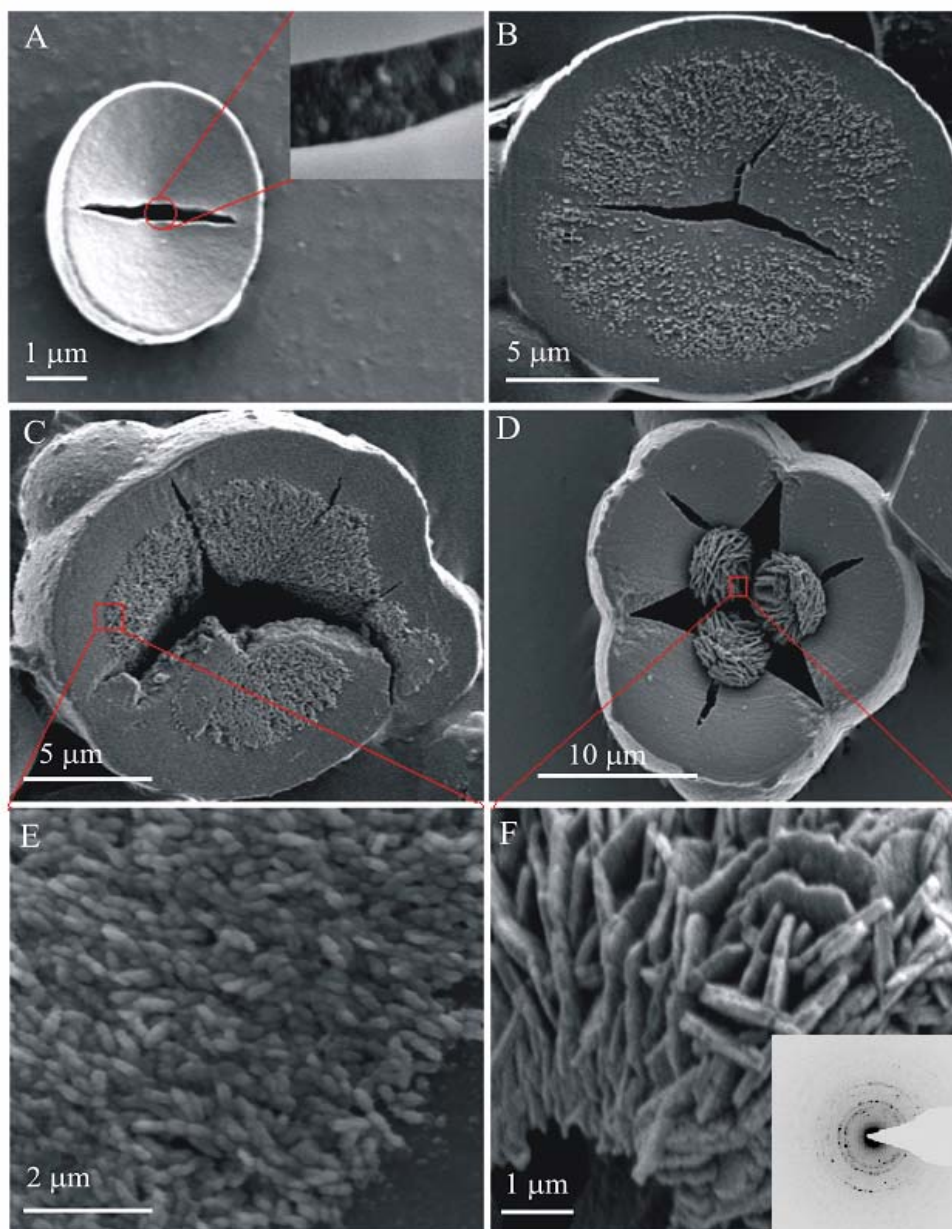


Figure 5.7 FESEM images of self-assembled $\text{SiO}_2/\text{casein}/\text{CaCO}_3$ aggregates which show the morphological evolution of the composite. $[\text{TEOS}] = 7.5 \text{ mM}$, $[\text{casein}] = 1 \text{ g/L}$, $[\text{Ca}^{2+}] = 7 \text{ mM}$, $[\text{EtOH}] = 0.17\%$, $\text{pH} = 11$, $T = 20 \text{ }^\circ\text{C}$. (A) Early hemispherical particle with a concavo-convex form that cracks on the concave side. Inset: the material from the particle interior. (B) Hemispherical particle showing how the flat surface cracked to display a star-like shape. Around the crack, silica particle accumulate. (C and D) Hemispherical particles showing how the silica particles penetrate into the surface and the layer-by-layer spheres-like particles inside the crack, respectively. (E) Enlarged image of the silica sphere arrangement. (F) Enlarged image of the multilayered structure and electron diffraction pattern.

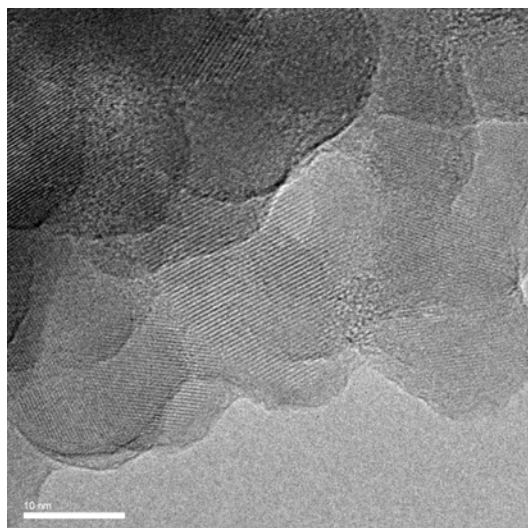


Figure 5.8 TEM image of amorphous silica particles with spherulitic morphologies.

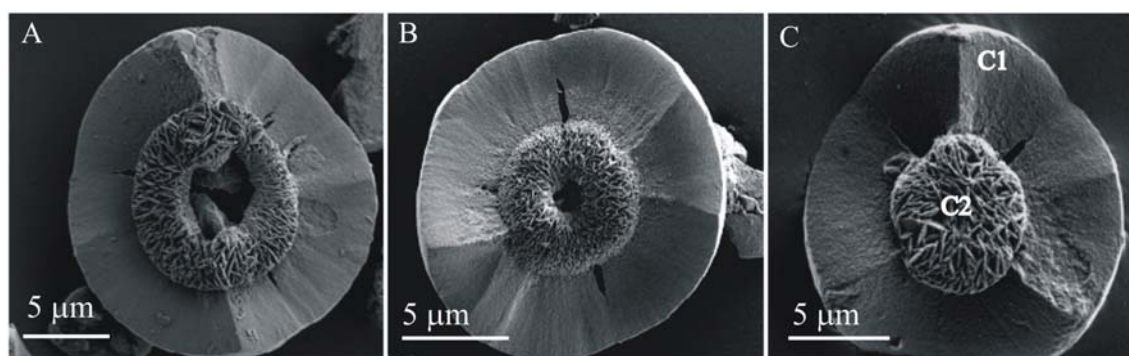


Figure 5.9 Crystal fragments from the originally cracked hemispherical particle showing the formation of the layer-by-layer spheres-like particles.

5.3.4.4. Chemical Composition

The EDX spectra, obtained from area indicated in Figure 5.9 C by C₁ and C₂, are consistent with the bulk composition provided by the synthesis. By comparing the two spectra (Figure 5.10), one can notice that the spectrum of the region labelled with C₁ shows a nitrogen peak (see arrow), which comes from the protein and which is not found in the region labelled C₂. Both peaks of *Si* and *Ca* are smaller in the C₁ area than in the area denoted by C₂. From these observations it follows that these particles are composites consisting of silica/casein/*CaCO*₃ with two notable differences. Firstly, the casein concentration is considerably lower in the layer-by-layer spheres-like particle than in the rest of the composite and secondly, the concentration of silicate and calcium ions is significantly higher in the layer-by-layer spheres-like particles.

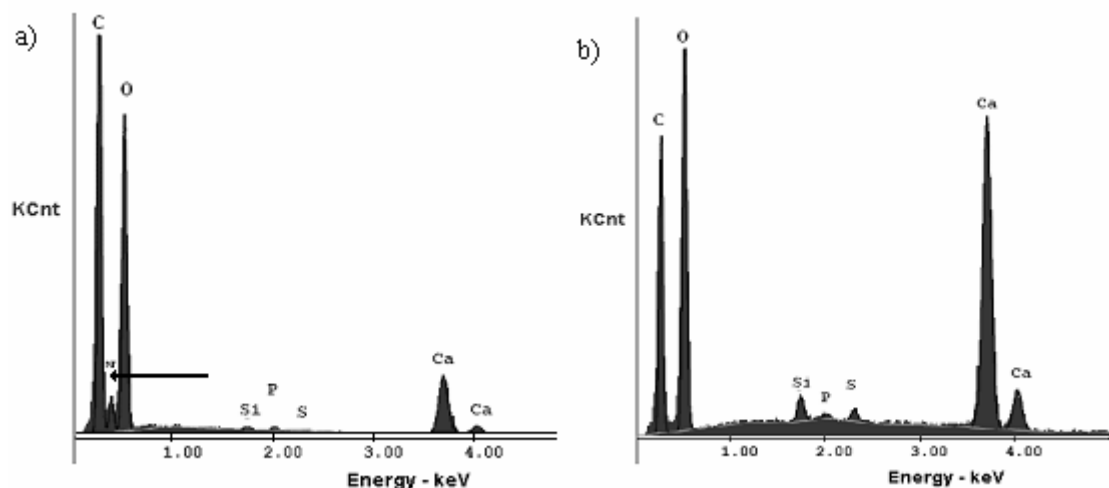


Figure 5.10 EDX spectra obtained from the regions C_1 and C_2 indicated in Figure 5.9 C.

5.3.4.5 Crystal Polymorphism

Figure 5.11 shows the infrared absorption spectrum of the composites. A comparison of the bands at 746, 877, 1088, 1442 and 1480 cm^{-1} with standard IR spectra of vaterite-type calcium carbonate reported by Anderson et al.⁴⁰, suggests that the structure contains the vaterite calcium carbonate crystal phase. Along with the vaterite bands, the spectrum reveals bands at 1660 cm^{-1} and in the range of 2000–3500 cm^{-1} , attributed to the OH^- and water vibration. Since the vaterite crystal phase is anhydrous, we believe that the hydration bands are due to the presence of casein and silica in the composite in good agreement with the EDX data. However, the water bands can indicate also the presence of amorphous calcium carbonate ($\text{CaCO}_3 \cdot \text{H}_2\text{O}$) in the composite and, thus, explaining the formation of the crack on the concave side of the particles.

The presence of vaterite phase in the composites is reinforced by powder XRD data. The XRD pattern (Figure 5.12) exhibits only reflection peaks characteristic of the vaterite phase (V_{110} , V_{112} , V_{114} , V_{300} , V_{304} , V_{118} and V_{224}). However, selected area electron diffraction pattern (Figure 5.7 F, inset) recorded on crushed layer-by-layer spheres-like particles indicate the presence of aragonite as the crystalline phase. The lack of aragonite peaks in the XRD is certainly owing to its low mass percentage, which is below the detection limit of the X-ray and FTIR diffractometer.

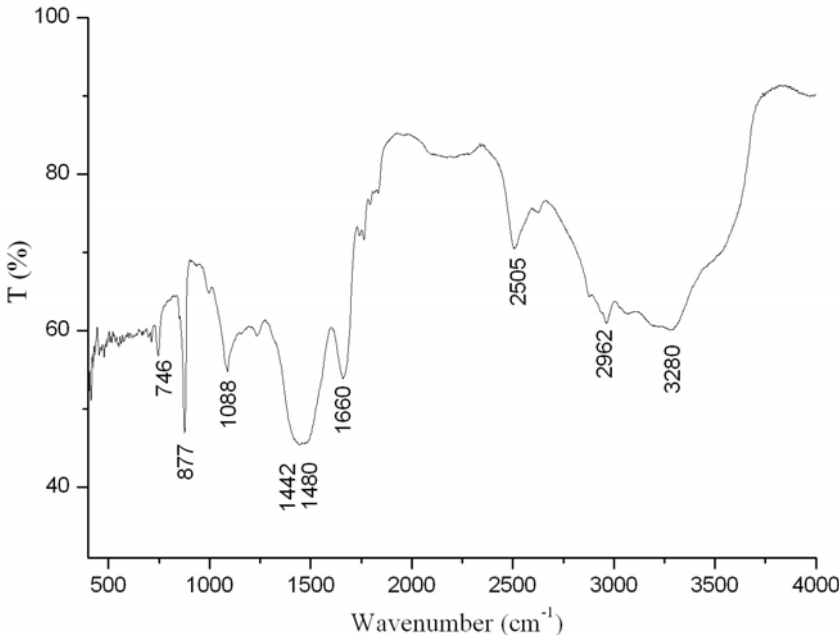


Figure 5.11 FTIR spectrum of the $SiO_2/casein/CaCO_3$ composites particle.

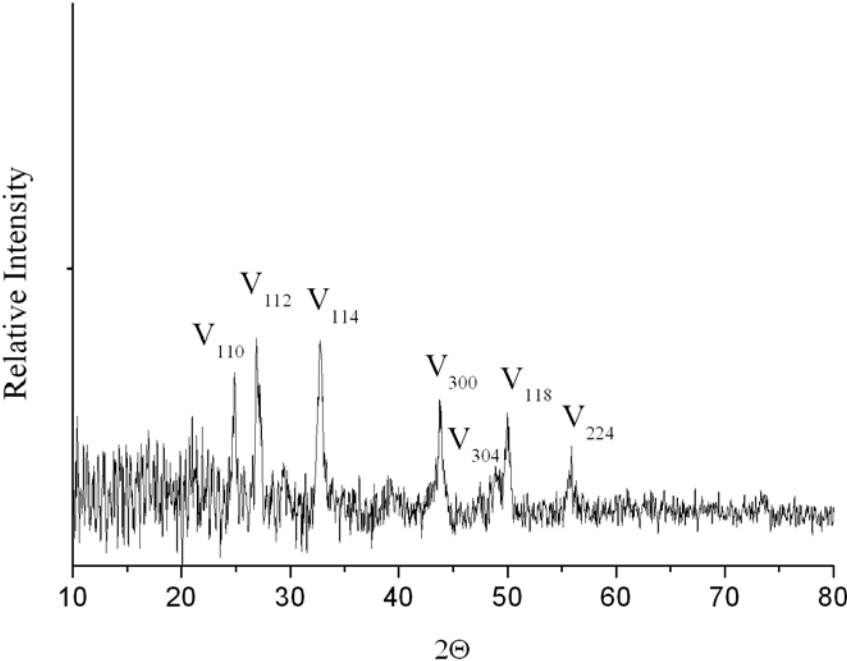


Figure 5.12 XRD pattern of the $SiO_2/casein/CaCO_3$ composite particles.

5.4. Discussion

Some anomalies that appear in the body, such as calculus, ganglions or gallstones, are due to organic-inorganic biological systems. Organic and (or) inorganic molecules serve as nucleators, modifiers or matrices and induce the biomineralization process, which results in unique inorganic-organic composites. Inspired by the biomineralization process one can try to use organic-inorganic systems in an effort to synthesise $CaCO_3$ materials in vitro with a comparable range of properties. Meldrum et al.⁴¹ focused on calcium carbonate crystals precipitated in the presence of Mg and organic additives (malic acid and citric acid). Deng et al.⁴² worked on a more complex system. They used a soluble ternary-additive system, i.e., PEG/PMAA/SDS, for production of well-defined hollow calcite spherical assemblies. The study showed that non-covalent interaction and cooperation between macromolecules play a key role in controlling the growth of minerals. Recently, Jiang et al.^{23, 24} prepared PMMA/ SiO_2 / $CaCO_3$ composite particles via emulsion polymerisation and observed that PMMA molecules are grafted at the surfaces of the modified inorganic particles. The present study shows that silicate ions change the protein structure, while in turn induces the vaterite calcium carbonate mineralization.

5.4.1. The Addition of Ca^{2+} Ions into the Alkaline Silica Solution and, subsequently, the Diffusion of Atmospheric CO_2

The addition of $CaCl_2$ and subsequent diffusion of atmospheric CO_2 to the alkaline silica solution result in the formation of deformed crystals (calcite and aragonite) and SiO_2 macroscopic flocs, as a coproduct of the reaction. The silica particles form owing to the presence of calcium ions, which decreases the solubility of amorphous silica in water, the commonly termed 'salting out' effect. Marshall et al.²⁸ shows that as the hydration number of the added cations increases, the solubility of amorphous silica particles decreases. The calcium cations having a very high hydration number (i.e., 12) bind the 'free' water molecules and decrease the solubility of silica. Qualitatively, a lowered amount of 'free' water would be expected to lower silica solubility, and this is what is actually observed.

5.4.2. The Addition of Ca^{2+} Ions into *Na* Caseinate Solution and, subsequently, the Diffusion of Atmospheric CO_2

DLS studies on sodium caseinate sols in the absence of calcium show a bimodal distribution consisting of small (as the dominant species, ~90%) and big aggregates with radii of 18 nm and 200 nm, respectively. According to the literature, the radius of 20 nm corresponds to casein submicelles¹⁷⁻¹⁹ and the radius of 200 nm corresponds to casein micelles^{15, 16}. The casein submicelles are composed of 20–25 casein molecules kept together mainly by hydrophobic interactions between proteins⁴³.

The serine monophosphate NMR signal provides information about the casein conformation in solution. Kakalis et al.⁴⁷ showed that the overlapping serine monophosphate peak of the casein micelle spectrum could be resolved into four asymmetric peaks in the casein submicelle spectrum. The casein spectrum presented in Figure 5.2 is comparable to that reported by Kakalis et al.⁴⁷ for casein submicelles.

The addition of calcium to the sodium caseinate solution and, subsequently, the diffusion of atmospheric CO_2 induce no change in the hydrodynamic radius and in the absorbance A_{280} within one hour, whereas between 1 h and 24 h the absorbance increases and the solution become milky. According to the literature⁴⁴⁻⁴⁶, the increase in the turbidity is attributed to the formation of casein micelles from the hydrophobic associated casein submicelles through calcium side-chain salt bridges. These calcium-protein interactions were caused by binding the calcium ions to both phosphate and carboxylate groups of glutamate and aspartate residues. On one hand, the calcium-phosphate interaction was demonstrated using ^{31}P NMR analysis⁴⁷. On the other hand, the calcium-carboxylate interactions were proven by examination of FTIR differences spectra of casein with and without calcium that reveal changes in the position of carboxylates bands when the calcium ions are present in the solution⁴⁸. Another prove that calcium is implicated in such interactions is the current study which showed that when the solution was in contact with the atmospheric CO_2 , no calcium carbonate particle are precipitated after 24 hours or even after four days. This demonstrates that nearly none of the added calcium remains in the soluble phase to bind with CO_3^{2-} . Moreover, after four days the solution has a gelled appearance due to the increased osmotic compressibility of the colloidal system⁴⁹. Dalgleish suggested that the increase in the coagulation rate of the casein sols arises from

the neutralisation of negative charges within the micelles, causing a decrease in repulsion allowing the close approach, thereby promoting hydrophobic interactions, which are necessary for gel formation to occur.⁵⁰

5.4.3. The Addition of Ca^{2+} Ions into the Silica-*Na* Caseinate Solution and, subsequently, the Diffusion of Atmospheric CO_2

Examination of ^{31}P NMR difference spectra of casein sols with and without silicate ions provides direct evidence for the interaction between silicate ions and serine phosphate groups. Silica and phosphoserin groups as well as aspartate and glutamate residues of the protein are negatively charged. Moreover, the amine containing residues should be almost neutral at the pH of 11 close to the pKa of most of these basic amino acids. So, electrostatic interactions can almost be excluded. Previously, the identification of *Si*-serine complexes was provided by ^{29}Si , ^{13}C and ^{17}O NMR shifts and involve *H*-bonds or direct *C-O-Si* covalent bonds⁵⁻¹¹. Additionally, we performed an NMR experiment in the presence of urea (6 M), hydrogen bond disrupter, to probe the hydrogen bonds formation between the silicate ions and the protein. We observed no differences in the NMR signals of the silicate-casein solution and silicate-casein-urea solution. So, the hydrogen bonds formation is also excluded. A transesterification of phosphate against silicate in the phosphoserin residues leading to a covalent C-O-Si bond also seems unlikely because the NMR signal for serine monophosphate group did not disappear, it is only shifted upfield. For the moment, we are not able to explain the type of the interaction between silica and the protein. However, we suppose that the silica species should interact with the serine monophosphate groups (assumption based on the NMR measurements) and, in turn, block these groups against precipitation with calcium.

The addition of calcium to the silicate-caseinate solution and, subsequently, the diffusion of atmospheric CO_2 induce an increase in the hydrodynamic radius and in the absorbance A_{280} intensity. We assign this increase to the formation of silica particle with added calcium due to the 'salting-out' effect. A comparable effect is observed when calcium is added to an alkaline silica solution, but with a significant difference. The silica particles formed in the alkaline silica sols are about 200 nm, while the particles precipitated in the silica-casein solution are ca. 20 nm in diameter. So, the silica particle size is controlled by

the *Si*-serine complexes. Likewise, the bovine serum albumin-silicate interactions induce protein aggregation that controls silica particle size⁵¹.

We reemphasize that silica/casein/ Ca^{2+} solution initially increase in size much more compared to casein/ Ca^{2+} , but after ~220 min the effect is opposite. In the absence of silicate ions, casein being a calcium sponge protein with integrated nucleation sites will bind calcium ions through both phosphate and carboxylate groups of glutamate and aspartate residues and, afterwards lead to the formation of casein micelle. In the presence of silicate ions, the calcium nucleation sites on the casein structure are blocked and, therefore, calcium will interact with free silica ions from the bulk solution and form silica particles.

After 24 hours in contact with atmospherical carbon dioxide, hemispherical calcium carbonate crystals in form of vaterite phase are precipitated, whereas comparable experiments made in the absence of silicate ions do not promote the formation of calcium carbonate particles. Occasionally, we saw that in the origin of the cracks, layer-by-layer sphere-like aragonite particles grow probably due to a secondary nucleation.

The formation of layer-by-layer sphere-like particles suggests that the growth process may involve the following steps: (1) At the early stage, tiny silica nanospheres form in the silica-casein supersaturated solution. (2) In time, these nanoparticles glue and, afterwards, attach to the hemispherical particle surface probably owing to electrostatic interaction between $Si-O^-$ and $-NH_3^+$ groups⁵² or Ca^{2+} . (3) The initially formed spheres assemble in an edge-to-edge way with the gradual enlargement of the 2D surface areas. (4) As soon as the 2D nanosheets have been formed, the protein starts selectively absorbing onto the sheets, which leads to the formed nanosheets being glued together. (5) Finally, the arrangement of the 2D sheets into 3D hierarchical microspheres takes place. For the formation of 3D microspheres, a layer-by-layer growth style can be considered⁴².

5.5. Conclusions

Novel hemispherical three-component vaterite microstructures were obtained in alkaline silica-casein sols by the diffusion of atmospherical carbon dioxide into the solution. The initiation of this process is due to the presence of silicate ions that interact with serine-monophosphate groups and modify the casein structure in aqueous solution and, as a

consequence, promote vaterite-aragonite particle formation. We conclude that crystallization processes that appear *in vivo* could be influenced by different modifications in protein structures that are controlled by inorganic ions, such as the pulmonary calcification process.

5.6. References

- (1) Wiercinski, F. J. *Biol. Bull.* **1989**, 176, 195.
- (2) Damen, J. J. M.; Ten Cate, J. M. *J. Dent. Res.* **1989**, 68(9), 1355.
- (3) Campbell, A. K. *Survey Biochem. Anal.* **1988**, 19, 485.
- (4) Cutress, T.W. *Arch. Oral Biol.* **1972**, 17, 1081.
- (5) Hecky, R.; Mopper, K.; Kilham, P.; Degens, T. *Marine Biol.* **1973**, 19, 323.
- (6) Sullivan, C. W. *Silicification by diatoms in Silicon biochemistry*, Ciba Foundation Symposium 121, John Wiley: Chichester, 1986.
- (7) Pickett-Heaps, J; Schmidt, A. M.; Edgar, L. A. *Prog. Phycol. Res.* **1990**, 7, 1.
- (8) Frauso da Silva, J. J. R.; Williams, R. J. P. *The biological chemistry of the elements: The inorganic chemistry of life*, Clarendon Press: Oxford, 1991.
- (9) Swift, D.; Wheeler, A. P. *J. Phycol.* **1992**, 28, 202.
- (10) Lobel, K. D.; West, J. K.; Hench, L. L. *Marine Biol.* **1996**, 126, 353.
- (11) Kinrade, S. D.; Del Nin, J. W.; Schach, A. S. *Science* **1999**, 285, 1542.
- (12) LeBlank, J. G.; Matar, C.; Valdéz, J. C.; LeBlank, J.; Perdigon, G. *J. Dairy Sci.* **2002**, 85, 2733.
- (13) Jenness, R. *Milk Proteins, Chemistry and Molecular Biology I*, Academic Press: New York, 1970.
- (14) Farrell, H. M. Jr.; Kumosinsky, T. F.; Malin, E. L.; Brown, E. M. *Methods in Molecular Biology* **2002**, 172(1), 97.
- (15) Brunner, J. R. *Milk Proteins, In Food proteins*, AVI Publishing Company, Inc.: Connecticut, 1977.
- (16) Holt, C., Horne, D. S. *Neth. Milk Dairy* **1996**, 50, 85.
- (17) McMahon, D. J.; McManus, W. R. *J. Dairy Sci.* **1998**, 81, 2985.
- (18) Walstra, P. *Int. Dairy J.* **1999**, 9, 189.
- (19) Rollema, H. S. *Adv. Dairy Chem.* **1992**, 1, 111.
- (20) Wong, N. P. *Fundamental of Dairy Chemistry*, 3rd edn., Van Nostrand Reinhold: New York, 1988.

- (21) Zhou, Y.; Shimizu, K.; Cha, J. N.; Stucky, G. D.; Morse, D. E. *Angew. Chem. Int. Ed.* **1999**, *38*, 780.
- (22) Kröger, N.; Lorenz, S.; Brunner, E.; Sumper, M. *Science* **2002**, *298*, 584.
- (23) Jiang, L.; Dan, Y. *Colloid Polym Sci.* **2004**, *282*, 1364.
- (24) Jiang, L.; Pan, K.; Dan, Y. *Colloid Polym Sci.* **2006**, *285*, 65.
- (25) Bacs, C. F Jr.; Mesmer, R. E. *The hydrolysis of cations*, Wiley: New York, 1974.
- (26) Voinescu, A. E.; Kellermeier, M.; Carnerup, A. M.; Larsson, A.; Touraud, D; Kunz, W.; Hyde, S. T. *J. Cryst. Growth* **2007**, *306*,152.
- (27) Kerr, G. T. *J. Phys. Chem.* **1966**, *70*, 1047.
- (28) Marshall, W. L.; Warakoski, M. *Geochim. Cosmochim. Acta* **1980**, *44*, 915.
- (29) Imai, H.; Terada, T.; Yamabi, S. *Chem. Commun.* **2003**, *4*, 484.
- (30) Matheis, G.; Penner, M. H.; Feeney, R.E., Whitaker, J. R., *J. Agric. Food Chem.* **1983** , *31*, 379.
- (31) Matheis, G.; Whitaker, J. R. *Int. J. Biochem.* **1984**, *16*(8), 867.
- (32) Van Hekken, D. L.; Dudley, R. L. *J. Dairy Sci.* **1997**, *80* (11), 2751.
- (33) Belton, P. S.; Lyster, R. L. J.; Richards, C. P. *J. Dairy Res.* **1985**, *52*(1), 47.
- (34) Addadi, L; Moradian, J.; Shay, E.; Maroudas, N. G.; Weiner, S. *Proc. Natl. Acad. Sci. USA* **1987**, *84*, 2732.
- (35) Voinescu, A. E.; Touraud, D.; Lecker, A.; Pfitzner, A.; Kunz, K.; Ninham, B. W. *Langmuir* **2007**, *23*(24), 12269.
- (36) Schmidt, D.G.; Payens, T. A. *J. Colloid Int. Sci.* **1972**, *39*, 655.
- (37) Leclerc, E.; Calmettes, P. *Phys. Rev. Lett.* **1997**, *78*, 150.
- (38) Li, Y.; Liu, J.; Huang, X.; Li, G. *Cryst. Growth Des.* **2007**, *7*(7), 1350.
- (39) Zhou, G.; Lü, M.; Yang, Z.; Tian, F.; Zhou, Y.; Zhang, A. *Cryst. Growth Des.* **2007**, *7*(2), 187.
- (40) Anderson, F. A.; Brecevic, L. *Acta Chem. Scand.* **1991**, *45*, 1018.
- (41) Meldrum, F. C.; Hyde, S. T. *J. Cryst. Growth* **2001**, *231*, 544.
- (42) Deng, S. G.; Cao, J. M.; Feng, J.; Guo, J.; Fank, B. Q.; Zheng, M. B.; Tao, J. *J. Phys. Chem. B* **2005**, *109*, 11473.
- (43) Kumosinsky, T. F.; Farrell, H. M. Jr. *J. Protein Chem.* **1991**, *10*(1), 3.
- (44) Chu, B.; Zhou, Z.; Wu, G.; Farrell, H. M. Jr. *J. Colloid Int. Sci.* 1995, *170*, 102.
- (45) Farrell, H. M. Jr. J.; Thompson, M. P. *Caseins as calcium binding proteins*, vol 2, CRC press, Inc.: Boca Raton, 1988.
- (46) Famelart, M. H.; Le Graet, Y.; Raulot, K. *Int. Dairy J.* **1999**, *9*, 293.

-
- (47) Kakalis, L. T.; Kumosinski, T. F.; Farrell, H. M. *Biophys. Chem.* **1990**, *38*, 87.
- (48) Byler, D. M.; Farrell, H. M. Jr. *J. Dairy Sci.* **1989**, *72*(7), 1719.
- (49) De Kruif, C. G. *J. Dairy. Sci.* **1998**, *81*, 3019.
- (50) Dalglish, D. G. *Adv. Dairy Chem.* **1992**, *1*, 779.
- (51) Coradin, T.; Coupé, A.; Livage, J. *Colloids Surf. B* **2003**, *29*, 189.
- (52) Coradin, T.; Livage, J. *Colloids Surf. B* **2001**, *21*, 329.

Chapter 6

Hierarchical Materials of $CaCO_3$ -Silica Composites

6.1. The Efficacy of TEOS as a new Silica Source for the Formation of Carbonate-Silica Composite Materials

Abstract

We explore the use of tetraethoxysilane (TEOS) as a silica source for the formation of carbonate-silica composite materials known as ‘biomorphs’. The basic hydrolysis of TEOS furnishes silica in a controllable fashion, allowing a significantly higher reproducibility of the obtained silica-barium and silica-strontium carbonate co-precipitates compared to commercial water glass silica used so far. We further discuss the influence of ethanol used as a co-solvent on the morphologies of biomorphs, which are examined by optical microscopy, field emission scanning electron microscopy (FESEM) and energy dispersive X-ray analysis (EDX).

6.1.1. Introduction

Silica-carbonate ‘biomorphs’ are characterized by a wide range of non-crystallographic, biomimetic morphologies. For example, micron-sized worm-like biomorphs¹ mimic closely the chemical composition and morphologies of oldest microfossils².

The formation of these crystalline aggregates (biomorphs) involves two simultaneous, likely coupled processes^{3,4}: the nucleation and growth of alkaline-earth carbonate crystals, and polymerisation of silicate species into silica. The resulting aggregates display striking structural features at many length scales, reminiscent of natural biominerals⁵. They are built in part of rod-shaped nano-crystallites of the alkaline-earth carbonate, typically 200 nm in length, that adopt the usual aragonite crystal structure, evidenced by X-ray diffraction. These rods are organised to form orientational ordering of the crystal axes, with a slight twist between adjacent crystallites, giving characteristic radial textures in transmission optical microscopy between crossed polarizers. The rods are embedded in an amorphous silica matrix, giving a nano-scale composite. The radial ordering imparts striking micrometer-scale morphologies to the biomorphs, discussed below.

Until now, biomorphs have been grown with water glass as the silicate source⁶. Commercial water glass solution contains 29.7 wt% SiO_2 , though its detailed chemistry is inherently complex, comprised of an undefined mixture of different silicate species and 14 wt% $NaOH$. Its alkaline character induces CO_2 dissolution which lowers the pH. In addition, aging of silica glass is likely to change the silica speciation in solution, due to the complex kinetics of silica oligomerization. The age of water glass solutions can therefore significantly affect the experiments. Indeed, in some cases, we have observed that a specific water glass batch fails to form biomorphs, despite its efficacy in earlier experiments. In those cases, a new batch of water glass (as supplied) has induced biomorph formation.

Since the pH of the growth solution and the concentration of silica species during precipitation are critical factors in the resulting morphologies of biomorphs, we are investigating other silica sources whose characteristics can be better controlled, in order to obtain firmer data linking material morphology to the chemical species and environment. To this end, we have studied the efficacy of tetraalkoxysilanes⁷, $Si(OR)_4$, as a silica source, due to its defined starting composition and pH stability under storage. These organic silanes produce silica solutions in situ by hydrolysis. We have used tetraethylorthosilicate (TEOS) as a precursor. Tetrapropylorthosilicate (TPOS) and tetrabutylorthosilicate (TBOS) were also considered, but they are not soluble even upon addition of a co-solvent. There is extensive literature on the hydrolysis of TEOS in aqueous solutions^{8,9}, and the subsequent silica polymerization. Acidic or basic catalysis is commonly used to induce and

control this process. As biomorphs form at pH values around 10.5, TEOS hydrolysis was done under basic conditions (formed by addition of $NaOH$). Since TEOS and H_2O are immiscible, the reaction was carried out with ethanol as a co-solubiliser for TEOS, though the addition of ethanol adds an extra dimension to the complexity of the silicate solution. We show here that TEOS can be effectively used as a silica source, allowing better chemical characterisation and tunability of the system compared with the water glass precursors. We also investigate the influence of EtOH on the self-assembly process of biomorphs to shed light on the complex issue of silica chemistry and its influence on biomorph formation.

The mechanism for the basic hydrolysis of TEOS was first proposed by Iler¹⁰. This follows a nucleophilic SN_2 -type reaction in which OH^- displaces the $-OR$ rests. Under most conditions, condensation commences before hydrolysis is complete. However, adequate choice of parameters like pH^{11,12}, time and H_2O/Si molar ratio can force completion of the hydrolysis before condensation starts¹³. According to Coradin et al.¹⁴, silicon alkoxides allow a better control of the reaction kinetics than otherwise possible.

6.1.2. Experimental Section

6.1.2.1. Materials Preparation

TEOS (purity >98%), barium chloride dehydrate ($BaCl_2 \cdot 2H_2O$, purity >99%), strontium chloride hexahydrate ($SrCl_2 \cdot 6H_2O$, purity 99%) and sodium hydroxide ($NaOH$, purity 99%) were purchased from Sigma-Aldrich and used without further purification. EtOH was purified by distillation before use. Purified water with an electrical conductivity of less than $10^{-6} \text{ S} \cdot \text{m}^{-1}$ was taken from a Milli-Q system.

The alkaline silica solution was prepared in a 100 mL plastic beaker by mixing TEOS (7.5 or 8.9 mM), EtOH, $NaOH$ and water in appropriate molar ratios and stirred for 60 min at ambient temperature. The EtOH content and the pH were varied from 0 to 10 vol% and from 9.5 to 12, respectively. The biomorphs were grown by adding 0.5 mL of a 1 M barium chloride dehydrate or strontium chloride dehydrate. The resulting mixture was transferred to open reaction cells (plastic circular wells (Linbro Tissue Culture from INC Biomedical Inc.) of 1.6 cm in diameter and 1.7 cm in depth) and left in contact to ambient atmosphere ($\sim 20^\circ \text{C}$). The barium biomorphs were grown in silica solutions for about

9–10h. Alternatively, strontium biomorphs were grown in silica solutions for 5 and 15 h. The diffusion of atmospheric CO_2 ($\sim 330 \text{ ppm}^{15}$) leads to the precipitation of self-assembled silica-barium or silica-strontium carbonates. The precipitates were washed several times with water and EtOH and examined by optical microscopy, then *Au/Pd* coated for scanning electron microscopy.

6.1.2.2. Analytical Methods

Light Microscopy was performed using a stereo reflection microscope from Leica (Model MZ 12). Pictures were taken with a digital camera (Nikon, Coolpix 5000) having a resolution of 5.24 megapixels and zooms of 4x digital or 3x optical.

Field-emission Scanning Electron Microscopy (FESEM) was performed using a microscope (Hitachi, Model S4500) operated at 3 kV. It has ‘upper and lower’ secondary electron detectors (Robinson, Model Mk 6). The samples were coated in *Au/Pd* with an Emitech sputter coater using a rotational stage.

The *pH* of the aqueous solutions was measured using an *Ag/AgCl* plastic-body electrode (TPS, Model smartCHEM-Laboratory).

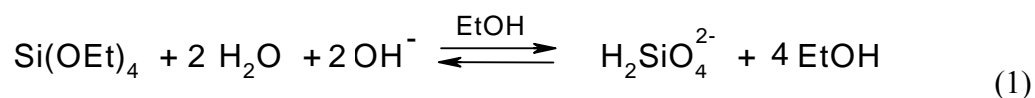
Energy Dispersive X-ray (EDX) analysis was performed using an EDX microanalyser mounted on a Jeol JSM 6400 scanning electron microscope.

Dynamic Light Scattering (DLS) measurements were done using a Zetasizer spectrometer (Malvern Instruments, Model Z3000) equipped with a 633 nm *He-Ne* laser. Measurements were carried out exclusively at a scattering angle of 90° .

6.1.3. Results and Discussion

6.1.3.1. Influence of the Ethanol on the Basic Hydrolysis of *TEOS*

The influence of EtOH on the basic hydrolysis of tetraethoxysilane was studied by varying its concentration whilst keeping the TEOS concentration constant at 7.6 mM and pH 11. The hydrolysis reaction can be written as follows¹⁶:



EtOH is both solvent and product of the hydrolysis reaction. In dilute solutions most of the monomers dimerize¹⁷ to form $\text{Si}_2\text{O}_3(\text{OH})_4^{2-}$.

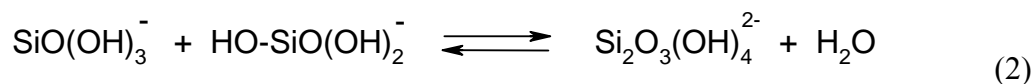


Figure 6.1 shows the change of the pH with time during TEOS hydrolysis at two different EtOH concentrations. At low EtOH content the curve exhibits two distinct parts. First, the pH decreases linearly as a function of time with a slope of $\alpha = -5.7 \times 10^{-4} \text{ sec}^{-1}$. Finally, the pH becomes nearly constant. The initial decrease in pH is due to the $\text{S}_\text{N}2$ substitution. As soon as equilibrium is reached, the pH remains constant.

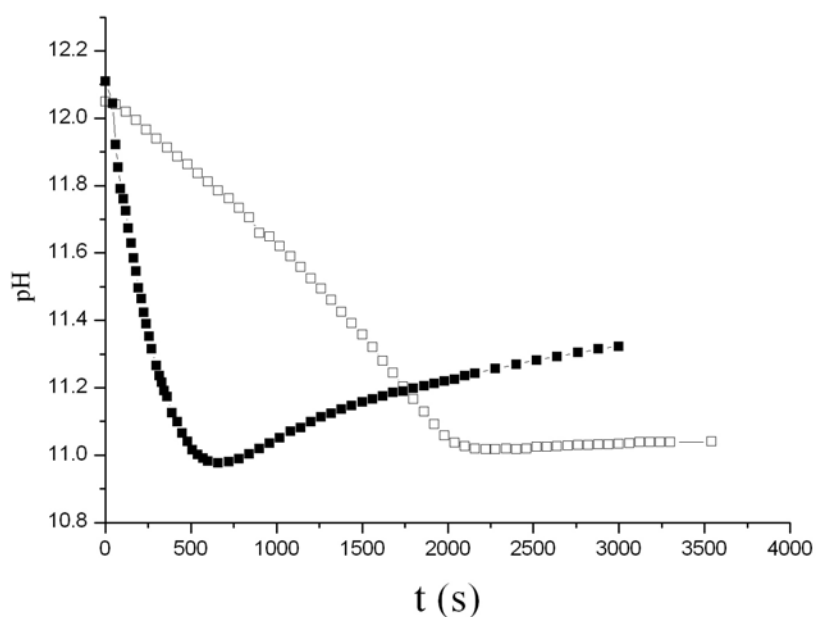


Figure 6.1 pH variation with time in the reaction mixture during TEOS hydrolysis at 0.17 vol% (\square) and 10 vol% (\blacksquare) EtOH.

At high EtOH content, the curve can also be divided in two parts. In the early stage of the reaction, the pH again decreases linearly, but with a slope of $\alpha = -2.6 \times 10^{-3} \text{ sec}^{-1}$. After about 500 sec, however, the pH increases again. The positive slope, in this part of the

curve, decreases towards zero at longer reaction times. Apparently, equilibrium is not completely reached after 1 h.

The difference of the slopes in the early stage of the reaction can be explained by the different solubilisation rates of TEOS in the two media. At low EtOH content, TEOS is not fully solubilised at the beginning of the reaction and it takes a certain time for both the solubility and the equilibrium to be achieved. The subsequent pH increase during the later stage of the reaction at high EtOH content is consistent with initial formation of acidic silanol groups ($Si-OH$) during TEOS hydrolysis followed by their disappearance by condensation reactions ($Si-O-Si$), proposed by Nagao et al.¹⁸. EtOH effectively enhances the propensity of the silica species to condense, via formation of relatively reactive $Si-OH$ species. The reaction medium is less polar, thus favouring the formation of polymeric silica.

As both the hydrolysis of TEOS and the subsequent polymerisation reactions are strongly dependent on time¹⁹, the kinetics of silica formation can be varied in a controllable manner, allowing preparation of aqueous silicate solutions with reproducible species in solution. Therefore, TEOS affords a better defined source of silica than commercial water glass, improving the reproducibility of biomorph growth. Indeed, this fact could help us to better understand the mechanism of biomorph formation.

6.1.3.2. Influence of EtOH on Structure Formation of Biomorphs

a. Nucleation and Initial Growth

Barium chloride was added immediately after TEOS hydrolysis was complete, as detected by pH measurements, discussed in the previous section. The growth of biomorphs was then followed by DLS from solutions with different EtOH content. The results are shown in Figure 6.2. In the presence of metal cations, silica species nucleate and grow¹⁹. Addition of the barium salt to hydrolyzed TEOS solutions containing 0.17 vol% EtOH led to the formation of detectable nucleates after an incubation time of 10 min or more. The onset of nucleation ($R_h = 105$ nm) was followed by a slow and gradual growth of the aggregates with time. Apparently, Ba^{2+} interacts with the negatively charged silicate species, thereby screening the surface charge of the anionic silica particles, leading to their aggregation.

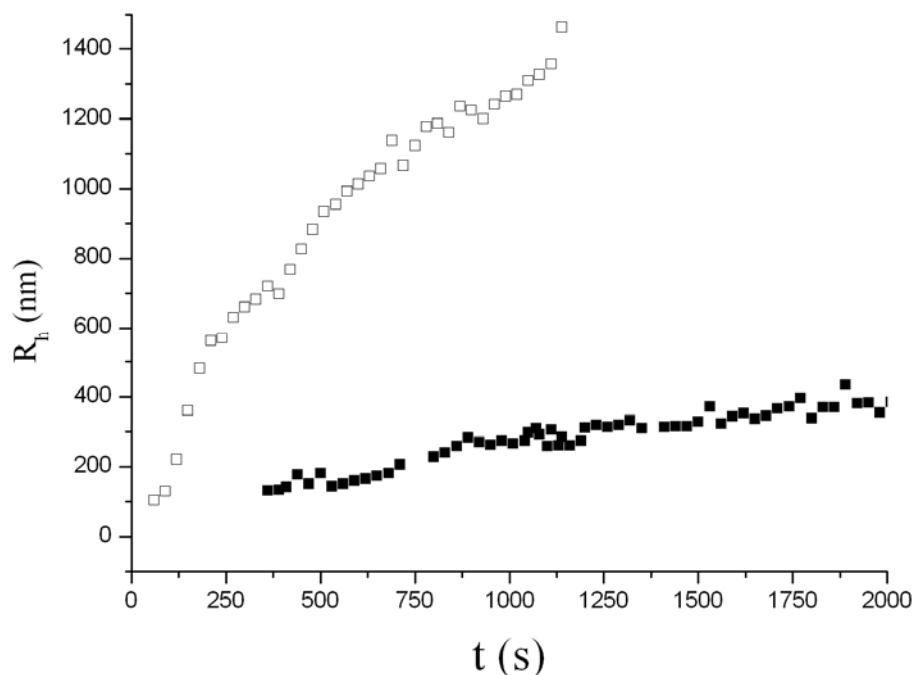


Figure 6.2 Comparison of the light scattering curves obtained after rapidly mixing solutions of $BaCl_2$ and TEOS hydrolysed at 0.17 vol% (■) and 10 vol% (□) EtOH.

In the alkaline TEOS solution rich in ethanol (10 vol%), the addition of barium cations dramatically enhanced the nucleation, giving a cloudy appearance to the reaction mixture within a few minutes. After 1 h, the resulting precipitate was collected and studied by means of SEM and EDX analysis. SEM images (Figure 6.3 A) show an amorphous-looking material consisting of *Si* and traces of *Ba* (EDX data). In a control experiment, in which no silica was present, well-defined micron-sized rod-like crystals characteristic of witherite were produced within the same timeframe (Figure 6.3 B).

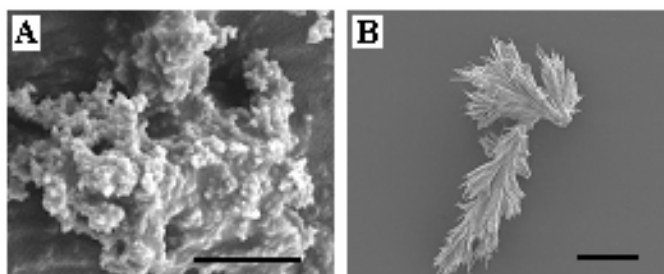


Figure 6.3 SEM images obtained in the presence (A) and absence (B) of TEOS after 1 hour from mixing solutions of $BaCl_2$ and TEOS hydrolysed. Scale bar: (A) 1.5 μm (B) 10 μm .

b. Biomorphs Characterisation after 9 h in Contact with Atmospheric CO₂

After a period of time comparable with that of water glass experiments²⁰, self-assembled silica-carbonate aggregates were formed. Figure 6.4 shows optical micrographs of biomorphs at different EtOH concentrations and pH~11 (corresponding to the optimal pH at which the non-crystallographic helical filaments are found when conventional water glass is used). At low EtOH content, the resulting carbonate-silica biomorphs give similar morphologies to those produced using water glass as silica precursors. The helical filaments grow to a similar length (100–200 μm) as found in ‘standard’ biomorphs. On raising the EtOH content, two, three or more helical filaments ramify from one nucleation point, a feature also observed in earlier work.

At 10 vol% EtOH, globular aggregates with apparently inter-grown filaments are observed. The size and shape of these globular clusters varies between 100 and 150 μm (Figure 6.5). The surface texture of the aggregates consists of orientationally ordered witherite nanorods. We could not find evidence of a surrounding silica skin, in contrast to the helical filaments grown from TEOS solutions with low EtOH content and already reported in water glass syntheses¹. Another important observation concerns the nuclei distribution. Increased EtOH content leads to faster formation of a smaller number of particles.

Although the EtOH content ensures high miscibility of silanol groups ($Si-OH$) with water, the formation of typical biomorphs only occurs at low EtOH content. On the one hand, higher EtOH content strongly favours nucleation and the growth of silica after combining the silica sol and metal solutions. Possibly, ethanol molecules interact with the silica surface via H-bonds and shield interactions with metal ions, at least to some extent²¹. More likely, the silica species interact with the EtOH molecules, forming reactive intermediates that subsequently condense to form silica oligomers. Consequently, the silica particles aggregate to form a concentrated colloidal phase. The light scattering data supports the hypothesis that the silica is removed from the solution via condensation. This allows us to correlate the observed changes in morphology with uncondensed silica species in the reaction mixture²².



Figure 6.4 Optically micrographs of self-assembled silica-carbonate at different EtOH vol%. [TEOS] = 7.5 mM, [Ba²⁺] = 5 mM, pH = 11, t = 9 h.

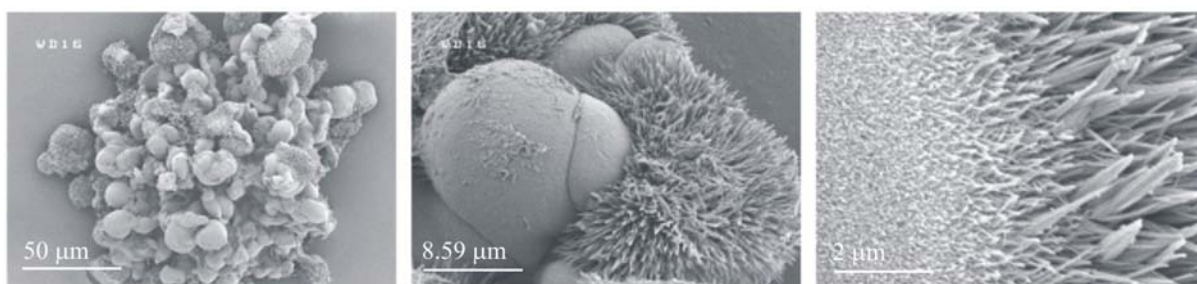


Figure 6.5 Zoom sequence of globular aggregates, showing details of the surface texture.

6.1.3.3. Effect of pH on the Formation of Silica-Carbonate Biomorphs

In the preceding section, it was shown that most biomorphs (helical filaments and worms) – hitherto grown in water glass – also appear in TEOS solutions at low EtOH content. Figure 6.6 gives FESEM images of silica-barium carbonate biomorphs grown in hydrolysed TEOS solutions containing 0.17 vol% EtOH and 5 mM barium chloride at various starting pH values. The given pH values correspond to the hydrolysed TEOS solutions after 60 min of mixing. The morphologies of the precipitates depend critically on the pH of the system. We observe pH–morphology relations for TEOS-induced biomorphs consistent with the progression seen in water glass experiments⁵.

Uniform aggregates showing cauliflower-like morphologies, of about 75 μm in length were produced by decreasing the pH from 10.5 to 9.7. The shape consists of several dendrite-like heads composed of radially aligned witherite (BaCO₃) crystals (see Figure 6.6 A–C)). When the pH is decreased to below 9.5, no precipitation occurs.

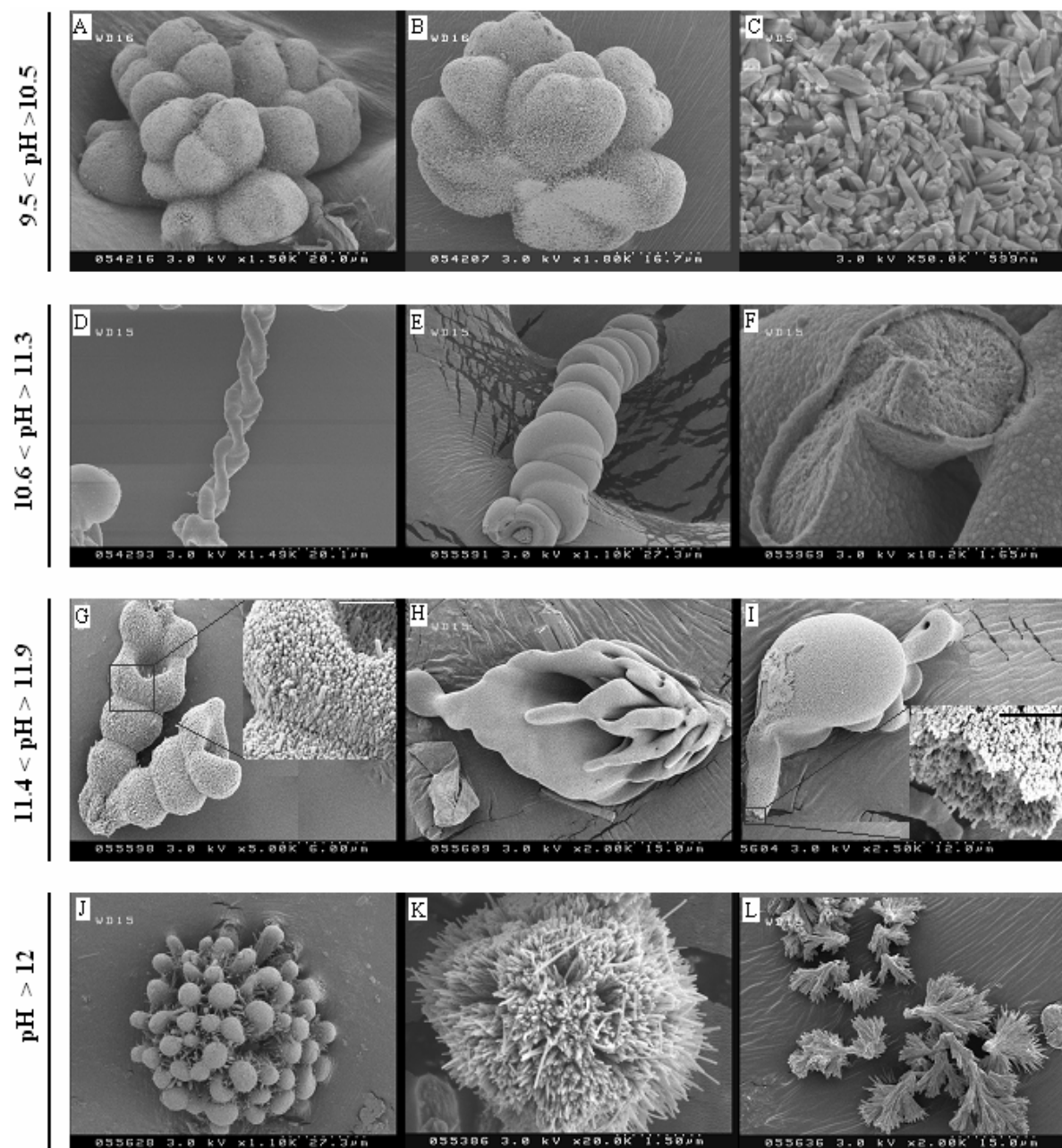


Figure 6.6 FESEM images of a selection of various aggregates grown at pH values between 9.5 and 12. $[\text{TEOS}] = 7.5 \text{ mM}$, $[\text{Ba}^{2+}] = 5 \text{ mM}$, 0.17 vol% EtOH, $t = 9 \text{ h}$, $T = 20 \text{ }^\circ\text{C}$. (A to C) Zoom sequence of ‘cauliflower’ biomorphs, showing details of the surface structure. (D, E) Helical barium carbonate biomorphs grown at $\text{pH} = 10.6\text{--}11.3$. (F) Silica skin, coating the exterior of the helical aggregates. (G to I) Non-crystallographic morphologies of BaCO_3 , showing the orientational ordering of crystallites (insets). (J) Colony-like aggregates of several globules arising from a single crystal core. (K) ‘Hairy’ spheres clusters with strong architectural resemblance to fluoroapatite-gelatin aggregates. (L) Micron-sized rod-like barium carbonate. Inset scale bar: (G) $1.2 \text{ }\mu\text{m}$ and (I) 857 nm .

Increasing the pH to 11 resulted in the formation of typical helical filaments of about 100–200 μm in length and 5–15 μm in width (see Figure 6.6 D–F). We have noted already the remarkable resemblance of these structures in size and shape to terrestrial bacteria and microfossils²³. The filaments, ‘twisted ribbons’ (Figure 6.6 D) and ‘worms’ (Figure 6.6 E), are assemblies of micron-size witherite crystallites coated with a continuous silica matrix, identical to comparable biomorphs produced using water glass as silica source. EDX measurements were performed to determine the *Si* and *Ba* content (averaged over the silica membrane as well as the inside of the worm).

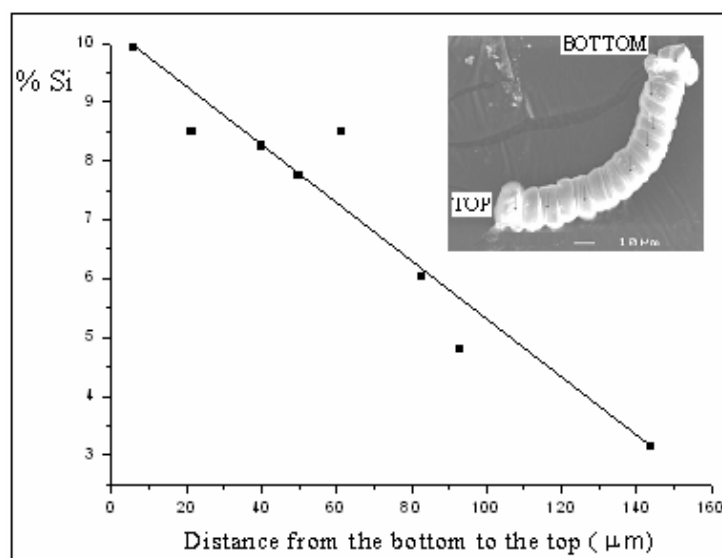


Figure 6.7 *Si* content (relative to *Ba*) on the surface of a biomorph ‘worm’ at different distances from the bottom of the worm.

Figure 6.7 visualizes the relative at% of *Si* (i.e., the fraction of *Si* atoms out of the total *Si* + *Ba* atom count) on the surface of a biomorph worm at different distances from the bottom. It is evident that the relative *Si* content decreases smoothly from the starting point of growth to the later stages, when barium carbonate predominates.

Significant changes in the biomorph morphologies occur upon increasing the pH further to 11.5, where a wide range of novel, astonishing non-crystallographic morphologies such as snail-like (Figure 6.6 G), arum-flower-like (Figure 6.6 H) and tortoise-like (Figure 6.6 I) aggregates appear. Higher magnifications of the surface texture reveal that these biomimetic morphologies too are composed of arranged rods (see Figure 6.6, insets) and

lack a silica membrane. The helical filaments observed at pH 11 are suppressed under these conditions.

Above pH 12, aggregates such as dendrite-shaped $BaCO_3$ or ‘hairy’ spheres grow (Figure 6.6 J and K). These clusters are composed of radially aligned crystals. Similar shapes have been reported for other composite structures such as fluoroapatite-collagen aggregates²⁴. Simultaneously, micron-sized particles consisting of witherite nanorods in parallel arrangement were generated in the reaction cells (Figure 6.6 L). The formation of these rods is not attributable to the presence of silicate anions since similar micron-scale morphologies were produced by diffusion of atmospheric CO_2 into silica-free barium chloride solutions. Under these conditions, the dissolution of carbon dioxide is fast, silica condensation is minimal and therefore the silica exerts little influence on the morphology.

Lastly, we point out that the use of TEOS is not confined to growth of silica-barium carbonate biomorphs. Silica-strontium carbonate biomorphs also readily form under ambient conditions with TEOS as a silica source. The growth sequence of these strontium biomorphs mirrors exactly that of the strontium biomorphs grown using water-glass solutions as a silica source. Initially, floral spherulites were produced (Figure 6.8 A). The size of these globular clusters varies between 40 and 70 μm and the thickness of the curvilinear sheets is about 2 to 4 μm .

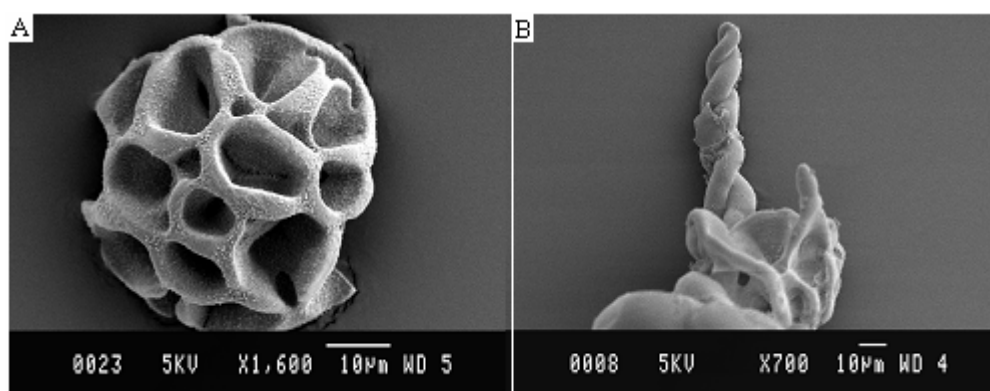


Figure 6.8 SEM images silica-strontium carbonate biomorphs grown for 5 (A) and 15 h (B) in TEOS solutions (8.9 mM) at pH 11 containing 5 mM Sr^{2+} .

If the cluster is left in solution for 15 h, twisted filaments grow outward from the tips of these sheets (Figure 6.8 B). We note that the morphological evolution of the cluster grown

in aqueous solution of TEOS bears a striking resemblance to that reported by Terada et al.²⁵. In their case, strontium carbonate clusters were prepared in a silica gel at pH 10.5.

6.1.4. Conclusions

Silica-carbonate biomorphs have been precipitated reproducibly using tetraethylorthosilicate (TEOS). Experiments were done in alkaline TEOS solutions at pH and concentrations identical to the former water glass experiments. It was found that TEOS offers an alternative silica source for the growth of biomorphs, provided the EtOH content remains low. Indeed, ethanol, an essential co-solvent for TEOS solubilisation, has a significant effect on the growth process. Experiments conducted at high EtOH content led to fast formation of a small number of globular morphologies strikingly dissimilar to biomorphs. This is most likely due to the promotion of silica condensation in the presence of raised EtOH levels. It is therefore likely that the speciation of silica and the associated availability of silica to co-condense with the metal carbonate in the reaction mixture is a critical parameter for the formation of the complex curvilinear forms characteristic of biomorphs.

In conclusion, TEOS offers a preferred silica source over water glass solutions for detailed investigations of material-structure aspects of these biomorphs, due to its better defined chemical properties. In summary, the use of TEOS in the presence of low concentrations of EtOH allows reproducible growth of biomorphs. We therefore recommend its use as a silica source for biomorph growth in place of water glass used previously. The control over kinetics and species of silica formation offered by hydrolysis of organic silanes (e.g. by variation of hydrolysis time) will allow us to tune the many parameters affecting biomorph formation more carefully, thereby improving our techniques for study of these fascinating materials.

6.1.5. References

- (1) García-Ruiz, J. M.; Hyde, S. T.; Carnerup, A. M.; Christy, A. G.; Van Kranendonk, M. G.; Welham, N. J. *Science* **2003**, *302*, 1194.
- (2) Grotzinger, J. P. *Early life on Earth*, University press: New York, 1994.
- (3) García-Ruiz, J. M. *Bulletin Mineralogique* **1981**, *104*, 107.
- (4) García-Ruiz, J. M. *J. Crystal Growth* **1985**, *73*, 251.

- (5) García-Ruiz, J. M.; Carnerup, A. M.; Larson, A.; Christy, A. G.; Welham, N. J.; Hyde, S. T. *Astrobiology* **2002**, *2*, 353.
- (6) Hyde, S. T.; Carnerup, A. M.; Larson, A.; Christy, A. G.; García-Ruiz, J. M. *Physica A* **2004**, *339*, 24.
- (7) Brinker, C. J.; Scherer, C. W. *Sol-Gel Science: The Physics and Chemistry of Sol-Gel Processing*, Academic Press: London, 1990.
- (8) Sefcik, J.; McCormick, A. V. *Catalysis Today* **1997**, *35*, 205.
- (9) Boonstra, A.; Baken, J. M. *J. Non-Crystalline Solids* **1990**, *122*, 171.
- (10) Iler, R. K. *The Chemistry of Silica: Solubility, Polymerisation, Colloid and Surface Properties, and Biochemistry*, Wiley-Interscience, New York, 1979.
- (11) Chen, S. L.; Dong, P.; Yang, G. H.; Yang, J. J. *Ind. Eng. Chem. Res.* **1996**, *35*, 4487.
- (12) Pohl, E. R.; Osterholtz, F. D. *Molecular Characterisation of Composite Interfaces*, New York, 1985.
- (13) Kim, S. H.; Liu, B. Y. H.; Zachariah, M. R. *Langmuir* **2004**, *20*, 2523.
- (14) Coradin, T.; Lopez, P. J. *ChemBioChem* **2003**, *3*, 1.
- (15) Tomoda, A. *Tokyo Ika Daigaku Zasshi* **2004**, *62*, 641.
- (16) Yang, S.; Navrotsky, A. *Chem. Mater.* **2004**, *16*, 3682.
- (17) Greenberg, S. A.; Sinclair, D. *J. Am. Chem. Soc.* **1955**, *9*, 436.
- (18) Nagao, D.; Osuzu, H.; Yamada, A.; Mine, E.; Kobayashi, Y.; Konno, M. *J. Colloid and Interface Sci.* **2004**, *279*, 143.
- (19) Kerr, G. T. *J. Phys. Chem.* **1966**, *70*, 1047.
- (20) García-Ruiz, J. M. *Orig. Life Evol. Biosph.* **1994**, *24*, 451.
- (21) Brindley, G. W.; Ray, S. *American mineralogist* **1964**, *49*, 106.
- (22) Larsson, A.; Carnerup, A. M.; Hyde, S. T. *Morphology of helical, self assembled silica carbonate biomorphs*, in preparation
- (23) Schopf, J. W.; Kudryavtsev, A. B.; Agresti, D. G.; Wdowiak, T. J.; Czaja, A. D. *Nature* **2002**, *416*, 73.
- (24) Kniep, R.; Busch, S. *Angew. Chem Int.* **1996**, *35* 2624.
- (25) Terada, T.; Yamabi, S.; Imai, H. *J. Crystal Growth* **2003**, *253*, 435.

6.2. Inorganic Self - Organised Silica Aragonite Biomorphic Composites

Abstract

The precipitation of calcium carbonate in alkaline silica solutions results in the formation of complex curvilinear forms if aragonite formation is encouraged by growth at elevated temperature (80 °C). The resulting coralline self-assembled silica-calcium carbonate particles are ‘biomorphs’, bearing a striking resemblance to natural coral forms. These materials, comprised of calcium carbonate nanocrystals and an amorphous silica matrix, have a complex ultrastructure, made of clusters of gathered sheets of variable curvatures formed by successive curling. The nanocrystals within these ‘ruled surfaces’ are thin, elongated, densely packed needles of aragonite. These clusters are outgrowths from central saddle-like cores that resemble developable petaloid surfaces. The size, shape, crystallography and chemical composition of the resulting biomorphs were examined by optical microscopy, field emission scanning electron microscopy (FESEM), powder X-ray diffractometry (XRD), Fourier transform infrared spectroscopy (FTIR), transmission electron microscopy (TEM and HRTEM) and energy dispersive X-ray analysis (EDX).

6.2.1. Introduction

Biomorphs are inorganic, self-assembled silica-carbonate aggregates showing a wide range of non-crystallographic, biomimetic morphologies and sizes¹. Their forms include curvilinear sheets, helical filaments, braids and floral spherulites, accompanied by the packing of crystalline rods within the self-assembled aggregates. They exhibit a complex structural hierarchy from the nano- to optical scales, composed of nanometer-sized carbonate crystals, densely packed with orientational ordering between crystallographic axes of adjacent rods.

To date, these aggregates were found when barium and strontium carbonates were precipitated in basic silica solution into which atmospheric carbon dioxide was allowed to diffuse, forming witherite and strontianite phases, respectively¹. Until now, the precipitation of calcium in basic silica has not produced the curvilinear forms characteristic of biomorphs². Given the presence of calcium carbonate polymorphs in many biominerals

as well as the geochemical abundance of calcium relative to barium and strontium, the possibility of forming curvilinear sheets of silica-calcium carbonate biomorphs deserves further exploration. $CaCO_3$ is often the most abundant chemical in sedimentary rocks and is widely used by nature as an inorganic component in exoskeletons and tissues of many mineralizing organisms³, thus giving them strength and shape⁴.

We note that non-crystallographic morphologies have been observed previously for $CaCO_3$ materials. García-Ruiz reported the formation of fan-like ‘sheaf-of-wheat’ aggregates of calcite grown in alkaline silica gels⁵⁻⁷, under similar conditions to those used to grow helical filaments of barium and strontium biomorphs. Although these dendritic calcites are non-crystallographic, they do not exhibit curvilinear surfaces common to biomorphs. Terada et al.⁸ have grown morphologically complex aragonite-silica composites in the presence of silica, but preferentially with the addition of pregrown needle-like aragonite seed crystals. In this case, the constituent crystalloid units are aragonite fibers, coated with silica. Gower et al. reported unusual helical morphologies of $CaCO_3$ (vaterite polymorph), somewhat reminiscent of biomorphs. These forms were grown in the presence of charged polypeptides⁹ with no added silica. Wang et al.¹⁰ synthesized complex ‘flower-type’ vaterite superstructures in the presence of urea at high temperatures. Kulak et al.¹¹ reported a variety of $CaCO_3$ particles of varying crystallinity in the presence of two double-hydrophilic block copolymers. Walsh et al.¹² described a method for synthesizing hollow porous shells of crystalline aragonite that resemble the coccospheres of certain marine algae. Mann¹³ reported sponge-like hollow vaterite spheroids (Figure 2.14 H), obtained from oil-water-surfactant microemulsions supersaturated with calcium bicarbonate. Gao et al.¹⁴ demonstrated that a hydrophobic polymer can induce the growth of $CaCO_3$ microrings in aqueous solution. The formations of non-crystallographic $CaCO_3$ morphologies have been recently reviewed^{15, 16}. Such biomimetic non-crystallographic aggregates are necessary for understanding biomineralization processes.

Here we report the formation of silica-calcium carbonate biomorphs which develop into ‘coralline’ composites through spontaneous self-assembly without the presence of organic additives (apart from the silica source) or seed crystals. The resulting biomimetic aggregates are able to form surfaces with variable curvatures by successive curling. These biomorphs display structural features over a range of length scales that are similar to

previously reported barium and strontium examples, however to date less morphological variety has been found in calcium biomorphs than in the barium or strontium counterparts.

6.2.2. Experimental Section

6.2.2.1. Materials Preparation

Tetraethylorthosilicate (TEOS, purity >98%), calcium chloride dihydrate ($CaCl_2 \cdot H_2O$, purity >99%) and sodium hydroxide ($NaOH$, purity 99%) were purchased from Sigma-Aldrich and used without further purification. Ethanol (EtOH) was purified by distillation before use. Purified water with an electrical conductivity of less than $10^{-6} \text{ S} \cdot \text{m}^{-1}$ was taken from a Milli-Q system.

Alkaline silica solutions were prepared in a 100 mL plastic beaker by mixing 0.17 mL tetraethylorthosilicate (TEOS), 0.17 mL ethanol, 7.5 mL $NaOH$ (0.1 M), and water and stirring for 60 min. The pH was adjusted to 11 ± 0.1 . The reaction was started by adding different amounts (0.25–1.5 mL) of 0.5 M calcium chloride solution. The total amount of the mixture was 100 mL. After the addition of calcium salt, the solutions were then transferred to open cells (plastic circular wells (Linbro Tissue Culture), 1.7 cm deep and 1.6 cm in diameter) and warmed to 80 °C for about 6 h. We emphasise the importance of the aforementioned experimental procedure (i.e., the mixing of alkaline silica solution with calcium chloride solution at 20 °C and then warming the mixture to 80 °C) to take account of two different effects: first, working at 20 °C, we avoided the increase in the rate of polymerization (that increases as the temperature increases¹⁷) upon mixing alkaline silica solution with calcium chloride solution and second, warming to 80 °C, we favored aragonite formation over other $CaCO_3$ polymorphs¹⁸. After 6h, precipitation and growth of biomorphs occurred, due to the slow diffusion of atmospheric CO_2 into the mixture. The products were then washed several times in water and ethanol and examined by optical microscopy, and Au/Pd coated for field emission scanning electron microscopy.

6.2.2.2. Analytical Methods

pH of the TEOS hydrolysed solutions before and after the addition of calcium chloride solution were measured using an $Ag/AgCl$ plastic-body electrode (TPS, Model smartCHEM-Laboratory).

Optical Microscopy was used to determine the crystal habit of the silica-calcium carbonate crystals. *Light microscopy* was performed using Nikon transmission microscope (Model Eclipse E400), and images were taken between cross polarizers and produced with a JVC CCD colour video camera (Model TKC1380). *Field-emission scanning electron microscopy (FESEM)* was performed using a microscope (Hitachi, Model S4500) operating at 0.5–30 kV equipped with ‘upper and lower’ secondary electron detectors (Robinson, Model Mk 6). The samples were coated with *Au/Pd* in an Emitech sputter coater using a rotational stage. *Scanning electron microscopy (SEM)* was performed either using a microscope FEI Quanta 400T or Jeol JSM 840, both operating at 0.2–30 kV. The sample was coated with *Au* in an Polaron Equipment LTD sputter coater.

Crystal Polymorphism. *X-ray diffraction (XRD)* measurements were done using a STOE STADI P diffractometer (STOE & CIE) providing *Cu K α ₁* radiation monochromated with a germanium single crystal ($\lambda = 1.540598 \text{ \AA}$). Typical diffraction patterns were recorded in the range of $8^\circ < 2\theta < 90^\circ$ at a scanning speed of $0.8^\circ/\text{min}$. *Fourier transform infrared spectroscopy (FTIR)* was recorded on a Jasco FTIR–610 spectrometer. The samples were mixed with *KBr* powder. Subsequently, the resultant mixture were ground for 3–5 minutes in an agate mortar and deposited on the sample holder. The spectra were recorded in reflection mode from 4000 to 400 cm^{-1} at a resolution of 2 cm^{-1} . *Transmission electron microscopy (TEM and HRTEM)* The biomorphic aggregates were crushed into crystal fragments. The resultant crystals were suspended in ethanol. A small amount of the crushed crystals were placed onto a holey carbon grid. HRTEM was performed with a Philips CM30 ST electron microscope (300 kV, *LaB₆* cathode, Gatan multiscan CCD camera). The multislice formalism¹⁹ was used for image simulations.

Chemical Composition. *Energy dispersive X-ray (EDX)* analysis was performed using an EDAX microanalyser mounted on a FEI Quanta 400T scanning electron microscope at 15 kV. This analyze was used to quantify the approximate composition of the ‘coralline’ self-assembled silica calcium carbonate before and after leaching the crystals in acidic medium.

6.2.3. Results

6.2.3.1. Histogram of Calcium Carbonate Crystal Fractions as a Function of the Ca^{2+} Concentration

Distinct $CaCO_3$ crystal morphologies form after 6 h of growth by varying the $CaCl_2$ concentration from 2 to 7.5 mM, (Figure 6.9). These include ‘coralline’ silica-calcium carbonate biomorphs, ‘floral dumbbells’ biomorphs (Appendix 8.3), dendrites, pseudo-hexagonal prisms and spherulites. In the following, we describe and characterise the complex ‘coralline’ self-organized morphology of silica-calcium carbonate.

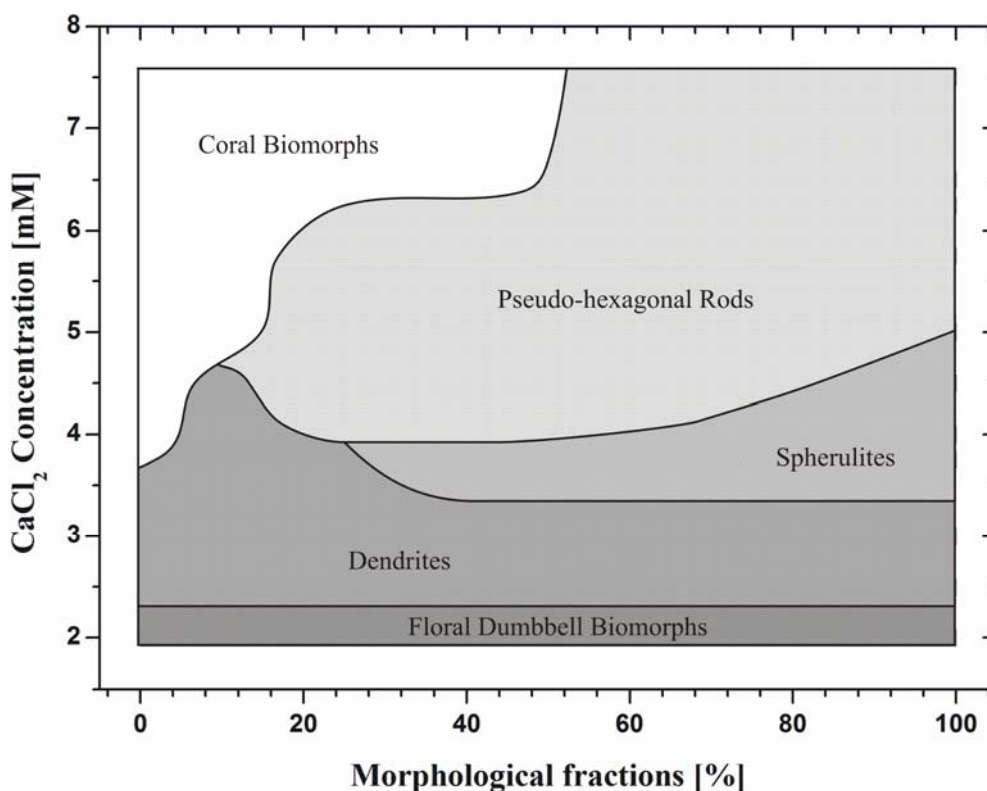


Figure 6.9 Schematic histogram of $CaCO_3$ crystal fractions as a function of the Ca^{2+} concentration at pH 11, obtained by averaging over many separate samples, incubated in separate runs. Given percentages are estimated values based on visual observation of at least tens of particles under polarized light.

6.2.3.2. Optical and Electron Microscope

In the absence of silica, calcite rhombs and bundles of aragonite needles (Figure 6.10 A) are obtained. The bundles of aragonite crystals are agglomerates of radially aligned needle-shaped single crystals. For small single crystal sizes, these aggregates had the appearance of spheres with the overall diameters around 30–50 μm . In the presence of hydrolysed TEOS solutions these bundles of aragonite crystals suffer dramatic changes. The particles grew in alkaline silica solutions are ‘coralline’ self-assembled silica-calcium carbonate biomorphs (Figure 6.10 B).

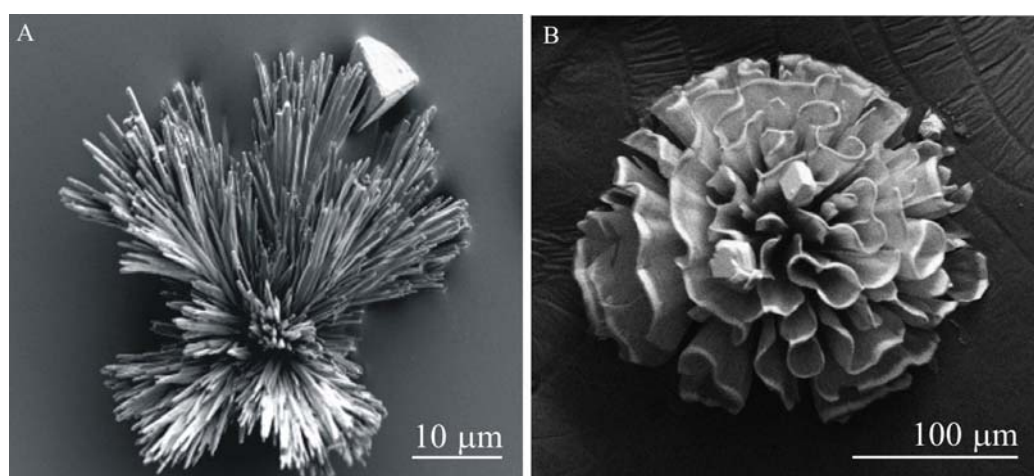


Figure 6.10 SEM images of a cluster precipitated in the absence (A) and in the presence (B) of silica sols.

The ‘coralline’ biomorphs are composed of sheet-like petaloid structures with almost zero Gaussian curvature (Figure 6.11 A). These sheets resemble closely ‘developable’ surfaces, swept out by the motion of a line along a generator spatial curve. The clusters are between 150 and 300 μm in diameter, depending on their form. High-magnification FESEM imaging of the curvilinear sheet surfaces reveals the presence of thin (typically 50–100 nm in diameter), elongated densely packed nanometer-sized crystallites that grow parallel to the surface (Figure 6.11 B, C). To further identify the chemical composition in whole composite, we measured the EDX spectra of several clusters. The spectrum (Figure 6.12) consists of *Si*, *Ca*, *C* and *O*. The EDX data suggest that the calcium coralline biomorphs contain more silica (30–45% *Si*, that is, the fractions of *Si* atoms out of the total calcium atom count) than the helical filaments (5–10% *Si*), previously grown in the presence of barium²⁰. This fact is supported by optical imaging that reveals greater transparency in

calcium ‘coralline’ biomorphs than in helicoidal microfilaments. It is worth noting that the clusters have flat faces (see Figures 6.11 D, E) where the nucleation start point and the first sheet-like projections can be observed. This three-dimensional crystal morphology has also been observed in strontium²¹ and barium²² carbonate biomorphs, and bears a striking resemblance to Australia natural corals (Figure 6.11 H).

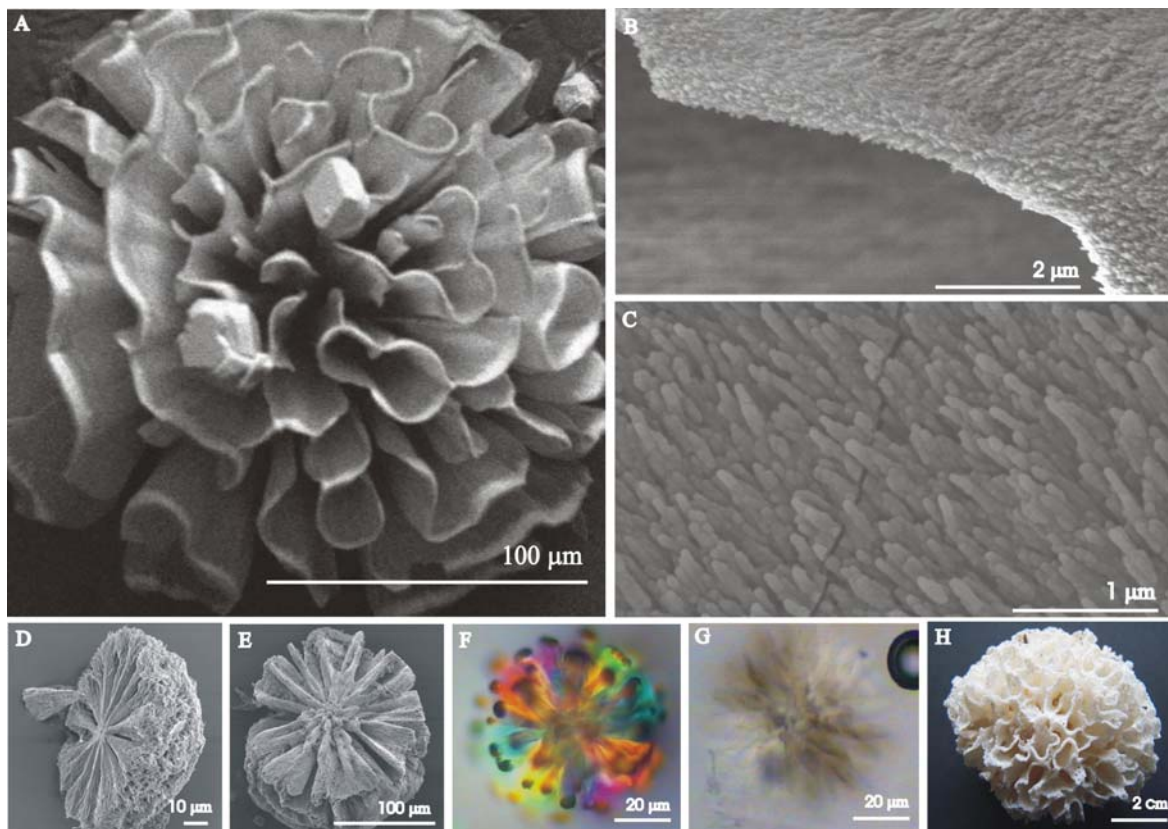


Figure 6.11 (A) Self-assembled ‘coralline’ silica-calcium carbonate. (B, C) High-magnification image of ‘coralline’ silica calcium carbonate showing the orientational ordering of crystallites. (D, E) Different positions of the silica-carbonate composites showing the starting point of nucleation and the orientation of the sheets. (F) Optical micrograph of silica-calcium carbonate aggregates, viewed between crossed polarizers. (G) Carbonate dissolution from the carbonate-silica material, leaving a silica ‘ghost’. (H) Natural coral from the southeastern Australian seaside.

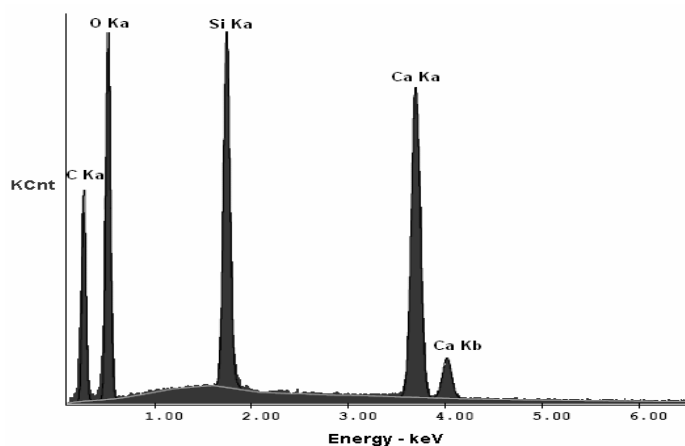


Figure 6.12 EDX spectrum of self organised silica-calcium carbonate biomorphs.

6.2.3.3. Leaching Experiments

Immersion of the biomorphs (Figure 6.11 F) in 0.1 M hydrochloric acid (dissolving all carbonate material) leaves a hollow silica ‘ghost’ (Figure 6.11 G). The surface texture of the leached particles is presented in the Figure 6.13. First, we observed that the overall structure is kept intact after leaching in the acidic medium. Second, on the surface texture, the thin densely packed crystals are no longer seen in the surface texture, and third, the surface is not smooth. The curved surface is dominated by sinuous narrow striations (ridges). The EDX spectrum (Figure 6.14) of this hollow silica skin left after immersion of the composites in the acidic medium 0.1 M *HCl*. The spectrum is comprised of *Si* and *O* elements, and no *Ca* is found.

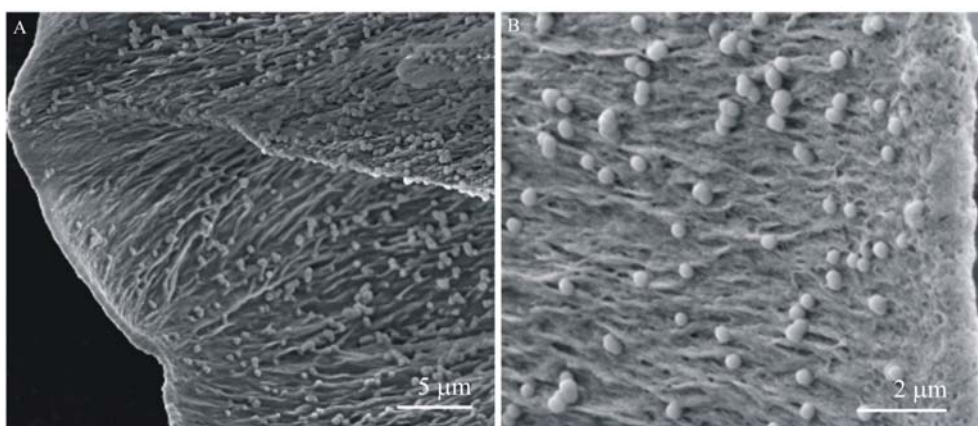


Figure 6.13 High-magnification FESEM images of biomorphs (after acidic leaching of carbonate) showing the silica skeleton. The small spheres may be an artifact of secondary deposition rather than intrinsic components of the biomorph during growth.

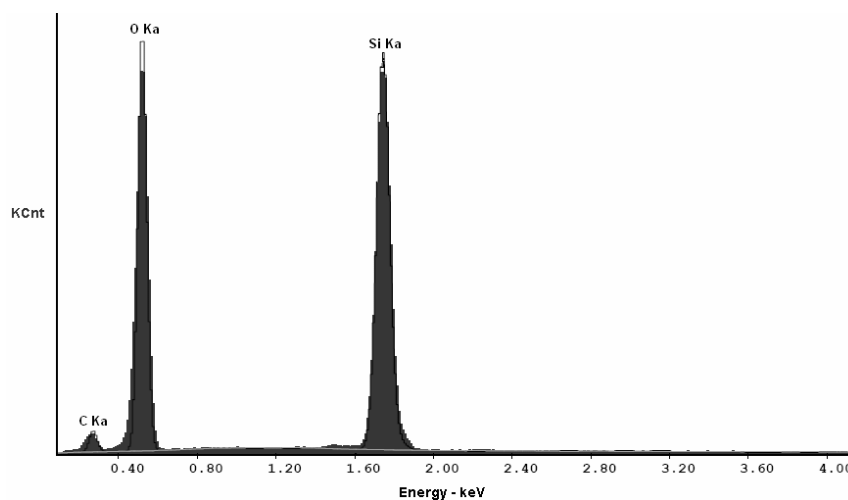


Figure 6.14 EDX spectrum of a hollow silica skin left after immersion of the ‘coralline’ silica-calcium carbonate biomorphs in 0.1M *HCl*.

6.2.3.4. Influence of the Counterion

To ensure that the observed new morphology is not dependent on the nature of the calcium salt counter ion (Cl^-), additional experiments were performed. Cl^- was exchanged with Br^- or NO_3^- , respectively, and precipitation was performed under the same conditions. Those experiments confirm that these structures do not depend on the nature of the calcium salt.

6.2.3.5. Crystal Polymorphism

Figure 6.15 shows the XRD pattern of the whole particles synthesized from the alkaline silica solution. The spectrum exhibits the characteristic reflections of aragonite (A_{111} , A_{121} , and A_{021}) and calcite (C_{104}) phases. Furthermore, the XRD spectrum displays a very broad line with a maximum at 2θ about 15° indicative of the presence of amorphous SiO_2 and a diffraction peak at 38.93° , which could not be identified by comparison with reference diffraction patterns. It is assumed that this phase is a ternary $Ca-Si-O$ phase.

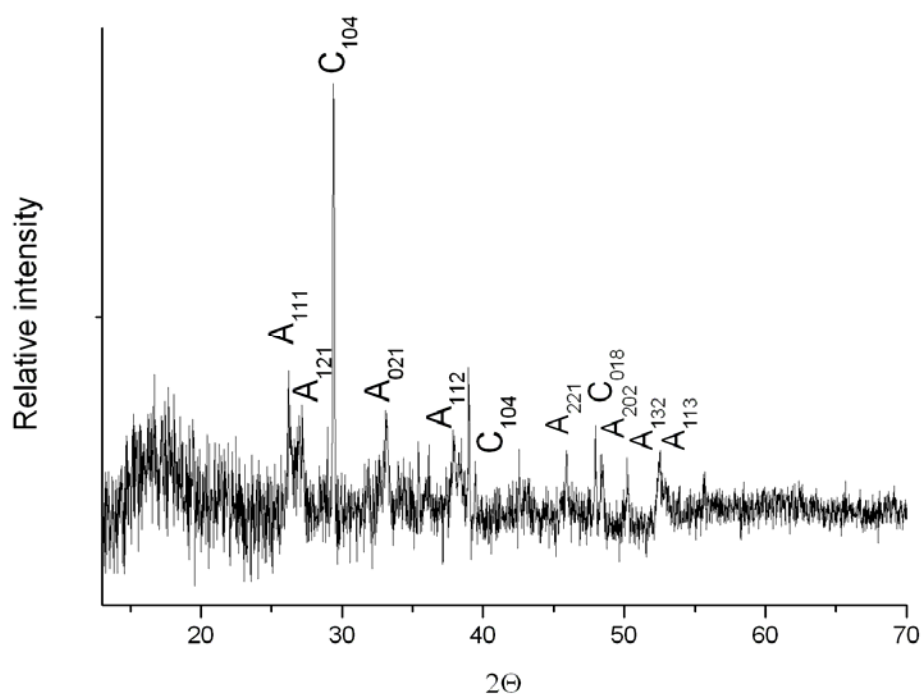


Figure 6.15 XRD spectrum of the self-assembled silica-calcium carbonate.

To get information about the crystal polymorphism of the coralline structures, FTIR analysis was performed (Figure 6.16). A comparison of the bands at 713, 855, 1092 and 1486 cm^{-1} with standard IR spectra of aragonite-type calcium carbonate (the symmetric stretch (ν_4) at 713 cm^{-1} , a broad absorption of the carbonate out-of-plane bending peak (ν_2) at 854 cm^{-1} , the symmetric stretch (ν_7) at 1080 cm^{-1} and a peak (ν_3) of the asymmetric stretch of the carbonate ion at 1488 and 1440 cm^{-1})^{23, 24}, suggests that the structure contains the aragonite calcium carbonate crystal phase. Along with the aragonite bands, the spectrum reveals bands at 467, 799, 959 and 1654 cm^{-1} attributed to silica²⁵: the bending vibration, symmetric stretching, *Si–O–Si* asymmetric stretching, and the *Si–OH* stretching modes, respectively. Bands in the range of 2000–3500 cm^{-1} are likely to be caused by *OH*⁻ and water vibrations.

According to TEM observations of small crystals deposited on a carbon film, the needle-like aragonite crystals (Figure 6.17 B) coexist with amorphous silica spheres (Figure 6.17 A) and amorphous *Ca–Si–O* particles. Figure 6.17 C shows a typical selected area electron diffraction (SAED) pattern recorded on the needle shown in Figure 6.17 B. The sharp

Bragg reflections can be indexed to the orthorhombic lattice of aragonite (zone axis [011]). Tilting experiments support this carbonate phase assignment (Figure 6.17 D–F). EDX analyses of the needles show the presence of *Ca*, *C* and *O* exclusively. Twinning or other kinds of micro-sized defects were never observed. HRTEM was used to probe for nanoscale crystal defects. A close analyses of several needles underlines their single crystalline nature, see for instance Figure 6.17 G, H for zone axis [101] and [011], respectively. The attached simulated micrograph was calculated on the basis of aragonite. The convincing agreement between experimental and simulated images confirms our assignment of these needles as aragonite.

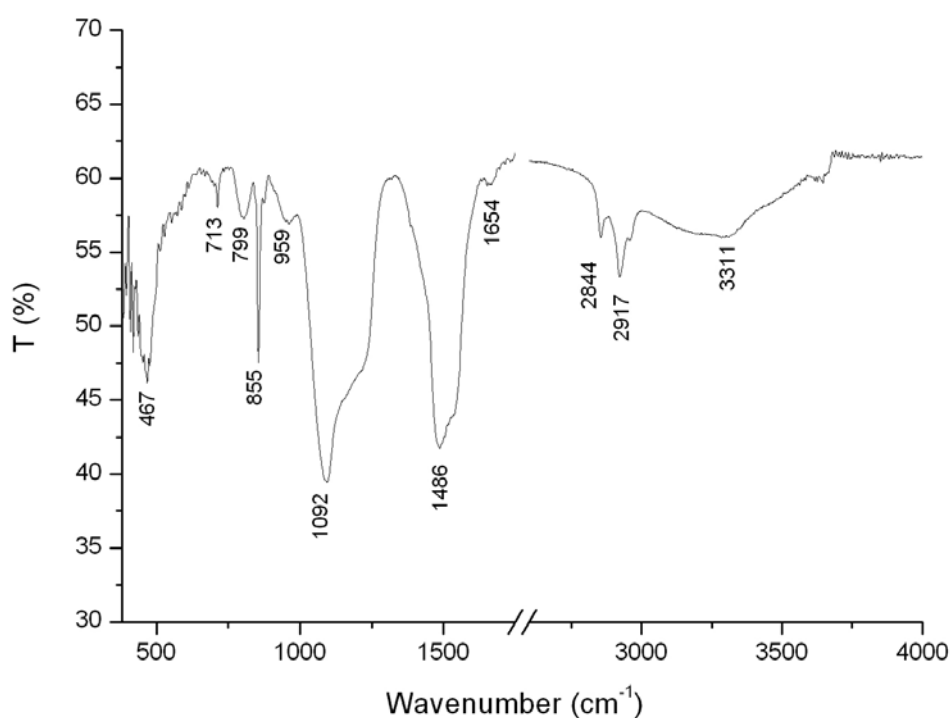


Figure 6.16 FTIR spectrum of the self-assembled silica-calcium carbonate.

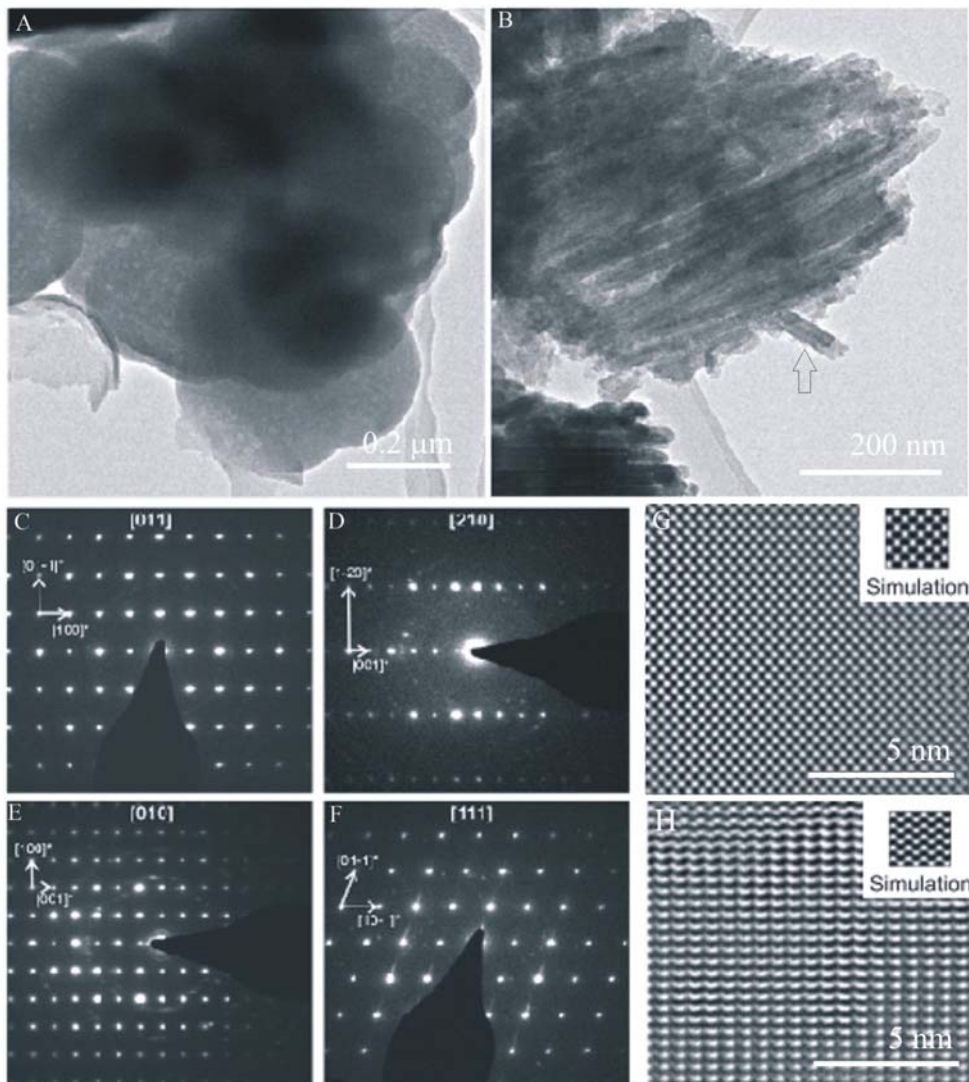


Figure 6.17 (A) TEM image of an amorphous silica particle with spherulitic morphology. (B) Densely packed nanometer sized aragonite needles and (C–F) the corresponding SAED diffraction patterns of a single needle (see arrow), and (G) HRTEM image (zone axis $[101]$) with simulated micrograph ($\Delta f = 0$ nm, thickness: 2.8 nm) and (H) HRTEM image (zone axis $[011]$) with simulated micrograph ($\Delta f = 10$ nm, thickness: 2.8 nm).

These EDX, XRD, FTIR and TEM results all confirm that these extraordinary structures are composed of calcium carbonate minerals in the form of an aragonite phase and a ‘silica matrix’.

6.2.3.6. Morphogenesis of ‘Coralline’ Particles

To get more information about the self-assembly process of ‘coralline’ silica calcium carbonate, we have monitored the morphological evolution of the clusters (see Figure 6.18) for up to 6 h. In these experiments, the reaction was stopped at different time intervals (every 30 min during 6 h). During the first two hours no ‘coralline’ particles could be detected, but between 2 h and 3 h *isotropic* skeletal architectures were seen between crossed polarizers. We note that the ‘coralline’ shapes obtained after 6 h are *anisotropic* composites due to the presence of aragonite in the structure (Figure 6.11 F). This difference in isotropy could be due to the thickness of the whole aggregate or to the presence of a (metastable) amorphous calcium carbonate.

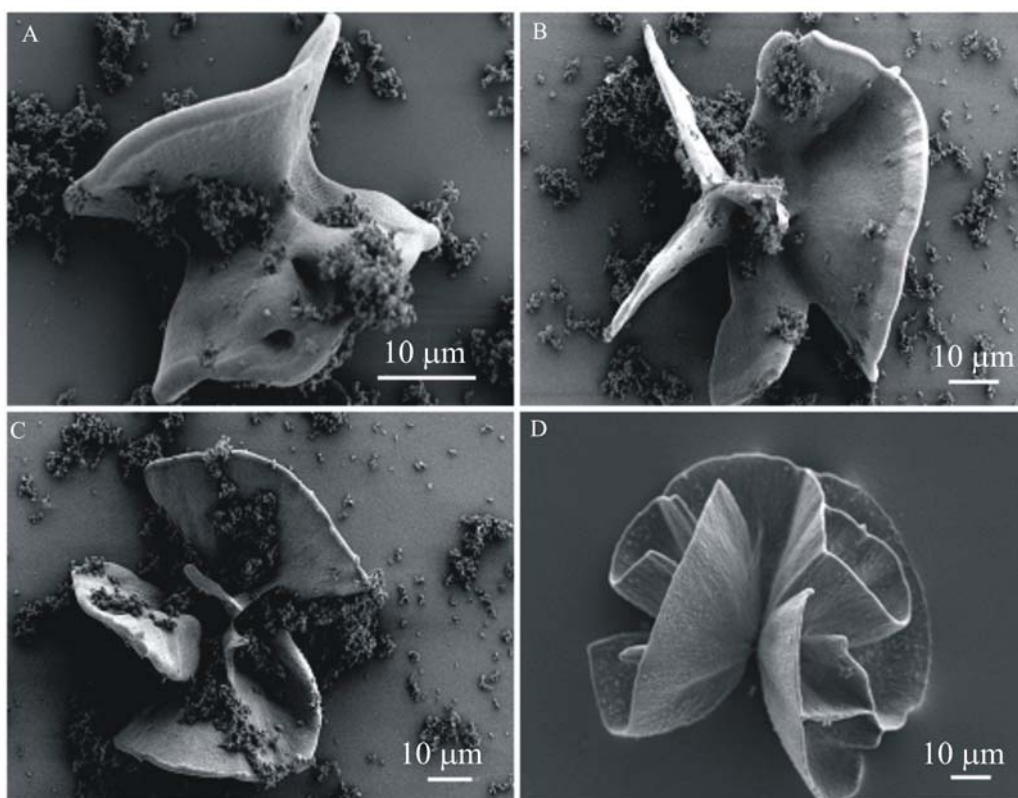


Figure 6.18 FESEM images of distinct self-assembled silica-calcium carbonate aggregates. The enhanced folding from A to D demonstrates the morphological evolution with time seen in some particles, although these images are not a time series of a single particle.

The *isotropic* self-assembled silica calcium carbonate clusters, collected in the early stages of the precipitation, occasionally present double layer surfaces (Figure 6.19). The external

and internal (i.e., the surface between the double layer) surface textures of the particles are identical, and both show striations on the surface. During outgrowth, we assume that either these double layer sheets develop into opened conical subunits or they collapse to form one layer.

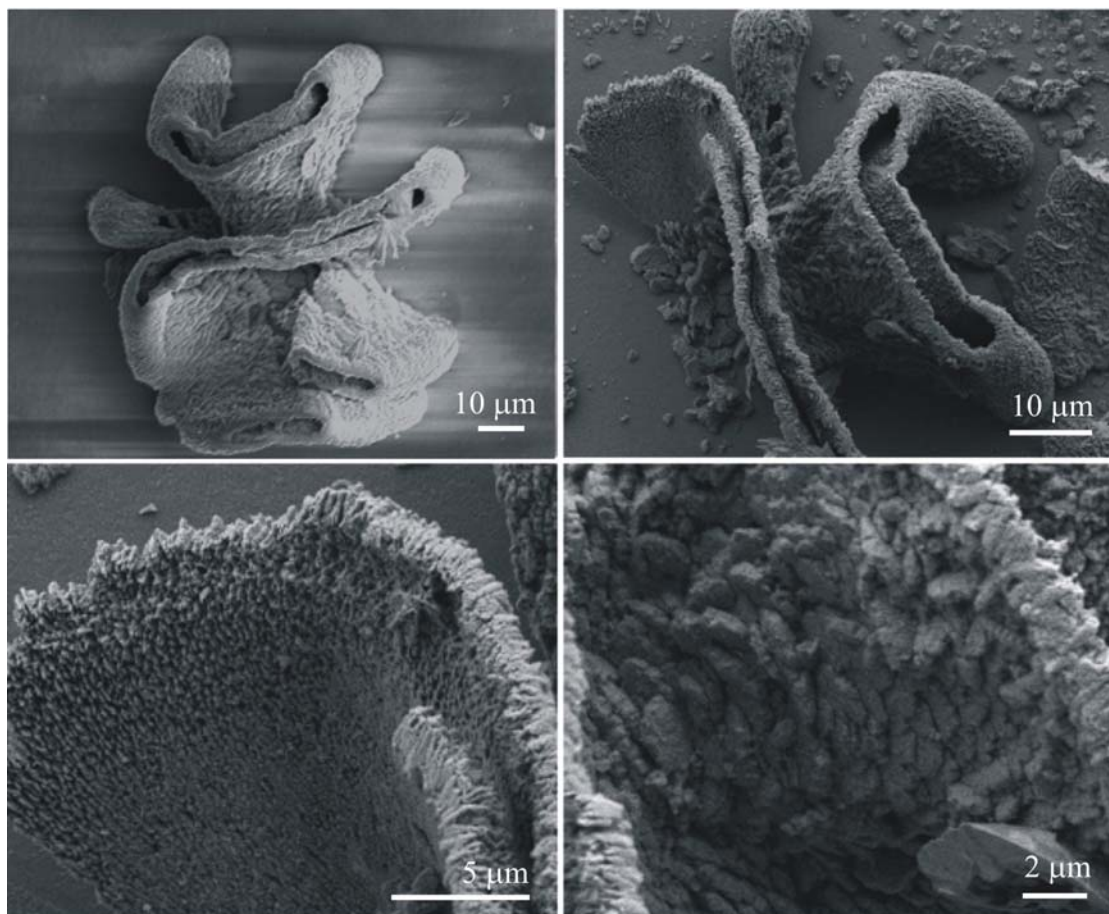


Figure 6.19 SEM images of self-assembled 'coralline' silica calcium carbonate collected after 3 h showing the surface texture of the particle.

6.2.4. Discussion

Biomorph syntheses were attempted in alkaline silica sols prepared by hydrolysis of tetraethyl orthosilicate (TEOS) over a range of temperatures. The addition of $CaCl_2$ and subsequent diffusion of atmospheric CO_2 into the solution results in the formation of carbonate. Experiments done at ambient temperature and pressure resulted mainly in calcite and failed to form biomorphs²⁶. Although Ca^{2+} is somewhat large for a 6-fold coordination (calcite) by oxygen atoms, it is relatively small for a 9-fold coordination

(aragonite) at room temperature. Thus, the rate of transition from calcite to aragonite is a function of pressure and temperature²⁷. Previous work²⁸ has shown that the relative abundance of calcium carbonate polymorphs is strongly influenced by the precipitation temperature; the higher the experimental temperature is, the easier is the formation of aragonite, due to enhanced kinetic stability. Therefore, because the aragonite structure seems to be crucial for biomorph formation¹, the experiments were performed at elevated temperature (80 °C).

Experiments conducted at this temperature furnished complex self-assembled aggregates of silica-calcium carbonate, structured at three distinct length scales (atomic, meso and micrometer scale), namely ‘coralline’ particles (Figures 6.10 B). Such hierarchical building principles are well known from biominerals produced by various kinds of creatures, such as nacre. These calcium biomorphs do not display the structural variety found in their barium counterparts; in particular we have been unable to detect twisted filaments^{1, 2}. We note that precipitates grown under identical conditions in the absence of silica are conventional aragonite crystals (Figure 6.10 A) and euhedral rhombohedral calcite.

The initial stage of these non-crystallographic particles is a ‘metal-silica matrix’ in a colloidal state. The formation mechanism of this metal-silica matrix is, we think, the following. The Ca^{2+} ions are initially complexed with anionic silica oligomers in the solution. As the pH drops, the molecular mass of silica oligomers increases as they cross-link, building the matrix. During this condensation process, the silica charge becomes less negative, due to cross-linking. Over time, the solution becomes supersaturated in carbonate species. The partially silica-bound Ca^{2+} ions from the ‘metal-silica matrix’ then combine with carbonate species and precipitate along the matrix, forming the silica-calcium carbonate composites. From our observations, it follows that these aggregates present a complex structure composed of calcium carbonate in form of an aragonite phase and a ‘silica matrix’.

The SEM images suggest that the ‘coralline’ clusters accreted from cores resembling hyperbolic (‘saddles’²⁹) domains (Figure 6.18 A), followed by outgrowth to developable surfaces (‘hats’³⁰) perfectly recognized in Figure 6.18 D. A developable surface is a ruled surface having Gaussian curvature zero everywhere. Developable surfaces are among the ‘ruled’ surfaces, i.e., surfaces generated by displacement of a straight line along a space curve (the ‘generatrix’). The linear generatrices seem more or less evident in Figure 6.18

D. When these lines are adjacent to the particle center (i.e., the oldest site) they curve gently, following a principal direction demarking the curves of minimal curvature on the directions of these generatrices (Figure 6.11 A and 6.18 D), or their curved extrapolations in the neighbourhood of the center (Figure 6.18 D). Clear lines are visible in Figure 6.11 A, normal to the generatrices reminiscent of striations that are seen in some shells in certain corals and in numerous crystals that grow by accretion.

There are some indications that the outer edges of the systems are slightly thickened (Figure 6.11 A), avoiding excessive curvatures, which are energetically costly, and that the boundaries are rather weakly consolidated.

The complex ternary structure (mineral *Ca*-carbonate, organic matrix and water³¹) which constitutes natural corals, are found also in biomorphs but with a fundamental distinction. Biomorphs are composed exclusively of inorganic matter. Nevertheless, the inorganic silica skeleton of the self-organised silica-calcium carbonate biomorphs seems to behave similarly to the organic skeleton of natural corals.

6.2.5. Conclusions

Self-assembled silica calcium carbonate biomorphs were successfully grown in alkaline silica solutions prepared at 20 °C and warmed at 80 °C for 6 h, to induce the formation of aragonite. These striking, hierarchically structured morphologies composed of curved sheet-like structures consist of orientationally ordered, nanometer-sized aragonite crystallites. The ‘coralline’ clusters were seeded from hyperbolic (‘saddles’) domains, followed by further growth to form coalesced developable surfaces (‘hats’). Two combined mechanisms lead to the formation of these ‘coralline’ self-assembled silica-calcium carbonate. First, the building process in solution of ‘metal-silica matrix’, which is composed of calcium ions and silica oligomers. Second, the transport of carbonates ions (in the case of calcification process) to the mineralizing sites.

6.2.6. References

- (1) García-Ruiz, J. M.; Hyde, S. T.; Carnerup, A. M.; Christy, A. G.; Van Kranendonk, M. J.; Welham, N. J. *Science* **2003**, *302*, 1194.

- (2) García-Ruiz, J. M.; Carnerup, A. M.; Christy, A. G.; Welham, N. J.; Hyde, S. T. *Astrobiology* **2002**, 2 (3), 353.
- (3) Mann, S. *Biom mineralization: Principles and Concepts in Bioinorganic Materials Chemistry*, Oxford University Press: Oxford, 2001.
- (4) Weiner, S.; Addadi, L. *J. Mater. Chem.* **1997**, 7 (5), 689.
- (5) García-Ruiz, J. M. *J. Cryst. Growth* **1985**, 73 (2), 251.
- (6) Dominguez Bella, S.; Garcia Ruiz, J. M. *J. Cryst. Growth* **1986**, 79 (1-3), 236.
- (7) Dominguez Bella, S.; Garcia Ruiz, J. M. *J. Mater. Sci.* **1987**, 22 (9), 3095.
- (8) Imai, H.; Terada, T.; Miura, T., Yamabi, S. *J. Cryst. Growth* **2002**, 244, 200.
- (9) Gower, L. A.; Tirrell, D. A. *J. Cryst. Growth* **1998**, 191, 153.
- (10) Wang, L.; Sondi, I.; Matijevic, E. *J. Colloid Interface Sci.* **1999**, 218, 545.
- (11) Kulak, A. N.; Iddon, P.; Li, Y.; Armes, S. P.; Coelfen, H.; Paris, O.; Wilson, R. N.; Meldrum, F. C. *J. Am. Chem. Soc.* **2007**, 129(12), 3729.
- (12) Walsh, D. and Mann, S. *Nature* **1995**, 377, 320.
- (13) Mann, S. *Angew. Chem. Int. Ed.* **2000**, 39, 3392.
- (14) Gao, Y.; Yu, S.; Cong, H.; Jiang, J.; Xu, A.; Dong, W.; Cölfen, H. *J. Phys. Chem. B* **2006**, 110 (13), 6432.
- (15) Cölfen, H. *Top. Curr. Chem.* **2007**, 271, 1.
- (16) Meldrum, F. C. *Handbook of Biom mineralization: Biomimetic and Bioinspired Chemistry*, Wiley-VCH: Weinheim, 2007.
- (17) Iler, R. K. *The Chemistry of Silica: Solubility, Polymerisation, Colloid and Surface Properties, and Biochemistry*, Wiley-Interscience, New York, 1979.
- (18) Yu, J.; Lei, M.; Cheng, B.; Zhao, X. *J. Cryst. Growth* **2004**, 261, 566.
- (19) Stadelmann, P. A. *Ultramicroscopy* **1987**, 21, 131.
- (20) Voinescu, A. E.; Kellermeier, M.; Carnerup A. M.; Larsson, A. K.; Touraud, D.; Hyde, S. T.; Kunz, W. *J. Cryst. Growth* **2007**, 306, 152.
- (21) Terada, T.; Yamabi, S.; Imai, H. *J. Cryst. Growth* **2003**, 353, 435.
- (22) Hyde, S. T.; Carnerup, A. M.; Larson, A. K.; Christy, A. G.; García-Ruiz, J. M. *Physica A* **2004**, 339, 24.
- (23) Falini, G.; Albeck, S.; Weiner, S.; Addadi, L. *Science* **1996**, 271, 67.
- (24) Anderson, F. A.; Brecevic, L. *Acta Chem. Scand.* **1991**, 45, 1018.
- (25) Martinez, J. R.; Ruiz, F.; Vorobiev Y. V. *J. Chem. Phys.* **1998**, 109, 751.
- (26) Imai, H.; Terada, T.; Yamabi, S. *Chem. Commun.* **2003**, 4, 484.
- (27) Klein, C; Hurlbut, C. S. *Manual of Mineralogy*, Wiley: New York, 1993.

-
- (28) Zhou, G. T.; Zheng, Y. F. *J. Mater. Sci. Lett.* **1998**, *17*, 905.
- (29) Bouligand, Y. *Liq. Cryst.*, **1999**, *26(4)*, 501.
- (30) Bouligand, Y. *J. Phys. (Paris)* **1980**, *41*, 1297.
- (31) Dauphin, Y.; Cuif, J. P.; Massard, P. *Chem. Geol.* **2006**, *231*, 26.

6.3. Why Calcium Ions Behave so Different from its Homologue, Barium, in Alkaline Silica Sol?

6.3.1. Introduction

Silica (SiO_2), the major component of the earth's surfaces, is found as a three dimensional polymer in both crystalline and amorphous forms. Soluble silica in water is initially in monomeric state as monosilicic acid ($Si(OH)_4$) and is mostly un-ionised at natural pH values. As pH increases, the degree of ionization also increases; at pH of 8.5 only 10% of the monosilicic acid is ionised, while as the pH reaches 10, 50% is ionised¹. Concomitantly, partial ionization initiates and favours the polymerisation of monosilicic acid. High degree of ionization (pH 11) prevents polymerisation and promotes formation of negatively charged species. However, even at this pH value the silica aggregation can be induced by the addition of coagulating ions^{2,3}, such as Ba^{2+} , Sr^{2+} , Ca^{2+} and Mg^{2+} .

As advanced hereinbefore (Section 6.1), silica biomorphs of barium and strontium carbonate easily form in silica rich solution at ambient temperature (20 °C) and pH ~11. They display non-crystallographic morphologies with positive or negative Gaussian curvature, leading to biomimetic morphologies, such as coral-like or helicoidal morphologies that mimic primordial filamentous Precambrian microfossils. Such structures can serve as models for the complex and often hardly accessible natural archetypes with the possibility to reveal principles of complex hierarchical structure formation. Therefore, the extension of the realm of biomorphs to calcium carbonate is an important step since $CaCO_3$ is the most abundant in biominerals. Up to now, silica biomorphs of barium and strontium carbonates have been fabricated only when the carbonates crystallize with the aragonite-type configuration, while when calcium carbonate was precipitated under the same conditions, not the aragonite-type but the more stable calcite form occurs. The global morphologies of these calcite-based silica-calcium carbonate have the memory of the crystallographic point symmetry of the calcite crystal structure. However, as described in the previous subheading of this chapter, increasing the temperature growth to 80 °C and keeping the other parameters constant, the resulting crystals display coral-like morphologies with structural similarity to previously studied barium and strontium carbonates, but the helicoidal morphologies – the most outstanding features of barium or

strontium carbonate silica biomorphs – were never achieved. Notoriously, the key question is why the inorganic hybrid structures with a helical morphology formation do not occur when calcium ions are used? In the following we will try to provide a reasonable explanation to this task.

6.3.2. Experimental Section

6.3.2.1. Materials Preparation

Tetraethylorthosilicate (TEOS, purity >98%), silicon dioxide (SiO_2 purity, 99.9%) calcium chloride dihydrate ($CaCl_2 \cdot 2H_2O$, purity >99%), barium chloride dehydrate ($BaCl_2 \cdot 2H_2O$, purity >99%), strontium chloride hexahydrate ($SrCl_2 \cdot 6H_2O$, purity 99%), magnesium chloride hexahydrate ($MgCl_2 \cdot 6H_2O$, purity 99%), sodium hydroxide ($NaOH$, purity 99%) as well as cetyltrimethylammonium bromide (CTAB), sodium dodecylbenzenesulfonate (SDBS), lysosyme (purity 95%, IP = 11.35) and ethylenediaminetetraacetic acid disodium salt dihydrate (EDTA) were purchased from Sigma-Aldrich. Lupasol WF was supplied by BASF. D (+)-glucose monohydrate and D (-)-fructose were supplied by Merck. Casein technical grade (pI = 4.7) and α -D-lactose were supplied by Lancaster. All chemicals were used as received. Ethanol (EtOH) was purchased from J. T. Baker. Purified water with an electrical conductivity of less than $10^{-6} \text{ S} \cdot \text{m}^{-1}$ was taken from a Milli-Q system.

I. Attempts to prepare filamentous particles of self-organised silica-calcium carbonate without using any type of additives.

The analyses were carried out by using the procedure as described in Chapter 5 with some differences. Herein, the temperature and the pH of the system as well as the TEOS, EtOH, and $CaCl_2$ concentration were varied in five different experiment series indicated in *Table 6.1*.

Table 6.1 The experimental series.

Series	T_1 °C	T_2 °C	t h	C_{TEOS} mM	C_{EtOH} %	pH	C_{CaCl_2} mM
(1)	20	20	24	7.6	0.17	9 to 12	2.5 to 10
(2)	20	40	15	7.6	0.17	11	7.5
(3)	20	80	6	0 to 15	0.17 to 40	9 to 12	2 to 20
(4)	80	80	6	7.6	0.17	11	2 to 10
(5)	5	20	24	7.6	0.17	11	2 to 10

Abbreviations:

T_1 the temperature at which the alkaline TEOS solution is hydrolysed;

T_2 the temperature of the growth period;

t the time of the growth period;

pH the pH values cited are the adjusted values of the alkaline silica solution before adding Ca^{2+} ions.

II. Attempts to prepare filamentous particles of self-organised silica-calcium carbonate using additives.

Figure 6.20 shows the used organic and inorganic additives.

a. *The precipitation of silica-calcium carbonate particles in the presence of the additives (1)–(4).* These additives were supposed to induce the aragonite structure of calcium carbonate at ambient temperature (20 °C). Barium and magnesium chloride were separately dissolved in calcium electrolyte solutions and subsequently added into the alkaline silica solution. Both surfactants were first dissolved in water at 50 °C. Afterwards, the TEOS hydrolysis was performed in the cooled aqueous surfactant solutions. Table 6.2 shows the additive concentration as well as the calcium chloride concentration present in the silica solution for each test.

b. *The precipitation of silica-calcium carbonate particles in the presence of sugars.* Sugar molecules have a large amount of polar hydroxyl groups. Therefore, they are supposed to be able to interact with calcium carbonate particles and thereby sugar molecules may show an influence in nucleation and crystal growth. Table 6.3 shows the sugar concentrations as well as the calcium chloride concentration present in the silica solution for each experiment performed.

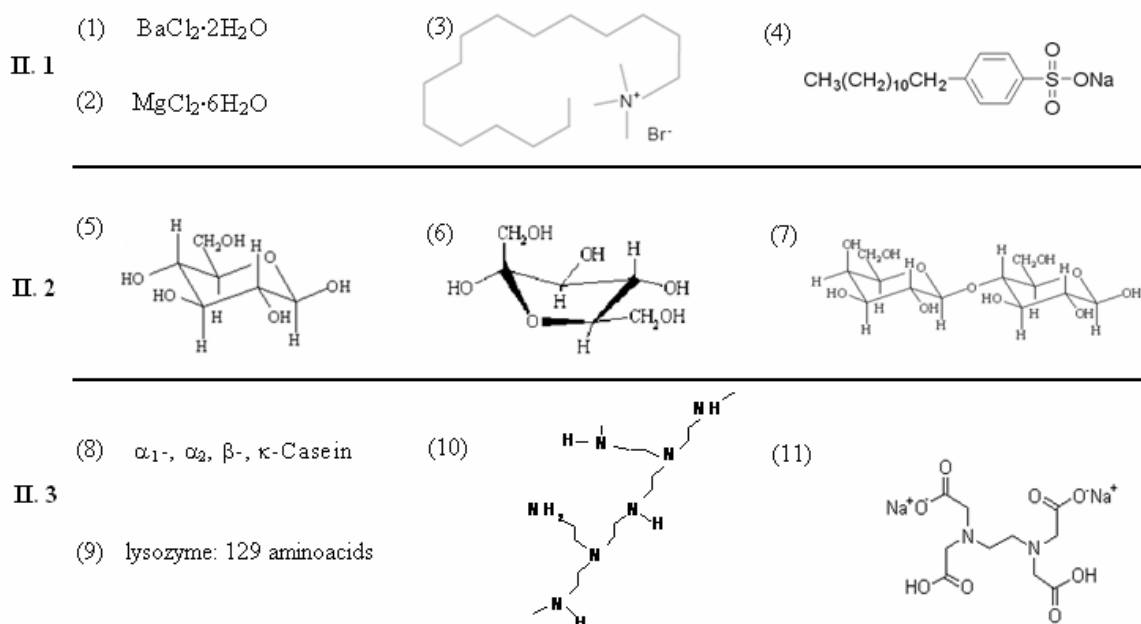


Figure 6.20 The additives used in the precipitation of silica-calcium carbonate particles. (1) barium chloride dehydrate ($BaCl_2 \cdot 2H_2O$, $M_w = 244.27$ g/mol); (2) magnesium chloride hexahydrate ($MgCl_2 \cdot 6H_2O$, $M_w = 203.30$ g/mol); (3) cetyltrimethylammonium bromide (CTAB, $M_w = 364.45$ g/mol); (4) sodium dodecylbenzenesulfonate (SDBS, $M_w = 348.48$ g/mol); (5) β -D-glucose ($C_6H_{12}O_6$, $M_w = 180.16$ g/mol); (6) β -D-fructose ($C_6H_{12}O_6$, $M_w = 180.16$ g/mol); (7) β -D-lactose ($C_{12}H_{22}O_{11}$, $M_w = 342.30$ g/mol); (8) casein ($M_w =$ not determined); (9) lysozyme ($M_w = 14$ kDa); (10) lupasol WF ($M_w = 25$ kDa); and (11) ethylenediaminetetraacetic acid disodium salt dihydrate (EDTA, $M_w = 372.24$ g/mol).

c. *The precipitation of silica-calcium carbonate particles in the presence of the additives (8) – (11).* These additives, known as calcium sponge molecules, remove the calcium cations from the bulk and, thus, the coagulation of silica particle by calcium cations could be avoided. For this reason, these additives were separately dissolved in calcium electrolyte solutions and subsequently added into the alkaline TEOS solution.

The influence of casein on the precipitation of silica-calcium carbonate particles is characterised in detail in Chapter 5. Lysozyme is known to attract calcium ions and to create a local distribution of calcium ions (see Chapter 4) which can play the role of calcium carbonate nucleation sites. Lupasol WF is a polyethylenimine with primary, secondary and tertiary amine functions. Its solution is isotropic, having a pH of 10.6.

Table 6.3 The Ca^{2+} and sugar concentrations in the alkaline silica solution (TEOS 7.6 mM; EtOH 0.17 mM; pH 11; $T_1 = 20\text{ }^\circ\text{C}$). The temperature, T_2 , at which the growth period takes place, is $20\text{ }^\circ\text{C}$ or $40\text{ }^\circ\text{C}$.

C_{CaCl_2} mM	Sample code	$C_{glucose}$ mM	Sample code	$C_{fructose}$ mM	Sample code	$C_{lactose}$ mM
7	M ₁₂₁	0.001	M ₁₃₃	0.001	M ₁₄₅	0.001
7	M ₁₂₂	0.005	M ₁₃₄	0.005	M ₁₄₆	0.005
7	M ₁₂₃	0.01	M ₁₃₅	0.01	M ₁₄₇	0.01
7	M ₁₂₄	0.05	M ₁₃₆	0.05	M ₁₄₈	0.05
7	M ₁₂₅	0.1	M ₁₃₇	0.1	M ₁₄₉	0.1
7	M ₁₂₆	1	M ₁₃₈	1	M ₁₅₀	1
2.5	M ₁₂₇	0.001	M ₁₃₉	0.001	M ₁₅₁	0.001
2.5	M ₁₂₈	0.005	M ₁₄₀	0.005	M ₁₅₂	0.005
2.5	M ₁₂₉	0.01	M ₁₄₁	0.01	M ₁₅₃	0.01
2.5	M ₁₃₀	0.05	M ₁₄₂	0.05	M ₁₅₄	0.05
2.5	M ₁₃₁	0.1	M ₁₄₃	0.1	M ₁₅₅	0.1
2.5	M ₁₃₂	1	M ₁₄₄	1	M ₁₅₆	1

Table 6.4 Lysozyme and lupasol WF concentrations in the alkaline TEOS sols (TEOS 7.6 mM; EtOH 0.17 mM; $T_1 = 20$ °C) as well as the temperature at which the growth period take place. The pH values cited are the adjusted values of the alkaline silica solution before adding the Ca^{2+} ions.

<i>Sample code</i>	C_{CaCl_2} mM	$C_{lysozyme}$ g/L	<i>pH</i>	T_2 °C	<i>Sample code</i>	C_{CaCl_2} mM	$C_{lupasol}$ g/L	<i>pH</i>	T_2 °C
M₆₅	7	0.5	10.93	20/40	M₇₉	7	0	11.11	40
M₆₆	7	0.1	11.09	20/40	M₈₀	7	1	11.03	40
M₆₇	7	0.2	11.05	20/40	M₈₁	7	2	10.95	40
M₆₈	7	0.5	10.91	20/40	M₈₂	7	3	11.03	40
M₆₉	7	1	11.02	20/40	M₈₃	7	4	10.89	40
M₇₀	7	2	10.98	20/40	M₈₄	7	5	11.00	40
M₇₁	7	0.5	10.66	20/40	M₈₅	7	6	11.06	40
M₇₂	7	0.5	11.54	20/40	M₈₆	2.5	7	11.02	40
M₇₃	7	0.5	12.03	20/40	M₈₇	2.5	5	10.99	40
M₇₄	7	0.5	12.42	20/40	M₈₈	2.5	5	10.88	40
M₇₅	7	0.7	10.68	20/40	M₈₉	2.5	5	10.96	40
M₇₆	7	0.7	11.40	20/40	M₉₀	2.5	5	11.01	40
M₇₇	7	0.7	11.89	20/40	M₉₁	2.5	5	11.00	40
M₇₈	7	0.7	12.33	20/40	M₉₂	2.5	5	11.12	40

Table 6.5 The CaCl_2 and EDTA concentrations in the alkaline silica sols (TEOS 7.6 mM; EtOH 0.17 mM; $T_1 = 20\text{ }^\circ\text{C}$) as well as the temperature at which the growth period take place.

<i>Sample code</i>	C_{CaCl_2} <i>mM</i>	C_{EDTA} <i>mM</i>	T_2 $^\circ\text{C}$	<i>Sample code</i>	C_{CaCl_2} <i>mM</i>	C_{EDTA} <i>mM</i>	T_2 $^\circ\text{C}$
M₉₃	5	0.17	20/80	M₁₀₇	8.5	0.17	20/80
M₉₄	5	0.5	20/80	M₁₀₈	8.5	0.5	20/80
M₉₅	5	1	20/80	M₁₀₉	8.5	1	20/80
M₉₆	5	1.7	20/80	M₁₁₀	8.5	1.7	20/80
M₉₇	5	2.5	20/80	M₁₁₁	8.5	2.5	20/80
M₉₈	5	5	20/80	M₁₁₂	8.5	5	20/80
M₉₉	5	7	20/80	M₁₁₃	8.5	7	20/80
M₁₀₀	5	10	20/80	M₁₁₄	8.5	10	20/80
M₁₀₁	5	20	20/80	M₁₁₅	8.5	20	20/80
M₁₀₂	5	30	20/80	M₁₁₆	8.5	30	20/80
M₁₀₃	5	0.7	20/80	M₁₁₇	8.5	0.7	20/80
M₁₀₄	5	0.7	20/80	M₁₁₈	8.5	0.7	20/80
M₁₀₅	5	0.7	20/80	M₁₁₉	8.5	0.7	20/80
M₁₀₆	5	0.7	20/80	M₁₂₀	8.5	0.7	20/80

6.3.2.2. Analytical Methods

pH of the TEOS hydrolysed solutions before and after the addition of calcium chloride solution were measured using an *Ag/AgCl* plastic-body electrode (TPS, Model smartCHEM-Laboratory).

Particle size. *Dynamic Light Scattering (DLS)* measurements were made using a Zetasizer spectrometer (Malvern Instruments Ltd., Model Z3000) equipped with a 5 mW *He-Ne* laser. *Light microscopy* was performed using a Nikon transmission microscope (Model Eclipse E400), images were taken between cross polarizers and produced with the help of a JVC CCD colour video camera (Model TKC1380). *Field-emission scanning electron microscopy (FESEM)* was performed using a microscope (Hitachi, Model S4500) operating at 0.5–30 kV. The samples were coated with *Au/Pd* in an Emitech sputter coater using a rotational stage. *Scanning electron microscopy (SEM)* was performed either using a microscope FEI Quanta 400 or Jeol JSM 840, both operating at 0.2–30 kV. The sample was coated with *Au* in an Polaron Equipment LTD sputter coater.

Crystal Polymorphism. *Fourier transform infrared spectroscopy (FTIR)* was recorded on a Jasco FTIR–610 spectrometer. The spectrum was recorded in reflection mode from 4000 to 400 cm^{-1} at a resolution of 2 cm^{-1} . *X-ray diffraction (XRD)* measurements were done using a STOE STADI P diffractometer (STOE & CIE) providing *Cu K α 1* radiation monochromated with a germanium single crystal ($\lambda = 1.540598 \text{ \AA}$).

6.3.3. Results

As stated in the Section 6.1, the addition of Ba^{2+} ions to an alkaline TEOS solution at pH 11 and ambient temperature (25 °C), led to the formation of helicoidal microfilaments (Figure 6.21 A). These complex aggregates have morphologies very similar to modern cyanobacteria. Attempts to achieve these extraordinary structures, using Ca^{2+} ions instead of Ba^{2+} ions, were done by García-Ruiz et al.⁴, who reported that ‘the metal ions of carbonate salts tested, that crystallize in the calcite structure (*Ca*, *Mg*, *Cd*), fail to give similar behaviour’ with barium. Later on, Terada et al.⁵ stated also that ‘although the CaCO_3 system provided porous projections consisting of platy aragonite (Figure 2.20 D), sheets composed of fibrous subunits were achieved only in the SrCO_3 or BaCO_3 system’.

Additionally, Kellermeier⁶ found this ‘task to be nontrivial’. For this reason, attempts to achieve these spiral shapes with calcium have been done also in this work. The results are described in the following.

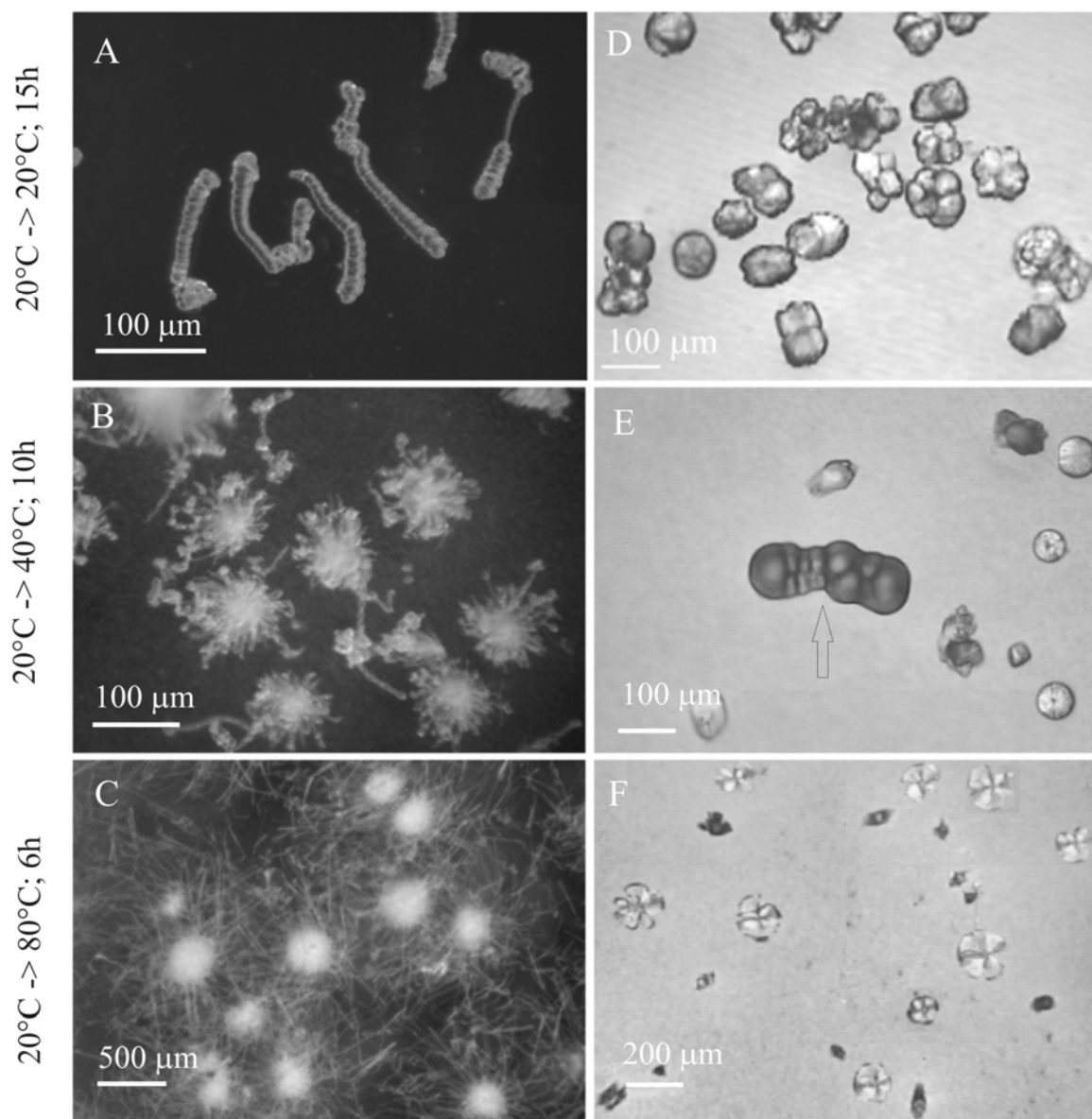


Figure 6.21 Optical micrographs of silica-barium carbonate (A–C) and silica-calcium carbonate (D–F) particles obtained when the growth temperatures were 20, 40 and 80 °C, respectively. The hydrolysis of TEOS was carried out at 20 °C. [TEOS] = 7.6 mM; [Ba²⁺] = [Ca²⁺] = 6 mM; pH = 11.

6.3.3.1. Attempts to Prepare Filamentous Particles of Self-Organised Silica-Calcium Carbonate without using any type of Additives

Immediately after mixing the alkaline silica solution with the Ca^{2+} solution, all mixtures, except for concentrations lower than 2.5 mM Ca^{2+} , become cloudy and the turbidity intensifies with increasing $CaCl_2$, TEOS and EtOH concentration. As a consequence, the initially adjusted pH value of the alkaline TEOS solution declines. Seconds later, fluffy material precipitates from the solution. Comparable silica- Ba^{2+} solutions are more or less transparent.

a. $T_1 = 20\text{ }^\circ\text{C}$; $T_2 = 20\text{ }^\circ\text{C}$

The experiments performed at ambient temperature (both hydrolysis of TEOS and the growth of crystals) and varying the other parameter results mainly in modified rhombohedra crystals (Figure 6.21 D) contaminated by bundles of aligned fibers. Simultaneously, quite a lot of fluffy material precipitates too. Furthermore, the initially pH values decline for ~ 0.2 units. The corresponding XRD spectrum (Figure 6.22) exhibits characteristic reflections of calcite (C_{104} , the dominant phase) and aragonite (A_{221}). Such experiments have been done at ambient temperature also by Imai et al.⁷, resulting in deformed calcite particles, where the regular rhombohedra of calcite was transformed into the self similar structure consisting of three pointed stars with specific absorption of silicate anions. Similar experiments performed with barium results in helical filament composites⁸ (Figure 6.21 A) consisting of intimate intergrowths of witherite and amorphous silica⁹.

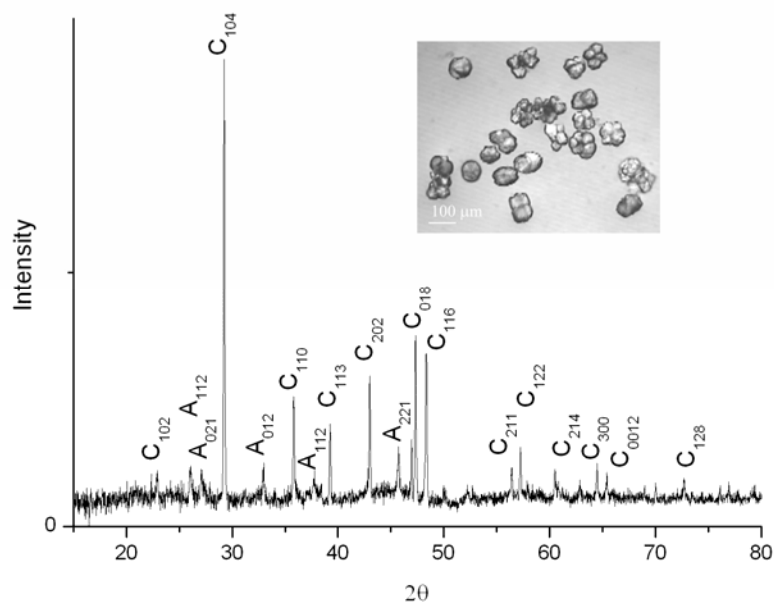


Figure 6.22 XRD spectrum of the CaCO_3 crystals synthesized from alkaline silica solution. $[\text{TEOS}] = 7.5 \text{ mM}$, $[\text{Ca}^{2+}] = 6 \text{ mM}$, $\text{pH} = 11$, $T = 20 \text{ }^\circ\text{C}$, $t = 24 \text{ h}$.

b. $T_1 = 20 \text{ }^\circ\text{C}$; $T_2 = 40 \text{ }^\circ\text{C}$

Since silica biomorphs of barium carbonates have been fabricated only when the carbonates crystallize with the aragonite-type configuration, in the following, we have encouraged the precipitation of aragonite form of calcium carbonate by conducting the crystal growth at $40 \text{ }^\circ\text{C}$. In this case, after 10 hours in contact with atmospheric CO_2 , distinct calcium carbonate crystal morphologies (Figure 6.21 E), including deformed rhombohedra (i.e., calcite) and spheroids (i.e., aragonite, Figure 6.23) have precipitated. It is worth to notify that similar globular shapes arise also when barium carbonate is precipitated in silica-rich solution¹⁰ at $\text{pH} 10$. In both cases, these shapes are made up of a radiating array of crystalline fibres that branch at non-crystallographic angles with continuous bending of crystal surfaces after bifurcation¹⁰. Surprisingly, we have detected also the presence of filaments (Figure 6.21 E, see arrow), which at first view are somehow similar to barium biomorphs (Figure 6.21 A). However, the SEM image shows that these forms (Figure 6.24) do not resemble the dual composite of helical biomorphs. Apparently, these clusters are composed of interconnected spheres consisting of needles. We note that the number of such clusters found in the reaction medium is very low ($\sim 2\%$).

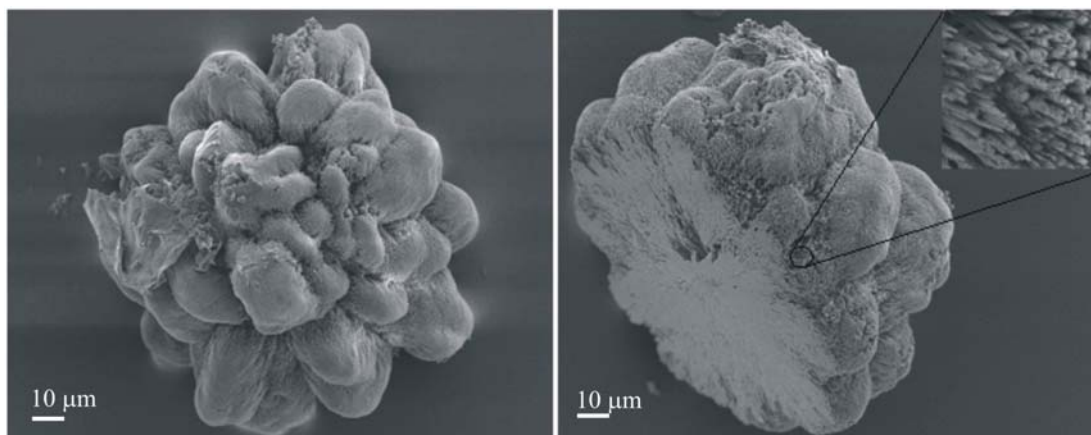


Figure 6.23 (A) Globules with non-linear swelling obtained at pH 10.5 to 10.8.

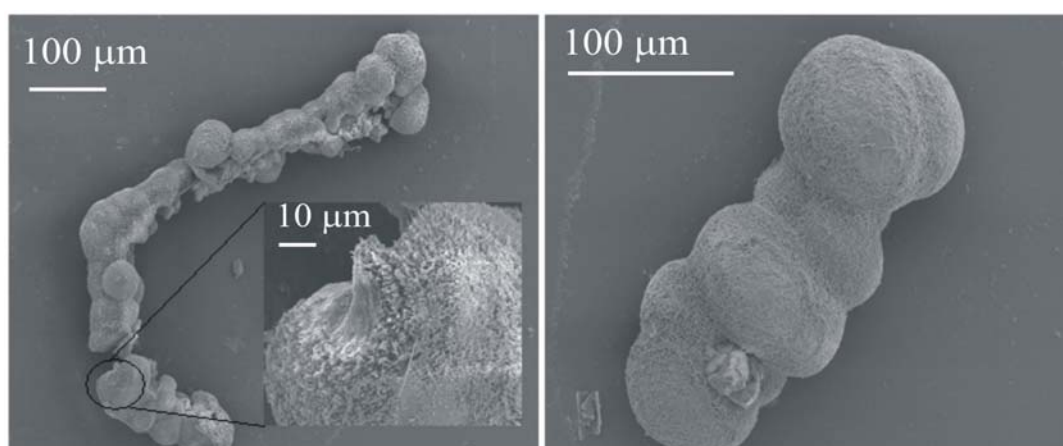


Figure 6.24 SEM images of self-organised silica-calcium carbonate clusters obtained when the crystal growth process is conducted at 40 °C.

c. $T_1 = 20\text{ °C}$; $T_2 = 80\text{ °C}$

Increasing the temperature of the growth process to 80 °C, results, besides other distinct CaCO_3 crystal morphologies, in the formation of coralline self-assembled silica-calcium carbonate particles (Figure 6.21 F), which bear a striking resemblance to natural coral forms. These materials, described in detail in Section 6.2, have a complex ultrastructure, made of clusters of gathered sheets of variable curvatures formed by successive curling. The nanocrystals within these ‘ruled surfaces’ are thin, elongated, densely packed needles of aragonite. Comparable experiments with barium lead to the formation of aggregates of an overall spherical shape (Figure 6.21 C and Figure 6.25). So, even in the case of barium, the increase of the temperature does not favour the formation of the filamentous particles.

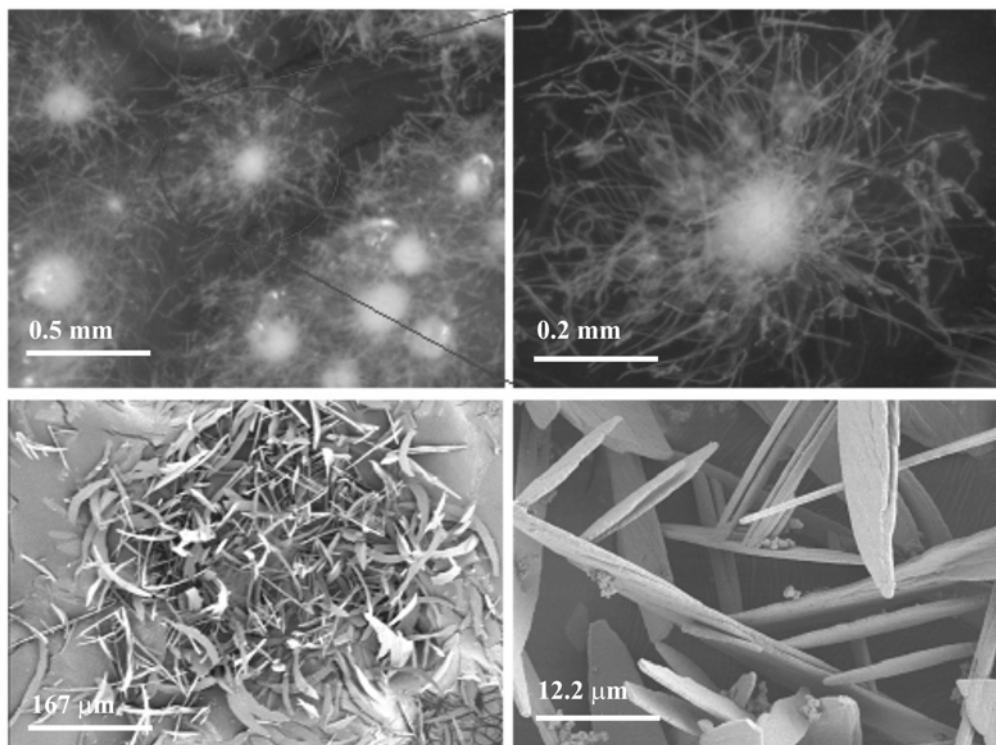


Figure 6.25 Optical and SEM micrographs of silica-calcium carbonate clusters obtained when the crystal growth process is conducted at 80 °C.

d. $T_1 = 80\text{ °C}$; $T_2 = 80\text{ °C}$

When both the TEOS hydrolysis and the crystallization process are conducted at 80 °C, it results mainly in aragonite crystals (Figure 6.26). Although the aragonite form of calcium carbonate is produced, the helicoidal forms are never achieved within the investigated concentration range. Furthermore, comparable experiments with barium do not result in helicoidal forms but in typically $BaCO_3$ witherite fibres. Under these conditions, it is noticeable that as soon as the metal cations get in contact with the alkaline silica sol, the turbidity and especially immediate precipitation of fluffy material occur. As a consequences, the initial pH values decline for 0.5 units. In comparison with the experiments performed at ambient temperature, the rate of precipitation is strongly enhanced by raising the temperature. Therefore, we believe that this phenomenon impedes the formation of helicoidal filaments. In the following, efforts to avoid the precipitation of fluffy material are done by conducting the TEOS hydrolysis at 5 °C.

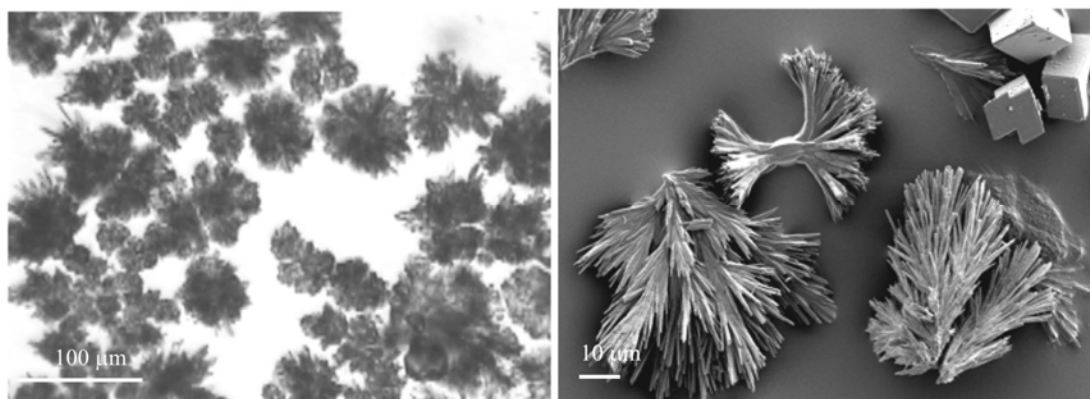


Figure 6.26 Optical and SEM images of silica-calcium carbonate clusters obtained when both TEOS hydrolysis and the growth process are performed at 80 °C.

e. $T_1 = 5\text{ °C}$; $T_2 = 20\text{ °C}$

In this experiment series, upon mixing the electrolyte salt solution with alkaline silica solution, all mixtures remain isotropic and the pH values remain almost constant. Since at this temperature the solubility of atmospheric CO_2 is very low, the crystallization process should be performed at least at 20 °C. Thus, when warming the mixtures to 20 °C, for the crystal growth, all mixtures become cloudy as soon as the temperature of 20 °C is reached. After 24 h in contact with atmospheric CO_2 at room temperature, the results are similar with the first experimental series, Section 6.3.3.1.a.

6.3.3.2. Attempts to Prepare Filamentous Particles of Self-Organised Silica-Calcium Carbonate using Additives

a. The precipitation of silica-calcium carbonate particles in the presence of the additives (1) to (4).

The alkaline earth metal ions are known to exert a significant effect on the $CaCO_3$ precipitation. When present in sufficient concentration, it generally results in the precipitation of aragonite¹¹ rather than the thermodynamical favoured phase, calcite. To induce structuring, Ba^{2+} and Mg^{2+} ions are separately mixed with calcium electrolyte solution and subsequently the resulting mixture is introduced into the alkaline silica solution. Within the investigated range, the addition of both ions does not reach our objective. Clouding and flocculation are very intensive as the Ba^{2+}/Ca^{2+} or Mg^{2+}/Ca^{2+} molar ratios exceed 1 and 0.25, respectively. It is worth to notice that when the Ba^{2+}/Ca^{2+}

molar ration is lower than 5, the filamentous spirals are not found at all. Kellermeier⁶ performed similar experiments at 60 °C and observed the same behaviour.

CTAB and SDBS surfactants are also known to induce the formation of the aragonite form of calcium carbonate, which is absolutely necessary for the formation of helical biomorphs. At CTAB concentrations lower than its CMC (critical micelle concentration, $9.2 \cdot 10^{-4}$ M)¹², the resulting particles grow as 100% perfect rhombohedra calcite (Figure 6.27 A) showing six $\{10\bar{1}4\}$ faces. At concentrations around CMC, the isolated crystals are a mixture of rhombohedra calcite and spherulitic aragonite (Figure 6.27 B). Counting the crystals in a population bigger than that shown in the micrograph of Figure 6.27 B, it comes out that the sample is composed of 66.03% calcite and 33.96% aragonite. At even higher CTAB concentrations, the aragonite particles in form of spherulitic shape become the dominant form. The sequence of progressive evolution of the spherulitic aragonitic aggregates (Figure 6.28) resembles the fluoroapatite-gelatin composites reported by Kniep et al.¹³. In addition, the turbidity of the solution is strongly dependent on its CMC. Whereas at concentrations lower than CMC, the solution are cloudy and seconds later precipitate appears, at concentration higher than CMC, the solution are more or less light bluish. Performing the growth of the crystals at 40 °C and 80 °C, distinct $CaCO_3$ habits occurs, but never filamentous biomorphs.

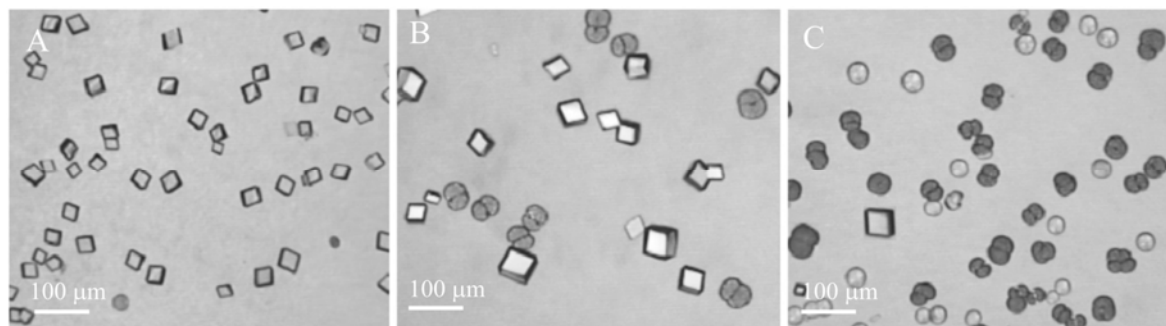


Figure 6.27 Optical micrographs of calcium carbonate particles synthesized from silica-CTAB solutions. (A) [CTAB] = 0.5 mM; (B) [CTAB] = 1 mM and (C) [CTAB] = 2 mM.

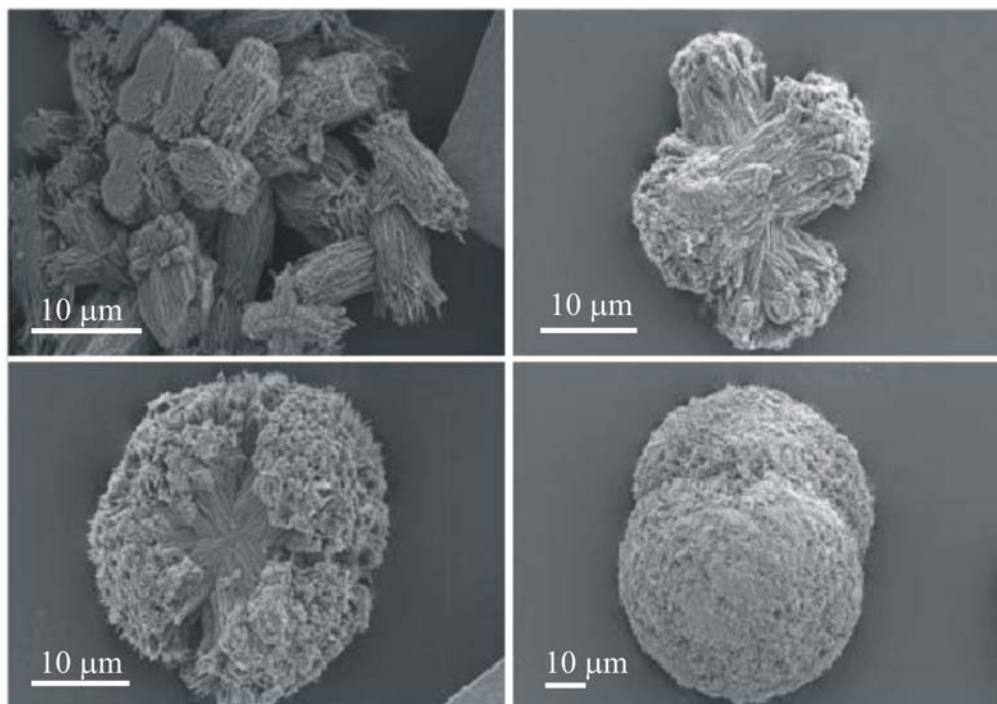


Figure 6.28 Sequence of progressive evolution of calcium carbonate aggregates precipitated from silica-CTAB solution. $[CTAB] = 3 \text{ mM}$, $[TEOS] = 7.5 \text{ mM}$, $[Ca^{2+}] = 7 \text{ mM}$, pH 11, $T_2 = 20 \text{ }^\circ\text{C}$, $t = 20 \text{ h}$.

The addition of calcium ions to a mixed silica-SDBS solution induces precipitation in the system immediately and during the crystallization process no calcium carbonate particles were obtained.

b. *The precipitation of silica-calcium carbonate particles in the presence of sugars.*

Starting from 0.01 M sugars, significant changes in morphology occur. However, filamentous particles do not form. Moreover, comparable experiments performed with barium instead of calcium ion, result in aggregates of an overall spherical shape (Figure 6.29). We remind that the addition of barium into a free sugar-silica solution furnished helicoidal filaments.

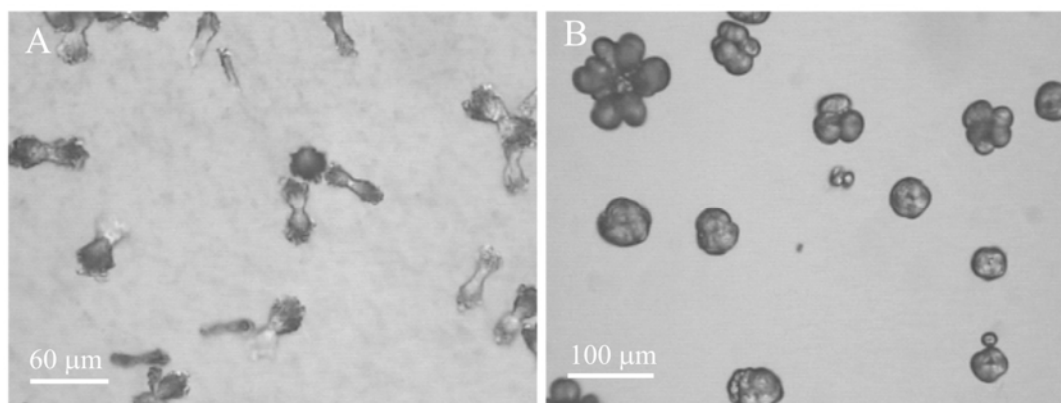


Figure 6.29 The precipitation of calcium (A) and barium (B) carbonate from silica-lactose solution. $[\text{TEOS}] = 7.6 \text{ mM}$, $[\text{Ca}^{2+}] = [\text{Mg}^{2+}] = 7 \text{ mM}$, $[\text{C}_{12}\text{H}_{22}\text{O}_{11}] = 0.01 \text{ M}$; pH 11, $T = 20 \text{ }^\circ\text{C}$, $t = 20 \text{ h}$.

c. *The precipitation of silica-calcium carbonate particles in the presence of the additives (8) – (11).*

The addition of calcium ions to the micellar alkaline silica-casein solution induces a bluish colour in the mixture immediately, whereas, in the absence of casein, macroscopic flocs (see Section 6.3.3.1.a) that settle down very quickly are formed. After 24 hours in contact with atmospheric carbon dioxide, the bluish solution is more intense and hemispherical calcium carbonate crystals in form of vaterite phase are precipitated (see Chapter 5 for a detailed characterisation). Anyway, no spiral particles form.

On the other hand, the introduction of calcium into the isotropic alkaline silica-lysozyme solution induces a slight turbidity after 5 minutes, which seconds later intensifies. Apparently, lysozyme, being negatively charged in the basic medium, attracts Ca^{2+} ions and, thus, diminishes the interaction between the calcium cation and the silica colloids. In other words, the rate of coagulation decreases and this phenomenon is proportional with the lysozyme concentration. Although the decay of turbidity is retarded; this effect does not lead to our objective. The resulting particle form is almost identical to the crystal shape precipitated from lysozyme-free solutions, except at high pH values (Samples M_{71} to M_{78}) where globular cauliflower-like aggregates form (Figure 6.30).

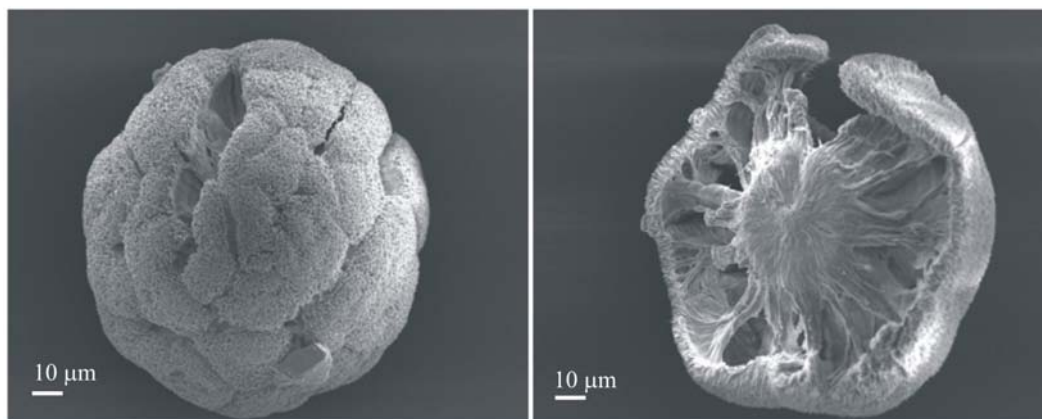


Figure 6.30 SEM images of silica calcium carbonate particles precipitated from aqueous solution in the presence of lysozyme 0.7 g/L. [TEOS] = 7.5 mM, $[Ca^{2+}] = 7$ mM, EtOH = 0.17%, pH = 11.9, T = 40 °C, t = 15 h.

Upon adding Ca^{2+} ions to the alkaline silica-lupasol solution, the mixture becomes immediately milky. In addition, the presence of this molecule does not induce changes in the resulting crystal morphology. According to literature, Ca^{2+} cations have a much stronger affinity for the OH^- groups than for the amino groups. Thus, it is likely that lupasol remains in solution and does not interfere in the electrostatic interaction between calcium and the silica colloids.

Upon mixing an electrolyte solution containing various amounts of EDTA with alkaline silica solution, first, all solutions remain clear, but minutes later the samples containing EDTA concentrations up to 4 mM start to get turbid. However, in the samples containing EDTA concentrations from 4 mM to 9 mM, the turbidity decreases. Moreover, the sample containing 10 mM EDTA is completely isotropic. At low EDTA concentrations (0.2 and 4 mM), the isolated crystals resemble a deformed calcite crystal, somehow similar with the particles in the absence of EDTA. At intermediate concentrations (5–7 mM) the resulting calcite crystals have a predominantly dumbbell-like shape (Figure 6.31) and the number of nuclei is considerably lower than at low EDTA concentrations. At high EDTA concentrations (10–11 mM), where the solutions are isotropic, no calcium carbonate particles form. Under these conditions, it is likely that the Ca^{2+} ions are complexed with EDTA and this effect prevents calcium to interact either with the silica colloidal particles or with CO_3^{2-} ions.

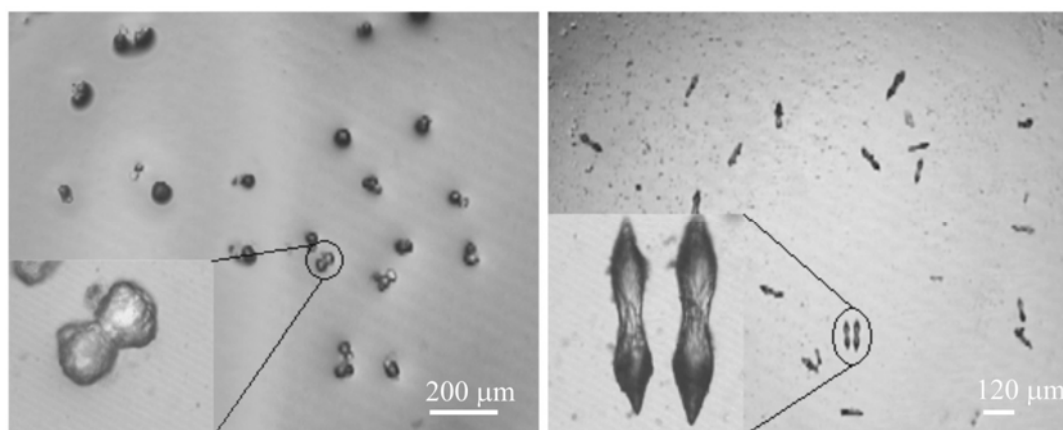


Figure 6.31 SEM images of silica calcium carbonate precipitated from aqueous solution in the presence of EDTA 5 mM at 20 °C (left) and 80 °C (right). [TEOS] = 7.5 mM, $[Ca^{2+}] = 8.5$ mM, [EtOH] = 0.17%, pH 11.

6.3.4. Discussion

According to the experiments described above, we observe that helicoidal morphologies that mimic the primordial filamentous Precambrian microfossils do not grow under all investigated conditions. Therefore, the key question is why the helical biomorphs formation fails when calcium ions are used instead of barium? At first glance, there are two distinct differences between calcium and barium cations: (1) the different behaviour of calcium ions in alkaline silica sols compared to barium ions and (2) the polymorphism of calcium carbonate with respect to barium carbonate.

The first signs of these differences come out when the two cations (separately) get in contact with the alkaline silica solutions. Thus, the introduction of calcium chloride to hydrolyzed TEOS solutions induces cloudiness in the mixture almost immediately, whereas comparable silica-barium solutions are more or less transparent (Figure 6.32).

According to Kerr¹⁴, in the presence of divalent cations, silica species nucleate and grow. The growth was followed by DLS and is shown in Figure 6.33. In the absence of metal cations, DLS indicates a hydrodynamic radius of circa 15 ± 10 nm and a polydispersity index around 0.2–0.4, which remain constant over time. In general, at this pH value, the surface of the particles has a negative electric charge that prevents aggregation (coagulation) of the particles due to electrostatic repulsive forces that ensures the stability of colloidal silica in the solution¹⁵.

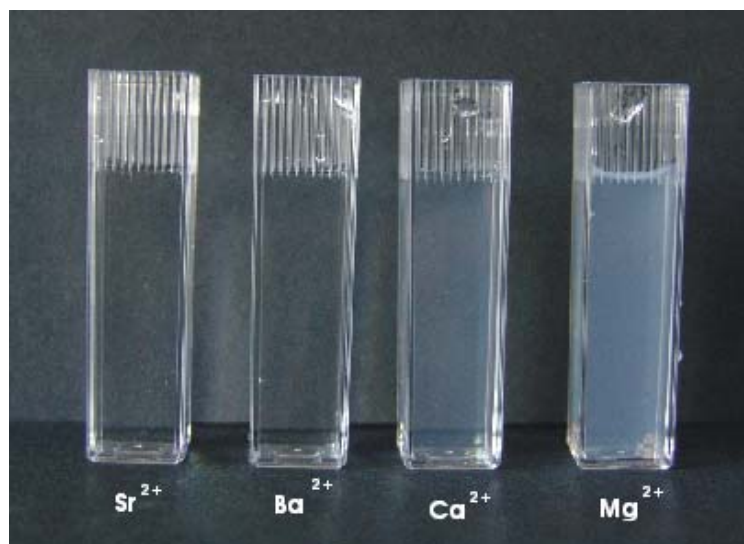


Figure 6.32 Visual observations performed when the hydrolysed TEOS solution (7.5 mM) is mixed with earth-alkaline metal ions (6 mM).

The introduction of the barium salt to hydrolyzed TEOS solution leads to the formation of detectable nucleates after an incubation time of 10 min or more⁸. The onset of nucleation ($r = 105$ nm) is followed by a slow and gradual growth of the aggregates with time. On the contrary, the addition of calcium cations to hydrolyzed TEOS solution dramatically enhances the nucleation giving a cloudy appearance to the reaction mixture within a few minutes. Furthermore, the turbidity increases with increasing Ca^{2+} concentration.

Along with other comparative studies^{16,17}, we presume that the appearance of turbidity is due to the silica precipitation phenomenon induced by calcium ions and followed by coagulation. Therefore, the solution was filtrated and the resulting precipitate was collected and studied by means of SEM, EDX, XRD and FTIR analysis.

SEM image (Figure 6.34) shows spherical particles of ~ 200 nm in diameter consisting of Si , O and traces of Ca . These nanoparticles are in some cases aggregated and in addition embedded in a faint network (Figure 6.35). XRD diffraction pattern performed for the obtained particles shows that the material is amorphous (Figure 6.36). Besides, the spectrum shows a broad line with a maximum at 2θ about 13° that indicates the presence of amorphous SiO_2 in agreement with Sobczynski¹⁸.

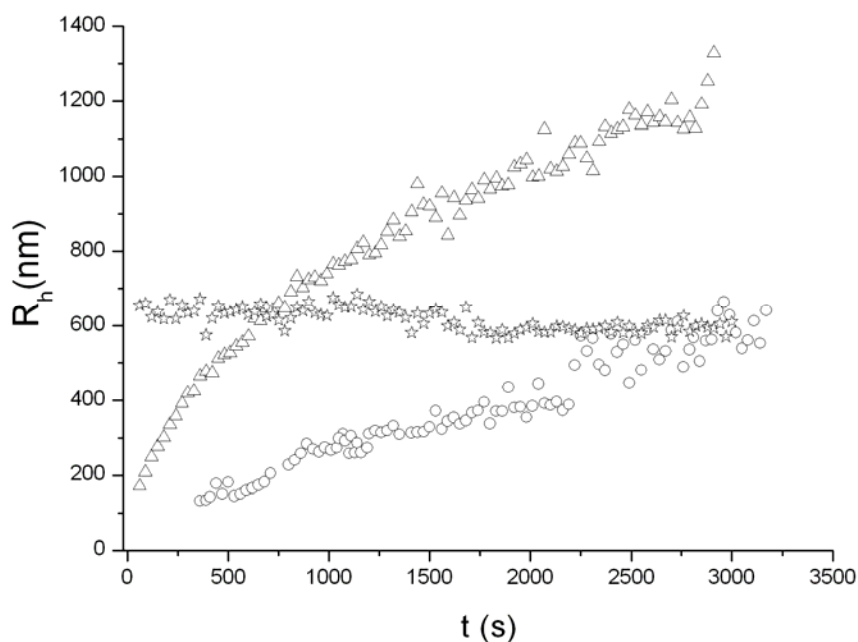


Figure 6.33 Comparison of the light scattering curves obtained after rapidly mixing solutions of $BaCl_2$ (\circ), $CaCl_2$ (Δ) and $MgCl_2$ (\star) with TEOS hydrolysed sol. $[MCl_2] = 6$ mM, $[TEOS] = 7.5$ mM.

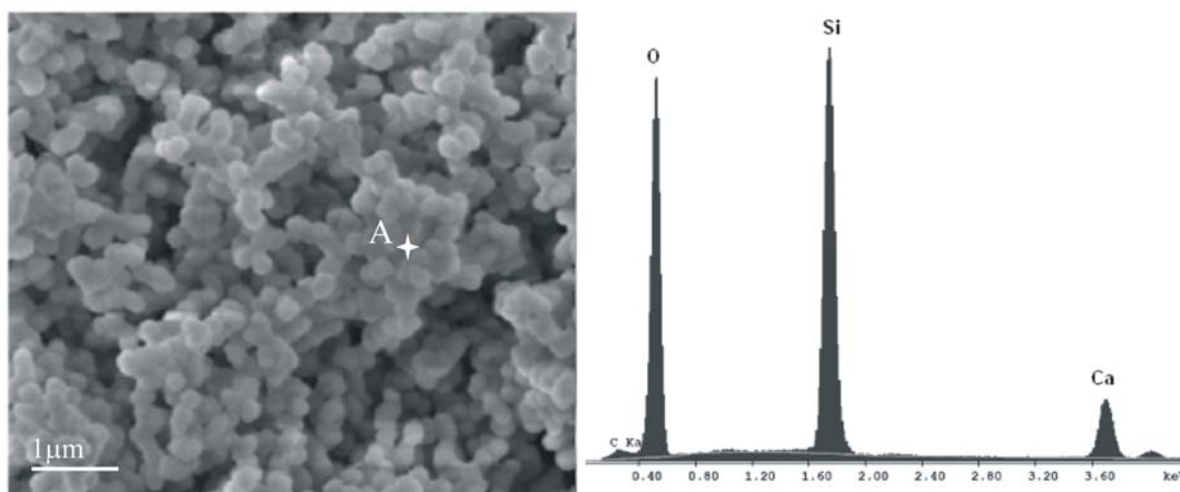


Figure 6.34 SEM image (left) of the precipitate obtained immediately after mixing the $CaCl_2$ with alkaline silica solution. EDX spectra (right) obtained from the regions 'A' indicated on the SEM picture.

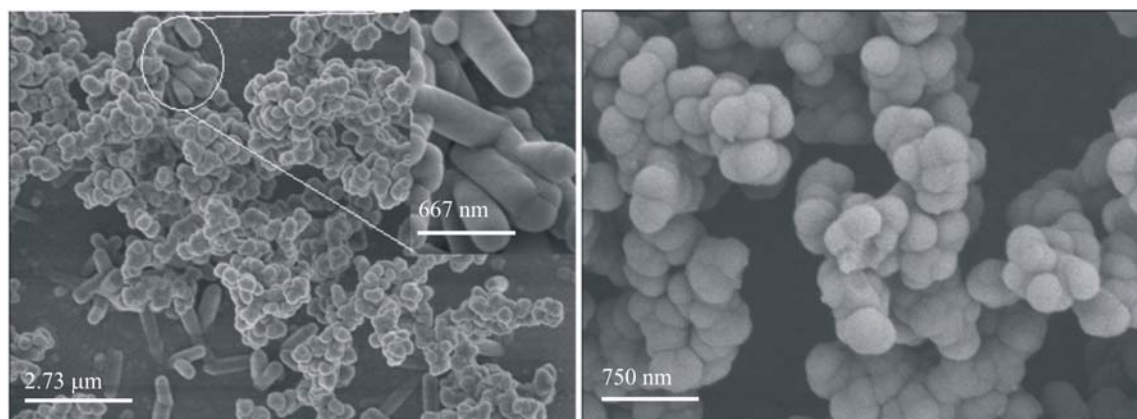


Figure 6.35 SEM image of the precipitate obtained after the crystallization process of calcium carbonate as a coproduct.

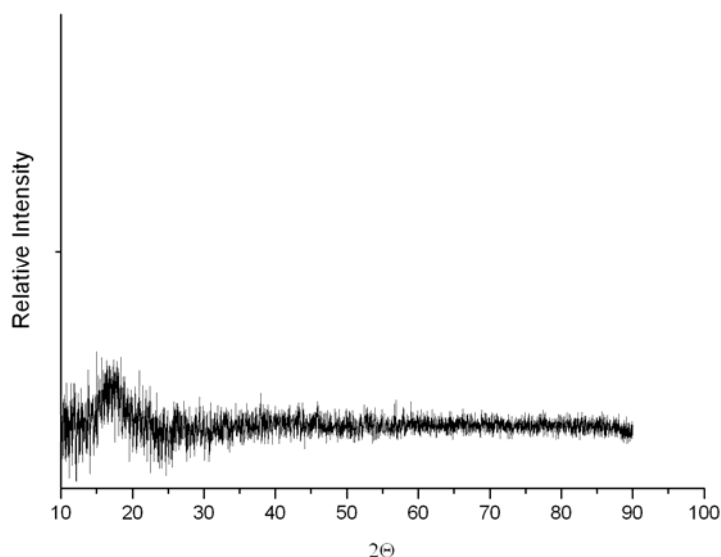


Figure 6.36 XRD pattern of silica particles obtained after mixing the $CaCl_2$ with alkaline silica solutions.

To further shed light on our hypothesis, FTIR analyses were conducted. Figure 6.37 shows absorbance spectra of commercial SiO_2 powder (curve a) and of the precipitate filtrated straight after the calcium electrolyte solutions was mixed with hydrolysed alkaline TEOS solution (curve b). Both spectra are perfectly overlapping. From this it follows that the addition of Ca^{2+} ions induces the formation of interconnected (i.e., coagulated) amorphous SiO_2 particles. The same effect occurs for barium ions when its concentration in alkaline silica solution is ~ 0.5 M (i.e., one hundred times higher than the barium ions concentration

in the standard biomorphs experiments). In this case, the particles resemble only coral-like morphologies (no filamentous particles were formed). After Iler¹⁶, the coagulation process occurs with the addition of a critical concentration of salt coagulant (c.c.c). Thus, when the c.c.c is reached in the system, the cations are chemically adsorbed on the surface of colloidal silica particles due to the substitution of calcium for hydrogen, H^+ , in $SiOH$ groups. The sorbet cations neutralise the negative surface charge of colloidal particles and participate in the formation of bridging bonds between particles¹⁶. As a consequence, this causes a drop in pH (observed in our experiments) as calcium ions were adsorbed and hydrogen ions released. As the calcium chloride content increases, the pH of the treated solution decreases more and the rate of coagulation is significantly higher. In turn, at Ca^{2+} concentrations lower than c.c.c. (<5mM), the solutions are isotropic but it is likely that the calcium concentrations are too low for biomorphs formation. Thus, it must be noted that the first distinction between the behaviour of calcium ions and barium ions in alkaline silica sols arises from a different salt c.c.c value; apparently, calcium ions have a lower c.c.c value than barium ions.

On the other hand, Iler¹⁷ reports that there is, in fact, no direct SiO^-Ca^+ linkage, but only $SiO^-H^+O_H \cdots Ca$, where the silica-calcium linkage is through the water of hydration of the Ca atom.

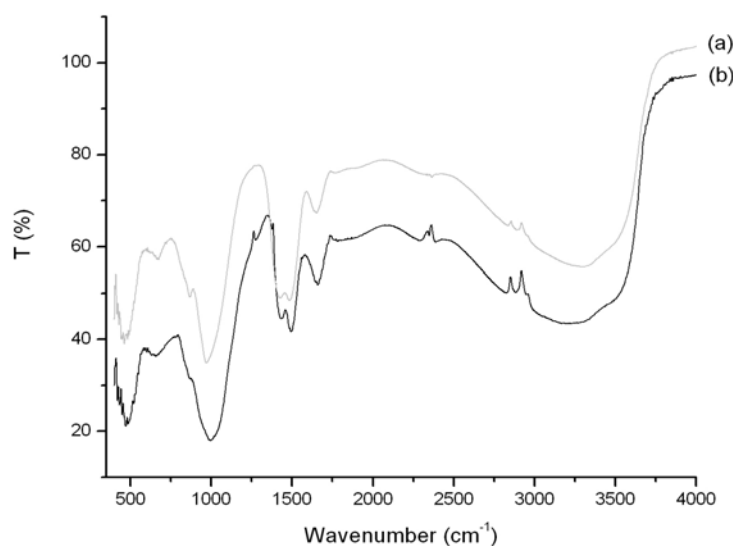


Figure 6.37 FTIR spectra of the commercial SiO_2 powder (curve a) and the precipitate which formed upon mixing calcium chloride and alkaline TEOS sols (curve b).

Another more plausible explanation for silica precipitation in the presence of calcium anions is in agreement with Marshall et al.¹⁹, who report that Ca^{2+} ions decrease the solubility of amorphous silica in water due to the commonly termed ‘salting-out’ effect. Moreover, they show that as the hydration number of the cations increases (Figure 6.38), the solubility of amorphous silica particles decreases.

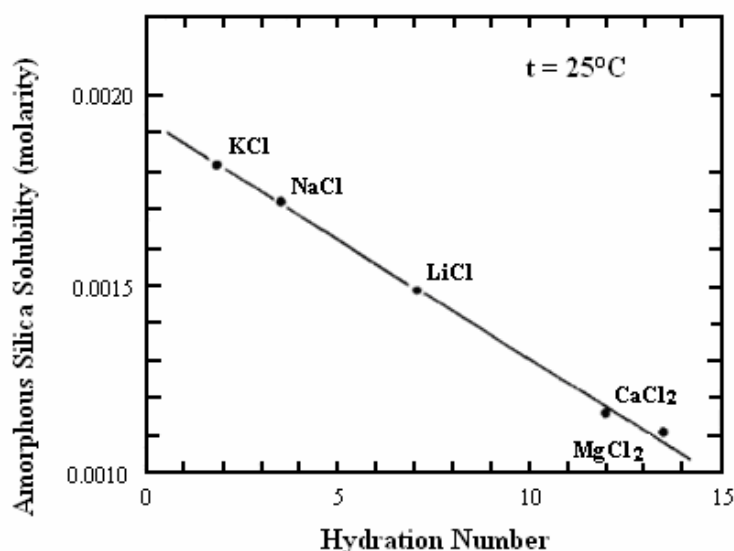


Figure 6.38 Solubility of amorphous silica in one molar salt solution at 25 °C compared with some hydration numbers for cations. (Redrawn after [19]). The hydration numbers are from Rombinson et al.²⁰.

Likewise, in our system, the calcium cations ($H = 10$) remove more ‘free’ water – defined to be that water not bound to dissolved silica or salts as water of hydration – from the solvent than its homologue, barium ($H = 1$ or 2), and decrease the solubility of silica to a greater extent (Table 6.6). Qualitatively, a lowered amount of ‘free’ water would be expected to lower silica solubility, and this is what is actually observed. This statement was checked by control experiments with the other two alkali metal cations, i.e., Sr^{2+} ($H = 2$) and Mg^{2+} ($H = 13$), that have a lower and, respectively, higher hydration number than Ca^{2+} but similar electrostatic binding capabilities. As expected, the addition of magnesium ions to hydrolyzed TEOS solution induces also cloudiness in the mixture immediately and the turbidity is more enhanced than silica-calcium solution, whereas comparable silica-strontium solution is isotropic just like silica-barium solution (Figure 6.32). We note that upon mixing the silica solution with magnesium solution the aggregates have a radius of

600 nm and the radius size remains constant over time. So, the flocculating process does not take place.

Table 6.6 Pauling crystallographic radii²¹ (r), Stokes hydrated radii²² (r_{hy}) and the hydration numbers²³ (H) of earth-alkaline cations.

<i>Cation</i>	<i>r</i>	<i>r_{hy}</i>	<i>H</i>
<i>Mg</i> ²⁺	0.65	3.47	13
<i>Ca</i> ²⁺	0.99	3.10	10
<i>Sr</i> ²⁺	1.13	3.10	2
<i>Ba</i> ²⁺	1.35	2..90	1 or 2

As mentioned above, the second difference between Ba^{2+} and Ca^{2+} ions is in connection with the crystallographic modification of the carbonate. Whereas barium has only one stable form (aragonite-type structure), the calcium carbonate exists in one stable form (calcite) and two unstable forms (aragonite and vaterite) at room temperature. Because the aragonite form seems to be trivial for biomorph formation, we assume that the stability of calcite relative to aragonite at room temperature is probably also responsible for our findings. Although Ca^{2+} is somewhat large for a 6-fold coordination (calcite) by oxygen atoms, it is relatively small for a 9-fold coordination (aragonite) at room temperature²⁴. However, earlier studies show that certain additives, such as alkali metal ions or surfactants, can induce the aragonite form at ambient temperature. However, we saw that the introduction of such additives into the silica-calcium solution enhances the salting out effect, and therefore decreases the concentration of silica in the aqueous solution.

Moreover, previous works^{25, 26} have shown that the relative abundance of calcium carbonate polymorphs is strongly influenced by the precipitation temperature (Figure 2.11); the higher the experimental temperature, the easier is the formation of aragonite, due to enhanced kinetic stability. Therefore, since the aragonite structure seems to be critical for biomorph formation², the experiments were performed at high temperatures (40 and 80 °C). Under these conditions, the results indicated that upon addition of flocculants, i. e. Ca^{2+} ions, the coagulation and the sedimentation velocity of flakes in the hot solution are substantially higher than those in the solution at 20 °C. This is in agreement with

Sheikholeslami¹, who indicates that lower temperatures runs at 25 °C do not reach equilibrium within the experimental time of 150 hours while the higher temperatures runs approach saturation concentration in much less time. For example, at 40 °C, the silica concentration in the solution dropped by about 50% (to 300 ppm) in less than 5 hours (Figure 6.39). Nevertheless, the polymerisation process is kinetically controlled and therefore silica polymerized faster at higher temperatures, though silica solubility increases with increasing temperatures.

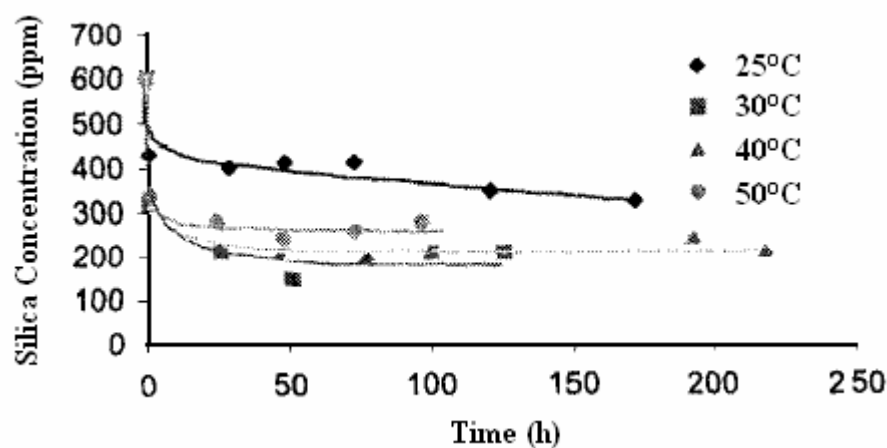


Figure 6.39 Effect of temperature on silica polymerisation. (Reproduced from [1])

Another approach was to find additives, such as EDTA or proteins, which can bind Ca^{2+} and therefore the coagulation and flocculation phenomena could be diminished or completely avoided. Though this was successfully achieved, the helical filaments were never formed. In this case, the reason is likely the type of calcium/additive binding and their behaviour during calcium carbonate formation.

6.3.5. Conclusions

Although the realm of biomorphs was shown to extend beyond the previously studied barium and strontium carbonates, to now include calcium carbonate, spiral shapes of silica-calcium carbonate biomorphs were not achieved in this work. In an attempt to answer the question, we observed that when barium is replaced by calcium ions, the silica particle formation occurs due to the salting-out effect and/or coagulation process. Thus, the silicate concentration in solution is significantly decreased and these phenomena prevent the biomorphs formation. A secondary reason can be the competition between the

crystallographic modifications (i.e., aragonite and calcite) of calcium carbonate at room temperature. Therefore, in order to favour the aragonite type, the experiments were conducted at higher temperature. But, by raising the temperature, the degree of coagulation phenomenon is also increased. Moreover, comparable experiments made with barium at 80 °C prevent the formation of spiral shapes. Therefore, we believe that working at high temperatures is not the right way. Future work should be focused on finding an additive which can compromise two effects: to lower the salting-out effect and to induce the aragonite form of calcium carbonate at ambient temperature.

6.3.6. References

- (1) Sheikholeslami, R.; Al-Mutaz, I. S.; Tan, S.; Tan, S. D. *Desalination* **2002**, *150*, 85.
- (2) Sheikholeslami, R.; Tan, S. *Desalination* **1999**, *126*, 267.
- (3) Sheikholeslami, R.; Zhou, S. *Desalination* **2000**, *132*, 337.
- (4) García-Ruiz, J.M.; Carnerup, A.M.; Christy, A.G.; Welham, N.J.; Hyde, S.T. *Astrobiology* **2002**, *2*, 363.
- (5) Terada, T.; Yamabi, S.; Imai, H. *J. Cryst. Growth* **2003**, *353*, 435.
- (6) Kellermeier, M. *Isocapillary gels and biomorphs as examples for equilibrium and non-equilibrium self-assembly*, Diplom Thesis: Regensburg, 2005.
- (7) Imai, H.; Terada, T.; Yamabi, S. *Chem. Commun.* **2003**, *4*, 484.
- (8) Voinescu, A. E.; Kellermeier, M.; Carnerup, A. M.; Larsson, A. K.; Touraud, D., Hyde, S. T.; Kunz, W. *J. Cryst. Growth*, **2007**, *306*, 152.
- (9) Hyde, S. T.; Carnerup, A. M.; Larson, A. K.; Christy, A. G.; García-Ruiz, J. M. *Physica A* **2004**, *339*, 24.
- (10) García-Ruiz, J. M. *Geology* **1998**, *26(9)*, 843.
- (11) Wary, J. L.; Daniels, F. *J. Am. Chem. Soc.* **1957**, *79*, 2031.
- (12) Riisager, A.; Hanson, B. E. *J. Mol. Catal. A: Chemical* **2002**, *189*, 195.
- (13) Busch, S.; Dolhaine, H.; DuChesne, A.; Heinz, S.; Hochrein, O.; Laeri, F.; Podebrad, O.; Vietze, U.; Weiland, T.; Kniep, R. *Eur. J. Inorg. Chem.* **1999**, *10*, 1643.
- (14) Kerr, G. T. *J. Phys. Chem.* **1966**, *70*, 1047.
- (15) Potapov, V. V. *Glass Phys. Chem.* **2004**, *30(1)*, 73.
- (16) Iler, R. K. *The chemistry of silica. Solubility, polymerization, colloid and surface properties*, New York: Wiley; 1979.

-
- (17) Iler, R. K. *J. Colloid Int. Sci* **1975**, 53(3), 476.
- (18) Sobczynski, A. *Monatshefte für Chemie* **1992**, 123, 211.
- (19) Marshall, W. L. and Warakoski, M. *Geochim. Cosmochim. Acta* **1980**, 44, 915.
- (20) Robinson, R. A.; Stokes, R. H. *J. Amer. Chem. Soc.* **1948**, 70, 1870.
- (21) Huheey, J. E. *Inorganic Chemistry*, 3rd ed, Harper and Row: New York, 1983.
- (22) Conway, B. E. *Ionic Hydration in Chemistry and Biophysics*, Elsevier Scientific: Amsterdam, 1981.
- (23) Huang, Z. Q. *Introduction of Theory about Electrolyte Solution*, Science Press: China, 1983.
- (24) Klein, C.; Hurlbut, C.S. *Manual of Mineralogy*, Wiley: New York, **1993**.
- (25) Zhou, G. T.; Zheng, Y. F. *J. Mater. Sci. Lett.* **1998**, 17, 905.
- (26) Terada, J. *Nature* **1953**, 171, 517.

Chapter 7

Conclusions and Summary

Based on the results described above, we are able now to give solutions to the initial questions stated in the introduction chapter.

Has the lysozyme-mineral interaction an implication in the building of amorphous materials and their ageing?

It is well established that the formation of inorganic materials in biological systems is commonly associated with the presence of specific proteins. Eggshell, for example, is a biomaterial that grows in the presence of a cocktail of proteins, in which lysozyme is an important component. Using this protein, we studied its influence on the size, shape, crystallography and chemical composition of amorphous calcium carbonate (ACC). From our experimental results, we observed that lysozyme considerably decreases the average diameter of the metastable amorphous calcium carbonate particles and promotes a network of associated particles. Moreover, the ageing of the Ly-ACC particle drives exclusively to crystalline calcite (like in avian eggshell), whereas comparable experiments in the absence of lysozyme leads to all kind of crystal polymorphs. Nevertheless, this protein has a great effect in the building of ACCs and the lysozyme-amorphous mineral interaction acts as a reservoir for calcitic crystalline material.

Can silicate-casein interaction to alter the CaCO_3 mineralization in aqueous sols?

Hemispherical aragonite-vaterite microstructures are obtained in alkaline silica-casein sols, whereas comparable experiments in the absence of silica lead to no visible calcium carbonate particles. The initiation of this mineralization process is due to the presence of

silicate ions that according to the results present in the Chapter 5 interact with serine-monophosphate groups and modify the casein structure in aqueous solution and, as a consequence, promote crystal formation. We conclude that crystallization processes that appear *in vivo* could be influenced by different modifications in protein structures that are controlled by inorganic ions, such as the pulmonary calcification process.

Is TEOS a better alternative silica source for the growth of biomorphs?

Until now, silica-carbonate biomorphs have been grown with water glass as the silicate source. However, in some cases, we have observed that a specific water glass batch fails to form biomorphs, despite its efficacy in earlier experiments. For this reason, experiments are done in alkaline TEOS solutions at pH and concentrations identical to the former water glass experiments in order to obtain biomorphs, and to confirm this transferability. It is found that TEOS is capable of serving as a preferred silica source for the growth of biomorphs, but at low ethanol content. Experiments conducted at high ethanol content led to fast formation of a small number of globular morphologies strikingly dissimilar to conventional precipitate. In summary, the use of TEOS in the presence of low concentrations of EtOH allows reproducible growth of biomorphs. We therefore recommend its use as a silica source for biomorph growth in place of water glass used previously.

Can biomorphs-like aggregates of calcium carbonate be prepared?

Chapter 6 shows clearly that we can grow non-crystallographic morphologies of silica-calcium carbonate particles, in the form of coralline structures, if we choose the correct conditions. These new particles share the complex interplay of order/disorder at the atomic scale, non-crystalline carbonate crystals and orientational ordering of nanocrystals at intermediate length scales as well as all characteristic of biomorphs and biominerals.

Why calcium ions behave so different from its homologue barium, in alkaline silica sols?

Although the realm of biomorphs is shown to extend beyond the previously studied barium and strontium carbonates, to now include calcium carbonate, spiral shapes of silica-calcium carbonate biomorphs were never achieved in this work. In an attempt to solve this task, we observed that as the hydration number of the cation increases, the solubility of amorphous silica decreases. Furthermore, it must be also considered that Ca^{2+} is a bivalent

cation, which can simply crosslink the negative silicate species and induces the coagulation process. Both phenomena prevent the biomorphs formation. A secondary reason can be the competition between the crystallographic modifications (i.e., aragonite and calcite) of calcium carbonate at room temperature. Therefore, to favour the aragonite type, the experiments are conducted at higher temperatures. But, raising the temperature, the degree of coagulation phenomenon is also increased. Moreover, comparable experiments made with barium at 80 °C prevent the formation of spiral shapes. Therefore, we believe that working at high temperatures is not the right way. Future work should be focused on finding an additive which can compromise two effects: to lower the salting-out effect and to induce the aragonite form of calcium carbonate at ambient temperature.

Chapter 8

Appendices

8.1. Reactions Occurring during the Precipitation of CaCO_3

<i>Reactions</i>
$H_2O \Leftrightarrow H^+ + OH^-$
$CO_{2(g)} \Leftrightarrow CO_{2(aq)}$
$CO_{2(aq)} + H_2O \Leftrightarrow H_2CO_3$
$H_2CO_3 \Leftrightarrow H^+ + HCO_3^-$
$HCO_3^- \Leftrightarrow H^+ + CO_3^{2-}$
$H_2CO_3 + CO_3^{2-} \Leftrightarrow 2HCO_3^-$
$2HCO_3^- \Leftrightarrow CO_3^{2-} + CO_2 + H_2O$
$HCO_3^- + OH^- \Leftrightarrow CO_3^{2-} + H_2O$
$CO_3^{2-} + H_2O \Leftrightarrow HCO_3^- + OH^-$
$HCO_3^- + H_2O \Leftrightarrow H_2CO_3 + OH^-$
$Ca^{2+} + HCO_3^- \Leftrightarrow CaHCO_3^+$
$CaHCO_3^+ \Leftrightarrow H^+ + CaCO_{3(aq)}$
$Ca^{2+} + HCO_3^- \Leftrightarrow CaCO_3 + H^+$
$Ca^{2+} + 2HCO_3^- \Leftrightarrow CaCO_{3(s)} + CO_{2(g)} + H_2O$
$Ca^{2+} + OH^- \Leftrightarrow CaOH^+$
$CaOH^+ + OH^- \Leftrightarrow Ca(OH)_{2(aq)}$
$Ca^{2+} + CO_3^{2-} \Leftrightarrow CaCO_{3(aq)}$
$CaCO_{3(aq)} \Leftrightarrow CaCO_{3(s)}$

8.2. Lysozyme - Calcium Interactions

We observe that the size of amorphous calcium carbonate particles depends strongly on the lysozyme concentration. A possible hypothesis regarding the effect of this organic molecule on the particle size is a high affinity of Ca^{2+} to the protein structure. To get evidence of this possible interaction DLS, ES-MS and FTIR were conducted.

DLS measurements were performed for a basic solution of lysozyme (1 g/ L, pH 12.6) in the absence and in the presence of calcium ions. In the absence of Ca^{2+} , DLS measurements indicated a hydrodynamic radius of 10 nm and a polydispersity index around 0.3, which remained constant over time. The addition of 0.147 g calcium chloride (0.01 M) to basic lysozyme solutions produced an onset of nucleation of objects (30 nm) and the mean polydispersity index significantly increases from 0.3 to 0.7 within one hour. We note that when the calcium ions were in contact with the lysozyme, large objects were produced.

Lysozyme-calcium binding has been further studied using the ES-MS (Figure 8.1) technique. Lysozyme (1 g/ L) is analysed under acidic electrospray mass spectrometer conditions at pH 4. The mass spectrum of egg white lysozyme indicated a multi-charged ion, having an m/z range from 1100 to 2000 Th. The most intense peak results from ions with 9 H^+ entrapped in the lysozyme (Figure 8.1 a) and the molecular mass was calculated to be 14304.6 ± 2 Da (M_w). The observed molecular mass is in good agreement with the molecular mass of hen egg lysozyme (14305.14 Da)⁴¹. The ES-MS spectrum also elucidated two other compounds having a molecular mass of M_w+59 Da and M_w+169 Da. They make up 10% and 14% of the total lysozyme relative abundance, respectively. These two minor peaks at higher mass are usually indicative of salt adducting to lysozyme⁴². Let us note that the purity of lysozyme is 95% and the remainder (~5%) is buffer salts⁴³. Subsequently, the protein was analysed in acetic acid with the addition of 0.01, 0.02 and 0.05 M calcium chloride (Figure 8.1 b-d). Under these conditions the obtained lysozyme- Ca^{2+} mass spectra revealed compounds of M_w+39 Da, M_w+79 Da and M_w+119 Da. These compounds corresponded to the binding of 1, 2 and 3 atoms of calcium with lysozyme, respectively. Additionally, the interaction between CO_3^{2-} and lysozyme was investigated by adding Na_2CO_3 (0.01 M) to the 1 g/ L lysozyme solution. The ES-MS technique revealed that there is no affinity of the carbonate anions to the lysozyme structure.

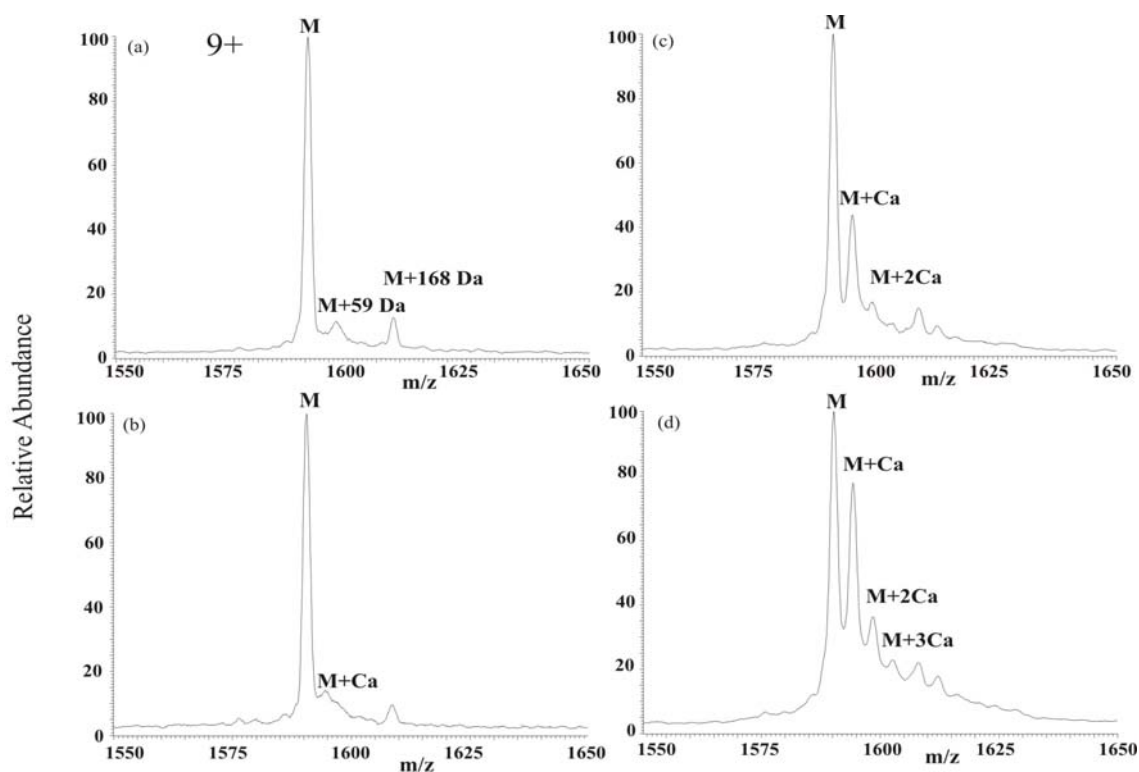


Figure 8.1 ES-MS spectrum of the lysozyme (based on the ions with 9 H^+) in the absence (a) and in the presence of calcium ions: (b) 10 mM, (c) 20 mM and (d) 50mM. The peak codes represent the calculated values obtained from each spectrum.

However, while the calcium carbonate growth experiments are performed at a very basic pH (12.6), the ES-MS analyses are conducted at pH 4. According to Imoto et al.⁴⁴ a stronger binding of calcium to lysozyme (UV measurements) is observed at pH values above 8. Therefore, we believe that at pH 12.6 calcium will have even a higher affinity to lysozyme, while the carbonate anions will not interact with lysozyme at the same sites where calcium is bound.

Therefore, our hypothesis is that lysozyme creates a local distribution of calcium ions, which can play the role of calcium carbonate nucleation sites. However, lysozyme does not interfere with the initial calcium carbonate interaction. We can also assume that the presence of lysozyme hinders the growth of calcium carbonate nucleate in its crystalline form.

To further analyse the Ly-ACC precipitate, FTIR experiments were conducted. Figure 8.2 shows absorbance spectra of pure lysozyme powder (Figure 8.2, curve b) and synthetic Ly-ACC precipitate (Figure S4.3, curve a). According to Addadi's results⁴⁶, the IR spectrum of

biogenic ACC shows: a split peak of the asymmetric stretch of the carbonate ion (ν_3) at 1420 and 1474 cm^{-1} , a broad absorption of the carbonate out-of-plane bending peak (ν_2) at 866 cm^{-1} and the symmetric stretch (ν_1) at 1080 cm^{-1} . Nevertheless, the infrared spectra of Ly-ACC precipitate (Figure 8.2, curve a) is characterised by a split peak at 1429 and 1480 cm^{-1} (ν_3) shifted to higher wavenumber (shift about 9 and 4 cm^{-1}), which illustrates the lack of symmetry in the environment of the carbonate ions⁴⁵ and therefore the amorphous state. This is accompanied by absorption peaks at 1070, 862 and 1654 cm^{-1} . The first two peaks are assigned to the characteristic absorption of ACC and the latest peak could be attributed to the amide I band. The amide I band⁴⁶ is the characteristic band of the $C=O$ stretching vibrations and is presented in the absorbance spectra of lysozyme at 1659 cm^{-1} . In comparison with the IR spectrum of the pure lysozyme (Figure 8.2, curve b), the amide I band of the IR spectrum of the Ly-ACC was shifted to a lower wavenumber. The shift may be a result of the interaction between the Ca^{2+} and the $C=O$ ⁴⁷. It should be pointed out that the presence of the amide I band in the spectrum of Ly-ACC shows evidence of a small amount of the protein in the precipitate. To quantify the percentage of lysozyme, an elementary analysis was carried out yielding approximately 5% mass percent of lysozyme in the precipitate, meaning approximately 2500 calcium carbonate molecules by one molecule of lysozyme.

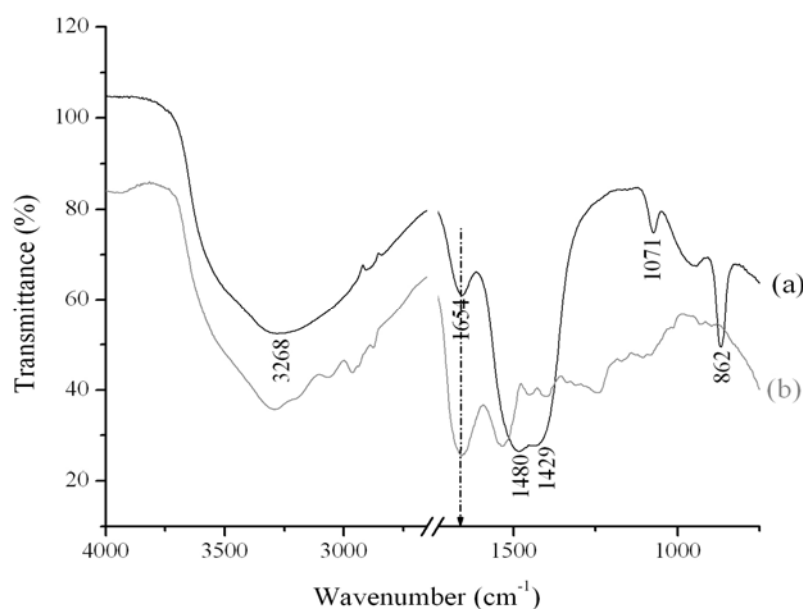


Figure 8.2 FTIR spectra of Ly-ACC particles (curve a) and the pure lysozyme (curve b).

8.3. Self-Assembled ‘Floral Dumbbell’ Silica-Calcium Carbonate

Figure 8.3 shows optical and FESEM images of biomorphic calcium carbonate-silica composites. Each dumbbell cluster is composed of two conical subunits, 90 μm in length and 30 μm in maximum diameter. The form is reminiscent of the wheat-sheaf forms reported previously⁵⁻⁷, though with important differences. First, most of the carbonate material in the aggregates is aragonite, rather than calcite. For example, Figure 8.3 A presents one conical subunit, in which two different crystalline modifications can be observed. The major component is aragonite (intergrown with amorphous silica, described below), with the usual rod-like habit (400–500 nm in width), accompanied by characteristic calcite rhombohedra lining the outer rims that form last (see Figure 8.3 B). Second, the ordering of the nanoscale aragonite rods is very similar to that observed previously in barium and strontium biomorphs²¹. The walls are composed of radially aligned aragonite-silica rods. The presence of calcite in later stages of growth is likely to be due to a secondary nucleation and not to a phase transition between aragonite and calcite. Indeed, aragonite clusters without calcite rims are occasionally found in the reaction cells.

Figure 8.4 shows the sequence of shapes of biomorphic floral dumbbell composites. Initially, a perfect dumbbell cluster forms which is composed of needle-like crystals. With time, the cluster appears to grow more in length than in width and finally develops into a ‘floral dumbbell’, composed of two open conical subunits. This growth behaviour might be related to the mutual orientation of the crystallites that intergrow with amorphous silica.

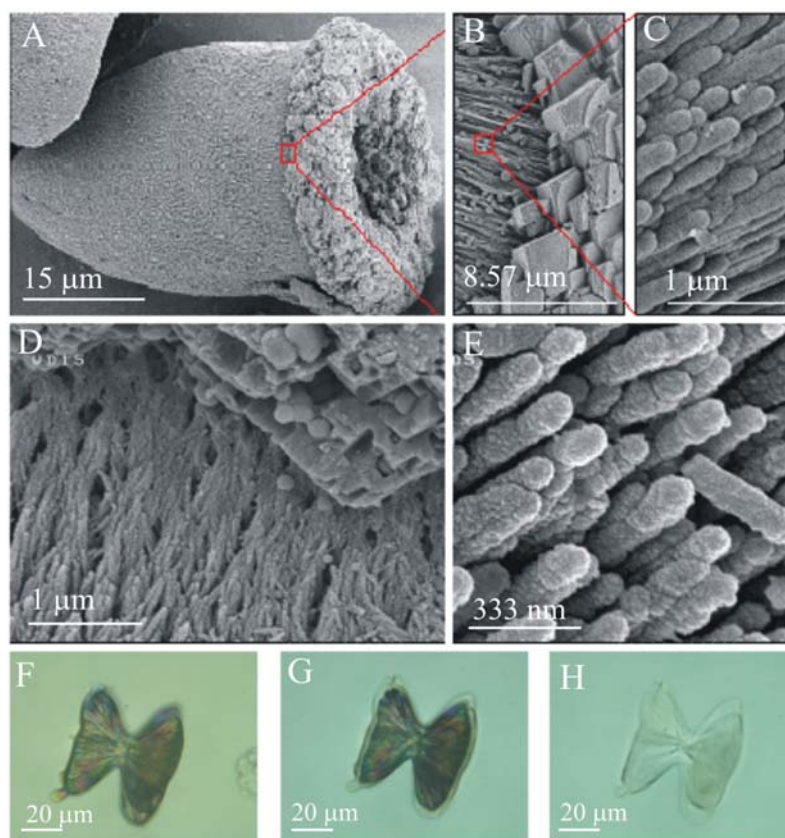


Figure 8.3 Self-assembled ‘floral dumbbell’ silica-calcium carbonate. (A to C) Zoom sequence, showing details of the surface texture. (D and E) High-magnification FESEM images of biomorphs (after alkaline leaching of silica) showing the orientational ordering of aragonite crystallites. (F to H) Optical micrographs of the aggregates, viewed under crossed polarizers, showing the progressive dissolution in dilute hydrochloric acid of aragonite from the carbonate-silica material, leaving a silica ‘ghost’. A–E show only half of the complete aggregate.

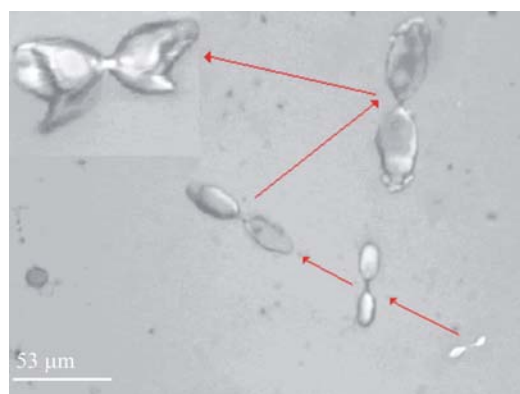


Figure 8.4 Optical micrograph of silica-calcium carbonate aggregates, viewed between crossed polarizers, which shows the growing sequence of a floral dumbbell structure.

8.4. List of Abbreviations

A	Aragonite
ACC	Amorphous calcium carbonate
ANU	Australia National University
ANUEMU	Australia National University electron microscopy unit
C	Calcite
c.c.c	Critical concentration of salt coagulant
CMC	Critical micelle concentration
CTAB	Cetyltrimethylammonium bromide
2D	Two-dimensional
3D	Three-dimensional
DLS	Dynamic light scattering
DMC	Dimethyl carbonate
EDTA	Ethylenediaminetetraacetic acid disodium salt
EDX	Energy dispersive X-ray
ES-MS	Electrospray ionization mass spectrometry
FESEM	Field-emission scanning electron microscope
FTIR	Fourier transformations IR spectroscopy
HRTEM	High resolution transmission electron microscope
ICDD	Internationally center for diffraction data
INRA	L'institut national de la recherche agronomique
IP	Isoelectric point
IR	Infrared
Ly-ACC	Amorphous lysozyme-calcium carbonate
N	Coordination number of spherical colloids
NMR	Nuclear magnetic resonance spectroscopy
NNLS	Non-negatively constrained least squares
PAA	Polyacrylic acid
PEG	Polyethylene glycol
PEG- <i>b</i> -PMAA	Poly(ethylene glycol)-block- poly(methacrylic acid)
PMAA	Poly(methacrylic acid)
³¹ P-NMR	Phosphorus-31 nuclear magnetic resonance

PSMA	Poly(styrene-alt-maleic acid)
PVA	Polyvinyl alcohol
SAED	Selected area electron diffraction
SDBS	Sodium dodecylbenzenesulfonate
SDS	Sodium dodecyl sulphate
SE	Secondary electrons
SEM	Scanning electron microscope
TBOS	Tetrabutylorthosilicate
TEM	Transmission electron microscope
TEOS	Tetraethylorthosilicate
TPOS	Tetrapropylorthosilicate
UV	Ultraviolet
UV-VIS	Ultraviolet and visible spectroscopy
V	Vaterite
VIS	Visible
XRD	X-ray diffraction

8.5. List of Symbols

A	absorbance
a	acceleration ($\text{m}\cdot\text{sec}^{-2}$)
α	slope (sec^{-1})
B	magnetic field (T)
C	speed of light ($2.99\cdot 10^{10} \text{ cm}\cdot\text{sec}^{-1}$)
c	concentration ($\text{g}\cdot\text{L}^{-1}$; $\text{mol}\cdot\text{L}^{-1}$; %)
D	diffusion coefficient ($\text{cm}^2\cdot\text{sec}^{-1}$)
d	particle diameter (nm)
d_{hkl}	spacing between the planes in the atomic lattice (nm)
ΔG_B	bulk energies ($\text{kJ}\cdot\text{mol}^{-1}$)
ΔG_I	interfacial surface energy ($\text{kJ}\cdot\text{mol}^{-1}$)
ΔG_N	free energy required for the formation of a cluster ($\text{kJ}\cdot\text{mol}^{-1}$)
ΔG_N^*	activation energy for homogeneous nucleation ($\text{kJ}\cdot\text{mol}^{-1}$)
E_f	electric field ($\text{N}\cdot\text{C}^{-1}$)
E	energy ($\text{kJ}\cdot\text{mol}^{-1}$)
ε	extinction coefficient ($\text{mol}^{-1}\cdot\text{L}\cdot\text{cm}^{-1}$)
η	viscosity ($\text{g}\cdot\text{cm}^{-1}\cdot\text{sec}^{-1}$)
f	frequency (Hz)
$g_2(\tau)$	autocorrelation function
Γ	decay rate (sec^{-1})
γ	magnetogyric ratio ($\text{sec}^{-1}\cdot\text{T}^{-1}$)
h	Plank's constant ($6.62608\cdot 10^{-34} \text{ J}\cdot\text{sec}$)
I	intensity ($\text{W}\cdot\text{m}^{-2}$)
I_s	spin quantum number
J_G	growth rate
K_{ap}	activity product ($\text{mol}^2\cdot\text{L}^{-2}$)
K_{sp}	solubility product ($\text{mol}^2\cdot\text{L}^{-2}$)
k	wave vector magnitude (cm^{-1})
k_b	Boltzmann constant ($1.38065\cdot 10^{-23} \text{ J}\cdot\text{K}^{-1}$)
l	path length (cm)

λ	wavelength (nm)
M_w	molecular weight ($\text{g}\cdot\text{mol}^{-1}$ or Da)
μ	magnetic moment ($\text{J}\cdot\text{T}^{-1}$)
n	refractive index
q	scattering vector magnitude (cm^{-1})
q_i	ionic charge
R_h	hydrodynamic radius (nm)
r^*	critical radius (nm)
S_A	absolute supersaturation
S_R	supersaturation
σ	interfacial free energy ($\text{erg}\cdot\text{cm}^{-2}$)
t	time (sec, min, hours, days)
T	temperature ($^{\circ}\text{C}$)
T_{IR}	transmittance (%)
τ	time delay (sec)
Θ	Bragg angle ($^{\circ}/\text{min}$)
θ	scattering angle ($^{\circ}/\text{min}$)
$\bar{\nu}$	wavenumber (cm^{-1})
V	molar volume ($\text{cm}^3\cdot\text{mol}^{-1}$)

8.6. List of Figures

- Figure 2.1** (A) Coccosphere of *E. huxleyi* composed of calcite plates called coccoliths. (Reproduced from [3]) (B) Cystolith from the leaves of *Ficus microcarpa* composed of stable ACC. (Reproduced from [21]) (C) Natural coral from the south-eastern Australian seaside composed of aragonite. (D) Whole shell of the foraminifera *Spirillina* supposed to arise from a transient of amorphous calcium carbonate phase. (Reproduced from [7]) (E) Fracture surface of a young spine, showing the sponge structure of the stereom. (Reproduced from [22]) (F) Eggs. Inset: a cross-section through a formed eggshell which reveals the vertical calcite crystal layers. (Reproduced from [23])..... 7
- Figure 2.2** The biogeochemistry of calcium. The precipitation of calcium carbonate and phosphate are the major inorganic constituents of skeletal structures. (Redrawn after [26]) 8
- Figure 2.3** Distributions of the carbonate species in relation to the pH of the solution. $H_2CO_3^*$, represents the sum of dissolved CO_2 and H_2CO_3 , and predominates at low pH range. HCO_3^- is the most abundant species at intermediate pH values; CO_3^{2-} dominates at high pH values. (Reproduced from [39])..... 9
- Figure 2.4** A concept of the crystallization process..... 10
- Figure 2.5** Free energy of nucleation as a function of cluster size..... 11
- Figure 2.6** (A) Layer-by-layer mechanism of crystal growth. (The scheme is partly based on that in [41]) (B) Two-dimensional mechanism. (Reproduced from [41]) (C) Screw-dislocation mechanism. (Reproduced from [2])..... 13
- Figure 2.7** Schematic representation of the crystal morphologies (Reproduced from [58]) and the crystal structure of anhydrous $CaCO_3$ polymorphs. The crystal structures were drawn with *Endeavour* software. 16
- Figure 2.8** Pathways to crystallization and polymorph selectivity: (A) direct and (B) sequential. (Reproduced from [49])..... 17
- Figure 2.9** Sequence of calcium carbonate polymorphs based on Ostwald-Lussac law of stages. 17
- Figure 2.10** Schematic virtual phase diagram that explains the formation of spherical particles by liquid-liquid phase segregation. (Reproduced from [67])..... 18
- Figure 2.11** Abundance of crystalline calcium carbonates as a function of temperature. (Reproduced from [82]). 20
- Figure 2.12** The pressure-temperature phase diagram of $CaCO_3$ 20

- Figure 2.13** SEM image showing the expression of (001) tabular faces in aragonite crystals grown in the presence of Li^+ . Scale bar: 10 μm 21
- Figure 2.14** Complex shapes of $CaCO_3$. (A). Complex $CaCO_3$ superstructure with block copolymers. (Reproduced from [134]) (B) Doughnut-like crystals produced in microemulsion. (Reproduced from [135]) (C) SEM image of vaterite flower-like shape. (Reproduced from [136]) (D) SEM image showing helicoids outgrowth of stacked vaterite disks grown in the presence of linear poly α,β -aspartate. (Reproduced from [91]) (E) A crystalline aggregate containing a helical protrusion resulting from the addition of poly α,L -aspartate. (Reproduced from [114]) (F) Hollow helix fractured by micro-manipulation. (Reproduced from [114]) (G) Cellular film of aragonite synthesized by using a biliquid foam as template. (Reproduced from [137]) (H) Hollow spheres of aragonite with cellular substrate synthesized by using both a biliquid foam and microbeads as templates. (Reproduced from [137]) (I) Templated single crystal of calcite precipitated in the polymeric replica of a sea urchin skeletal plate. (Reproduced from [138]) (J) Calcite crystals grown on colloidal polystyrene monolayer after dissolution of polystyrene spheres, showing the crystal phase growing in contact with the monolayer. (Reproduced from [140]). 25
- Figure 2.15** Scanning electron micrographs illustrating the highly ordered calcareous structure of the chicken eggshell. (a) cross-section through a fully formed eggshell which reveals the eggshell membranes, the cone mammillary layer, the palisade layer and the cuticle; (b) the inner shell membranes showing the network of interlacing fibbers; (c) cross-section through the cone layer showing the insertion of fibbers into the tips of the cone; (d) the vertical crystal layer at the upper part of the palisade layer and the cuticle overlying on the mineralized eggshell. (Reproduced from [146]) 27
- Figure 2.16** The structure of casein micelle in the sub-micelles model showing the protruding C-terminal parts of κ -casein as proposed by Walstra. κ -casein plays a role of colloid protector towards the other caseins. (Reproduced from [150]) 28
- Figure 2.17** Solubility of casein as a function of pH at 20 °C. 1Φ and 2Φ denote the monophasic regions, where casein is highly soluble, and the two-phase precipitation region, respectively. The pH was adjusted by addition of concentrated HCl or $NaOH$ without using a buffer. 29
- Figure 2.18** FESEM images of a selection of various barium-carbonate biomorphs. [Reproduced from García-Ruiz's lecture, Regensburg] 30
- Figure 2.19** A plot of the relative concentrations of species derived from SiO_2 and CO_2 dissociation as a function of pH. (Reproduced from [161]) 31
- Figure 2.20** (A–C) SEM images of sheaf of wheat aggregates with banding calcite structure. (Reproduced from [162]) (D and E). Coral-like (D) and spherical (E) morphologies of aragonite produced with silica gel at pH 10.5. (Reproduced from [163]) 31

- Figure 2.21** Comparison of synthetic filaments with the ancient microfossils. (A) Biomorphs worms synthesized at pH 11. (Reproduced from [164]) (B) Carbonate aggregate in the Martian meteorite ALH84001. (Reproduced from [164]) (C) Raman spectrum of heat-cured biomorphs compared with the spectrum of kerogen-like Warrawoona microfossils. (Reproduced from [155]) (D) Computer-generated twisted spheres..... 33
- Figure 2.22** (A) FESEM images of hollow silica skin left after immersion of the biomorphs in dilute acid. (B) Removal of silica by immersion in weak base, leaving the aggregated carbonate nanorods. (C) As-prepared biomorphs, with the orientational ordering of silica-coated carbonate nanorods indicated by the arrows. (Reproduced from [168]) 33
- Figure 2.23** The coordination number of spherical colloids (N) and their effect on the membrane curvature: $N = 5$ (left), $N = 6$ (center) and $N = 7$ (right). (Reproduced from [172]). 34
- Figure 3.1** Schematic of light scattering experiment. 44
- Figure 3.2** (A) Basic components of a polarizing microscope. (Reproduced from [8]) (B) Light passing through crossed polarizers. 46
- Figure 3.3** Basic components inside the (A) SEM's column and (B) TEM's column. (Redrawn after [9]) 48
- Figure 3.4** Principle regions of the electromagnetic spectrum and the association spectroscopic techniques. (Redrawn after [5])..... 49
- Figure 3.5** Schematic diagram of a Fourier transform instrument..... 51
- Figure 3.6** Basic components of the UV-VIS spectrometer..... 52
- Figure 4.1** FESEM images of calcium carbonate obtained in aqueous solutions in the presence of different lysozyme concentrations: (A) 0, (B) 0.4, (C) 0.7, and (D) 1 g/ L. (E) Histograms of $CaCO_3$ particle size distributions as a function of lysozyme concentration based on FESEM images..... 65
- Figure 4.2** TEM images of (A) ACC grown in the control experiment, i.e., in a lysozyme-free solution and (B) Ly-ACC particles synthesized in 2 g/ L lysozyme solution. 66
- Figure 4.3** XRD pattern of Ly-ACC particles obtained in the presence of 1 g/ L lysozyme and collected after 2 min. 66
- Figure 4.4** FTIR spectra of the $CaCO_3$ solution at various intervals after the rapid mixing of the reactants..... 68
- Figure 4.5** FESEM images of $CaCO_3$ crystals synthesized in the absence (A) and in the presence (B) of 1 g/ L lysozyme. The precipitates were in contact with the mother liquor for 24 h. 70

- Figure 4.6** XRD pattern of CaCO_3 particles obtained in the absence (A) and in the presence (B) of 1 g/ L lysozyme and collected after 24 h. V and C denote peaks from vaterite and calcite, respectively. 70
- Figure 5.1** The light scattering curve obtained after the addition of calcium chloride to alkaline silica solution. $[\text{TEOS}] = 7.5 \text{ mM}$, $[\text{Ca}^{2+}] = 7 \text{ mM}$, $\text{pH} = 11$ 80
- Figure 5.2** The liquid state ^{31}P -NMR spectra of Na caseinate sols in the absence (left) and in the presence (right) of silicate ions at $\text{pH} 11$ and $25 \text{ }^\circ\text{C}$. Protein and silica concentrations were 5 g/ L and 7.5 mM, respectively. 81
- Figure 5.3** Dynamic light scattering curves obtained after rapidly mixing solutions of CaCl_2 with either Na caseinate (\circ) or silica-casein (\bullet) solution. 82
- Figure 5.4** (A) Changes of the absorbance at 280 nm during ageing of casein/ Ca^{2+} solution (\circ) and silica/casein/ Ca^{2+} solution (\bullet). Inset is the enlarged image of the surrounded area. (B and C) Visual observations made during the absorbance measurements showing the transition from colourless sols to either a milky casein/ Ca^{2+} solution (B) or a blue silica/casein/ Ca^{2+} solution (C) within 24 hours. The cuvette labelled with '0 h' corresponds to the solution before the addition of calcium, i.e., Na caseinate solution (B) and alkaline silica-casein solution (C), respectively. 82
- Figure 5.5** The dependence of the average size of $\text{SiO}_2/\text{casein}/\text{CaCO}_3$ three-composite particles as a function of increasing casein concentration. (A to E) Optical micrographs and SEM images of the hemispherical crystals. $[\text{TEOS}] = 7.5 \text{ mM}$, $[\text{Ca}^{2+}] = 7 \text{ mM}$, $\text{pH} = 11$, $t = 24 \text{ h}$ 84
- Figure 5.6** Dependence of the particle size on the reaction time of $\text{SiO}_2/\text{casein}/\text{CaCO}_3$. $[\text{TEOS}] = 7.5 \text{ mM}$, $[\text{casein}] = 1 \text{ g/ L}$, $[\text{Ca}^{2+}] = 7 \text{ mM}$, $\text{pH} = 11$ 85
- Figure 5.7** FESEM images of self-assembled $\text{SiO}_2/\text{casein}/\text{CaCO}_3$ aggregates which show the morphological evolution of the composite. $[\text{TEOS}] = 7.5 \text{ mM}$, $[\text{casein}] = 1 \text{ g/ L}$, $[\text{Ca}^{2+}] = 7 \text{ mM}$, $[\text{EtOH}] = 0.17\%$, $\text{pH} = 11$. (A) Early hemispherical particle with a concavo-convex form that cracks on the concave side. Inset: the material from the particle interior. (B) Hemispherical particle showing how the flat surface cracked to display a star-like shape. Around the crack, silica particle accumulate. (C and D) Hemispherical particles showing how the silica particles penetrate into the surface and the layer-by-layer spheres-like particles inside the crack, respectively. (E) Enlarged image of the silica sphere arrangement. (F) Enlarged image of the multilayered structure and electron diffraction pattern. 87
- Figure 5.8** TEM image of amorphous silica particles with spherulitic morphologies. 88
- Figure 5.9** Crystal fragments from the originally cracked hemispherical particle showing the formation of the layer-by-layer spheres-like particles. 88

Figure 5.10	EDX spectra obtained from the regions C ₁ and C ₂ indicated in Figure 5.9 C.	89
Figure 5.11	FTIR spectrum of the <i>SiO</i> ₂ / <i>casein</i> / <i>CaCO</i> ₃ composites particle.....	90
Figure 5.12	XRD pattern of the <i>SiO</i> ₂ / <i>casein</i> / <i>CaCO</i> ₃ composite particles.	90
Figure 6.1	pH variation with time in the reaction mixture during TEOS hydrolysis at 0.17 vol% (□) and 10 vol% (■) EtOH.....	103
Figure 6.2	Comparison of the light scattering curves obtained after rapidly mixing solutions of <i>BaCl</i> ₂ and TEOS hydrolysed at 0.17 vol% (■) and 10 vol% (□) EtOH.	105
Figure 6.3	SEM images obtained in the presence (A) and absence (B) of TEOS after 1 hour from mixing solutions of <i>BaCl</i> ₂ and TEOS hydrolysed. Scale bar: (A) 1.5 μm (B) 10 μm.	105
Figure 6.4	Optically micrographs of self-assembled silica-carbonate at different EtOH vol%. [TEOS] = 7.5 mM, [<i>Ba</i> ²⁺] = 5 mM, pH = 11, t = 9 h.....	107
Figure 6.5	Zoom sequence of globular aggregates, showing details of the surface texture.	107
Figure 6.6	FESEM images of a selection of various aggregates grown at pH values between 9.5 and 12. [TEOS] = 7.5 mM, [<i>Ba</i> ²⁺] = 5 mM, 0.17 vol% EtOH, t = 9 h, T = 20 °C. (A to C) Zoom sequence of ‘cauliflower’ biomorphs, showing details of the surface structure. (D, E) Helical barium carbonate biomorphs grown at pH = 10.6–11.3. (F) Silica skin, coating the exterior of the helical aggregates (G to I) Non-crystallographic morphologies of <i>BaCO</i> ₃ , showing the orientational ordering of crystallites (insets). (J) Colony-like aggregates of several globules arising from a single crystal core. (K) ‘Hairy’ spheres clusters with strong architectural resemblance to fluoroapatite-gelatin aggregates. (L) Micron-sized rod-like barium carbonate. Inset scale bar: (G) 1.2 μm and (I) 857 nm.	108
Figure 6.7	<i>Si</i> content (relative to <i>Ba</i>) on the surface of a biomorph ‘worm’ at different distances from the bottom of the worm.	109
Figure 6.8	SEM images silica-strontium carbonate biomorphs grown for 5 (A) and 15 h (B) in TEOS solutions (8.9 mM) at pH 11 containing 5 mM <i>Sr</i> ²⁺	110
Figure 6.9	Schematic histogram of <i>CaCO</i> ₃ crystal fractions as a function of the <i>Ca</i> ²⁺ concentration at pH 11, obtained by averaging over many separate samples, incubated in separate runs. Given percentages are estimated values based on visual observation of at least tens of particles under polarized light.	117
Figure 6.10	SEM images of a cluster precipitated in absence (A) and in the presence (B) of silica sols.....	118

- Figure 6.11** (A) Self-assembled ‘coralline’ silica-calcium carbonate. (B, C) High-magnification image of ‘coralline’ silica calcium carbonate showing the orientational ordering of crystallites. (D, E) Different positions of the silica-carbonate composites showing the starting point of nucleation and the orientation of the sheets. (F) Optical micrograph of silica-calcium carbonate aggregates, viewed between crossed polarizers. (G) Carbonate dissolution from the carbonate-silica material, leaving a silica ‘ghost’. (H) Natural coral from the south-eastern Australian seaside. 119
- Figure 6.12** EDX spectrum of self organised silica-calcium carbonate biomorphs. ... 120
- Figure 6.13** High-magnification FESEM images of biomorphs (after acidic leaching of carbonate) showing the silica skeleton. The small spheres may be an artifact of secondary deposition rather than intrinsic components of the biomorph during growth. 120
- Figure 6.14** EDX spectrum of a hollow silica skin left after immersion of the ‘coralline’ silica-calcium carbonate biomorphs in 0.1M *HCl*. 121
- Figure 6.15** XRD spectrum of the self-assembled silica-calcium carbonate. 122
- Figure 6.16** FTIR spectrum of the self-assembled silica-calcium carbonate. 123
- Figure 6.17** (A) TEM image of an amorphous silica particle with spherulitic morphology. (B) Densely packed nanometer sized aragonite needles and (C to F) the corresponding SAED diffraction patterns of a single needle (see arrow) and (G) HRTEM image (zone axis [101]) with simulated micrograph ($\Delta f = 0$ nm, thickness: 2.8 nm) and (H) HRTEM image (zone axis [011]) with simulated micrograph ($\Delta f = 10$ nm, thickness: 2.8 nm). 124
- Figure 6.18** FESEM images of distinct self-assembled silica-calcium carbonate aggregates. The enhanced folding from A to D demonstrates the morphological evolution with time seen in some particles, though these images are not a time-series of a single particle. 125
- Figure 6.19** SEM images of self-assembled ‘coralline’ silica calcium carbonate collected after 3h showing the surface texture of the particle. 126
- Figure 6.20** The additives used in the precipitation of silica-calcium carbonate particles. (1) barium chloride dehydrate ($BaCl_2 \cdot 2H_2O$, $M_w = 244.27$ g/mol); (2) magnesium chloride hexahydrate ($MgCl_2 \cdot 6H_2O$, $M_w = 203.30$ g/mol); (3) cetyltrimethylammonium bromide (CTAB, $M_w = 364.45$ g/mol); (4) sodium dodecylbenzenesulfonate (SDBS, $M_w = 348.48$ g/mol); (5) β -D-glucose ($C_6H_{12}O_6$, $M_w = 180.16$ g/mol); (6) β -D-fructose ($C_6H_{12}O_6$, $M_w = 180.16$ g/mol); (7) β -D-lactose ($C_{12}H_{22}O_{11}$, $M_w = 342.30$ g/mol); (8) casein ($M_w =$ not determined); (9) lysosyme ($M_w = 14$ kDa); (10) lupasol WF ($M_w = 25$ kDa); and (11) ethylenediaminetetraacetic acid disodium salt dihydrate (EDTA, $M_w = 372.24$ g/mol). 134

- Figure 6.21** Optical micrographs of silica-barium carbonate (A–C) and silica-calcium carbonate (D–F) particles obtained when the growth temperatures were 20, 40 and 80 °C, respectively. The hydrolysis of TEOS was carried out at 20 °C. [TEOS] = 7.6 mM; [Ba²⁺] = [Ca²⁺] = 6 mM; pH = 11. 140
- Figure 6.22** XRD spectrum of the CaCO₃ crystals synthesized from alkaline silica solution. [TEOS] = 7.5 mM, [Ca²⁺] = 6 mM, pH = 11, T = 20 °C, t = 24 h. 142
- Figure 6.23** (A) Globules with non-linear swelling obtained at pH 10.5 to 10.8. 143
- Figure 6.24** SEM images of self-organised silica-calcium carbonate clusters obtained when the crystal growth process is conducted at 40 °C..... 143
- Figure 6.25** Optical and SEM micrographs of silica-calcium carbonate clusters obtained when the crystal growth process is conducted at 80 °C..... 144
- Figure 6.26** Optical and SEM images of silica-calcium carbonate clusters obtained when both TEOS hydrolysis and the growth process are performed at 80 °C.. 145
- Figure 6.27** Optical micrographs of calcium carbonate particles synthesized from silica-CTAB solutions. (A) [CTAB] = 0.5 mM; (B) [CTAB] = 1 mM and (C) [CTAB] = 2 mM. 146
- Figure 6.28** Sequence of progressive evolution of calcium carbonate aggregates precipitated from silica–CTAB solution. [CTAB] = 3 mM, [TEOS] = 7.5 mM, [Ca²⁺] = 7 mM, pH 11, T₂ = 20 °C, t = 20 h. 147
- Figure 6.29** The precipitation of calcium (A) and barium (B) carbonate from silica-lactose solution. [TEOS] = 7.6 mM, [Ca²⁺] = [Mg²⁺] = 7 mM, [C₁₂H₂₂O₁₁] = 0.01 M; pH 11, T = 20 °C, t = 20 h..... 148
- Figure 6.30** SEM images of silica calcium carbonate particles precipitated from aqueous solution in the presence of lysozyme 0.7 g/L. [TEOS] = 7.5 mM, [Ca²⁺] = 7 mM, EtOH = 0.17%, pH = 11.9, T = 40 °C, t = 15 h. 149
- Figure 6.31** SEM images of silica calcium carbonate precipitated from aqueous solution in the presence of EDTA 5 mM at 20 °C (left) and 80 °C (right). [TEOS] = 7.5 mM, [Ca²⁺] = 8.5 mM, [EtOH] = 0.17%, pH 11..... 150
- Figure 6.32** Visual observations performed when the hydrolysed TEOS solution (7.5 mM) is mixed with earth-alkaline metal ions (6 mM)..... 151
- Figure 6.33** Comparison of the light scattering curves obtained after rapidly mixing solutions of BaCl₂ (○), CaCl₂ (Δ) and MgCl₂ (☆) with TEOS hydrolysed sols. [MCl₂] = 6 mM, [TEOS] = 7.5 mM..... 152
- Figure 6.34** SEM image (left) of the precipitate obtained immediately after mixing the CaCl₂ with alkaline silica solutions. EDX spectra (right) obtained from the regions ‘A’ indicated on the SEM picture. 152

- Figure 6.35** SEM image of the precipitate obtained after the crystallization process of calcium carbonate as a coproduct. 153
- Figure 6.36** XRD pattern of silica particles obtained after mixing the $CaCl_2$ with alkaline silica solutions. 153
- Figure 6.37** FTIR spectra of the pure SiO_2 (curve a) and the precipitate which formed upon mixing calcium chloride and alkaline TEOS sols (curve b). 154
- Figure 6.38** Solubility of amorphous silica in one molar salt solution at 25 °C compared with some hydration numbers for cations. (Redrawn after [19]). The hydration numbers are from Rombinson et al.²⁰ 155
- Figure 6.39** Effect of temperature on silica polymerisation. (Reproduced from [1]). 157
- Figure 8.1** ES-MS spectrum of the lysozyme (based on the ions with 9 H^+) in the absence (a) and in the presence of calcium ions: (b) 10 mM, (c) 20 mM and (d) 50mM. The peak codes represent the calculated values obtained from each spectrum. 168
- Figure 8.2** FTIR spectra of the pure lysozyme (curve a) and Ly-ACC (curve b) particles. 169
- Figure 8.3** Self-assembled ‘floral dumbbell’ silica-calcium carbonate. (A to C) Zoom sequence, showing details of the surface texture. (D and E) High-magnification FESEM images of biomorphs (after alkaline leaching of silica) showing the orientational ordering of aragonite crystallites. (F to H) Optical micrographs of the aggregates, viewed under crossed polarizers, showing the progressive dissolution in dilute hydrochloric acid of aragonite from the carbonate-silica material, leaving a silica ‘ghost’. A–E show only half of the complete aggregate. 172
- Figure 8.4** Optical micrograph of silica-calcium carbonate aggregates, viewed between crossed polarizers, which shows the growing sequence of a floral dumbbell structure. 172

8.7. List of Tables

<i>Table 2.1</i>	Crystallographic and physical data of the different calcium carbonate phases. (The table is partly based on that in [49])	15
<i>Table 2.2</i>	Influence of additives on the yield of vaterite (<i>V</i>), calcite (<i>C</i>) and aragonite (<i>A</i>)	23
<i>Table 3.1</i>	Characteristic bands for $CaCO_3$. (Reproduced from [13]).....	51
<i>Table 6.1</i>	The experimental series.....	133
<i>Table 6.2</i>	The electrolyte ($T_2 = 20$ or 40 °C) as well as the surfactant ($T_2 = 20, 40$ or 80 °C) concentrations in the alkaline silica sols (TEOS 7.6 mM; EtOH 0.17 mM; pH 11 ; $T_1 = 20$ °C).....	135
<i>Table 6.3</i>	The Ca^{2+} and sugar concentrations in the alkaline silica solution (TEOS 7.6 mM; EtOH 0.17 mM; pH 11 ; $T_1 = 20$ °C). The temperature, T_2 , at which the growth period takes place, is 20 °C or 40 °C.....	136
<i>Table 6.4</i>	Lysozyme and lupasol WF concentrations in the alkaline TEOS sols (TEOS 7.6 mM; EtOH 0.17 mM; $T_1 = 20$ °C) as well as the temperature at which the growth period take place. The pH values cited are the adjusted values of the alkaline silica solution before adding the Ca^{2+} ions.....	137
<i>Table 6.5</i>	The $CaCl_2$ and EDTA concentrations in the alkaline silica sols (TEOS 7.6 mM; EtOH 0.17 mM; $T_1 = 20$ °C) as well as the temperature at which the growth period take place.....	138
<i>Table 6.6</i>	Pauling crystallographic radii ²¹ (r), Stokes hydrated radii ²² (r_{hy}) and the first order hydration number ²³ (H) of earth-alkaline cations.....	156

8.8. List of Publications and Presentations

8.8.1. Publications

1. **Alina E. Voinescu**, D. Touraud, A. Lecker, A. Pfitzner, W. Kunz and B. W. Ninham *The mineralization of CaCO₃ in the presence of egg white lysozyme*, **Langmuir** **2007**, 23(24), 12269–12274
2. **Alina E. Voinescu**, M. Kellermeier, A. M. Carnerup, A. Larsson, D. Touraud, W. Kunz and S. T. Hyde *Co-precipitation of silica and alkaline-earth carbonates using TEOS as silica source*, **J. Cryst. Growth** **2007**, 306, 152–158
3. **Alina E. Voinescu**, P. Bauduin, M. C. Pinna, D. Touraud, B. W. Ninham, and W. Kunz *Similarity of salt influences on the pH of buffers, polyelectrolytes and proteins*, **J. Phys. Chem. B** **2006**, 110, 8870–8876
4. **Alina E. Voinescu**, M. Kellermeier, B. Bartel, A. M. Carnerup, A. Larsson, D. Touraud, W. Kunz and S. T. Hyde *Inorganic self-organised silica-aragonite biomorphic composites*, **J. Cryst. Growth & Design** **2008** (accepted)
5. **Alina E. Voinescu**, D. Touraud, A. Lecker, A. Pfitzner, L. Kienle, W. Kunz *Initiation of vaterite-aragonite particles from silicate-casein sols* **J. Phys. Chem. C** **2008** (to be submitted)

8.8.2. Presentations

8.8.2.1. Oral Presentations:

1. *Biomorphs-like calcium carbonate-silica aggregates*, International Conference of Physical Chemistry, Romphyschem-12, Bucharest, Romania, September 06th – 08th, 2006
2. *pH and specific ionic effects in buffer, polyelectrolyte and protein solutions – a comparative study*, 29th International Conference on Solution Chemistry, Portorož, Slovenia, August 21st – 25th, 2005
3. *Why NaCl decreases the milk pH and increases the pH of human eyes?* Institute of Physical and Theoretical Chemistry, University of Regensburg, Germany, November 30th, 2004

8.8.2.2. Presentations of Posters

1. *Studiul cinetic al reactiei de obtinere a intermediarului cheie in prepararea moscurilor nitrice*, 8th Romanian International Symposium of Cosmetic and Flavor Products, Iassy, Romania May 29th – June 01st 2007

2. *Influence of lysozyme on the formation of calcium carbonate particles*, Faraday Discussion 136: Crystal Growth and Nucleation, University College London, United Kingdom, April 02nd–04th 2007
3. *Silica-alkaline-earth carbonate biomorphs*, Tag der Naturwissenschaften, University of Regensburg, Regensburg, Germany, October 15th–18th, 2007
4. *pH and specific ionic effects in buffer, polyelectrolyte and protein solutions – a comparative study*, 29th International conference on Solution Chemistry, Portorož, Slovenia, August 21st – 25th, 2005
5. *The influence of pH and additives on the precipitation of amorphous and crystalline calcium carbonate*, 29th International Conference on Solution Chemistry, Portorož, Slovenia, August 21st – 25th, 2005
6. *Striking similarity of salt influences on the pH of buffers, polyelectrolytes and proteins*, 4th World Congress of Cellular and Molecular Biology, Poitiers, France, October 07th – 12th, 2005

8.9. Curriculum Vitae

Personal Information

Born	Iasi, Romania, April 19, 1980
Nationality	Romanian
Marital Status	Single

Education

02/2005 onwards	<i>PhD Student</i> , Institute of Physical and Theoretical Chemistry, University of Regensburg, Germany in collaboration with Department of Applied Mathematics, Australian National University, Australia
10/2002–09/2004	<i>Master of Science</i> , Colloidal Chemistry Department, University of Al.I.Cuza, Romania, in collaboration with the Department of Solution Chemistry, University of Regensburg, Germany
10/1998–09/2002	<i>University Degree</i> , Faculty of Chemistry, University of Al. I. Cuza, Romania

Work Experience

02/2005–05/2008	Teaching Assistant on 3 topics: pH determination with the glass electrode, Liquid-solid phase diagram, Biomorphs, University of Regensburg, Germany
10/2004–02/2005	Research Student organising laboratory rooms, lab equipment and chemicals, University of Regensburg, Germany
09/2003–09/2004	Research Student working on the formulation of a universal solubiliser for perfumes and a deodorising fragrance for cat litter, University of Regensburg, Germany
10/2001–10/2002	Training of high school pupils in chemistry and physics, University of Al.I.Cuza, Romania

Scientific Activity 5 publications and 6 posters (see Appendix 8.8)

Visiting Academic

07/2006	University of Erlangen, Erlangen, Germany
09/2005–12/2005	Department of Applied Mathematics, Research School of Physical Sciences, Australian National University, Canberra, Australia
02/2005	Max Planck Institute for Polymer Research, Mainz, Germany

Awards

10/2002–07/2003	Socrates-Erasmus Scholarship, University of Regensburg, Germany
10/1998–07/2002	Praiseworthy Grand, University of Al. I. Cuza, Romania

Declaration

I hereby declare that this thesis, apart from the help recognized, is my own work and effort, and it has not been formerly submitted to another university for any award.

.....
(Alina-Elena Voinescu)

Regensburg, April 2008